Post-Processing of the Additively Manufactured Biomedical Implants through Hybrid Electrochemical Magnetorheological Finishing Process

A thesis submitted

in partial fulfillment of the requirements

for the degree of

Doctor of Philosophy

By

Atul Singh Rajput

(196103009)

Under the guidance of

Dr. Manas Das and Dr. Sajan Kapil

Department of Mechanical Engineering

Indian Institute of Technology Guwahati

Guwahati- 781039

November 2023

Department of Mechanical Engineering
Indian Institute of Technology Guwahati
Guwahati-781039
INDIA

CERTIFICATE

It is certified that the work contained in the thesis entitled "**Post-Processing of the Additively Manufactured Biomedical Implants through Hybrid Electrochemical Magnetorheological Finishing Process**", submitted by **Atul Singh Rajput**, Roll No. **196103009** to the Indian Institute of Technology Guwahati for the degree of Doctor of Philosophy has been carried out under my supervision in the Department of Mechanical Engineering, Indian Institute of Technology Guwahati. This work has not been submitted elsewhere for any other degree or diploma award.

In my opinion, the thesis has reached the standard of fulfilling the requirements for the award of degree of Doctor of Philosophy in accordance with the institute's regulations.

21/08/2023

Dr. Sajan Kapil
Deaprtment of Mechanical Engineering
Indian Institute of Technology Guwahati
Guwahati-781039, Assam, India

21/08/2023

Dr. Manas Das
Deaprtment of Mechanical Engineering
Indian Institute of Technology Guwahati
Guwahati-781039, Assam, India

Declaration

I declare that this written submission represents my ideas in my own words, and where others' ideas or words have been included, I have adequately cited and referenced the sources. I also declare that I have adhered to all principles of academic honesty and integrity and have not misrepresented or fabricated or falsified any idea/data/fact/source in my submission. I understand that any violation of the above will cause disciplinary action by the Institute and can also evoke penal action from the sources which have thus not been properly cited or from whom proper permission has not been taken when needed.

Date: 21/8/2023

Atul Singh Rajput (21/8/23)

Atul Singh Rajput

Roll No. 196103009

Dedicated to

माँ एवं पिताजी

ACKNOWLEDGEMENT

I would like to take this opportunity to pay my deep sense of respect and sincere gratitude to my supervisors Dr. Manas Das and Dr. Sajan Kapil, Department of Mechanical Engineering, Indian Institute of Technology Guwahati, Assam-781039, for their invaluable advice, resourceful guidance, inspiring instructions, active supervision and constant encouragement without which it would not have been possible for me to reach to this point.

I also wish to thank my doctoral committee members, Dr. Deepak Sharma, Dr. Pankaj Biswas, and Dr. Sandip Das for their guidance, moral support and encouragement to my ideas in the subject and other areas of innovations. I must not miss the opportunity to thank all the Professors of the Mechanical Engineering Department, Indian Institute of Technology Guwahati, whose motivation and timely help molded me in all possible forms.

I am very much thankful to workshop superintendent Mr. N. K. Das and workshop technicians Mr. Mrinal Sarma, Mr. Dipak Kr. Deka, Mr. Upen Gohain, and Mr. Dhaneswar Khaklary for their help in fabricating my experimental setup and workpieces. I would like to acknowledge the Central instrument facility (CIF), Department of Physics, Department of Chemistry, North East Centre for Biological Science and Healthcare Engineering of IIT Guwahati for their kind assistance in my research work.

I thankfully acknowledge Science & Engineering Research Board (SERB), New Delhi, India, for financial support for project No. EEQ/2017/000597 entitled "Fabrication of Prosthetic Implants and further Nanofinishing Using Magnetic Field Assisted Finishing (MFAF) Process" and Department of Science and Technology (DST), New Delhi, India, for financial support for project No. SR/FST/ET-II/2017/111 (C) under Fund for Improvement of S&T Infrastructure in Universities and Higher Educational Institutions (FIST) Program. I also acknowledge Technology Innovation Hub (TIH), IIT Guwahati, to provide experimental facilities. I am deeply indebted to my family for the sacrifices they have borne to ensure the fulfillment of my dreams.

The time I spent with all my friends and seniors at IIT Guwahati, Ambrish Singh, Anand Mohan Pandey, Ritam Sarma, Ranajit Mahanti, Hari Narayan Singh Yadav who made my life enjoyable and memorable on the campus. I would also like to thank Umesh, Satish, Abhishek, Phul, Abhijit, and Shafique of the 3D printing and precision manufacturing lab.

Atul Singh Rajput 21/8/23

Atul Singh Rajput

ABSTRACT

Additive Manufacturing (*AM*) or 3D printing provides the benefits of individualizing the implant per patient requirements. However, the poor surface quality of additively manufactured components is a major limitation as it increases its wear rate on their tribological interaction. The higher wear rate increases the generation of debris particles, spread inside the human body through blood circulation, responsible for the systematic toxicity of various organs, including kidneys, eyes, levers, etc. Furthermore, these small metal particles cause Aseptic Loosening or *Adverse Reactions to Metal Debris* (*ARMD*), which may instigate *Aseptic Lymphocytic Vasculitis and Associated Lesions* (*ALVAL*) or Pseudotumours, inflammatory masses and metal hypersensitivity. Therefore, this work proposed a novel post-processing method to improve the surface quality of additively manufactured alloys. *Hybrid Electrochemical Assisted Magnetorheological* (*H-ECMR*) utilizes the synergic action of mechanical abrasion and electrochemical reaction to enhance the surface quality of the parts without affecting their surface topography. The electrochemical reaction forms a uniform and thick oxide layer on the Ti-6Al-4V surface as layer thickness increases to 78 nm from its initial value of 8 nm, further improving its corrosion resistance. This work details the working principle of the H-ECMR finishing process with an analysis of the impact of process parameters on the reduction in surface roughness.

Various features (including holes and pockets) on the workpiece surface produce a challenge during their polishing through the H-ECMR finishing process; the *Carbonyl Iron Particles* (*CIPs*) chains get trapped inside the holes during the finishing operation and generate irregular surface quality on the polished surface. The present work outlines a *Feature-based Hybrid MRF Planning System* (*FHMRF-PS*) developed based on the geometrical data inputs to produce automated process planning for the paraffin wax deposition into the hole and pocket features of the workpiece before the H-ECMR finishing. An external module is developed to deposit paraffin wax in the holes and pockets to ensure a uniform finish over the target surface. Moreover, as the H-ECMR finishing is a CNC-based polishing method, an appropriate toolpath is required to map the workspace to produce uniform surface quality. This work investigates different toolpath strategies such as Zig-Zag, Hilbert, Peano, Spiral, and Trochoidal for the H-ECMR finishing process. A comparison is made among these toolpaths on the magnitude of the final surface roughness (R_a) and its variation on the finished profiles on a similar domain with the same process parameters. Moreover, a critical analysis is made on the Trochoidal

toolpath to determine the factors affecting the surface quality during the polishing as it produces uniform surface roughness compared with other toolpath strategies.

The *H-ECMR* finishing process effectively applies to parts with initial *surface roughness* (R_a) in the sub-micron range. Hence, chemical etching or milling operation is used as an intermediated process after fabricating the Ti-6Al-4V biomedical implants by *Laser Powder Bed Fusion* (*LPBF*) or *Selective Laser Melting* (*SLM*) to reduce the surface roughness in the sub-micron range. The surface finishing operation is performed on the Ti-6Al-4V femoral head and bone plate to improve its surface quality and biocompatibility. Moreover, Scanning Electron Microscope (SEM), Atomic Force Microscope (AFM), and optical profilometer are used to examine the change in the surface quality before and after post-processing of the LPBF fabricated femoral head. The laser scanning study confirms that the femoral head's dimensional accuracy remains intact during the H-ECMR finishing process. The *average surface roughness* (R_a) value is reduced to 33.14 nm from its initial surface roughness value of 14.67 µm after the H-ECMR finishing to produce a mirror-like polished femoral head surface. The wear, corrosion, and wettability tests signify that the biocompatibility of the fabricated parts is enhanced after post-processing. The corrosion rate for the LPBF manufactured Ti-6Al-4V is 0.081 mm/year, further reduced to 0.0103 mm/year after the chemical etching as surface irregularities of LPBF fabricated surface are very high, creating the grooves for confined corrosion products. The wear rate value on the final polished surface is further reduced to 0.0046 mm/year as an electrochemical reaction during the H-ECMR finishing process, providing a uniform and thick passive oxide layer on the surface of Ti-6Al-4V. The wear rate corresponding to the LPBF fabricated, chemically etched, and polished surfaces are 18.86×10^{-5}, 6.36×10^{-5}, and 0.96×10^{-5} mm^3/min, respectively. A negative skewness and the kurtosis value of less than three after post-processing the LPBF fabricated Ti-6Al-4V is a primal reason for the enhancement in the wear resistance of the biomaterial.

CONTENTS

Abstract i

List of Figures vii

List of Tables xiii

CHAPTER 1 INTRODUCTION AND LITERATURE REVIEW **1**

1.1 Introduction **1**

1.2 Additively manufactured biomedical implants **2**

1.3 Motivation **6**

1.4 Methods for surface finishing of prosthesis **9**

1.4.1 Abrasive flow finishing 10

1.4.2 Large-area electron beam irradiation 12

1.4.3 Electropolishing 13

1.4.4 Electrolytic in-process dressing (ELID) grinding 15

1.4.5 Chemical mechanical polishing 17

1.4.6 Magnetorheological assisted finishing (MFAF) 19

1.5 Selection of a suitable surface super-finishing process **23**

1.5.1 Surface finishing parameters 23

1.5.2 Biocompatibility 23

1.6 Scope and objectives of present work **25**

1.7 Organization of thesis **25**

CHAPTER 2 DEVELOPMENT OF MAGNETORHEOLOGICAL FLUID ASSISTED FINISHING PROCESS **27**

2.1 Introduction **27**

2.2 Permanent magnet-based MFAF process **28**

2.3 Experimental details **28**

2.3.1 Methodology 30

2.3.1.1 Standoff distance 30

2.3.2 Determination of magnetostatic scalar potential for cylindrical magnet 31

2.3.3 Polishing tool speed 35

2.3.4 Polishing tool feed rate 35

2.4 Electromagnet-based MFAF process **36**

2.5 H-ECMR finishing principle and polishing medium **38**

2.6 Experimental setup **42**

2.7 Analytical model of H-ECMR finishing **44**

2.7.1 Normal indentation force (F_n) 49

2.7.2 Tangential force (F_t) 51

2.7.3 Surface roughness modeling 52

2.8 Results and discussion **54**

2.8.1 Impact of mu-metal on effectiveness of polishing tool 54
2.8.2 Impact of process parameters 56
2.8.2.1 Rotational speed of polishing tool 56
2.8.2.2 Electrolyte concentration (Vol. %) 56
2.8.2.3 Finishing time 57
2.8.2.4 Applied current 58
2.8.3 Characterization of workpiece surface 58
2.8.4 Oxide layer thickness 62
2.9 Summary 64
CHAPTER 3 COMPUTER AIDED PROCESS PLANNING FOR H-ECMR FINISHING 67
3.1 Introduction 67
3.2 Feature-based hybrid MRF planning system 67
3.2.1 Process planning 67
3.2.2 FHMRF-PS decision path 68
3.2.3 External deposition module 70
3.2.4 Various area-filling toolpath strategies during H-ECMRF 72
3.2.5 Zig-Zag Toolpath 74
3.2.6 Fractal curves-based toolpaths 75
3.2.7 Spiral toolpath 76
3.2.8 Trochoidal toolpath 76
3.3 Analytical model 78
3.4 Methodology 79
3.5 Results and discussion 80
3.5.1 Surface improvement of workpiece having holes and pockets 80
3.6 Impact of underfilling and overfilling 82
3.7 Different area-filling toolpath strategies 84
3.8 Critical analysis of trochoidal toolpath 91
3.8.1 Process modeling 92
3.8.1.1 Engagement angle 93
3.8.1.2 Finishing force modeling for trochoidal toolpath 96
3.8.1.3 Stepover 98
3.8.2 Comparison between Trochoidal and zig-zag toolpath 100
3.8.3 Experimental investigation on Trochoidal toolpath process parameters on surface roughness 102
3.8.3.1 Regression analysis 103
3.8.3.2 Stepover 107
3.8.3.3 Curve radius 108
3.8.3.4 Feed rate 108
3.9 Summary 112

CHAPTER 4 POST-PROCESSING OF ADDITIVELY MANUFACTURED IMPLANTS 113

4.1 Introduction 113

4.1.1 Post-processing of femoral head 116

4.1.1.1 Methodology 118

4.1.1.2 Chemical etching 119

4.1.1.3 Hybrid-electrochemical magnetorheological finishing 122

4.1.1.4 Results and discussion 124

4.1.2 Post-processing of bone plate 130

4.1.2.1 Surface quality 134

4.1.2.2 Abbott-Firestone curve 135

4.1.3 Metallurgical analysis 137

4.1.4 Biocompatibility test 139

4.1.4.1 Wettability test 139

4.1.4.2 Corrosion test 140

4.1.4.3 Wear test 142

4.2 Summary 144

CHAPTER 5 CONCLUSIONS AND FUTURE PLAN 147

5.1 Conclusions 147

5.1.1 Development of Magnetorheological Fluid Assisted Finishing process 147

5.1.2 Computer-aided process planning of H-ECMR finishing process 148

5.1.3 Surface enhancement of additively manufactured implants 149

5.2 Scope for future work 149

APPENDIX A ..MAGNETORHEOLOGICAL FLUID ASSISTED FINISHING (MFAF) PROCESS 153

A.1 Introduction 153

A.2 Magnetorheological fluid (MR fluid) 153

A.3 MR fluid assisted finishing processes 157

A.4 Critical analysis 166

APPENDIX B. NANOFINISHING OF DIRECTED ENERGY DEPOSITED TOPOLOGICALLY OPTIMIZED BONE PLATES 169

B.1 Introduction 169

B.2 Methods and materials 172

B.3 Experimental details 175

B.4 Results and discussion 177

References 183

Publications 201

List of Figures

Fig. 1.1 Biomedical prostheses for different body parts 1
Fig. 1.2 Conventional manufacturing Vs. additive manufacturing 4
Fig. 1.3 Types of additive manufacturing processes 5
Fig. 1.4 Classification of powder during Laser Powder Bed Fusion (PBF) and different surface defects on fabricated surface 7
Fig. 1.5 Impact of poor surface quality on additively manufactured implant 9
Fig. 1.6 Different finishing processes based on utilization of energy 10
Fig. 1.7 Surface roughness of knee implant at different faces 11
Fig. 1.8 Different parts of a knee prosthesis with surgical tools [36] 13
Fig. 1.9 Hip implant after ELID grinding [53] 16
Fig. 1.10 Placing implant in animal experiment [55] 17
Fig. 1.11 Surface modification of titanium dental implant (a) SEM image showing oxide layer to prevent bacterial growth, (b) implant without any surface treatment, and (c) dental implant [68] 18
Fig. 1.12 Surface roughness (R_a) obtained by different finishing processes 20
Fig. 1.13 Classification of finishing processes 20
Fig. 1.14 Finishing tool (a) bonded tool (i.e., grinding), (b) unbonded tool (i.e., ball end magnetorheological finishing) 21
Fig. 1.15 Formation of chain-like structure of magnetorheological fluid (a) in normal condition and (b) influenced by an external field 22
Fig. 1.16 Classification of MFAF process based on working principle 22
Fig. 2.1 Permanent magnet and electromagnet-based MFAF process 27
Fig. 2.2 Distribution of magnetic field due to permanent magnet on (a) ferromagnetic (b) non-ferromagnetic workpiece 29
Fig. 2.3 Experimental setup of magnetorheological finishing 29
Fig. 2.4 Energy Dispersive X-ray analysis of Mu-meatal 30
Fig. 2.5 Schematic of a cylindrical shaped magnet 31
Fig. 2.6 Magnetic field variation at different standoff distances (z) 34
Fig. 2.7 Magnetic field variation along axial direction of polishing tool 34
Fig. 2.8 Comparison between reduction in average surface roughness and finishing time for permanent magnet-based MFAF process 36
Fig. 2.9 Different categories of skewness and kurtosis 38
Fig. 2.10 Magnetorheological fluid with and without influence of external magnetic field and mechanism of material removal during magnetorheological finishing process 39
Fig. 2.11 (a) Chemical reactions at electrodes and (b) formation of uniform and thick oxide layer on Ti alloy surface during electrochemical reactions 42
Fig. 2.12 Hybrid-electrochemical magnetorheological (H-ECMR) finishing experimental setup 44
Fig. 2.13 a) Magnetic flux generated inside electromagnet core and (b) equivalent magnetic circuit 46

Fig. 2.14 M-H curve comparison between (a) pure iron and mild steel and (b) electrolytic iron and carbonyl iron (CIPs) particles 47
Fig. 2.15 (a) Contour plot of simulated magnetic field at different standoff distances and (b) comparison of magnitude of magnetic field between simulation study, experimental measurement, and analytical model 49
Fig. 2.16 (a) Variation of normal force with standoff distance at different applied electromagnet current and (b) magnetic field variation with applied current for different standoff distances from tool tip 50
Fig. 2.17 (a) Abrasive particle indented into workpiece surface, (b) diameter and depth of indented abrasive particle, and (c) M-H curve of MR fluid 52
Fig. 2.18 Surface irregularities (a) before and (b) after polishing; (c) Flowchart showing algorithm to calculate final surface roughness profile 53
Fig. 2.19 Simulation study of polishing tool (a) with and (b) without mu-metal 55
Fig. 2.20 Variation of magnetic field (a) along axial direction (i.e., Z axis) from tool tip and (b) EDX study for mu-metal composition 55
Fig. 2.21 Variation of percentage reduction in % reduction in R_a with (a) rotational speed of polishing tool and (b) electrolyte concentration (Vol. %) in MR fluid 57
Fig. 2.22 Variation of % reduction in R_a with (a) finishing time and (b) applied current 58
Fig. 2.23 Comparison between (a) area and (b) linear surface roughness profiles before and after finishing 59
Fig. 2.24 Kurtosis Vs. skewness mapping, and workpiece images from atomic force microscope and scanning electron microscope before and after polishing 60
Fig. 2.25 Comparison of Avg. surface roughness between (a) H-ECMR and MRF at different finishing times and (b) experimental measurement and analytical model at different standoff distances 61
Fig. 2.26 Comparison between oxide layers by EDX, SEM, XPS studies on Ti-6Al-4V biomaterial surface before and after H-ECMR finishing process 63
Fig. 2.27 Depth profiles of different constituents on Ti-6Al-4V surface (a) before and (b) after finishing using XPS analysis 64
Fig. 3.1 Flow chart of feature-based hybrid MRF planning system (FHMRF-PS) 69
Fig. 3.2 (a) STL file representation of a hole and (b) toolpath generation for deposition at different holes 70
Fig. 3.3 (a) Flow chart for feature extraction & recognition and hole depth and Vol. calculation, and (b) algorithm for toolpath generation for depositing paraffin wax 70
Fig. 3.4 Schematic diagram of external module to deposit paraffin wax 71
Fig. 3.5 Schematic diagram of dewaxing process 72
Fig. 3.6 Different toolpaths (a) Zig-Zag, (b) Hilbert, (c) Peano, (d) Spiral, and (e) Trochoidal 73
Fig. 3.7 Trajectory of abrasive placed at tool periphery during Zig-Zag toolpath 75
Fig. 3.8 Trajectory of abrasive placed at tool periphery during Trochoidal toolpath 77
Fig. 3.9 MR fluid under (a) normal, (b) squeezed condition, (c) unstable due to holes, and (d) trapped in hole . 81
Fig. 3.10 Optical microscopic images of trapped MR fluid inside holes of diameter (a) 2 mm, (b) 2.5 mm, (c) 3 mm, and (d) 3.5 mm 82
Fig. 3.11 Flat Ti-6Al-4V plates with holes (a) before and (b) after polishing 82
Fig. 3.12 Schematic diagrams showing finishing mechanism of holes in bone plate by MRF (a) without paraffin wax, (b) overfilled with paraffin wax, and (c) paraffin wax trapped in MR fluid while polishing 83

Fig. 3.13 Impact of % overfilling of paraffin wax on (a) yield stress and viscosity of MR fluid, and (b) surface roughness 84
Fig. 3.14 Schematic diagrams showing finishing mechanism of holes in bone plate by MRF (a) without paraffin wax, (b) underfilled with paraffin wax, and (c) MR fluid trapped in hole while polishing 84
Fig. 3.15 Surface roughness (R_a) obtained through the Zig-Zag toolpath from 223 nm to 4.81 nm 85
Fig. 3.16 Surface roughness at the change in the direction of polishing tool 85
Fig. 3.17 Surface roughness (R_a) obtained through Hilbert toolpath from 314 86
Fig. 3.18 Surface roughness (R_a) obtained through Peano toolpath from 335 to 10.23 nm 86
Fig. 3.19 Surface roughness (R_a) obtained through spiral from 243 nm to R_a = 6.12 nm 87
Fig. 3.20 Roughness (R_a) obtained through Trochoidal toolpath from 379 nm to 1.06 nm 87
Fig. 3.21 Scratch marks during the abrupt change in the direction of the polishing tool using a) Zig-Zag toolpath b) Hilbert c) Peano 89
Fig. 3.22 Optical microscopic images of (a) unfinished workpiece, at (b) start, (c) end, and (d) center of Trochoidal toolpath 90
Fig. 3.23 Difference between surface profile for trochoidal and zig-zag with same effective length 91
Fig. 3.24 Different models of Trochoidal toolpaths (a) circular with clockwise direction, (b) circular with counterclockwise direction, (c) *TR* model with clockwise direction, and (d) *TR* model with counterclockwise direction 92
Fig. 3.25 Tool engagement angle during (a) Zig-Zag and (b) Trochoidal toolpath 93
Fig. 3.26 Polishing tool located on the Trochoidal toolpath 94
Fig. 3.27 Relation between inclination angle and tool engagement angle for (a) stepover and (b) radius of Trochoidal curve 95
Fig. 3.28 Deflection in MR fluid chain during (a) Trochoidal and (b) Zig-Zag toolpaths 97
Fig. 3.29 Impact of step over during the Trochoidal toolpath 99
Fig. 3.30 Three-dimensional surface plot for area of uncovered region (Au) 99
Fig. 3.31 Comparison between chain deflection between (a) Trochoidal and (b) Zig-Zag toolpaths 100
Fig. 3.32 Comparison between angle of deflection during (a) finishing operation and (b) stationary condition 100
Fig. 3.33 Comparison between the Skewness and Kurtosis for Trochoidal and Zig-Zag toolpath at different stepovers 102
Fig. 3.34 F-value corresponds to different process parameters combination 105
Fig. 3.35 Comparison between the experimental and predicted results for (a) surface roughness (R_a), (b) kurtosis (R_{ku}), (c) Skewness (R_{sk}), and (d) finishing time (T) 106
Fig. 3.36 Impact of stepover on the (a) uncovered area, finishing time, and (b) surface roughness parameters 107
Fig. 3.37 Variation of surface roughness parameters with (a) radius of Trochoidal curve (b) feed rate 108
Fig. 3.38 Scanning electron microscopic images of SS316L (a) powder particles and (b) enlarged view of a single particle 109
Fig. 3.39 Surface defects showing (a) unmelted powder and (b) pores on SLM fabricated workpiece surface using SS316L powder 110
Fig. 3.40 1D and 2D surface roughness profiles on selective laser melted, milled, and H-ECMR polished surfaces 111

Fig. 3.41 Optical microscopic images of (a) SLM fabricated, (b) milled, (c) H-ECMR polished surfaces.....111
Fig. 4.1 Case study on surface enhancement of bone plate and femoral head fabricated through powder bed fusion 113
Fig. 4.2 Schematic diagram explaining working principle of selective laser melting (SLM) 115
Fig. 4.3 Flowchart of present work, including pre-processing, motivation, and post-processing of the femoral head surface.....117
Fig. 4.4 Experimental setup and chemical reactions at Ti-6Al-4V surface during chemical etching 122
Fig. 4.5 (a) CAD model and (b) experimental setup for H-ECMR finishing process of femoral head 123
Fig. 4.6 Impact of (a) HF concentration and (b) polishing time during chemical etching 125
Fig. 4.7 1D and 2D surface profile before and after chemical etching 126
Fig. 4.8 1D and 2D surface roughness profiles, atomic force microscopic, scanning electron microscopic images of femoral head surface before and after chemical etching 127
Fig. 4.9 1D and 2D surface roughness profiles, atomic force microscopic, scanning electron microscopic images of femoral head surface before and after H-ECMR finishing.....128
Fig. 4.10 Kurtosis Vs. skewness plot for LPBF fabricated, chemically etched, and H-ECMR finished surfaces 128
Fig. 4.11 (a) Thermal analysis and (b) temperature variation along line AB during H-ECMR finishing process; Comparison between femoral heads surface topography (c) before and (d) after H-ECMR finishing .130
Fig. 4.12 Workflow of feature-based hybrid MRF planning system (FHMRF-PS) 132
Fig. 4.13 (a) Flow chart of FHMRF-PS for bone plate and (b) determination of hole dimension from STL file 133
Fig. 4.14 Overview of feature-based hybrid MRF planning system (FHMRF-PS) for H-ECMR finishing of bone plate 133
Fig. 4.15 Surface profiles of bone plate (a) initial surface, after (b) milling and (c) H-ECMRF process.....135
Fig. 4.16 Abbott-Firestone curves for (a) SLM fabricated, (b) milled, and (c) H-ECMR polished surfaces 136
Fig. 4.17 Surface reflectance for (a) SLM fabricated, (b) milled, and (c) H-ECMR polished surfaces 137
Fig. 4.18 Optical microscopic images of (a) SLM fabricated, (b) milled, (c) H-ECMR polished surfaces.....138
Fig. 4.19 Optical microscopic images of workpiece cross-section and zoomed view on a spot for (a) SLM fabricated, (b) milled, and (c) H-ECMR polished surfaces.....138
Fig. 4.20 Contact angle on LPBF fabricated, chemically etched, and H-ECMR finished surfaces.....140
Fig. 4.21 (a) Experimental setup for corrosion test, (b) potentiodynamic polarization behavior of LPBF fabricated, chemically etched, and H-ECMR finished surfaces, and (c) pits on polished surface of biomaterial after corrosion test.....141
Fig. 4.22 (a) Wear experimental test set up, (b) coefficient of friction, and (c) wear rate for LPBF fabricated, chemically etched, and H-ECMR finished surfaces 143
Fig. 4.23 Schematic diagram explaining mechanism of (a) two-body, (b) three-body abrasive wear during H-ECMR process, and (c) scanning electron microscopic image of polished surface.....144
Fig. 5.1 Toolpath for freeform surfaces.....151
Fig. A.1 Features of MR fluid.....154
Fig. A.2 Features of an MR fluid timeline of the development of magnetorheological fluid-assisted finishing process.....157

Fig. A.3 Schematic diagram of MRF process……158
Fig. A.4 (a) Detailed view of MRF process and (b) forces acting on abrasive……159
Fig. A.5 Ishikawa cause and effect diagram of MRF process……..159
Fig. A.6 Tool design of disc-based magnetorheological finishing……160
Fig. A.7 BEMRF tool with different components……161
Fig. A.8 Material removal in BEMRF process (a) tip of tool embedded with MR fluid approaching for finishing process, (b) enhanced surface roughness after removing some workpiece material, and (c) final surface roughness after removing undulations from workpiece surface……161
Fig. A.9 Ishikawa cause and effect diagram of BEMRF……. 162
Fig. A.10 Experimental setup of MRAFF with different components……163
Fig. A.11 Finishing action of an abrasive on a single peak: (a) abrasive particle rolling over roughness peak, (b) abrasive particle takes a small cut on roughness peak, and (c) abrasive grain takes a big cut on roughness peak……..163
Fig. A.12 Ishikawa cause and effect diagram of MRAFF process……..164
Fig. A.13 Experimental setup of R-MRAFF……165
Fig. A.14 Traced path of a single abrasive particle on cylindrical workpiece during (a) R-MRAFF, (b) MRAFF, and (d) different forces acting during R-MRAFF……165
Fig. A.15 Ishikawa cause and effect diagram of R-MRAFF……166
Fig. A.16 Surface roughness achieved by different finishing processes……166
Fig. B.1 Schematic representation of Directed Energy Deposition……..171
Fig. B.2 Overview of the surface enhancement of the directed energy deposited part……172
Fig. B.3 SEM and EDX analysis of SS316L powder particles……175
Fig. B.4 Overview of surface enhancement of the directed energy deposited part……..176
Fig. B.5 Total deformation and stiffness of fixation plates at different mass retention……178
Fig. B.6 Variation of (a) stiffness and (b) strain rate with mass retention……178
Fig. B.7 Surface profile of DED fabricated part……179
Fig. B.8 Surface defects on DED fabricated fixation plate (a) unmelted powder particle and (b) pores…….180
Fig. B.9 Surface profile of milled surface of fixation plate……..180
Fig. B.10 SEM image of (a) milled surface and (b) polished surface……180
Fig. B.11 Surface analysis of fixation plate polished surface……181
Fig. B.12 (a) Surface defects on holes edge, uniform (b) hole, and (c) curvatures on the polished surface after H-ECMR finishing process……...181

List of Tables

Table 1.1 Different types of surface defects during PBF process 8
Table 1.2 Different compositions of electrolytes to finish Titanium alloy [48] 14
Table 1.3 Capabilities of various surface super finishing processes with their limitations 23
Table 2.1 Composition of MR fluid 30
Table 2.2 Number of available abrasive particles at different standoff distances 34
Table 2.3 Different magnetorheological fluid-assisted finishing processes 41
Table 2.4 Compositions of MR fluid and process parameters of H-ECMR finishing 44
Table 2.5 Magnitude of relative permeability 47
Table 3.1 Comparison between the different toolpath techniques 88
Table 3.2 Comparison between Skewness and Kurtosis 89
Table 3.3 Coded levels and actual values of the process parameters 103
Table 3.4 Details of design of experiments 104
Table 3.5 ANOVA for surface roughness 104
Table 3.6 ANOVA for surface roughness 105
Table 4.1 MR fluid compositions and process parameters values during H-ECMR finishing 124
Table A.1 Composition of MR fluid to reduce particle agglomeration 155
Table A.2 Compositions of MR fluid for different materials 156
Table A.3 Mathematical models to analyze relationship between shear stress and shear strain of MR fluid 157
Table A.4 Key capabilities and limitations of various MR-fluid-based finishing processes 167
Table A.5 Critical research area of MR fluid-assisted finishing processes 167
Table B.1 Mechanical strength of different mass retention of fixation plate 179

NOMENCLATURES

R_a	Average surface roughness
K	Consistency index
S_k	Core area
J_i	Current density is associated with ions
D	Diameter of polishing tool
i	Electric current
J_e	Electron current density
ϵ_u.	Elongation of the material at failure
ϕ	Engagement angle
$C_6H_6O_2$	Ethylene glycol
S_{pk}	Hill area
h	Hole depth
θ	Inclination angle
d	Indentation diameter
R_{ku}	Kurtosis
n	Level
L	Load on workpiece
$MgCl_2$	Magnesium Chloride
ΔH	magnetic field gradient
H	Magnetic field intensity
ϕ	Magnetic flux
B	Magnetic flux density
F	Magnetomotive force
ϕ_m	Magnetostatic scalar potential
χ_m	Mass-susceptibility of metal particles
M_r	Material Removal Rate
ρ	MR fluid density
F_n	Normal force
μ_0	Permeability in free space
v_{feed}	Polishing tool's feed

N	Polishing tool's rotational speed
P	Power
p	Pressure
r	Radial distance of the abrasive particle from the center of the polishing tool
D	Rate of deformation
μ_r	Relative permeability
R_{SK}	Skewness
u	Specific energy
z	Standoff distance
$\dot{\gamma}$	Strain rate
F_t	Tangential force
σ_u	Tensile strength of workpiece
S_{vk}	Valley area
u_i	Velocity in X direction
u_j	Velocity in Y direction
ΔV	Volume loss
τ_o	Yield stress

Acronym

AFM	Abrasive Flow Finishing
ALVAL	Aseptic Lymphocytic Vasculitis and Associated Lesions
AM	Additive Manufacturing
ARMD	Adverse Reactions to Metal Debris
BASF	Badische Anilin- und SodaFabrik
BEMRF	Ball End Magnetorheological Finishing
BHN	Brinell Hardness Number
CAD	Computer Aided Design
CAPP	Computer Aided Process Planning
CCD	Central Composite Design
CIP	Carbonyl Iron Particle
CMMRF	Chemo-Mechanical Magnetorheological Finishing

CMP	Chemical-Mechanical Polishing
CNC	Computer Numerical Control
DAC	Digital analog converter
DOF	Degrees of Freedom
DSS	Duplex Stainless Steel
EDX	Energy Dispersive X-ray
ELID	Electrolytic in-process dressing
EP	Eelctropolishing
EPDM	Ethylene Propylene Diene Monomer
FHMRF-PS	Feature-based Hybrid MRF Planning System
H-ECMR	Hybrid Electrochemical Magnetorheological
LAEB	Large Area Electron Beam
LPBF	Laser Powder Bed Fusion
MFAF	Magnetorheological Fluid Assisted Finishing
MR	Magnetorheological
MR Jet Finishing	Magnetorheological jet finishing
MRAFF	Magnetorheological Abrasive Flow Finishing
MRAH	Magnetorheological Honing
MRF	Magnetorheological Finishing
PBF	Powder Bed Fusion
PBS	Polyborosillixane
R-MRAFF	Rotational Magnetorheological Flow Finishing
RSM	Response Surface Methodology
SBR	Styrene-Butadiene Rubber
SEM	Scanning Electron Microscope
THA	Total Hip Arthroplasty
VSM	Vibrating Sample Magnetometer
XPS	X-ray Photoelectron Spectroscopy

Chapter 1 Introduction and Literature Review

1.1 Introduction

The continuous upsurge in modern people's living patterns and faster growth of medical sciences consequence in an extended life span. However, the human living machine hasn't been designed for so long period. Our ligaments, linkages of bones, "pumps" and "hinges" are subject to wear. Due to a person's movement, significant tension is applied to his joints and spine. At a higher age, due to wrong postures and heavy workload, wear in the joints starts. These fallouts in inflammatory situations, common in old-age humans, require medical involvement by implanting prostheses [1]. However, the implantation technique in medical science was introduced in the first half of the twentieth century, and a few of the prostheses are shown in Fig. 1.1. However, the development of additive manufacturing provides an advantage to fabricating biomedical implants as per patient-specific with any complex geometry.

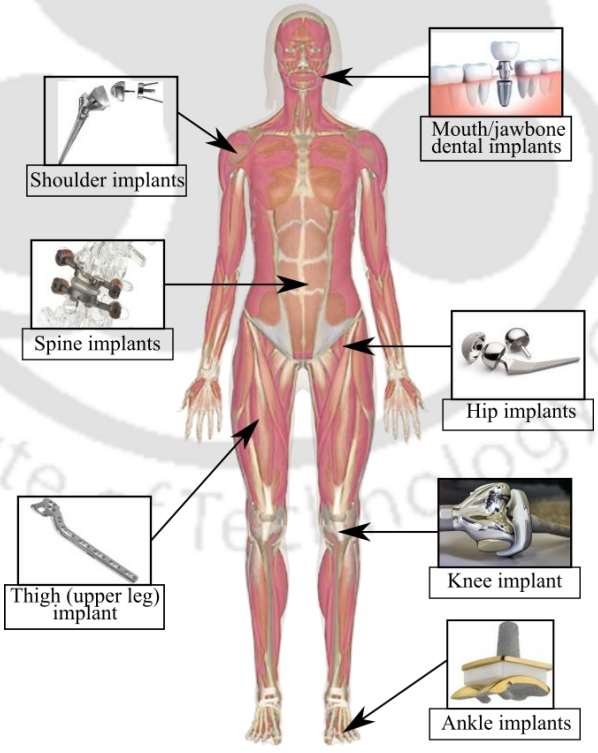

Fig. 1.1 Biomedical prostheses for different body parts

Additive manufacturing, commonly known as 3D printing, has emerged as a revolutionary technology in medical device manufacturing, particularly for the fabrication of implants. Additively manufactured or 3D-printed implants represent a groundbreaking

approach for addressing complex clinical challenges and enhancing patient outcomes in various medical disciplines, including orthopedics, dentistry, and maxillofacial surgery. Traditional implant manufacturing processes often involve subtractive techniques, removing the material from a bulk form to achieve the desired implant shape. In contrast, additive manufacturing offers a novel paradigm by building implants layer-by-layer using *computer-aided design* (CAD) models. This layer-by-layer approach provides exceptional design flexibility, allowing for the creation of highly customized and patient-specific implants tailored to individual anatomical requirements. The application of additively manufactured implants extends beyond the realm of standard implants. It has opened new avenues for developing complex geometries, intricate porous structures, and functionally graded materials, enabling implants with enhanced mechanical properties and improved biocompatibility. Moreover, additively manufactured implants can be fabricated using various biocompatible materials, such as titanium alloys, cobalt-chromium alloys, and biodegradable polymers, further expanding their utility across different medical specialties. The inherent advantages of additively manufactured implants are manifold. The precise and customizable nature of the fabrication process allows for optimal fitting, reducing the risk of implant failure, minimizing complications, and potentially reducing postoperative recovery time. Furthermore, additive manufacturing techniques enable the integration of drug delivery systems, growth factors, and other bioactive substances directly into the implant, fostering enhanced osseointegration and promoting tissue regeneration.

Despite these remarkable advancements, the poor surface quality of additively manufactured implants is the major challenge, leading to health-related consequences. The present work aims to design and develop a post-processing method to produce a uniform surface on an additively manufactured implant.

1.2 Additively manufactured biomedical implants

Doctors and patients rely upon custom-made designs or individualized small series to produce medical devices, and additive manufacturing enables the fabrication of those desired devices. Additive manufacturing, also known as 3D printing, is a manufacturing technique that involves layering materials to form a three-dimensional object. Initially, subtractive manufacturing techniques such as milling, drilling, or turning, additive manufacturing involves selectively removing materials from an object to fabricate the biomedical implants. Moreover, components were made by extracting materials or creating a mould and stamping them. The machinery required to complete such a part is costly. These industries strive to achieve low-cost, high-volume production methods. Thus, the cost of the first hundred units is high. Per unit, costs

decline only when they are mass-produced before assembling. Assembly makes the design phase complex and costly. Moreover, these manufacturing methods are inefficient in handling materials, geometric complexities, and customized solutions. Furthermore, the high costs of metallic biocompatible materials and their processing increase total expenses. Compared with various metallic biomaterials, cobalt alloys are difficult to machine as shape complexity rises. Therefore, some implants are obtained by casting or traditional metal powder processing methods, requiring costly tooling for small or unique series. As titanium is relatively challenging to cast in complicated shapes, titanium ingots are machined. Medical equipment manufacturers are increasingly adopting metal additive manufacturing technologies (direct metal laser sintering and electron beam melting) to design and manufacture medical implants. The early use of this advanced manufacturing route for patient-specific implants is encouraging. In conjunction with surgeons, engineers can produce more advanced and anatomical conforming implants and prostheses, exploiting the power of medical imaging (X-ray, MRI, CT scans, etc.). 3D printing and additive manufacturing companies create customized goods that meet unique needs. Medical and allied industries, as well as the aerospace industry, use additive manufacturing extensively. Since 3D printing is a niche and new domain, it has no global qualification and certification norms. However, maintaining uniform product quality is far more accessible because it builds the part simultaneously, and assembly is not required. This technology can eliminate significant capital investment because inventory can be small and space requirements are not substantial. Metal additive manufacturing is a technology that produces three-dimensional metal parts using wire or metal powder as feedstock materials. As discussed earlier, conventional manufacturing processes are based on removing materials or shape changes, as in the machining and metal forming process. However, metal is successively added layer by layer in the additive manufacturing process. This process turns the complete object into thousands of tiny slices, then makes it from the bottom up, slice by slice. Those tiny layers stick together to form a solid object. This manufacturing process required a suitable heat source such as a laser, arc, or electron beam. This heat source melts the feedstock and molten materials deposited on the substrate. According to ASTM F42, the technical committee defined additive manufacturing (AM) as joining materials to make an object from 3D model data, usually layer upon layer addition of materials, instead of subtractive manufacturing methodologies. A comparison between additive and subtractive manufacturing is shown in Fig. 1.2. AM can build medical implants in nearly any imaginable geometry, sometimes within 24 hours. Rapid manufacturing of custom

implants is a precious ability where standard implants are often insufficient for some patients facing complex cases.

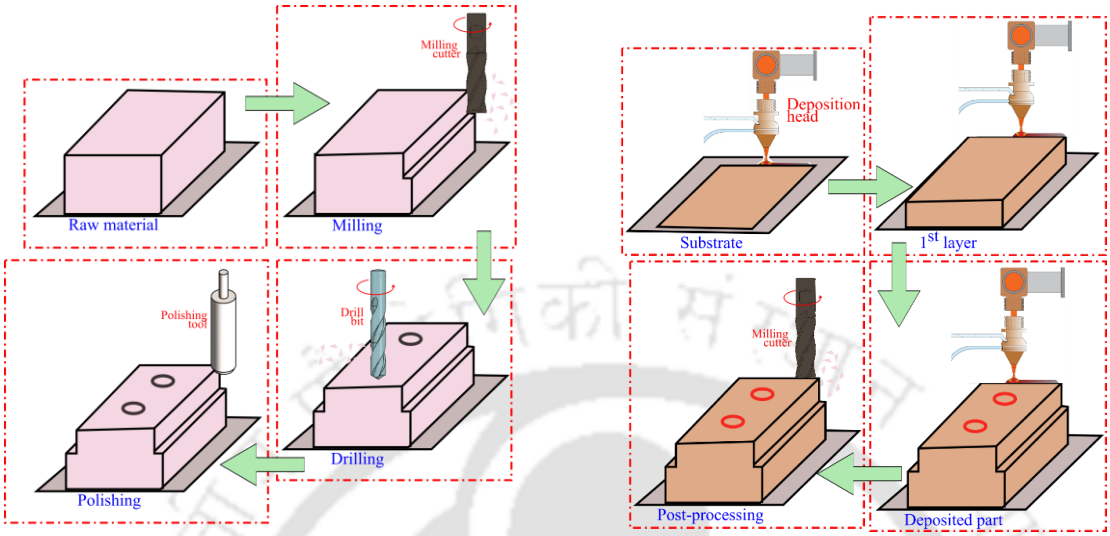

(a) (b)

Fig. 1.2 Conventional manufacturing Vs. additive manufacturing

The advantages of additive manufacturing for medical applications are:

- **Individualization**: Customized prostheses/implants involve a shorter, less painful, and stressful adaptation phase for the patient. Best-fit devices make the surgical operation less complicated and stressful for the surgeon.
- **Complex geometries**: Some free-form structures are hardly or not feasible with conventional manufacturing methods (milling, turning or casting, etc.). There is a growing desire to mimic bionic principles of complexity to accelerate the patient's healing process.
- **Functional integration**: Additively manufactured medical devices can fulfill multiple functions with fewer components and manufacturing steps. Post-built, they can feature both a porous structure and a rough surface, improving bone integration. No further additional spray-on coating or surface texturing is required.
- **Reduced surgical costs**: When a patient is cared for with an efficient product, financial outlays for the hospital stay and follow-on treatment are reduced. As AM productivity increases and the in-hospital process of 3D-scan-to-part speeds up, finely customized devices will enable ambulatory surgery to suffice so patients are not kept in the hospital.
- **Rapid availability**: The lead time is shortened, and 3D-printed medical devices can be applied sooner to patients, which is better.

Additive manufacturing is called additive fabrication, additive process, direct digital manufacturing, rapid prototyping, layer manufacturing, rapid manufacturing, and solid

freeform fabrication. The classification of additive manufacturing technology as per ASTM is shown in Fig. 1.3.

Powder Bed Fusion (*PBF*) is a group of 3D printing techniques that use heat to fuse small particles of metal, plastic, or ceramic powders into a solid object. PBF will further be used to fabricate the topologically optimized orthopedic implant. PBF enables the creation of these optimized shapes by allowing for precise control of the build process, including the laser's movement, the layer thickness, and the powder's properties. Additionally, PBF can produce parts with delicate internal structures, such as internal channels and lattice structures, common in topologically optimized designs. Furthermore, PBF is a highly versatile manufacturing process that can be used with various materials, including metals, polymers, and ceramics, making it suitable for multiple applications. The ability to produce parts with complex shapes, delicate internal structures, and various materials makes PBF ideal for topologically optimized components.

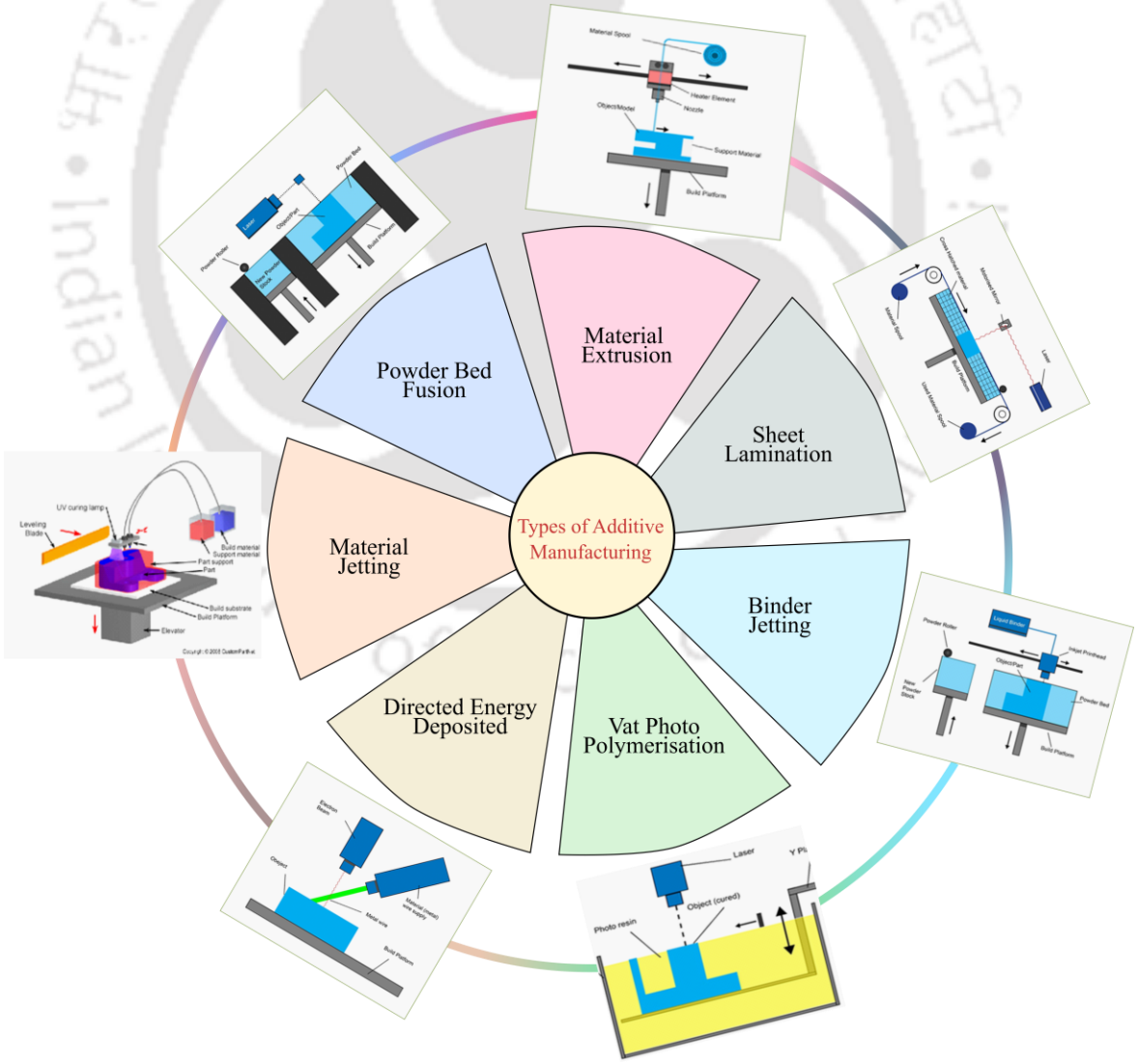

Fig. 1.3 Types of additive manufacturing processes

1.3 Motivation

Additive Manufacturing (*AM*), often known as 3D printing, fabricates products by depositing several layers and has immense capacity to bring manufacturing revolution in bio-fabrication [2]. Furthermore, *Powder Bed Fusion* (*PBF*) is an AM process that utilizes a high-power laser to melt and fuse successive layers of powder to produce complex structures. The PBF process can handle many materials and have complex geometries with high accuracy. However, the higher surface roughness with defects produced on the PBF fabricated parts is still a significant challenge.

While scanning a single layer, the unused powder is not part of the manufactured product and is further classified into three categories, as illustrated in Fig. 1.4. Powder particles far away from the heat source and do not experience any changes are classified as Group 1. Powder particles in the neighborhood of the heat source and the possibilities of change in the microstructural and shape are higher and are categorized in Group 2. The Group 3 powder particles primarily alter the surface imperfection and quality. Group 3 combines spatter powder particles and is further classified into Types a, b, and c based on their formation mechanism. A metallic jet, type a, forms when the spatter is expelled into the laser beam, while ejected outside quickly, cools, and forms the smooth spherical shape on the interaction with the gas flow. The recoil pressure leads to ejects molten pool and produces type b spatters termed the droplet spatter. During their flight, the molten metals are divided into small particles and partially solidify and adhere to the surface. The interaction of ejected droplets and laser beam causes vaporization and creates shock waves leading to type c spatters. These spatters are irregular in shape and adhere to the surface before solidification. These satellite powder particles produce imperfections on the surface of the implants manufactured through the PBF; a few other defects are listed in Table 1.1.

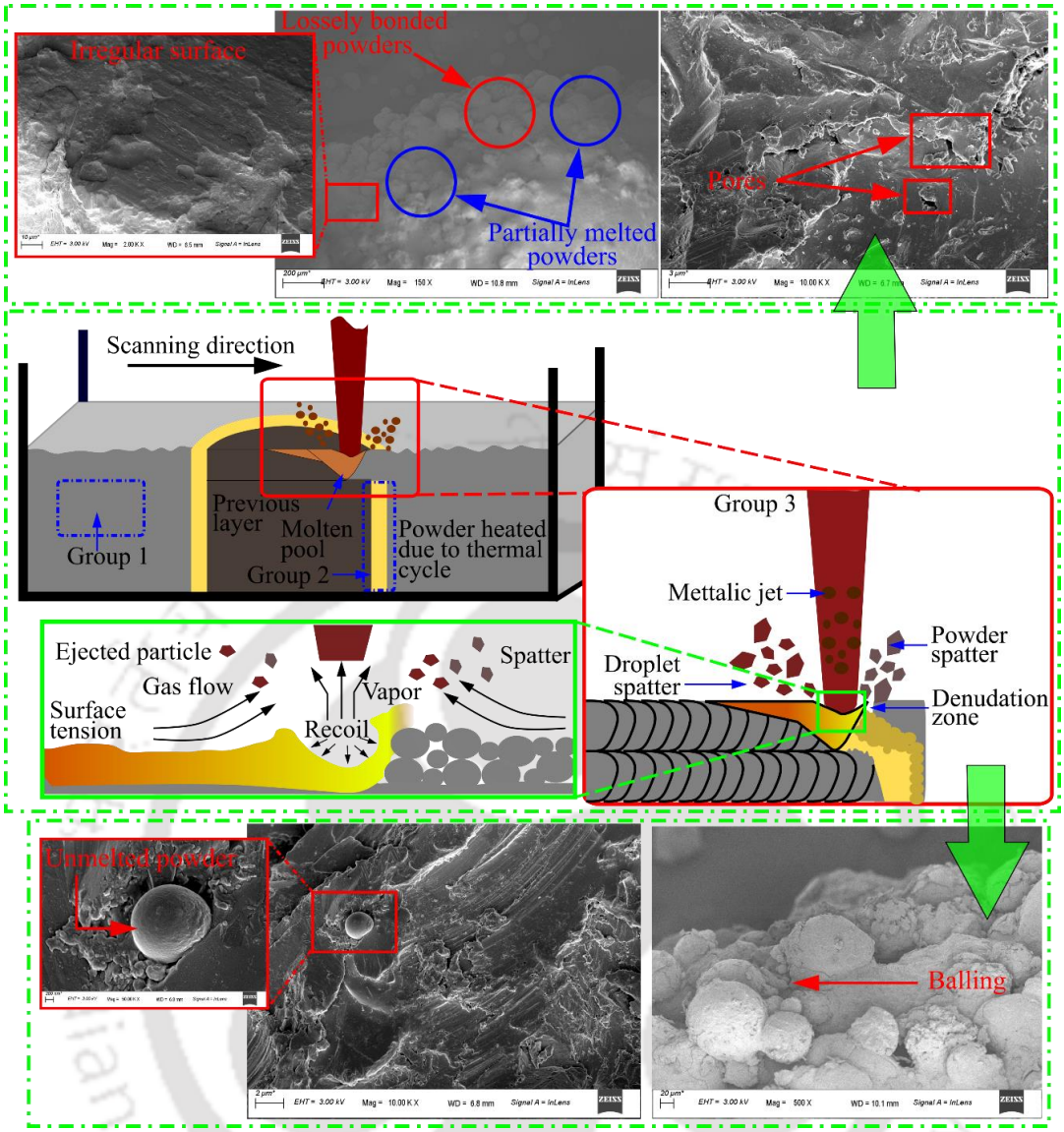

Fig. 1.4 Classification of powder during Laser Powder Bed Fusion (PBF) and different surface defects on fabricated surface

The metal-on-metal bearing couple in *Total Hip Arthroplasty* (*THA*) glides smoothly during physical activity of the human body, with reduced wear rate compared with metal on polyethylene. However, the poor surface quality of the femoral head of THA fabricated through the LPBF surface leads to an increase in its wear rate on their tribological interaction, which is a function of *average surface roughness* (R_a) as represented in Eq. (1.1) [2].

$$k = a(R_a)^b \tag{1.1}$$

Table 1.1 Different types of surface defects during PBF process

Name	Cause	Ref.
Loosely bonded powders	Raw powder particles adhere to surface.	[3]
Partially melted powders	Heat diffuses from molten pool lead to melting of powder particles in surrounding partially.	[4]
Surface pores	High laser scan speed and low liquid front rate.	[5]
Stair casing	Layer height thickness.	[6]
Balling melts	Spherical entities separated from the melted zones.	[7]
Semi welds	Insufficient melting of metal powder.	[6]
Step discontinuity	High temperature between molten pool and moving laser source.	[8]

Where material-dependent constants are denoted by a and b that can be evaluated experimentally. Wang et al. [9] have established a theoretical relation between wear per cycle $\frac{\Delta V}{N}$ and surface roughness as shown in Eq. (1.2),

$$\frac{\Delta V}{N} \propto L^{1.5} R_a^{1.5} \frac{1}{\sigma_u^{1.5} \epsilon_u} \tag{1.2}$$

Where the load is defined by L, ultimate tensile strength is determined by σ_u and elongation of the material at failure is defined as ϵ_u. This relation shows that surface roughness (R_a) significantly contributes to wear. The increased wear rate of the femoral head produces a higher number of debris particles, each having size of nanometres. The interaction of debris particles (or foreign particles) with the human body leads to phagocytosis, a cellular process for removing these foreign particles from the human body having sizes larger than 0.5 µm [10]. The phagocytosis-activated macrophages lead to the generation of the cell responsible for the destruction of foreign particles. Furthermore, the potential cells release small proteins, namely cytokines, to maintain the activity of the immune system, further accountable for the generation of the osteoclasts, multinucleated giant cells which absorb foreign particles [11]. The generation of osteoclasts in higher numbers starts to absorb the different components of the THA, leading to its dislodge, as shown in Fig. 1.5. Moreover, the debris particles are spread inside the human body through blood circulation, responsible for the systematic toxicity of various organs, including kidneys, eyes, levers, etc. [12]. Furthermore, these small metal

particles cause Aseptic loosening or *Adverse Reactions to Metal Debris* (*ARMD*), which may instigate *Aseptic Lymphocytic Vasculitis and Associated Lesions* (*ALVAL*) or Pseudotumours, inflammatory masses and metal hypersensitivity [13]. However, an appropriate super-finishing process is required to enhance the prosthesis's surface quality.

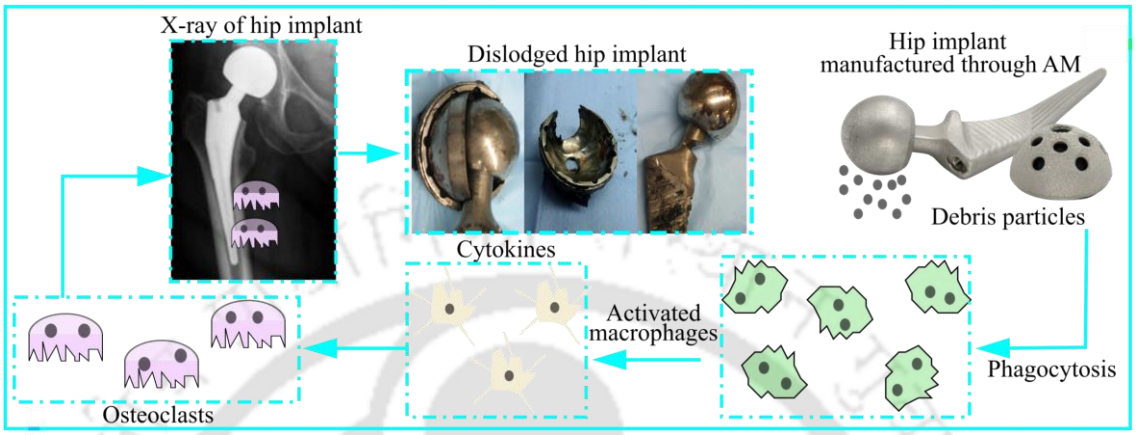

Fig. 1.5 Impact of poor surface quality on additively manufactured implant

1.4 Methods for surface finishing of prosthesis

Various surface finishing processes have been developed in the last few decades' such as *Magnetorheological Fluid Assisted Finishing (MFAF), Abrasive Flow Finishing (AFM), Electropolishing (EP), Large Area Electron Beam (LAEB) irradiation, Electrolytic in-process dressing (ELID) Grinding*, and *Chemical-Mechanical Polishing (CMP)* to provide better surface quality for prostheses. However, the energy utilized to perform the surface finishing for different techniques depending upon the processes' requirement, such as electrical energy, is used to provide non-contact-based finishing methods. On the contrary, the utilization of mechanical energy in the finishing operation results in diminished heat generation compared to processes involving electrical energy. Hence, these surface super-finishing processes can be classified based on energy utilized, as shown in Fig. 1.6. In this section, a detailed discussion is made on the mechanism involved during these surface-finishing processes. However, the Key capabilities of these finishing processes are also discussed along with their limitations, and a comparative study is made to provide an overview at a glance.

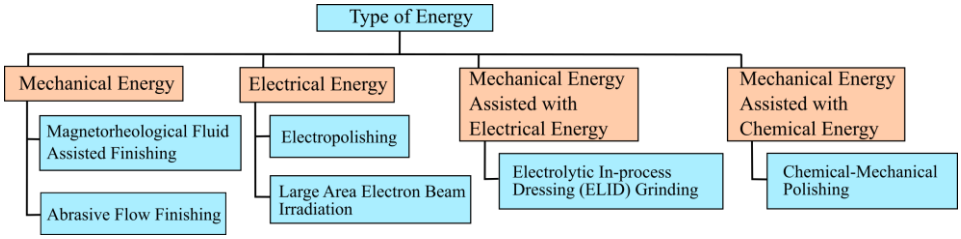

Fig. 1.6 Different finishing processes based on utilization of energy

1.4.1 Abrasive flow finishing

In 1960, Extrude Hone Corporation, USA, developed *Abrasive Flow Finishing* (*AFF*). In the prior development phase of AFF, three different experimental set-ups were established.

- One-way Abrasive Flow Finishing [14]
- Two-way Abrasive Flow Finishing [15]
- Orbital Abrasive Flow Finishing [16]

Frequently exploited abrasive flow finishing is two-way AFF. Herein, the workpiece is placed between two vertical cylinders that are opposite to each other [17]. This two-cylinder movement is synchronized so that they always move in the opposite direction having the same velocity. Because of moving fluid, shear stress is generated in the workpiece's targeted region, where the surface finish is required. However, AFF achieves a high surface finish on freeform surfaces using the abrasive embedded medium with unique rheological properties. The abrasive embedded medium must have superior self-deformability, easy flowability, and well-abrading ability.

Meanwhile, with the assistance of AFF, the minimum removed layer thickness is around 1 to 10 µm, and surface roughness up to 50 nm can be attained with +/- 0.5 µm tolerance. However, in AFF, tooling is crucial throughout this progression, as it is a fluidic medium; it is quite easy to finish unattainable areas. It can generate factual round radii on intricate surfaces, reducing 70 to 90 percent of initial surface roughness. Although AFF upholds suppleness, it reduces the human efforts and time required to finish a prosthesis; produces uniform, precise, and accurate products on an influential variety of surface finishing operations. However, the significant advantage of AFF, which distinguishes it from other finishing processes, is that with the proper design of the workpiece fixture and varying process parameters, it is conceivable to control and select the strength and position of abrasion. However, the surface finishing operation on the knee prosthesis achieved a roughness (R_a) of 42.9 nm to 62.5 nm over different surfaces. During this

process, the total reduction in the surface roughness was around 75% of its initial value, as illustrated in Fig. 1.7 [18].

Apart from prostheses, it is used to finish air cooling holes on a turbine disk, like dies and molds, aerospace and automotive industries. However, to analyze the mechanism behind the surface finishing process, different analytical models were proposed, and a linear relationship was noticed between shear stress applied on the prosthesis surface due to the action of medium flow and material removal [19]. Meanwhile, a capillary rheometer obtains the relationship between the polyborosiloxane medium's viscosity and wall shear stress. However, it was found that its shear rate increases during the flow of medium through restricted areas (reduced cross-sectional area). Meanwhile, the polyborosiloxane medium's viscosity decreases with a surge in shear rate, leading to a rise in the material removal. Similarly, with increased piston stroke duration, finishing action increases due to higher wall shear stress [20]. However, a collection of neural network simulations forecasts surface quality and structural modification to optimize the process parameters during AFF. Meanwhile, these neural network models are combined with a heuristic search algorithm to choose essential process parameters for AFF [21]. However, Lam and Smith [22] [23] practiced Cascade-Correlation neural network modeling; with this algorithm, the time required to achieve the desired output in the surface finish can be determined.

Faces	Initial R_a (nm)	Final R_a (nm)	% Reduction
 Face-1	187.5	46.6	75.15
 Face-2	192.4	47.3	75.42
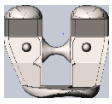 Face-3	184.8	42.9	72.86
 Face-4	186.1	50.5	72.86

Fig. 1.7 Surface roughness of knee implant at different faces

However, apart from several advantages of the AFF process, some limitations are associated with it; the productivity is very low compared to other polishing techniques,

and the time required to achieve the surface finish is high. Hence, this process needs some hybridization to overcome these limitations and increase AFF's efficiency. [24]–[27].

1.4.2 Large-area electron beam irradiation

Electron Beam (*EB*) with high energy density can be obtained without focusing the beam, and large-area EB can be used for instantly melting or evaporating the metal surface [28]–[30]. However, with high heat transfer due to the focused energy source, the material's phase changes and provides enhanced mechanical properties, which cannot be attained by the available surface treatment processes [31]. This method was developed by Proskurovsky et al. in 1997 [32]; after that, lots of modifications were made to this experimental set-up [29], [33], [34]. However, *Large Area Electron Beam* (*LAEB*) irradiation was developed to enhance electron beam irradiation performance. Meanwhile, apart from the conventional electron beam irradiation that is performed in a vacuum, in LAEB irradiation, argon gas is provided inside the chamber with a pressure of (5–15) × 10^{-2} Pa before the experiment. With a solenoid coil's help, magnetic flux was created to beset the compartment's external surface. Although the time at which the generated magnetic flux is maximum, the pulse voltage is laden to the anode. Because of the peening effect, the electron is generated inside the chamber and moves in the anode direction. However, the electron simultaneously moves spirally because of Lorentz's force. After colliding these energized electrons with argon atoms inside the chamber, argon atoms get ionized and create plasma near the anode [35].

Meanwhile, at the instant when the intensity of plasma is maximum, the pulse voltage is applied to the cathode. Consequently, because of the formation of a double electric layer at the cathode, electrons are accelerated by a high field. Then, EB with high energy density is exposed to the material. However, From the Langmuir equation, as shown in Eq. (1.3), the current density of EB can be calculated.

$$J_e = j_i \left(\frac{M}{m}\right)^{0.5} \tag{1.3}$$

Where J_e represents the electron current density, J_i current density is associated with ions, and m is the mass of the ions. However, it can be analyzed that with an increase in ion mass and ionic current density, the current density of EB increases. When an electron passes through the plasma region, Coulomb's force acting between them gets weaker, and

consequently, the straightness of LAEB is frequently enhanced. Hence, plasma improves the effectiveness of LAEB; all through this system, a series of pulses are generated to cause EB irradiation. However, the surface quality of different orthopedic tools made of stainless steel was improved with LAEB irradiation, as shown in Fig.1.8 [36]. Meanwhile, the surface quality variation was compared with different pulses for various energy densities; it was found that with an upsurge in energy density, the surface quality of the prosthesis gets enhanced.

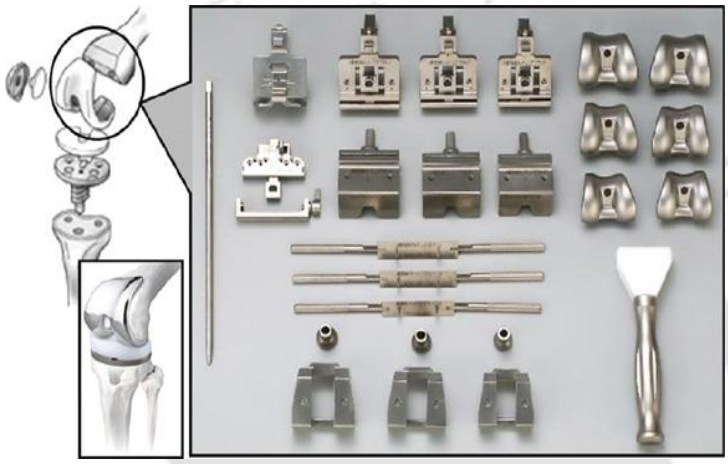

Fig. 1.8 Different parts of a knee prosthesis with surgical tools [36]

However, as observed from experimental investigations, the prosthesis's surface quality and shininess improved with an increase in the electron beam's energy density. Meanwhile, by controlling the process parameters, the surface roughness of 1 µm can be achieved from the initial surface roughness of 10 µm in a few minutes by this process, which is not feasible by any other existing methods. Moreover, the material's corrosion resistance improves after finishing, and high surface finish and modification can be attained on bio-titanium alloy by LAEB irradiation [37].

The benefit of LAEB is that the time required to achieve better surface quality is relatively low; in a few minutes, the prosthesis's surface finishes improved. The limitation of LAEB is that surface roughness can be improved up to 1 micrometer; further improvement in the surface quality is impossible with this process. Another problem associated with LAEB irradiation is the formation of the recast layer on the bio-titanium alloy after finishing.

1.4.3 Electropolishing

Electropolishing comprises electrochemical reactions, which help to reduce unevenness from the metallic surface at the micro-level by anodic dissolution. However, the potential difference

applied between the workpiece and the tool leads to the flow of electric current, which leads to the formation of the viscous layer at the interface of the electrolyte and workpiece. Meanwhile, at the peak of the unevenness on the material, the viscous layer is thinner and provides dissolution of the material at the micro-level. As a consequence of the abovementioned phenomenon, surface quality gets enhanced with a reduction in the surface's coarseness. The advantages of using electropolishing are the easiness of automation and polishing multiple workpieces at a time in a single workbench. Hence, it is economically feasible with better surface quality and enhanced mechanical properties [38]. In the case of mechanical polishing, normal stress is generated in the workpiece that initiates micro-cracks because of the mechanical action. The use of electropolishing overcomes this problem. This advantage of electropolishing is best suited for surface improvement of biological prostheses [39].

In the case of electropolishing, the electric current is supplied in the form of a pulse with different characteristics. The control module in the workbench controls the various parameters of electric current characteristics. However, the prosthesis surface is enhanced by a couple of surrounded graphite rods used as electrodes. The reason to select graphite as electrodes is that they don't dissolve under the electrolyte and hence don't contaminate it [40]. As for biomedical, titanium alloys are preferred over other materials; several electrolytes were examined to achieve better results, as shown in Table 1.2Table 1.2 Different compositions of electrolytes to finish Titanium alloy [48][41]–[47]. However, the electrolytes were selected based on their effectiveness, difficulties associated with the chemical composition, and easiness in process execution.

Table 1.2 Different compositions of electrolytes to finish Titanium alloy [48]

Electrolytes	1	2	3	4	5
H_2SO_4	20–40%	–	60–65%	60%	–
HF	10–18%	160 ml	20–25%	30%	3–4%
$HClO_4$	–	–	–	–	–
Other	CH_3COOH 42–62%	CrO_3 500g, H_2O to 11	Glycerine 10–20%	Glycerine 10–20%	Ethylene glycol to 100%

However, to perform finishing operations, materials having high hardness (titanium and titanium alloy), Perchloric acid, chromium oxide, and hydrofluoric acid are most commonly used [49]. The electrolytes, as mentioned earlier, are highly toxic or destructive. Often the circumstances essential to the experiment are challenging to obtain. For example, some

electrolytes need a negative temperature range, i.e., –72 °C, to experiment. Results from the tests performed with the less troublesome are unsatisfactory [50]. Meanwhile, the maximum surface quality achieved with electropolishing for steel and titanium alloy is 0.05-0.15 µm. Approximately 25–30% enhancement in the surface quality with the help of electropolishing was obtained on the finishing surface.

The shape error build-up in the material is the problem associated with electropolishing. Two appropriately formed and located electrodes were used to overcome this problem [51]. However, after finishing the prosthesis, some uncomplimentary consequence of electrolytes was noticed on the finished surface. E.g., in the case of electrolytes containing hydrofluoric acids, local defilement was observed while removing the prosthesis material. A suitable finishing and speedy extinction of the electrolyte action is required to eliminate the adverse effect. Meanwhile, the pulsed current's surface quality was observed to be better than the direct current in electropolishing. Because of the high surface quality obtained through electropolishing and the ability to finish multiple workpieces simultaneously, it is highly suggested for the surface super finishing of biomedical prostheses [52]. However, because of the use of chemicals in electropolishing, a long-term impact can be seen on the finished surface. Moreover, apart from the several advantages, the initial setup cost is higher for electropolishing than other finishing operations.

1.4.4 Electrolytic in-process dressing (ELID) grinding

In conventional fixed abrasive grinding, the wheel requires dressing before grinding the particular sample. However, this dressing ensures new sharp grit protrudes from the wheel surface. Meanwhile, Ohmori et al. [53] introduced *Electrolytic In-process Dressing* (*ELID*) as a significant improvement on this traditional method, whereby continuous wheel dressing occurs during the grinding cycle. Herein, the axis of a metal-bonded abrasive wheel is connected to an influence supply with a brush. One side of the wheel performs grinding on the prosthesis, while the opposite side undergoes electrochemical dressing inside a little gap (usually around 0.1 mm) crammed with alkaline liquids. These liquids generally serve both as electrolytes and coolants. The electrolytic reaction causes stripping of the metal bond, thus continuously revealing fresh and sharp grit, which will perform in the ductile regime. However, one of the biggest challenges of this process is controlling the grinding wheel’s shape since the wheel diameter is continuously reducing during the method. Nevertheless, ELID grinding has been tested with suitable materials and shapes (including freeform) of the workpiece [54].

However, while performing the surface finishing operation on biocompatible Co-Cr alloy (the most reliable material to produce biomedical prosthesis because of its properties to resist corrosion, wear, and biocompatibility) to analyze its grinding characteristics and surface modifying effects, the final *surface roughness* (R_a) of a hip prosthesis achieved is 7 nm, as shown in Fig. 1.9 with the subsequent process parameters [53].

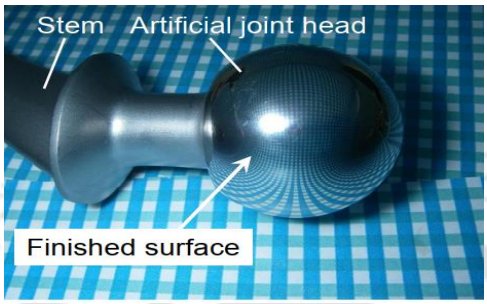

Fig. 1.9 Hip implant after ELID grinding [53]

- **Grinding Wheel** – 8000 average grain size made of copper and chromium-diamond abrasives with resinoid hybrid bonding.
- **Grinding Fluid** – A chemical solution-based grinding fluid with 5% dilution of water and pH 8.2.
- **Process Parameters** – Rotational speed of wheel: 100 min^{-1}, Rotational speed of workpiece: 100 min^{-1}.
- **Electrical condition** – pulse wave: square, pulse timing (on/off): 2/2 µs, Open voltage: 90 V.

However, further investigation was made to analyze hip implants' biocompatibility on biological tissue through animal experiments, as shown in Fig. 1.10. It was found that ELID grinding is very useful and efficient for long-term living body safety [55]. However, the cytokines' concentration, the confrontation to implant pull out, and histopathology at the implant site was assessed. It was found that implants processed using the ELID method performed well compared to the other surface-finishing process [56].

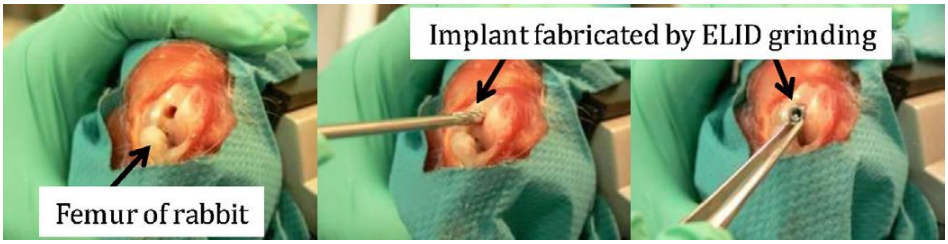

Fig. 1.10 Placing implant in animal experiment [55]

However, the ELID grinding benefit forms a diffused layer of oxygen and carbon due to the electrochemical reaction within the biomaterial Ti alloy process. Meanwhile, the modified layer causes improved surface characteristics, such as mechanical properties and corrosion resistance. To enhance the corrosion resistance through a hybrid process, i.e., ELID grinding/ thermal oxidation is performed on Co-Cr-Mo alloy. It was observed that the oxide layer formed on the specimen through ELID grinding/ Thermal oxidation hybrid process is thicker than when it was processed through surface finishing, followed by the thermal oxidation hybrid process (P/TO). Another advantage of the ELID/TO process is that the percentage of cobalt within the specimen decreases, reducing metal implant corrosion [57]. However, while experimenting on efficient-ground Alumina and zirconia ceramics used for dental application, the *surface roughness* (R_a) of 130 nm was achieved on glass-impregnated and sintered ceramics. While processing the prosthesis through ELID grinding, iron was not spotted in sintered and glass-impregnated ceramics. It was observed that sintered and glass-impregnated ceramics is more appropriate than semi-sintered ceramics for dental prosthesis [58]. However, the problem associated with ELID grinding is to retain the grinding wheel shape accuracy throughout the finishing process.

1.4.5 Chemical mechanical polishing

Chemical Mechanical Polishing (*CMP*) was developed at IBM in 1986 to achieve the super finishing on electronics made of silicon oxide. This process was first utilized to finish metal-based workpieces in 1988 [59]. Afterward, lots of efforts were made to establish this finishing process for several decades [60] [61]. In CMP, mechanical and chemical actions simultaneously improve the prosthesis's surface quality with an enhanced material removal rate [62]. Material removed from the prosthesis is in the form of micro, nano, or atomic level, so any desired surface quality can be achieved with this finishing process with a controlled finishing rate as both mechanical forces in the form of abrasive polishing and chemical forces in the form of etching are responsible for material removal from prosthesis [63].

The CMP media is a colloidal solution of chemical slurry and abrasive combined with a polishing pad and retaining ring, whose diameter is higher than the wafer [64]. With the dynamic polishing head, the wafer and the pad were pressed together and placed undisturbed through the retaining ring. Rotational motion is provided to the dynamic polishing head with eccentric rotation axes; this action removes irregularity from the wafer surface to make it flat or plane. For the formation of additional circuit elements, it is essential to line up the wafer [65]. However, dimensional accuracy obtained through CMP during the surface finishing of prostheses is high compared to other processes. [66]. Four different kinds of experimental set-up were developed in the CMP process:

- A wafer carrier assisted rotatory type polisher with an oscillation motion.
- A carrier-assisted rotatory-type polisher with an oscillation motion.
- A platen has orbital motion in an orbital-type polisher.
- A linear motion polishing bed with a liner-type polisher.

Meanwhile, different experiments were performed to determine the impact of oxidizer in CMP on the titanium-based alloy. It was found that when 3-5% H_2O_2 was added as an oxidizer in the chemical slurry, the material removal rate of the prosthesis increased because of the formation of a passive oxide layer; however, this oxide layer also helps to limit the bacterial growth on the prosthesis surface as shown in Fig. 1.11. It's identified that bio-species' adhesion on implant surface improves with the increase in surface microstructure and surface oxidation. Wettability is another crucial parameter to determine the effect of surface roughness over bio-activity on the surface, which is enhanced through CMP [67]. However, the nonuniform surface finish due to the Variation in relative cutting speed across the prosthesis surface is the primary concern during this finishing process.

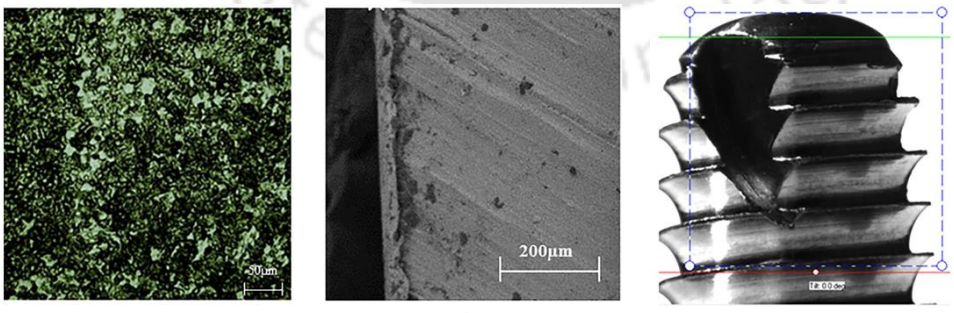

(a) (b) (c)

Fig. 1.11 Surface modification of titanium dental implant (a) SEM image showing oxide layer to prevent bacterial growth, (b) implant without any surface treatment, and (c) dental implant [68]

1.4.6 Magnetorheological assisted finishing (MFAF)

In today's biomanufacturing sector, it is required to manufacture implants that have an exceptionally low tolerance. The desired high precision (or low tolerance) can be obtained through various finishing processes, which consist of bonded (honing, grinding, lapping, etc.) or unbonded (abrasive flow finishing) forms of the tool. An unbonded tool form is more reliable and beneficial because it helps achieve a highly polished surface without affecting the material topography of the product. From the different literature surveys, it has been emphasized that an effective unbonded finishing tool form can be produced through the assistance of *Magnetorheological (MR) Fluid*, as it has in-situ control on its rheological properties. The MR fluid mainly comprises abrasives and metal powder mixed in the viscoelastic solid base. Over the last few decades, several MR fluid-assisted finishing processes have been developed, such as *Magnetorheological Finishing (MRF)*, *Magnetorheological Honing (MRAH)*, *Rotational Magnetorheological Flow Finishing (R-MRAFF)*, *Ball End Magnetorheological Finishing (BEMRF)*, *Magnetorheological Abrasive Flow Finishing (MRAFF)*, *Chemo-Mechanical Magnetorheological Finishing (CMMRF)* and *Magnetorheological jet finishing (MR Jet Finishing)*. This section explores the evolution of MR fluid-assisted finishing processes, their development, applications, influencing process parameters, the composition of MR fluids, and governing analytical models. The key capabilities & limitations of different MR fluid-assisted finishing processes are also discussed, and a comparison was made to provide an overview at a glance and shown in Appendix A.

Finishing is essential in the biomanufacturing sector to enhance a product's surface quality and accuracy. Poor surface quality may lead to high wear rates, high frictional losses, decreased fatigue strength, reduced corrosion resistance, etc. Although conventionally, the surface quality can be improved through secondary finishing processes, such as grinding, lapping, honing, centrifugal barrel finishing, etc. [69][70]. However, it has been noticed that these conventional finishing processes are subjected to the following limitations:

- Failed to handle the complicated geometrical features such as overhangs/undercuts, freeform surfaces, and cavities.
- Failed to attend the *surface roughness* (R_a) in the range of nanometers as required in the biomedical industry. The surface roughness that can be produced through various finishing techniques is shown in Fig.1.12.
- Time-consuming and labor intense, e.g., for lapping, *Material Removal Rate (MRR)* is 7.4 µm/min on nickel-zinc ferrite specimens [71].

- Most conventional finishing processes use a bonded tool (rigid tool), which produces residual stresses in the component, generating micro cracks.

On the other hand, the advanced finishing processes use a non-contact (e.g., Ion Beam Machining, Electropolishing, etc.) and unbonded form of tool (e.g., Abrasive Flow Machining, *Magnetorheological (MR)* Fluid assisted finishing, etc.) which overcome several limitations of the conventional finishing processes. The popular traditional and advanced finishing methods are listed in Fig. 1.13. In advanced finishing operations, the non-contact tools are limited to only electro-conductive materials [72]–[74]. However, the exploitation of an unbonded tool (flexible tool) is beneficial, as the shape of the tool changes according to the workpiece profile, as shown in Fig. 1.14 [75]. Several media is available to form unbonded tool, such as *Styrene-Butadiene Rubber (SBR), Ethylene Propylene Diene Monomer (EPDM), Polyborosillixane (PBS), MR Fluid, etc.* [76].

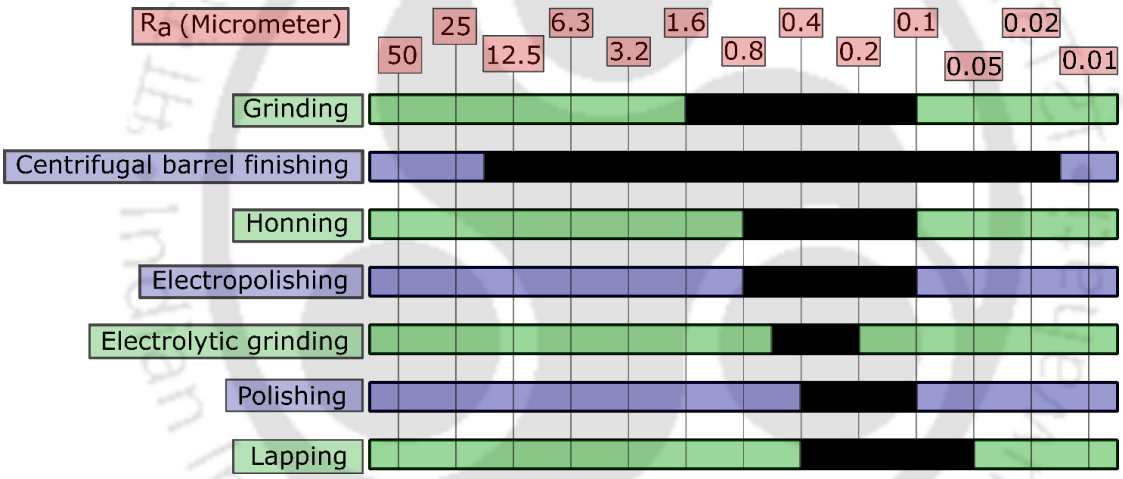

Fig. 1.12 Surface roughness (R_a) obtained by different finishing processes

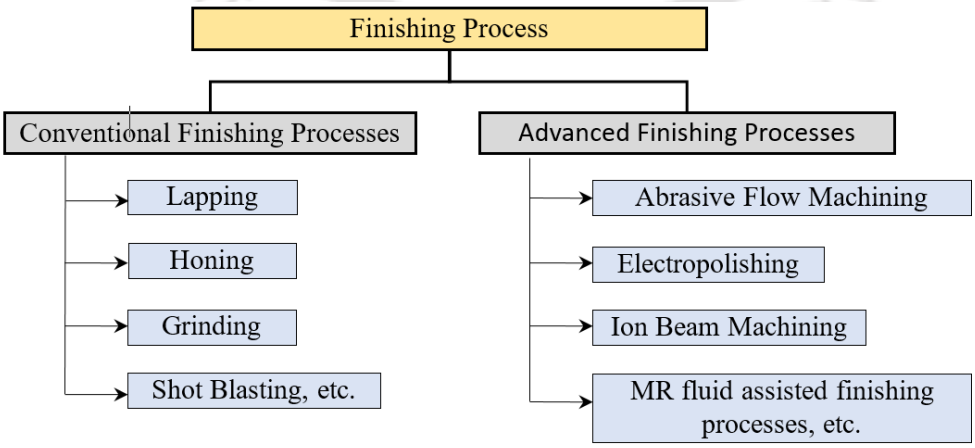

Fig. 1.13 Classification of finishing processes

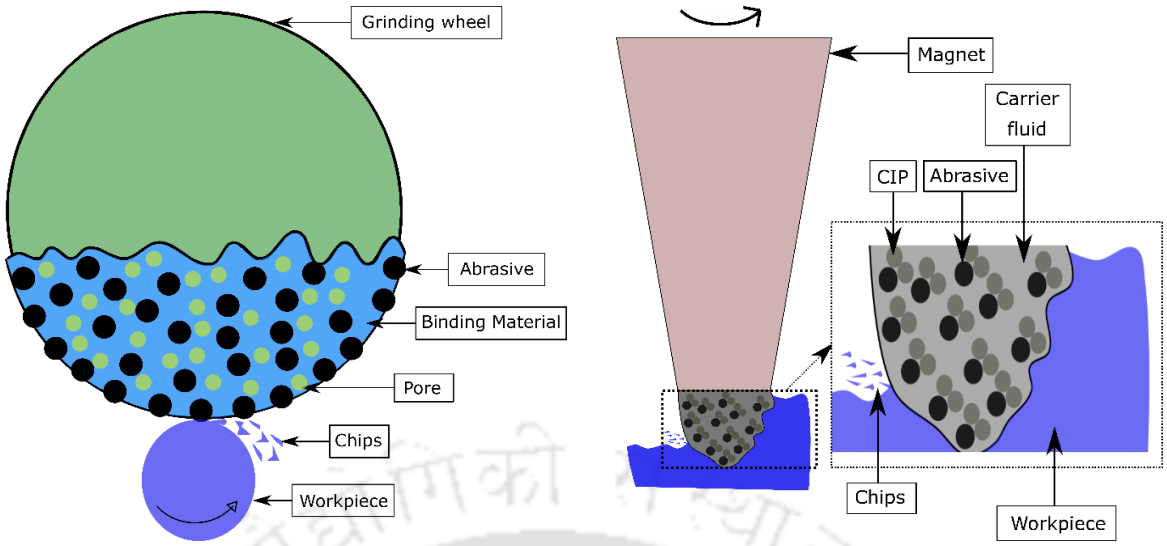

(a) (b)

Fig. 1.14 Finishing tool (a) bonded tool (i.e., grinding), (b) unbonded tool (i.e., ball end magnetorheological finishing)

A typical MR fluid comprises abrasives and metal powder mixed in a viscoelastic solid. When a magnetic field is applied to the MR fluid, the metal particles gain a magnetic moment, attract each other, and form a columnar structure, as shown in Fig. 1.15. This phenomenon increases the viscosity of the MR fluid; moreover, a significant amount of yield stress is required to onset the flow. The magnetic force applied to the MR fluid by the magnetic field can be understood by Eq. (1.4).

$$F_m = m\mu_0\chi_m H\,\Delta H \tag{1.4}$$

Where m is the mass of metal particles, χ_m is the mass-susceptibility of the metal particles, H is the magnitude of the magnetic field, ΔH is the gradient of the magnetic field, and μ_0 is permeability in free space. However, this magnetic force helps to hold magnetic particles together to form a stiff medium with increased viscosity. Hence the required shear stress to perform the finishing operation is generated on the workpiece through this controllable stiff medium [77]–[79]. Therefore, MR fluids are a suitable option to form an unbounded finishing tool as one can have in-situ control of its rheological properties.

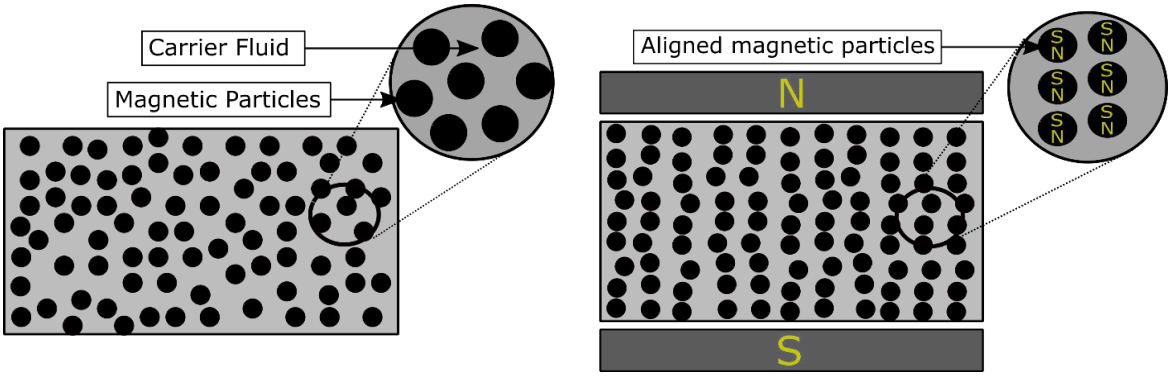

(a) (b)

Fig. 1.15 Formation of chain-like structure of magnetorheological fluid (a) in normal condition and (b) influenced by an external field

Typically, two types of energy sources are used in these finishing processes, viz., (i) mechanical energy and (ii) chemical energy. While finishing the freeform surfaces, a variable cutting force needs to be applied, which is attained by an electromagnet; though to finish regular surface profiles (such as cylindrical, spherical, etc.), permanent magnets are adequate. The motion of MR fluid, which can be rotating or reciprocating, greatly influences the pattern of residual stresses generated on the workpiece. Based on the geometric complexity of the object, appropriate *Degrees of Freedom* (*DOF*) are required between the workpiece & magnet. This acceptable DOF can be obtained by moving the workpiece, the magnet, or both relative to each other. Based on these requirements from the machine tool of an MR fluid-assisted finishing process, a rudimentary classification is suggested and is illustrated in Fig. 1.16 [80].

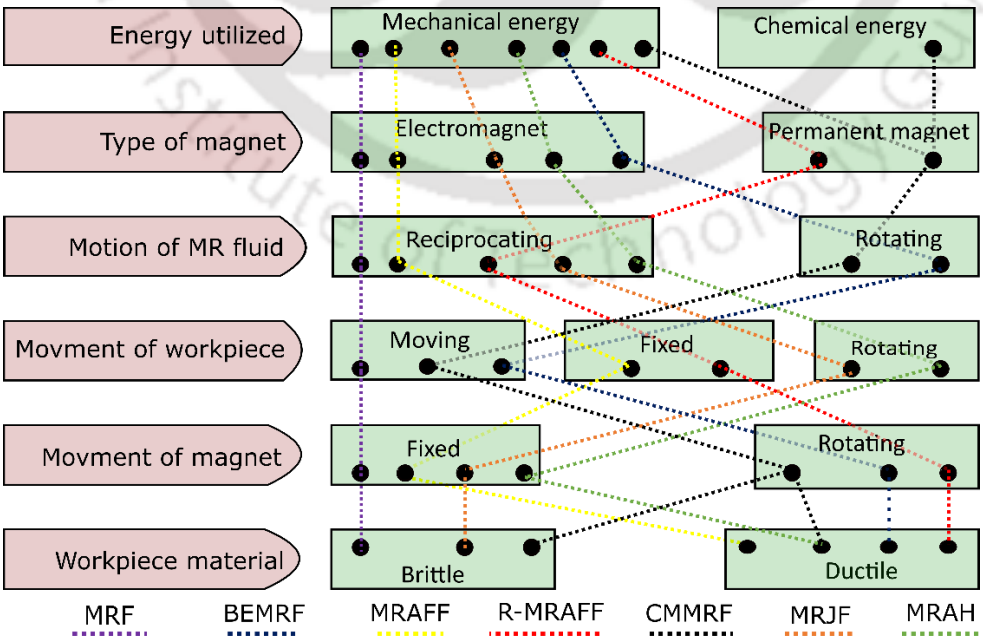

Fig. 1.16 Classification of MFAF process based on working principle

1.5 Selection of a suitable surface super-finishing process

Choosing an appropriate surface super-finishing process for a prosthesis mainly depends upon the final surface roughness provided by the process with enhanced biocompatibility. However, the finishing process can be selected based on surface finishing parameters and biocompatibility.

1.5.1 Surface finishing parameters

The output parameters required to perform well for a prosthesis mainly depend upon the surface finishing parameters, such as minimum surface roughness that can be attained through the finishing process, surface finishing time to enhance productivity, and uniformity of the surface roughness throughout the surface.

1.5.2 Biocompatibility

It is always essential to determine how a prosthesis will interact with the biological tissue after the implantation. However, the parameters defining a prosthesis's biocompatibility form an oxide layer on the surface to prevent bacterial growth. Hydrophilicity or hydrophobicity determines the prosthesis interaction with the biological tissue and corrosion resistance. Each super finishing process's capabilities and limitations are listed in Table 1.3.

Table 1.3 Capabilities of various surface super finishing processes with their limitations

Processes		Benefits	Limitations
MFAF	**MRAFF and R-MRAFF**	Almost uniform surface quality can be achieved.	Every time a change in the workpiece fixture is required with a slight change in the workpiece design.
	BEMRF	Freeform surfaces can be finished.	Low surface finishing rate.
AFF		Provide uniform surface roughness throughout the surface .	Low productivity.
LAEB Irradiation		Low surface finishing rate.	Formation of the recast layer on the prostheses surface.
EP		Surface quality of multiple prostheses can be enhanced simultaneously.	Chemical reactions may ruin the surface quality.
ELID grinding		Provide an oxide layer on prosthesis's surface to limit bacterial growth.	Very difficult to enhance surface quality of freeform surface.
CMP		A highly smooth surface can be obtained.	Low efficiency due to low surface finishing rates.

Different surface super finishing techniques to enhance metallic prostheses' surface quality for enhanced functionality have been discussed in this chapter. It is essential to achieve a smooth finish surface for medical prostheses; otherwise, it may lead to Pseudotumours or Aseptic Lymphocytic Vasculitis and Associated Lesions (ALVAL), metal hypersensitivity, and inflammatory masses. However, from the study, it can be concluded that

- *Abrasive Flow Finishing (AFF)* utilizes it is conceivable to control and select the strength and position of abrasion, which helps finish unattainable areas. However, low productivity is a genuine concern in AFF.
- The surface finishing time required during the *Large Area Electron Beam (LAEB) irradiation* is relatively low; the prostheses' surface roughness improved in a few minutes. However, surface roughness can be improved up to 1 micrometer; further improvement in surface roughness is impossible with this process. Meanwhile, forming the recast layer on the prostheses surface is a significant drawback of LAEB.
- *Electropolishing (EP)* provides the benefits of enhancing the surface quality of multiple prostheses simultaneously. However, because of the use of electrolyte chemicals, a long-term impact can be seen on the prostheses' finished surface.
- *Chemical Mechanical Polishing (CMP)* can reduce the surface roughness to the nanometers. Still, it has certain disadvantages, i.e., Low efficiency due to low removal rates, nonuniform surface finish due to the Variation in relative cutting speed across the prosthesis surface, and relatively high cost involved in this process.
- *Electrolytic in-process dressing (*ELID*)* is an efficient method that eliminates wheel loading and glazing problems generated during the grinding process and provides an oxide layer on the prosthesis's surface to prevent bacterial growth. However, performing surface finishing operations on the freeform surface is very tough through this process.
- Magnetorheological Fluid Assisted Finishing (MFAF) process can be used to enhance prostheses' roughness with close tolerance without damaging the surface integrity. The MFAF process can improve the surface roughness of freeform surfaces of hard materials such as titanium, steel, cobalt-chromium, etc. However, a tool with higher degrees of freedom is required in the machinery for freeform surface finishing. Meanwhile, different experimental setups are modified to accommodate the prostheses and enhance process performance.

1.6 Scope and objectives of present work

The inadequate surface quality observed in additively manufactured biomedical implants has detrimental effects on the human body, necessitating the development of post-processing methods to enhance both surface quality and biocompatibility. Moreover, the developed process must enable surface finishing operations for complex surfaces to improve their biocompatibility. The literature survey indicates a prolonged time requirement for achieving the necessary enhanced surface quality of prosthetic implants. Commercial setups available for finishing prosthetic implants have inherent limitations, and scant literature is available on finishing and further improving the surface integrity of additively manufactured implants for enhanced biocompatibility. The MFAF process emerges as a promising technique for improving the surface quality and biocompatibility of additively manufactured implants without altering their topography. However, the surface quality enhancement of workpiece with holes and pockets remains a challenge in the MFAF process, as MR fluid can become trapped during finishing operations. Consequently, an appropriate surface finishing strategy is required to address this issue. The primary objectives of the current research work are as follows:

- Development of a Hybrid Electrochemical Magnetorheological (H-ECMR) finishing process to enhance process efficiency for nano-finishing implants manufactured through Powder Bed Fusion (PBF).
- Integration of the proposed tool with a specially designed 5-axis CNC milling machine enables the H-ECMR finishing process.
- Development of computer-aided process planning for the H-ECMR finishing process to enhance the surface quality of workpieces having holes and pocket features.
- Identification and optimization of suitable toolpath with H-ECMR finishing process.
- Experimental investigation of prosthetic hip implant and bone plates to enhance implant's biocompatibility.

1.7 Organization of thesis

The thesis is organized into five chapters, four appendixes with references. The introduction to the finishing processes and related literature review is introduced in the **First chapter**. The literature review of different finishing processes for freeform surfaces is mentioned. Also, the advanced finishing processes and magnetic field-assisted finishing processes are discussed along with previous studies on the processes reported by different researchers. Moreover, a

comparison between the several post-processing processes mentioning their benefits and limitations is included.

Development in *Magnetorheological Fluid Assisted Finishing* (*MFAF*) process is discussed in **Chapter 2**. A detailed discussion on the permanent magnet and electromagnet-based MFAF process is discussed. Moreover, the novel *Hybrid-Electrochemical Magnetorheological* (*H-ECMR*) finishing process is developed to reduce the surface finishing time during the surface enhancement of the additively manufactured implants. The developed process also provides a thick and uniform oxide layer on the biomaterial to improve its corrosion resistance. Details regarding the experimental setup process and the mechanism behind the surface finishing process are included. Moreover, an analytical model is developed to predict the surface roughness during the surface finishing operation.

In **Chapter 3**, computer-aided process planning for the developed process is included. The surface finishing of the workpiece having hole and pocket features is infeasible during the H-ECMR finishing process. Hence *Feature-based Hybrid MRF Planning System* (*F-HMRFS*) is developed to eliminate the above-mentioned problems. Moreover, an analysis is made between the different area-filling toolpath strategies, including Peano, Hilbert, raster, spiral, and trochoidal. The trochoidal toolpath is critically analyzed to study its impact during the surface finishing operation.

Surface enhancement of the additively manufactured implant is discussed in **Chapter 4**. The surface finishing operation is performed on the metallic biomaterials. The surface quality of *Powder Bed Fusion* (*PBF*) fabricated femoral head of the total hip arthroplasty and bone plate is improved through the developed process. Moreover, chemical etching is performed on metallic workpieces before the H-ECMR finishing process to reduce their surface roughness in the range of a few nanometers. A detailed analysis of the impact of the process analysis on the surface quality of the polished surface is also discussed in the chapter. The biocompatibility of the additively manufactured implant is analyzed before and after the post-processing. Discussion about the conclusions and findings of the present work with future scope is presented in **Chapter 5**.

The comprehensive review of the MFAF process is included in **Appendix A**. A topologically optimized *Laser-Directed Energy Deposition* (*L-DED*) is fabricated and further post-processed through developed F-HMRFS is included in **Appendix B**. The references are added at the end of the thesis.

Chapter 2 Development of Magnetorheological Fluid Assisted Finishing process

2.1 Introduction

The *Magnetorheological Fluid Assisted Finishing* (*MFAF*) process is an advanced finishing process that produces a high level of surface quality, even on complex freeform surfaces. Although the MFAF process was developed in the late '90s, the evolution process is still in progress to increase process effectiveness and efficiency. With the assistance of *Magnetorheological* (*MR*) fluid consisting of ferromagnetic particles, abrasives, carrier fluid, and stabilizers, the unbonded multipoint cutting tool is generated during the finishing operations to achieve surface roughness (R_a) in the nanometer range. Hence, the MFAF process produces fine surface quality without affecting the component's surface topography.

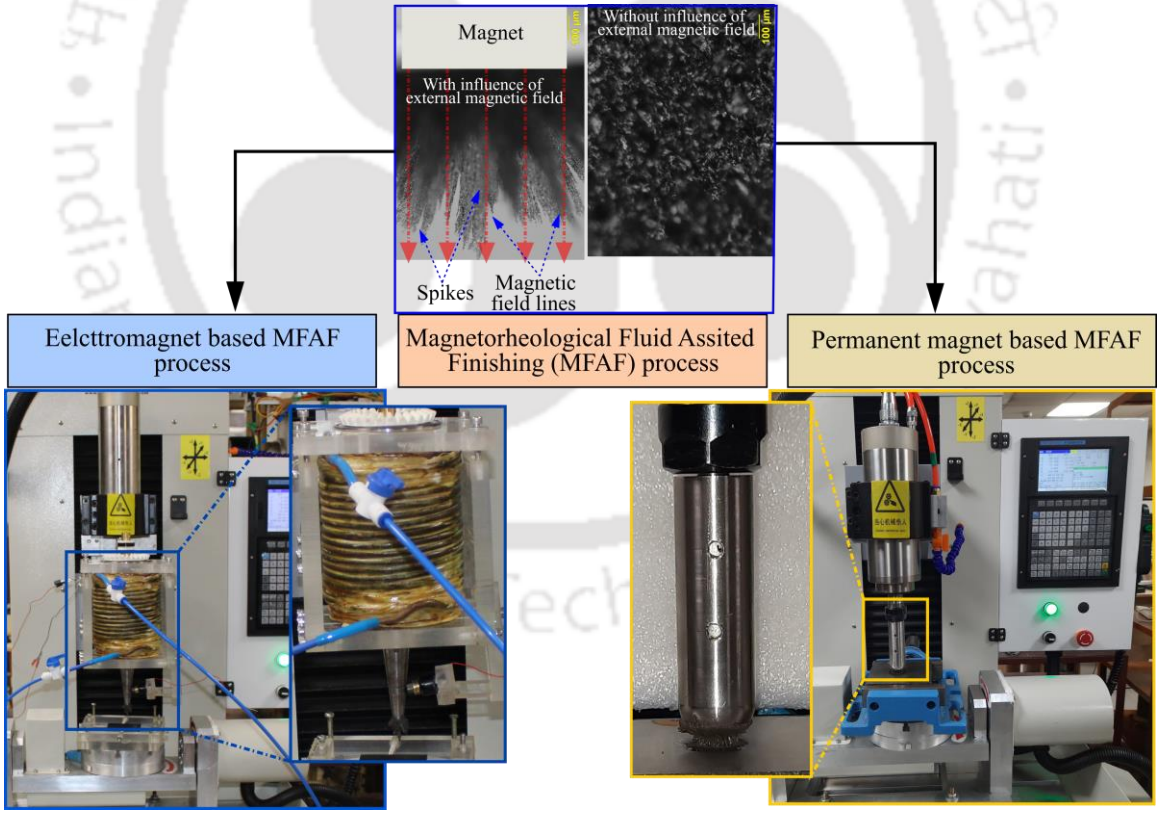

Fig. 2.1 Permanent magnet and electromagnet-based MFAF process

In the MFAF process, the properties of MR fluid can be controlled in situ, with the help of an external magnetic field, according to the process's necessity. The different types of magnets are used to produce the external magnetic field, i.e., permanent magnet and electromagnet, as

shown in Fig. 2.1. The impact of these magnetic field sources over the surface roughness is discussed in the subsequent sections.

2.2 Permanent magnet-based MFAF process

During MFAF, a permanent magnet is typically used to generate the required magnetic field during the surface finishing operation. The magnet is positioned near the workpiece surface, and the MR fluid is applied between the magnet and the workpiece. When the magnetic field is applied, the suspended iron particles align along the magnetic field lines, causing the MR fluid to become more viscous and show solid-like characteristics. This change in rheological properties allows precise control over the material removal during polishing. The MFAF process involves moving the magnet and the workpiece relative to each other while maintaining a constant gap between them. As the MR fluid solidifies under the influence of the magnetic field, it forms a thin polishing layer between the magnet and the workpiece. This layer removes material from the workpiece surface through mechanical abrasion. The permanent magnet ensures a consistent and controlled magnetic field throughout polishing, enabling precise material removal. The use of a permanent magnet in MFAF offers several advantages. Permanent magnets are compact, durable, and generate a stable magnetic field without an external power source. They provide a consistent magnetic field strength, which ensures uniform material removal across the workpiece surface. Additionally, permanent magnets allow for greater flexibility in the design and construction of MFAF systems, as they can be easily integrated into the polishing apparatus.

2.3 Experimental details

A ferromagnetic material, a circular block of Mild Steel (diameter 300 mm), is selected as the experiment's workpiece. The ferromagnetic property of the material assists in distributing the magnetic flux uniformly over the workpiece, as shown in Fig. 2.2. The uniform distribution of the magnetic field controls the MR fluid's stability over the workpiece. A specially designed tool is fixed in the 3-axis CNC milling machine's spindle. The workpiece is placed on the X-Y table, as shown in Fig. 2.3. The polishing tool's magnet holder is made of the Mu-metal (constituents are shown in Fig. 2.4) to shield the magnetic field around the neodymium N52 grade cylindrical magnet (ϕ=15 mm & length=75 mm). The composition of the different MR fluid constituents, as listed in Table 2.1, is applied at the tool's tip. Magnetically soft, *Carbonyl Iron Particle (CIP)* has opted as metal particles in MR fluid, categorized by their high saturation magnetization [81]. Glycerol is a carrier fluid that is highly viscous, biocompatible,

and polar and easily dissolves in distilled water. Diamond abrasive is selected as an abrasive for its high hardness.

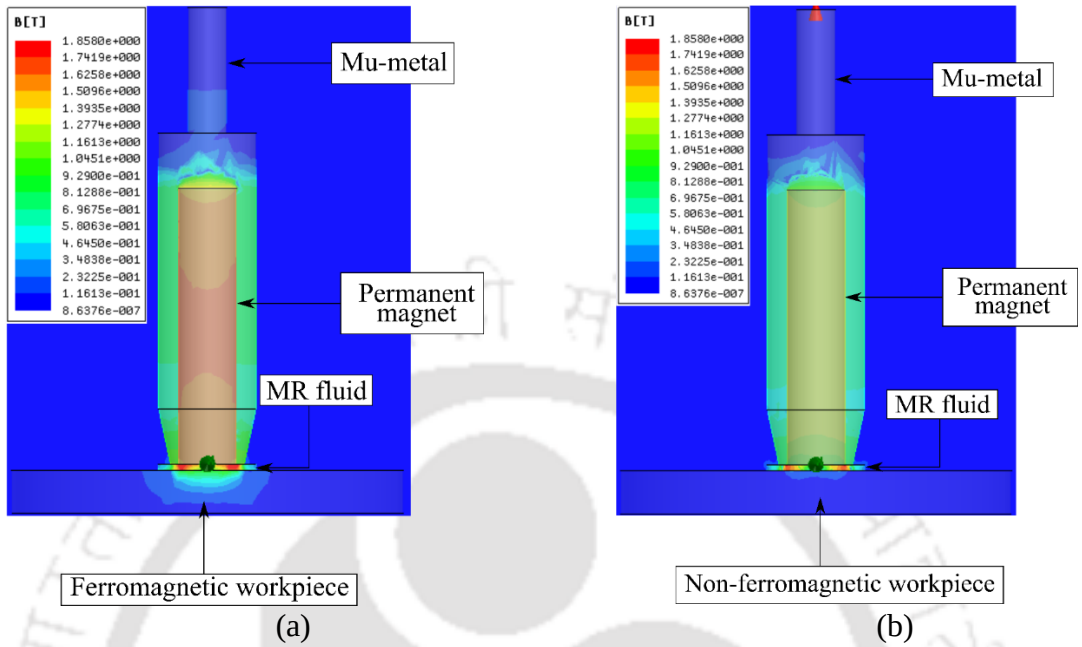

Fig. 2.2 Distribution of magnetic field due to permanent magnet on (a) ferromagnetic (b) non-ferromagnetic workpiece

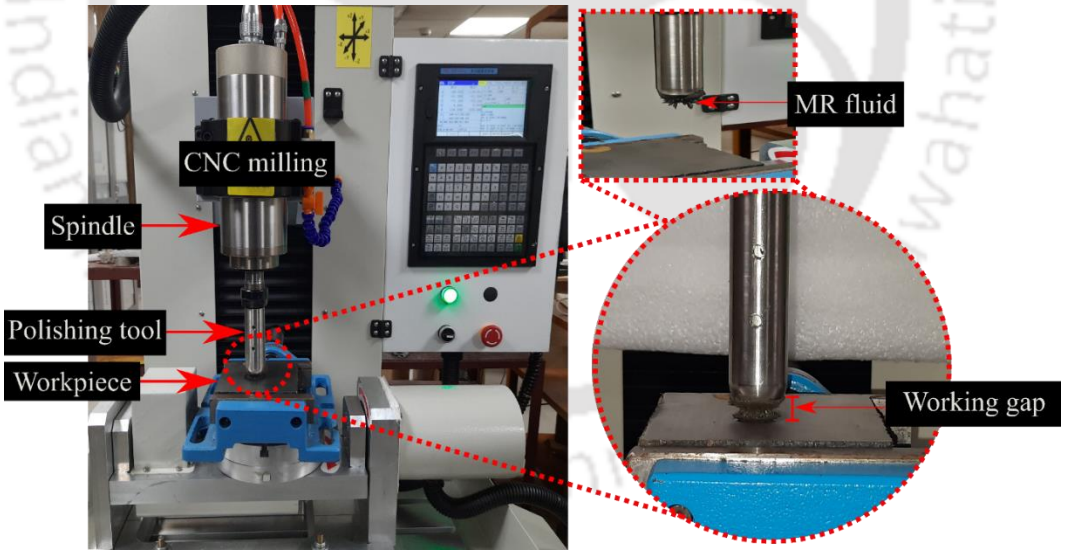

Fig. 2.3 Experimental setup of magnetorheological finishing

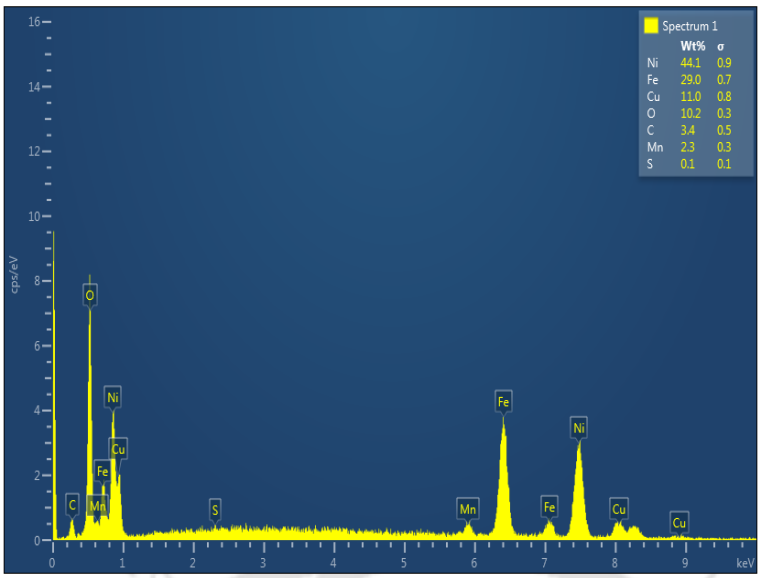

Fig. 2.4 Energy Dispersive X-ray analysis of Mu-meatal

Table 2.1 Composition of MR fluid

Constituents	Composition (%Vol.)
CIP (ϕ= 6µm)	40
Diamond (ϕ= 6µm)	7.1
Glycerol	8
H_2O_2	1.3
Distilled water	43.6

2.3.1 Methodology

The critical input process parameters such as standoff distance, polishing tool speed, and polishing tool feed rate can significantly influence the object's surface roughness to be processed. These process parameters are studied through analytical models in the subsequent sections.

2.3.1.1 Standoff distance

The variation of the standoff distance between the workpiece and the polishing tool leads to varying the impact of the magnetic force. However, the distribution of the *magnetic flux density* (B) of the cylindrical-shaped permanent magnet can be expressed in terms of *magnetic field intensity* (H), as shown in Equation 2.1 [82].

$$B = \mu_0 H \tag{2.1}$$

Where, μ_0 is the permeability of the vaccum. The magnetic field can be determined through the gradient of the *magnetostatic scalar potential* (ϕ_m) as shown in Equation 2.2.

$$H = -\nabla\phi_m \tag{2.2}$$

The analytical analysis to determine the magnetostatic scalar potential of a cylindrical shape permanent magnet is discussed in the subsequent sections.

2.3.2 Determination of magnetostatic scalar potential for cylindrical magnet

The magnetic field can be determined through the gradient of the magnetostatic scalar potential (ϕ_m) as shown in Eq. (12). The variation of the magnetostatic potential along r on the cylindrical magnet is given in Eq. (2.3) [83].

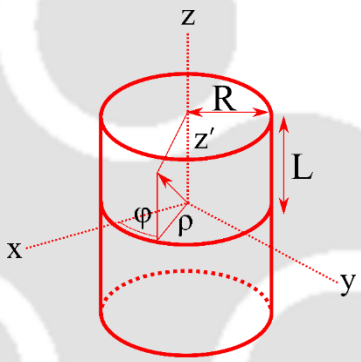

Fig. 2.5 Schematic of a cylindrical shaped magnet

$$\phi(r) = \int_V dr' \frac{\rho(r')}{4\pi|r - r'|} \tag{2.3}$$

The total value of the magnetostatic potential over the cylinder in the cylindrical coordinate system, as illustrated in Fig. 2.5, can be obtained by Eq. (2.4) [84].

$$\phi(\rho, \varphi, z) = \frac{M}{4\pi}\int_0^{2\pi} d\varphi' \int_{-L}^{L} dz' \frac{Rcos\varphi'}{\rho^2 + R^2 - 2\rho Rcos(\varphi - \varphi') + (z - z')^2} \tag{2.4}$$

After evaluating the integral form over z', the integral form is reduced to Eq. (2.5).

$$\frac{M}{4\pi}\int_0^{2\pi} d\varphi' cos\varphi' \ln\left(\xi + \sqrt{(\xi^2 + \rho^2 + R^2 - 2\rho Rcos(\varphi - \varphi')}\right)\Big|_{\xi_-}^{\xi_+} \tag{2.5}$$

Where, $\xi_{\pm} = z \pm L$. applying integration by part, Eq. (2.6) is obtained as

$$\left\{\frac{M}{4\pi}\left[sin\varphi' \ln\left(\xi + \sqrt{(\xi^2 + \rho^2 + R^2 - 2\rho R cos(\varphi - \varphi')}\right)\Big|_{\xi_-}^{\xi_+}\Big|_{\varphi'=0}^{\varphi'=2\pi}\right]\right. \\ + \int_0^{2\pi} d\varphi' sin\varphi' \left[\frac{\rho R sin(\varphi - \varphi')}{\sqrt{(\xi^2 + \rho^2 + R^2 - 2\rho R cos(\varphi - \varphi')}}\right. \\ \left.\left.\times \frac{1}{\xi + \sqrt{(\xi^2 + \rho^2 + R^2 - 2\rho R cos(\varphi - \varphi')}}\right]\right|_{\xi_-}^{\xi_+} \tag{2.6}$$

After further simplification, Eq. (2.6) is further expressed as Eq. (2.7).

$$\frac{2M\rho R^2 cos\varphi}{\pi(\rho + R)^2(1 - \gamma^2)}\left(\frac{\gamma^2}{1 - \gamma^2}\int_{-cos\frac{\varphi}{2}}^{cos\frac{\varphi}{2}} dx \frac{\beta_{\pm}}{\sqrt{(1 - x^2)\left(1 - x^2\left(1 - k_{\pm}^2\right)\right)}}\Bigg|_{\xi_-}^{\xi_+}\right. \\ + \int_{-cos\frac{\varphi}{2}}^{cos\frac{\varphi}{2}} dx\, x^2 \frac{\beta_{\pm}}{\sqrt{(1 - x^2)\left(1 - x^2\left(1 - k_{\pm}^2\right)\right)}}\Bigg|_{\xi_-}^{\xi_+} \\ \left. - \frac{\gamma^2}{1 - \gamma^2}\int_{-cos\frac{\varphi}{2}}^{cos\frac{\varphi}{2}} dx \frac{1}{1 - x^2(1 - y^2)} \frac{\beta_{\pm}}{\sqrt{(1 - x^2)\left(1 - x^2\left(1 - k_{\pm}^2\right)\right)}}\Bigg|_{\xi_-}^{\xi_+}\right) \tag{2.7}$$

Where, $\beta_{\pm} = \frac{\xi_{\pm}}{\sqrt{(\xi_{\pm}^2 + (\rho + R)^2)}}$ and $k_{\pm}^2 = \frac{\xi_{\pm} + (\rho - R)^2}{\xi_{\pm} + (\rho + R)^2}$

The final magnetostatic potential can be represented by Eq. (2.8).

$$\phi = \frac{MRcos\varphi}{\pi}[\beta_+ P_1(k_+) - \beta_- P_1(k_-)] \tag{2.8}$$

Where,

$$P_1(k) = \frac{1}{1 - k^2}(\mathcal{K} - \mathcal{E}) - \frac{\gamma^2}{1 - \gamma^2}(\mathcal{P} - \mathcal{K})$$

Where, $= \int_0^{\frac{\pi}{2}} \frac{d\theta}{\sqrt{(1 - (1 - k^2)\sin^2\theta\ )}}$, $\mathcal{E} = \int_0^{\frac{\pi}{2}} d\theta \sqrt{(1 - (1 - k^2)\sin^2\theta\ )}$ and

$\mathcal{P} = \int_0^{\frac{\pi}{2}} \frac{d\theta}{(1-(1-\gamma^2)\sin^2\theta)\sqrt{(1-(1-k^2)\sin^2\theta\ )}}$ indicates the elliptical integrals of the first, second, and third kinds.

$$H_\rho = -\frac{\partial \phi}{\partial \rho} = \frac{MR\cos\varphi}{2\pi\rho}[\beta_+ P_4(k_+) - \beta_- P_4(k_-)] \tag{2.9}$$

$$H_\varphi = -\frac{1}{\rho}\frac{\partial \phi}{\partial \varphi} = \frac{MR\sin\varphi}{\pi\rho}[\beta_+ P_3(k_+) - \beta_- P_3(k_-)] \tag{2.10}$$

$$H_z = -\frac{\partial \phi}{\partial z} = \frac{MR\cos\varphi}{\pi}[\alpha_+ P_2(k_+) - \alpha_- P_2(k_-)] \tag{2.11}$$

Where,

$$P_2(k) = \mathcal{K} - \frac{2}{1-k^2}(\mathcal{K} - \mathcal{E})$$

$$P_4(k) = \frac{\gamma^2}{1-\gamma^2}(\mathcal{P} - \mathcal{K}) + \frac{\gamma^2}{1-\gamma^2}(\gamma^2\mathcal{P} - \mathcal{K}) - P_2(k)$$

From Eq. (2.11), it is observed that the magnetic field strength is inversely proportional to the standoff distance. Hence, with increased standoff distance, the force applied due to the magnetic field on the workpiece decreases. This result can also be analyzed using an Ansys Maxwell, as shown in Fig. 2.6. Experimentally, the Gauss meter helps to validate the same magnetic field trend on the workpiece surface, as illustrated in Fig. 2.7. The number of abrasive particles is required to perform the surface finishing operation. The number of available abrasive particles during the finishing at different standoff distances is listed in Table 2.2. The standoff distance is selected as 1 mm for the experiment [85]. However, with a further increase in the standoff distance, the magnitude of the magnetic field produced at the finishing spot is insufficient to perform the finishing process.

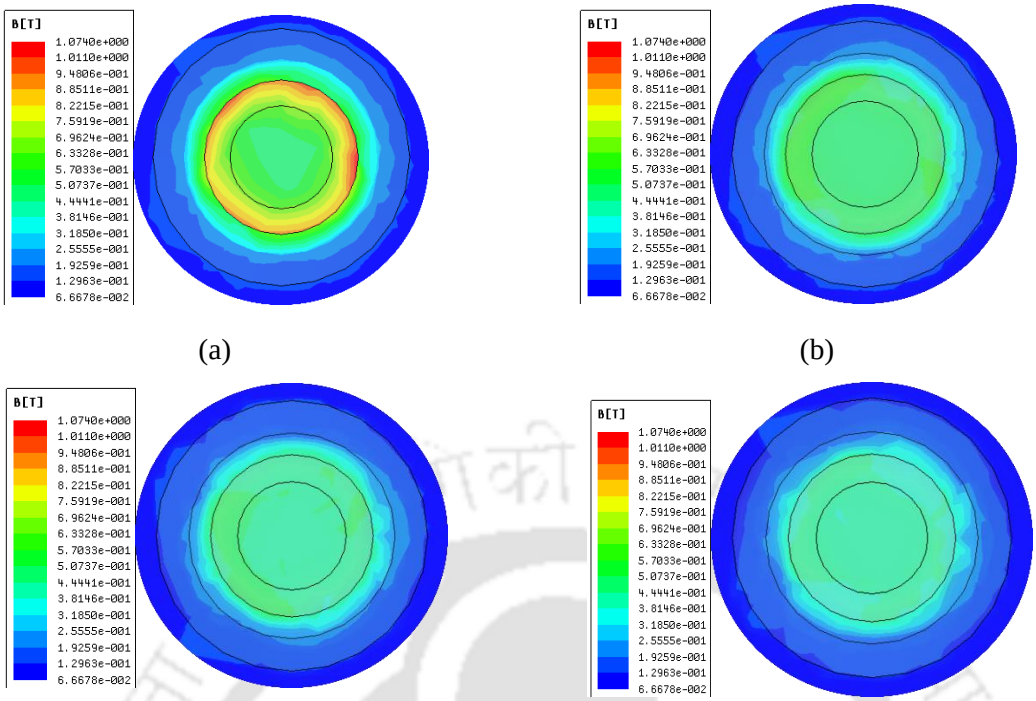

Fig. 2.6 Magnetic field variation at different standoff distances (z) (a) 0 mm, (b) 0.5 mm, (c) 1 mm, and (d) 1.5 mm

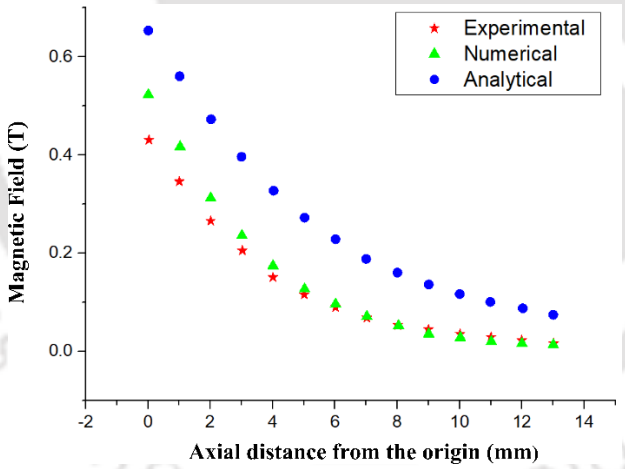

Fig. 2.7 Magnetic field variation along axial direction of polishing tool

Table 2.2 Number of available abrasive particles at different standoff distances

Standoff distance (z)	Number of abrasive particles	Magnetic field (T)
0	0	0.69
0.5	3.328×10^{6}	0.57
1	6.656×10^{6}	0.44
1.5	9.984×10^{6}	0.31

2.3.3 Polishing tool speed

The tool's rotational speed increment increases the centrifugal force on the abrasive particles, as shown in Eq. (2.12).

$$F = m\left[\frac{2\pi N}{60}\right]^2 r \tag{2.12}$$

Where N represents the polishing tool's rotational speed, r denotes the radial distance of the abrasive particle from the center of the polishing tool, and m means the single abrasive particle mass. The increased centrifugal force leads to an increase in the abrasion over the workpiece surface. However, the centrifugal force starts dominating the MR fluid's chain strength after a certain speed, breaking the MR fluid structure. From the literature survey [86], the optimum value of the polishing tool's rotational speed is 800 rpm.

2.3.4 Polishing tool feed rate

It has been observed that the decrease in the feed rate, surface roughness (R_a) of the workpiece reduces as the abrasion time for the abrasive particles increases. However, abrasive particles start producing scratch marks over the polished surface after the optimum time. Hence, the feed rate for the current research work is selected as 1 mm/min [87]. The experiments were performed with the combination of process parameters with standoff distance, polishing tool speed, and feed rate at 1 mm, 800 rpm, and 1 mm/min, respectively. Figure 2.8 shows the variation of reduction in surface roughness with polishing time during permanent magnet-based MFAF polishing. The initial average surface roughness value reduces from 495.26 nm to 59.43 nm for the polishing time of 160 mins.

The surface finishing time for the permanent magnet-based MFAF process is very high. Hence a novel MFAF-based surface finishing operation is required to improve the process efficiency. Moreover, the Electromagnet based MFAF process offers precise and dynamic control over the magnetic field strength, direction, and distribution. This level of control allows operators to tailor the finishing process according to specific workpiece geometries, materials, and surface requirements. The magnetic field can be adjusted in real-time during the finishing operation, enabling adaptability and fine-tuning of the finishing process. The controllable magnetic field in electromagnet-based MFAF ensures a uniform distribution of MR fluid particles across the workpiece surface. This uniformity results in consistent material removal rates, improved surface finish, and enhanced reproducibility of finishing outcomes.

Furthermore, Electromagnets consume power only when the magnetic field is actively adjusted, allowing for better energy efficiency. The ability to control the magnetic field dynamically minimizes unnecessary power consumption during idle periods. Moreover, the flexibility of electromagnets allows the MFAF to process a wide range of workpiece geometries and materials. The real-time adjustability of the magnetic field for electromagnet enables the processing of complex shapes and varying surface conditions. Hence the present work focuses on developing a novel electromagnet-based MFAF process to improve the process efficiency and provide in-situ control over the magnetic field applied during polishing.

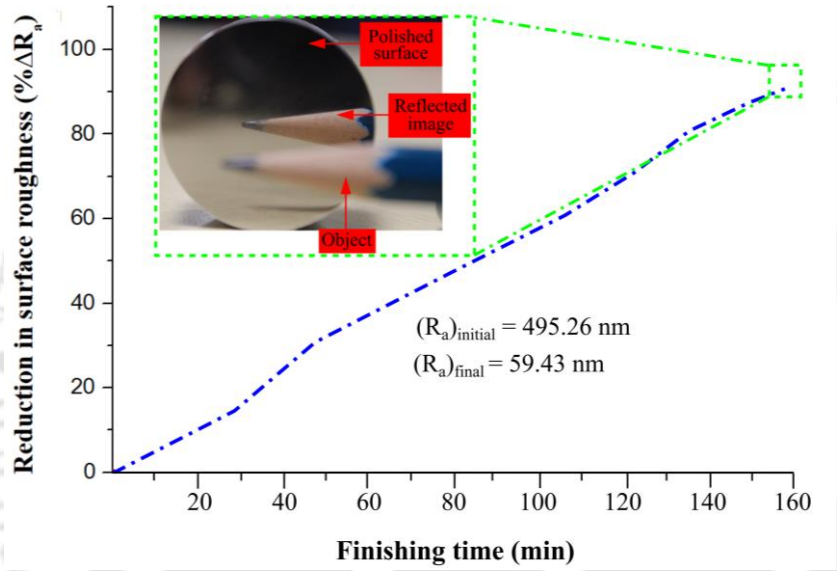

Fig. 2.8 Comparison between reduction in average surface roughness and finishing time for permanent magnet-based MFAF process

2.4 Electromagnet-based MFAF process

The surface characteristics of the biomaterials impact their functionality while operating inside the human body. A highly polished surface having surface roughness (R_a) in the nanometer range is essential for orthopedic implants to reduce the wear rate during their tribological interaction [88]. The debris particles produced due to wear spread in the human body through the blood circulation and cause systematic toxicity of different organs. Moreover, aseptic loosening caused by mechanical failure of implants during their operation may lead to pseudotumors, metal hypersensitivity, and inflammatory masses [89]. The improved surface quality also affects the wettability of orthopedic implants facilitating hydrophilic surface and further decreasing coagulation and platelet adhesion [90]. However, the lower polishing rate of the MFAF process is a challenge. Singh et al. [91] developed an MFAF-based method and performed the finishing operation on a flat workpiece (50 mm ×10 mm) made of ferromagnetic

material (i.e., iron). They achieved a final surface roughness (R_a) of 16.6 nm in 120 min. Nagdeve et al. [92] carried out the MFAF process on a Ti alloy knee implant with optimized process parameters achieving a final R_a value of 50 nm for 120 min finishing time. Similarly, Barman et al. performed a surface finishing operation for 390 min on a Ti alloy knee implant to achieve a surface roughness of 10 nm using a magnetic field-assisted finishing process. Several researchers have introduced different methods to reduce the polishing rate during the MFAF process, including the design and development of an effective experimental setup [92], optimization of the process parameters [93], and new development of MR fluid [94].

The chapter presents a novel *Hybrid Electrochemical Magnetorheological (H-ECMR)* finishing process to reduce the polishing time. The synergic mechanical action (i.e., MFAF process) and chemical integration (i.e., electrochemical reaction) enhance the Ti-6Al-4V surface quality. Apart from reducing the finishing time, the electrochemical reactions help to generate a uniform and thick oxide layer on the biomedical material of Ti alloy to increase its biocompatibility. Also, the material removal and oxide layer formation mechanism during the H-ECMR finishing process is discussed. In this chapter, surface characteristics, including *average surface roughness* (R_a), *kurtosis* (R_{ku}), and *skewness* (R_{sk}) analyzed on the surface before and after polishing. The analysis of the experiments during the surface finishing operation is primarily based on the arithmetic mean of the height of the peaks and valleys from the centerline (i.e., *average surface roughness* (R_a)). However, *average surface roughness* (R_a) occasionally provides inaccurate surface quality information as these arithmetic measurements are sensitive to extreme values. Hence, a scratch produced on the polished surface may mislead the information regarding the surface quality of the entire surface [95]. Meanwhile, the *average surface roughness* (R_a) is the function of the height only; the structural information of the peaks and valleys cannot be analyzed. Identical surface roughness values are possible for a surface having flat peaks and narrow valleys or isotropy [96]. Structural information on the peaks and valleys is required to analyze the biomedical implant's polished surface. Hence, *average surface roughness* (R_a) is insufficient for surface characterization [97]. Therefore, kurtosis and skewness are analyzed in the current research work to gather the nature of the distinct spatial features after performing the MFAF process on the biomaterial. The symmetry of the roughness shape is represented by the *skewness* (R_{sk}), which assists in determining the dominance of peaks or valleys, as shown in Fig. 2.9 [98]. The negative skew values lead to more valleys than the peaks in the surface roughness profile, help retain the fluid, and provide good lubricating properties. However, the positive skewness represents the higher number of peaks, increasing the chance of wearing during their tribological interactions. The sharpness of peaks and valleys

is analyzed through *kurtosis* (R_{ku}), as shown in Fig. 2.9 [99]. The magnitude of the kurtosis higher than 3 ($R_{ku} > 3$) on the polished surface represents the pointed peaks. Meanwhile, $R_{ku} < 3$ illustrates the surface profile having flat peaks; the probability of higher wear is maximum in the earlier case. Therefore, this work aims to analyze the surface characteristics of the biomaterial *Duplex Stainless Steel* (*DSS*), enhancing with the MFAF process's assistance. The surface quality is determined by the *average surface roughness* (R_a) and two other distinct parameters for better visualization.

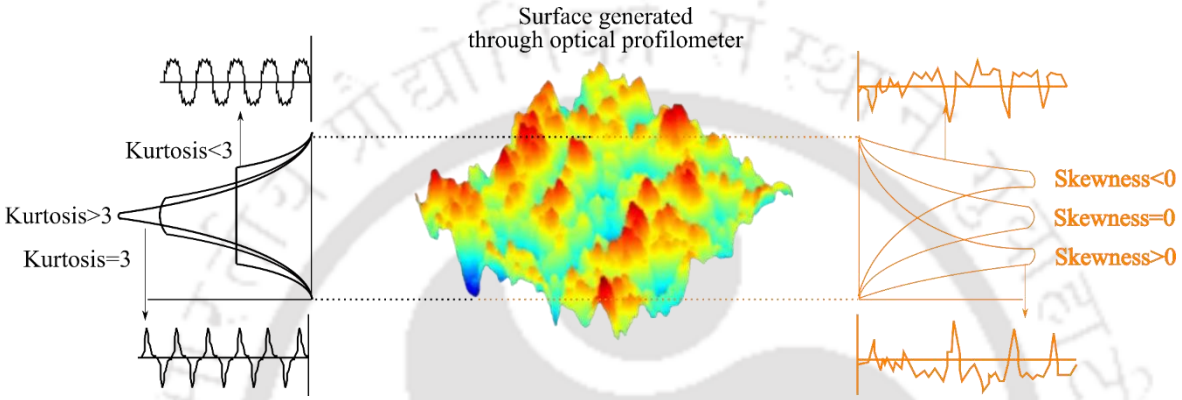

Fig. 2.9 Different categories of skewness and kurtosis

Furthermore, an analytical model is developed to evaluate the R_a from the developed finishing process. Different input parameters' influence on surface roughness output responses is further examined during the H-ECMR finishing process to assess their best combinations to produce a uniform surface quality over the entire polished surface. Additionally, *Scanning Electron Microscope* (*SEM*), *X-ray Photoelectron Spectroscopy* (*XPS*), and *Energy Dispersive X-ray* (*EDX*) are used to determine the change in the passive (TiO_2) layer over the Ti-6Al-4V biomedical surface.

2.5 H-ECMR finishing principle and polishing medium

The *Hybrid Electrochemical Magnetorheological (H-ECMR)* finishing utilizes the synchronized action of the electrochemical reaction and mechanical abrasion for the surface roughness reduction of the biomaterials. This section discusses the mechanism involved in the H-ECMR finishing process and the chemical reactions between the polishing tool and workpiece due to the electrochemical reaction.

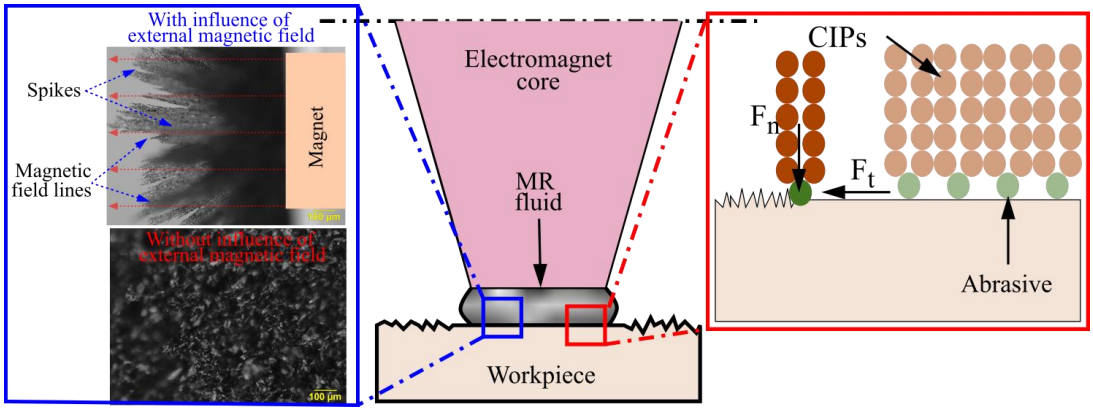

Fig. 2.10 Magnetorheological fluid with and without influence of external magnetic field and mechanism of material removal during magnetorheological finishing process

The MFAF process uses the *Magnetorheological* (*MR*) fluid's rheological properties during the surface finishing process. The ferromagnetic (Carbonyl Iron Particles) and abrasive particles (diamond) are mixed in a carrier fluid to prepare the MR fluid. However, the chances of sedimentation are high due to the higher density of powder particles. Hence, glycerol is used as the stabilizer in the MR fluid. The MR fluid is in the liquid phase in the ambient environment, as illustrated in Fig. 2.10. However, under the influence of the external magnetic field, it gets stiffened and produces the required finishing forces for the surface roughness reduction of the targeted region. An electromagnet is used during the present work to deliver in–situ control of the magnetic field during the H-ECMR finishing, which is unattainable with a permanent magnet. The electromagnet design provides the desired magnetic field at the bottom of the conical core. However, the details regarding the electromagnet design are discussed in the subsequent section. The stiffened MR fluid is squeezed between the electromagnet and the workpiece, and their relative motion produces the required forces (i.e., normal and tangential force) during the surface finishing. The *normal force* (F_n) is created due to the alignment of abrasive particles in the magnetic flux direction generated through the electromagnet. Whereas the *tangential force* (F_t) is produced from the polishing tool's rotational and feed motion, as illustrated in Fig. 2.10. The normal force indents the CIPs chain into the substrate, and the tangential force assists in the detachment of the indented material from the targeted workspace. Hence, the combined action of normal and tangential forces for the surface roughness reduction of the biomaterial.

Ti-6Al-4V, a biomaterial with high mechanical strengths and biocompatibility compared to other biomaterials, is preferable in the biomedical industry. The Ti-6Al-4V reacts with the atmospheric oxygen and forms a passive oxide layer of TiO_2. The pH value of the passive oxide layer is the same as the human body and helps to reduce corrosion during their interaction.

However, the thickness of the oxide layer on the biomaterial surface is nonuniform, with a layer thickness in the range of a few nanometers (i.e., 5-10 nm) [100], which provides the potential sites for initiating corrosion. Different surface finishing methods, including the MFAF, cannot produce a uniform, thick oxide layer on the biomaterial surface. Hence, it is essential to synergically integrate an electrochemical reaction with the MFAF process to achieve the desired objective. Furthermore, the polishing time for the MFAF is very high; as shown in Table 2.3, including an electromagnetic reaction with the MFAF process reduces the finishing time. The synergic combination of the above-mentioned process contributes to the newly developed H-ECMR finishing process to produce surface roughness value in nanometers with a uniform and thick oxide layer.

The electrochemical reaction produces the oxide layer on the Ti alloy from the simultaneous action of the anodic oxidation and dissolution. Electrolytes replace the MR fluid's carrier medium to perform the electrochemical reaction, as shown in Fig. 2.11(a). *Magnesium Chloride* ($MgCl_2$) is combined with *Ethylene glycol* ($C_6H_6O_2$) in distilled water to form an electrolyte to increase the efficiency of the electrochemical reaction [101][102]. Potential difference is applied between the electromagnet's core (acts as an electrode) and the workpiece (Ti alloy). Herein, Ti alloy is attached to the positive end (anode), and the electromagnet's core is attached to the power supply's negative end (cathode). The applied voltage between the biomaterial and core leads to the discharge of electrons from the surface of the biomaterials and Ti^{4+} is formed. Due to similar effect the electrolytes breakdown in Mg^{2+} and the Cl^{-},where the anion reacts with Ti^{4+} and forms $TiCl_4$ as shown in Eq. (2.13) [103].

$$Ti^{4+} + 4Cl^{-} = TiCl_4 \qquad (2.13)$$

The viscosity of $TiCl_4$ is very high, and removal from the Ti alloy surface is challenging. Hence, a layer of the $TiCl_4$ slowly forms on the substrate. Moreover, the unequal balance of electrons between the Ti^{4+} and Cl^{-} leads to the thickening of the layer of Cl^{-}.However, the higher polarity of water compared with Ethylene glycol leads to the react H_2O with the $TiCl_4$ and produced the TiO_2 as shown in Eq. (2.14)

$$TiCl_4 + 2H_2O = TiO_2(s) + 4H^{+} + 4Cl^{-} \qquad (2.14)$$

Table 2.3 Different magnetorheological fluid-assisted finishing processes

Sl. No.	Authors	MFAF process	Workpiece material	Final surface roughness (R_a)	Finishing time	Ref.
1	Kim et al., (2004)	Disc based MRF	Silicon	11.1 nm	5 min	[104]
2	Seok et al. (2007)	Disc based MRF	NA	40 nm	140 min	[105]
3	Jung et al. (2009)	Disc based MRF	Al_2O_3-TiC	255.1 nm reduction	60 min	[106]
4	Jang et al. (2010)	MFAF	Glass carbon	11.8 nm	10 min	[107]
5	Singh et al. (2011)	BEMRF	EN31 steel[a] Copper[b]	70 nm[a] 102 nm[b]	100 min[a] 60 min[b]	[108]
6	Singh et al. (2012)	BEMRF	Iron	16.6 nm	120 min	[91]
7	Jang et al. (2012)	MFAF	Stainless steel[a] Brass[b]	147.1 nm[a] 14 nm[b]	4 min	[109]
8	Sidpara and Jain (2012)	MFAF	Ti alloy	28 nm	64 hour	[110]
9	Kumar et al. (2015)	R-MRAFF	Stainless steel	36 nm	24.8 hours	[111]
10	Maan et al. (2017)	BEMRF	Tool steel	30 nm	120 min	[112]
11	Bedi and Singh (2018)	MRAH*	Mild steel	78% reduction in R_a value	90 min	[113]
12	Barman and Das (2019)	MFAF	Ti alloy	10 nm	6.30 hour	[114]
13	Yadav and Singh (2019)	MFAF	EN 24 steel	25.3 nm	20 nm	[115]
14	Nagdeve al. (2020)	R-MRAFF	Ti alloy	50 nm	2 hour	[116]
15	Zhang et al. (2020)	MFAF	Stainless steel	308 nm	20 min	[117]

**MRAH: Magnetorheological abrasive honing; MRF: Magnetorheological finishing; Magnetorheological fluid assisted finishing; MRAFF: Magnetorheological abrasive flow finishing: R-MRAFF: Rotational magnetorheological abrasive flow finishing*

Furthermore, the reaction of Ethylene glycol with $TiCl_4$ also leads to the form of the TiO_2 as shown in Eqs. (2.15), (2.16), (2.17), and (2.18).

$$TiCl_4 + 2HO(CH_2)_2OH = Ti[O(CH_2)_2O]_2 + 4H^+ + 4Cl^- \quad (2.15)$$

$$\mathrm{Ti[O(CH_2)_2O]_2} + 2H_2O = TiO_2(s) + 2\mathrm{HO(CH_2)_2OH} \quad (2.16)$$

$$TiCl_4 + 4\mathrm{HO(CH_2)_2OH} = \mathrm{Ti[O(CH_2)_2O]_4} + 4\mathrm{H^+} + 4\mathrm{Cl^-} \quad (2.17)$$

$$\mathrm{Ti[O(CH_2)_2O]_4} + 2H_2O = TiO_2(s) + 4\mathrm{HO(CH_2)_2OH} \quad (2.18)$$

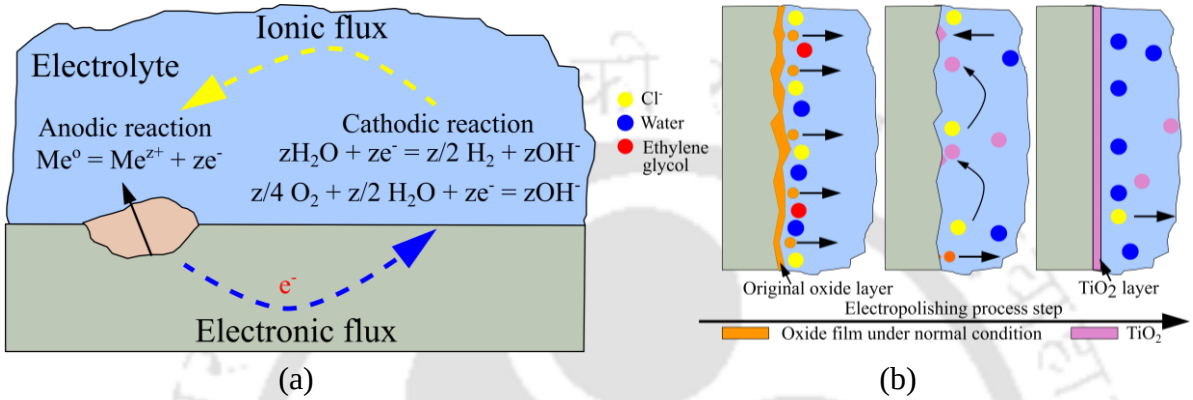

(a) (b)

Fig. 2.11 (a) Chemical reactions at electrodes and (b) formation of uniform and thick oxide layer on Ti alloy surface during electrochemical reactions

The newly formed $TiO_2(s)$ shows a substantial adhesion property with the surface of the Ti alloy and is inactive to react with other ions available in the electrolyte [118]. The series of electrochemical reactions produces a uniform and thick passive layer of the oxide layer on the surface of the Ti alloy, as demonstrated in Fig. 2.11(b).

2.6 Experimental setup

An electromagnet-based H-ECMR finishing is developed to increase the biocompatibility and surface quality of the Ti-6Al-4V. The non-varying magnetic field generated with the assistance of the electromagnet affects process efficiency during the surface finishing. In situ variation in the rheological properties of MR fluid, as required in different biomedical implants, is attainable with an electromagnet-based H-ECMR finishing process. The pure iron core provides a concentrated magnetic field at the polishing zone, as illustrated in Fig. 2.12. Furthermore, the cooling coils are wrapped over the electromagnet, and coolant is circulated through these coils to reduce heat produced because of the resistive heating of the electromagnetic coil. Four mounting plates provide housing for the electromagnet and ensure its fixed position during the surface finishing operation. Provision for threaded joints in each mounting plate can be used to lock their respective positions once. The magnetic shield material

(i.e., mu-metal) confines the tip of the electromagnet core to restrict the magnetic field's leakage and provide a uniform and concentrated magnetic field at the polishing spot. Due to the higher permeability value for mu-metal, a low reluctance path for the magnetic field provides a shield against a static magnetic field. It further allows the passing of a magnetic field around the shield area, overpassing the protected space. However, due to its high permeability, direct contact of mu-metal with core material results in its magnetization. A thin insulating material tightly fitted over the core of the material is provided between the core and the mu-metal to prevent its magnetization. The developed polishing tool helps produce a concentrated magnetic field at the polishing zone. Figure 2.12 shows the *Hybrid-electrochemical magnetorheological* (*H-ECMR*) finishing experimental setup. Moreover, the electromagnet-based H-ECMR finishing setup is retrofitted over a 5-axis *Computer Numerical Control* (*CNC*) milling machine to provide an appropriate *Degree of Freedom* (*DOF*) required between the workpiece and the polishing tool, as shown in Fig. 2.12.

The potential difference is applied between the polishing tool and workpiece; a carbon brush is connected to the electromagnet's core for the desired purpose. Moreover, Electrolytes replace the MR fluid’s carrier medium to enable the electrochemical reaction between the polishing tool and the workpiece. The different process parameters and composition of MR fluid during the polishing are listed in Table 2.4. Ti-6Al-4V is a biomaterial used as the workpiece (50×50 mm) during H-ECMR finishing operation; the improved biocompatibility and mechanical strength make it more favorable than other biomaterials. The surface characteristic of the polished and unpolished surfaces are examined with an optical profilometer. XPS, EDX, and SEM are used to explore the characteristics of the oxide layer developed on the biomaterial.

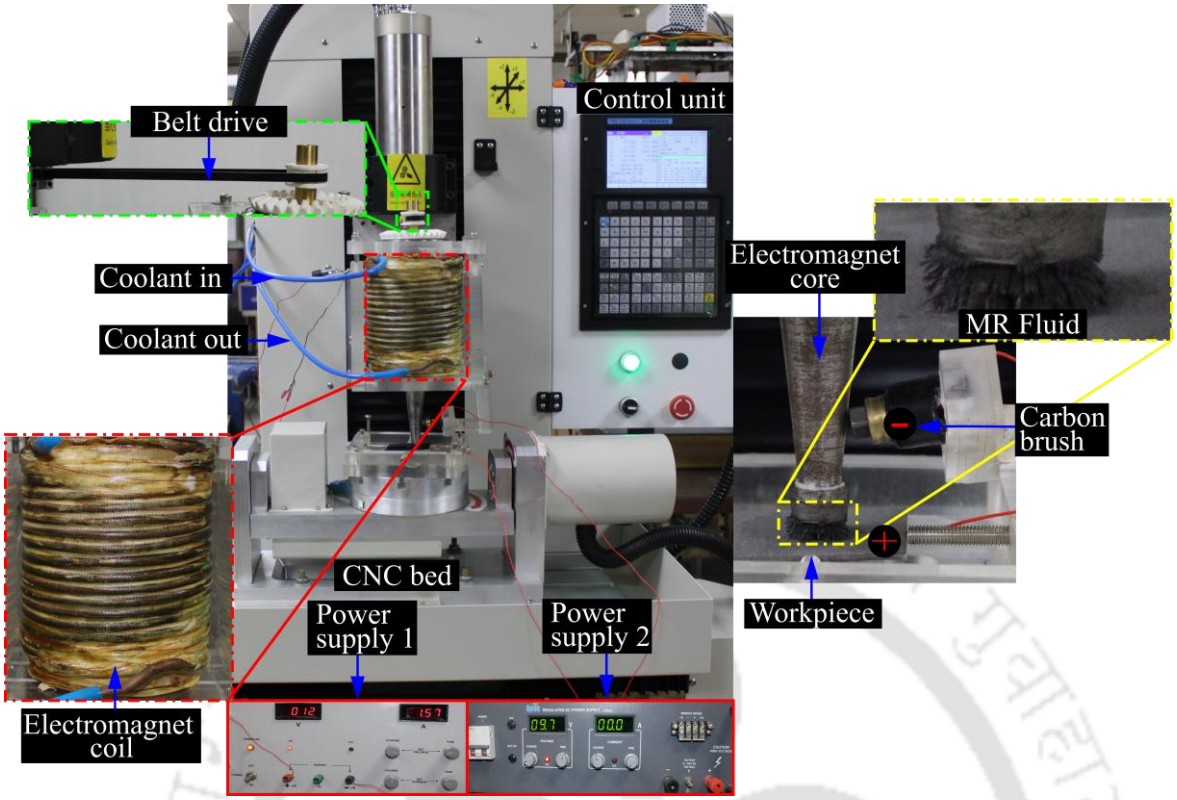

Fig. 2.12 Hybrid-electrochemical magnetorheological (H-ECMR) finishing experimental setup

Table 2.4 Compositions of MR fluid and process parameters of H-ECMR finishing

Constituents / Parameters	Composition (Vol. %) / Magnitude
Diamond	7%
Carbonyl Iron Particles (CIPs)	40 %
Magnesium chloride	16.35%
Ethylene glycol	6.15%
Glycerol	8 %
H_2O	22.5%
Feed rate	1 mm/min
Standoff distance	0.5–2 mm
Polishing tool's rotational speed	600–1600 mm
Applied current	1–2.4 A

2.7 Analytical model of H-ECMR finishing

An analytical model is developed to determine the R_a achieved after the H-ECMR finishing process; a few assumptions are made. The direct current energizes the electromagnet for the generation of magnetic flux. Hence, the production of the magnetic field because of the time-dependent electric field in the ampere's law is eliminated (termed as the displacement current). The reduced Maxwell equation, as shown in Eq. (2.19), states that the *total current* ($J.da$) passes through a *closed surface* (S) is equal to *magnetic field intensity* (H) about the *closed*

contour (*C*). Moreover, Eq. (2.20) states the *magnetic field density* (*B*) conservation over a closed contour [119].

$$\oint_C Hdl = \int_S J.da \tag{2.19}$$

$$\oint_C B.da = 0 \tag{2.20}$$

The second assumption states that a highly permeable core material has confined the magnetic flux path along its structure. Fig. 2.13(b) illustrates the magnetic flux produced by the electromagnet during the surface finishing operation incorporating the above assumption. The permeability of the core material is higher than its surroundings ($\mu >> \mu_o$) is also a valid reason for the justification of the second assumption. Winding of the copper wire (a good conductor of electricity) is provided over the core material to produce the magnetic field. The *turns number* (*N*) and the *electric current* (*i*) supplied to the winding are 5472 and 3 Amp, respectively, exciting the electromagnet's core. The high permeability of the core makes it possible to confine its magnetic field during the H-ECMR finishing. The product of ampere and the turns number (i.e., *Ni*) is also termed the *magnetomotive force* (*F*), which is used to generate the *magnetic flux* (ϕ) in the equivalent circuit diagram. Moreover, the *magnetic flux* (ϕ) is defined by the normal component of the *B* passing over the *surface* (*S*) as shown in Eq. (2.21); however, the total ϕ entering and leaving the closed surface is zero.

$$\phi = \int_S B.da \tag{2.21}$$

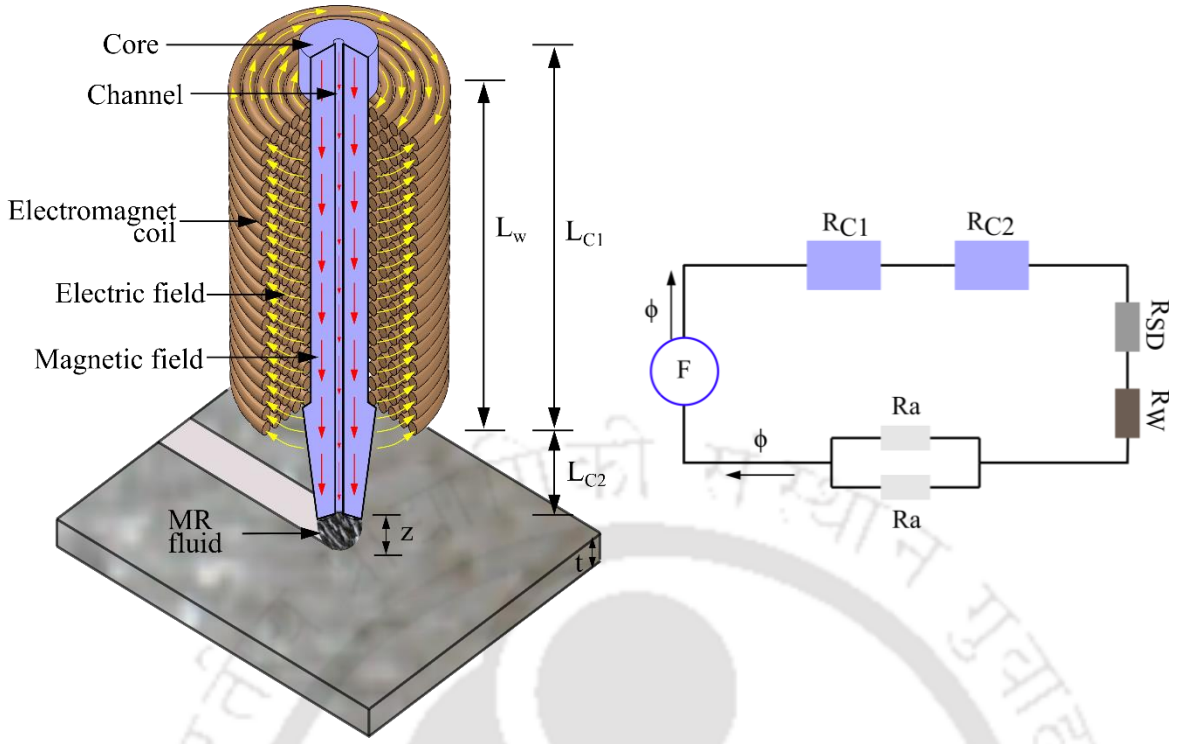

(a) (b)

Fig. 2.13 a) Magnetic flux generated inside electromagnet core and (b) equivalent magnetic circuit

The conical shape at the bottom of the core provides a concentrated magnetic field at the finishing spot. Hence, the core part is divided into sections C1 and C2, representing cylindrical and conical shapes. The length corresponds to the core sections denoted by L_{C1} and L_{C2}, respectively. Similarly, the standoff distance and the workpiece's thickness are denoted as z and t in Fig. 2.13(a). Equation (2.22) shows the scalar representation of the ϕ at the different cross-sections of the core.

$$\phi_C = B_{C_1} A_{C_1} + B_{C_2} A_{C_2} \tag{2.22}$$

Where, B_{C_1} and B_{C_2} Signifies the magnetic field density of sections C_1 and C_2, respectively. Similarly, the A_{C_1} and A_{C_2} represents the crosswise area of sections C_1 and C_2, respectively. Moreover, Eq. (2.23) represents the relation between the magnetomotive force and the H of the circuit shown in Fig. 2.13(b).

$$F = Ni = \oint_C Hdl \tag{2.23}$$

The relation between the magnetic field intensity and magnetic field density, as shown in Eq. (2.24), material's permeability (μ) dependent function. The permeability of the material (μ) is a product of free space permeability ($\mu_o = 4\pi \times 10^{-7}\ N/A^2$) and its relative permeability (μ_r). The relative permeability of the materials used during the H-ECMR finishing process, including core, MR fluid, and biomaterial, is listed in Table 2.5. However, before selecting the core material, the pure iron's relative permeability is compared with the mild steel (conventionally used as the core material) through a vibrating sample magnetometer, as shown in Fig. 2.14(a). It is noticed that the permeability of almost 99.9% pure iron is higher than mild steel; further, it is used as the electromagnet's core material to produce high magnetic field density. Moreover, the comparison is made between the magnetic strength of the CIPs manufactured by *Badische Anilin- und SodaFabrik* (*BASF*) and electrolytic iron particles, as illustrated in Fig. 2.14(b). Furthermore, the strength of CIPs particles is higher than the iron particle, with reduced hysteresis loss; hence it has opted as a ferromagnetic particle during the preparation of MR fluid [120].

$$B = \mu H \tag{2.24}$$

Table 2.5 Magnitude of relative permeability

Material	Relative permeability (μ_r)
Electromagnet core (99.9% pure iron)	10,000
MR fluid	5
Air	1
Workpiece (Ti-6Al-4V)	1

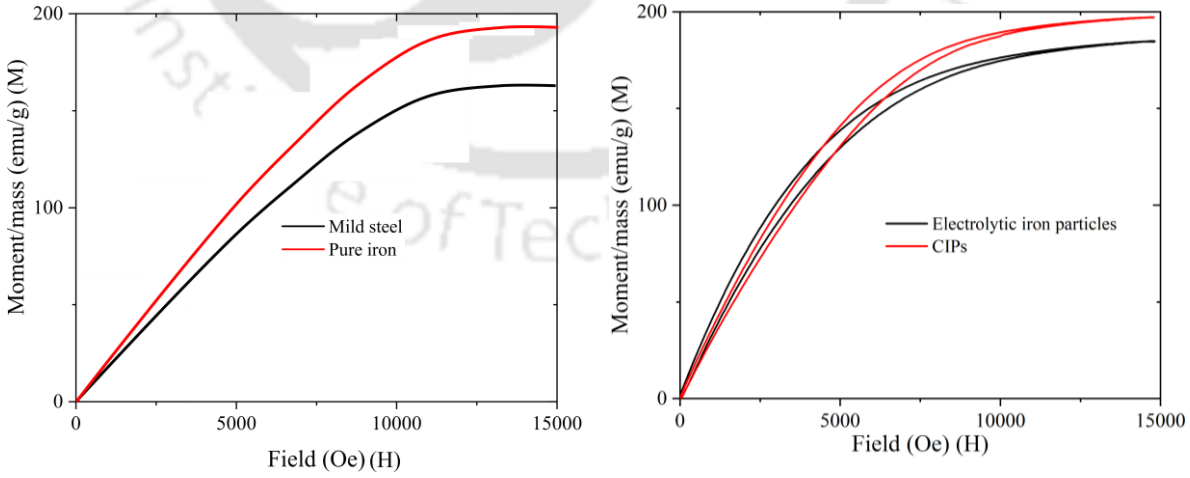

Fig. 2.14 M-H curve comparison between (a) pure iron and mild steel and (b) electrolytic iron and carbonyl iron (CIPs) particles

The magnetic flux (ϕ) is determined by Eq. (2.25). The equivalent reluctance of the circuit is further calculated through Eq. (2.26).

$$\phi = \frac{F}{R_{eqv}} \tag{2.25}$$

$$R_{eqv} = R_{c1} + R_{c2} + R_{SD} + R_W + \frac{R_a}{2} \tag{2.26}$$

Where reluctance produced by the core C_1 and C_2 is represented by the R_{C1} and R_{C2}, respectively. The reluctance caused by the Magnetorheological fluid, standoff distance, workpiece, and air is represented by the R_{MR}, R_{SD}, R_W, and R_a, respectively. However, reluctance is a material property determined by Eq. (2.27) [121].

$$R = \frac{l}{\mu A} \tag{2.27}$$

Where l is the equivalent length of the material, and A is its crosswise area. After implementing the geometrical data and the permeability of the materials, Eq. (2.25) is deduced to Eq. (2.28). Where L_{C1}, L_{C2}, D_1, D_2, d, and t are 145, 90, 30, 10, 4, and 10 mm, respectively. The equivalent reluctance of the circuit is determined through Eq. (2.27), and the *magnetic flux* (ϕ) generated from the electromagnet-based polishing tool is shown in Eq. (2.29).

$$\phi = \frac{Ni}{R_{eqv}} \tag{2.28}$$

$$\phi = \frac{Ni}{(5.35 + 20.27z) \times 10^9} \tag{2.29}$$

The magnetic field primarily depends upon the *standoff distance* (z). For an electric current of magnitude 3 Amp with 5472 turns in an electromagnet, the calculated magnetic field is shown in Eq. (2.30), where z is in mm. However, computational analysis for variation of the magnetic field over the workpiece at different stepovers is evaluated through finite element-based COMSOL software and illustrated in Fig. 2.15(a). The magnetic field variation is calculated experimentally through a Gauss meter to validate the analytical and computational

results. The magnetic field is studied at a different standoff distance; its variation is plotted in Fig. 2.15(b). It is found that the analytical and computational results follow a similar trend as observed from the experimental data. However, the magnetic field also depends upon the electric current, and a higher value produces a strong magnetic field, as shown in Fig 2.15(b).

$$B = \frac{327.5}{(419.97 + 2694.23z)} \tag{2.30}$$

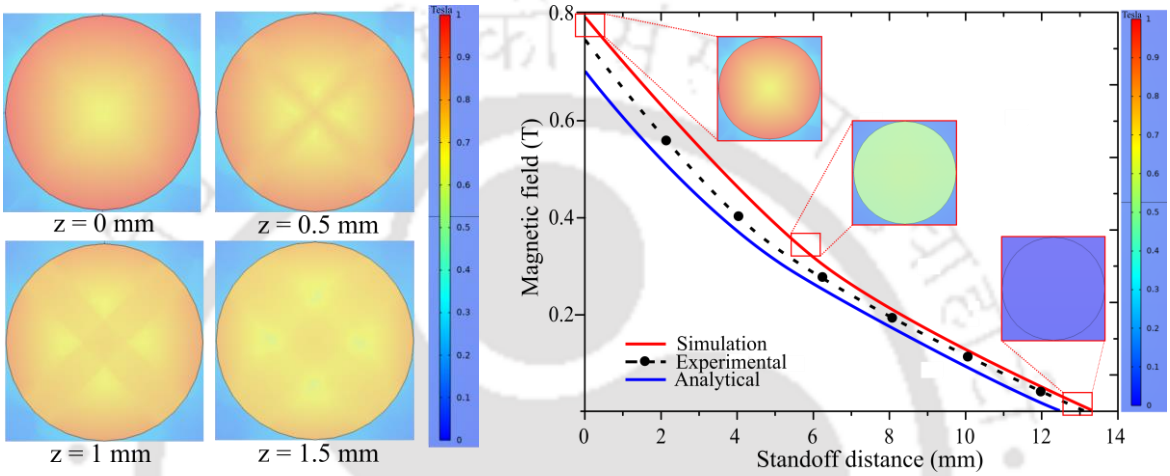

(a) (b)

Fig. 2.15 (a) Contour plot of simulated magnetic field at different standoff distances and (b) comparison of magnitude of magnetic field between simulation study, experimental measurement, and analytical model

2.7.1 Normal indentation force (F_n)

The magnetic field generated from the electromagnet applied *normal force* (F_n) on the diamond particles and evaluated from Eq. (2.31), assists in penetrating diamond particles in the substrate [122].

$$F_n = nf_n = \frac{B^2}{2\mu_o}\left(1 - \frac{1}{\mu_m}\right)S \tag{2.31}$$

Where n is the number of particles, f_n is the normal force applied on the individual diamond particle, S is the surface area factor, and μ_m is MR fluid's permeability. The normal force deduced from the derived magnetic field for the specified electromagnet is shown in Eq. (2.32).

$$f_n = \frac{193.36 \times 10^{-7}}{(419.97 + 269.42z)^2} \tag{2.32}$$

The number of abrasive particles (n) is calculated from the MR fluid composition, as listed in Table 2.4. The diameter of the CIPs (d) used during the experiment is 6 µm, and n is calculated from Eq. (2.33).

$$n = \frac{Vol.of\ MR\ fluid \times Vol.\%\ of\ abrasive}{Vol.of\ a\ single\ abrasive\ particle} = 0.11\frac{D^2 z}{d^3} \tag{2.33}$$

Where D is the diameter of the polishing tool (i.e., 10 mm) and z is the standoff distance (i.e., 1 mm). The Vol. % of the abrasive particle is 7% in the MR fluid. The number of the abrasive particle is 5.08×10^8, calculated from Eq. (2.33). Moreover, the normal force variation with standoff distance is calculated from Eq. (2.34) and is plotted in Fig. 2.16(a). It is observed that with an increase in the standoff distance, the normal force applied to the abrasive particle is decreased. Furthermore, the variation of the magnetic field with the applied current to the electromagnet is illustrated in Fig. 2.16(b), suggesting that a higher value of electric current leads to producing high-strength magnetic field density in the polishing region.

$$F_n = nf_n = \frac{9822.68}{(419.97 + 269.42z)^2} \tag{2.34}$$

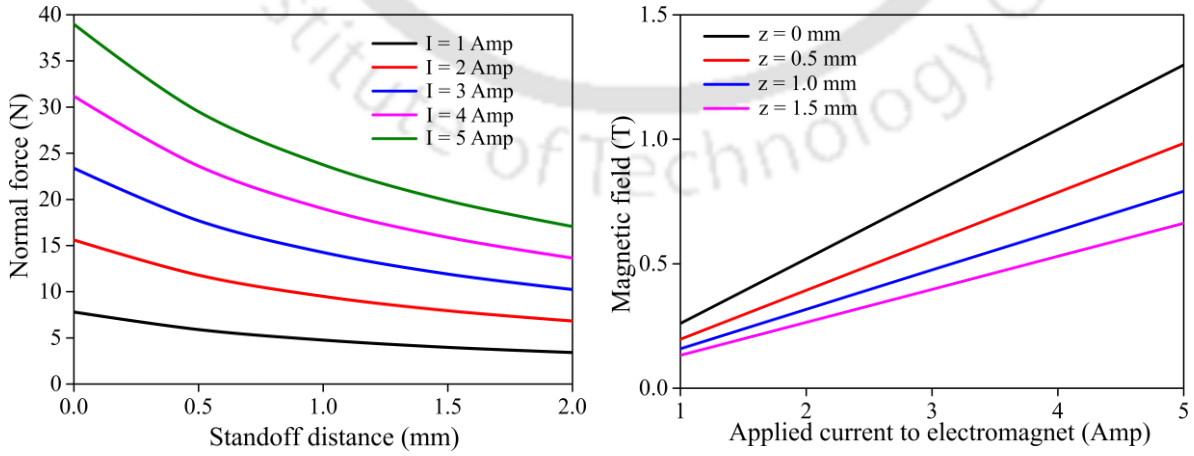

(a) (b)

Fig. 2.16 (a) Variation of normal force with standoff distance at different applied electromagnet current and (b) magnetic field variation with applied current for different standoff distances from tool tip

2.7.2 Tangential force (F_t)

The tangential force on the diamond particle separates the indented material from the biomaterial surface. As shown in Eq. (2.35), the tangential force is the summation of the *centrifugal force* (F_{cen}) and *shear force* (F_{shear}) generated on the abrasive particles during finishing.

$$F_t = F_{cen} + F_{shear} \tag{2.35}$$

The centrifugal force developed because of the rotational motion of the finishing tool and is calculated from Eq. (2.36).

$$F_{cen} = m\left(\frac{2\pi N}{60}\right)^2 r \tag{2.36}$$

Where *N* is the rotational speed of the polishing tool, *m* is the single abrasive particle's mass, and *r* is its radial distance. Similarly, the shear force on the abrasive particle is given by Eq. (2.37). Where the projected area of the indented abrasive particle into the workpiece surface is represented by A_p and calculated from Fig. 2.17(a) and shown in Eq. (2.38). Where *D* is the diamond particle diameter, and *t* represents the indented thickness. τ is the shear stress in the polishing zone and is represented by the subquadratic power law as shown in Eq. (2.39) [123].

$$F_{shear} = \tau A_p \tag{2.37}$$

$$A_p = \frac{\pi}{3} t^2 \left(\frac{3D}{2} - t\right) \tag{2.38}$$

$$\tau = \sqrt{6}\phi \mu_0 M^{\frac{1}{2}} H^{\frac{3}{2}} \tag{2.39}$$

Where ϕ is the CIP volume fraction in MR fluid, μ_0 is the free space permeability, *H* is magnetic field intensity, and *M* is saturation magnetization. The *Vibrating Sample Magnetometer* (*VSM*) reading of MR fluid, as shown in Fig. 2.17(c), is used to determine the correlation among the magnetic field density (*B*, Tesla) and magnetization (*M*, emu), as shown in Eq. (2.40).

$$M = -5.66 \times 10^{-14}B^3 + 8.44 \times 10^{-10}B^2 - 3.91 \times 10^{-6}B + 7.32 \times 10^{-2} \quad (2.40)$$

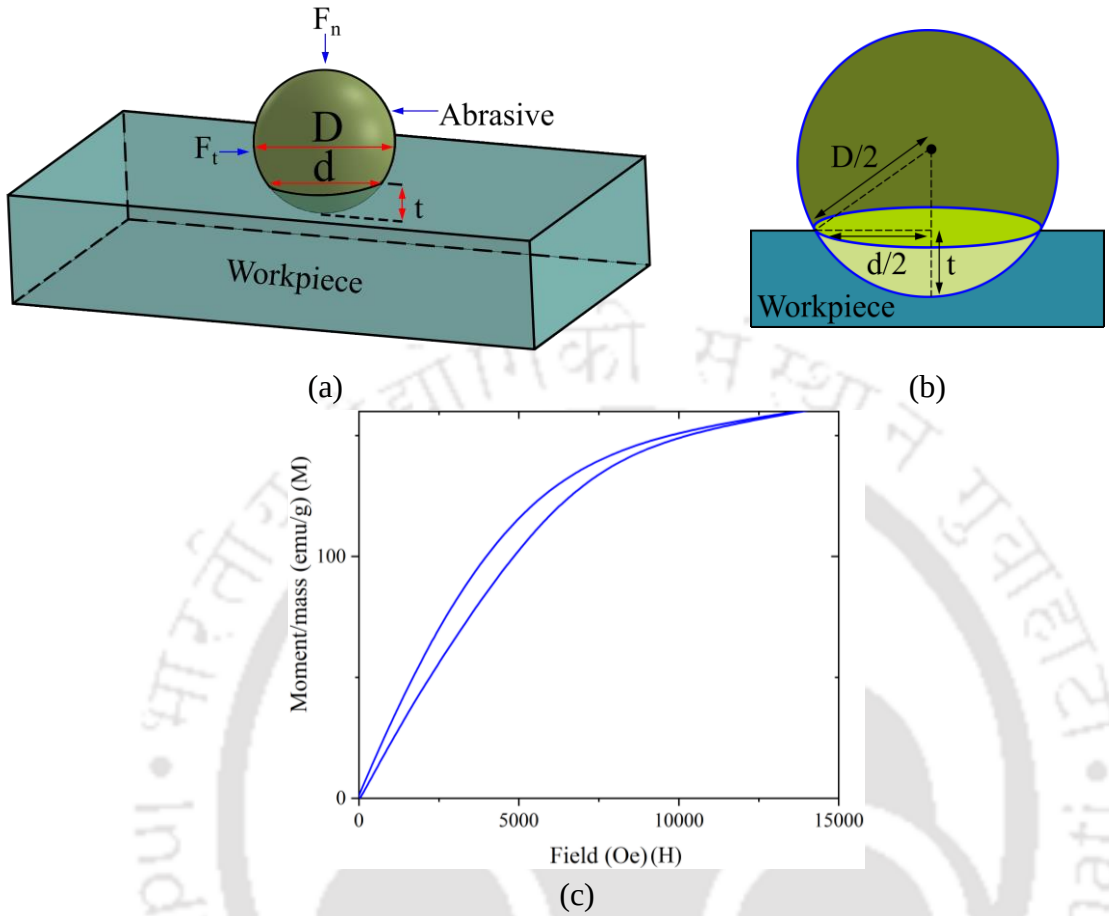

Fig. 2.17 (a) Abrasive particle indented into workpiece surface, (b) diameter and depth of indented abrasive particle, and (c) M-H curve of MR fluid

2.7.3 Surface roughness modeling

The initial surface roughness profile is generated from the optical profilometer for the biomaterial surface. The forces developed during the surface finishing operation are used to calculate the reduction in the average surface roughness; abrasive particles get indented inside the workpiece under the normal force impact, and the indented thickness is calculated from Eq. (2.41) and also shown in Fig. 2.17(b). The *diameter of the indentation* (d) is further calculated from the *Brinell Hardness Number* (*BHN*) of the workpiece material, as shown in Eq. (2.42).

$$t = \frac{D}{2} - \frac{1}{2}\sqrt{D^2 - d^2} \quad (2.41)$$

$$d = \sqrt{\left(D^2 - \left(D - \frac{2F_n}{\pi D(BHN)}\right)\right)} \quad (2.42)$$

The average width of the valley from the mean line is 0.68 µm on the surface of biomaterial before polishing; however, the diameter of the abrasive particle is 6 µm; hence, the narrow valleys are initially unattainable. Therefore, the abrasive particle will remove the higher peaks (max(P_i)) during the first stroke of the surface finishing process. The indented thickness (t) from the initial peaks is removed, and the new coordinate of the peak is defined by Eq. (2.43).

$$P_{i,new} = P_{i,max} - t \tag{2.43}$$

Figure 2.18(a) illustrates the material removal from the higher peaks; however, the valleys of the surface profile will remain the same. Furthermore, the mean line is defined as the area of peaks and valleys below and above the line is equal. Material reduction from the biomaterial surface shifts the mean line and is calculated from Eq. (2.44).

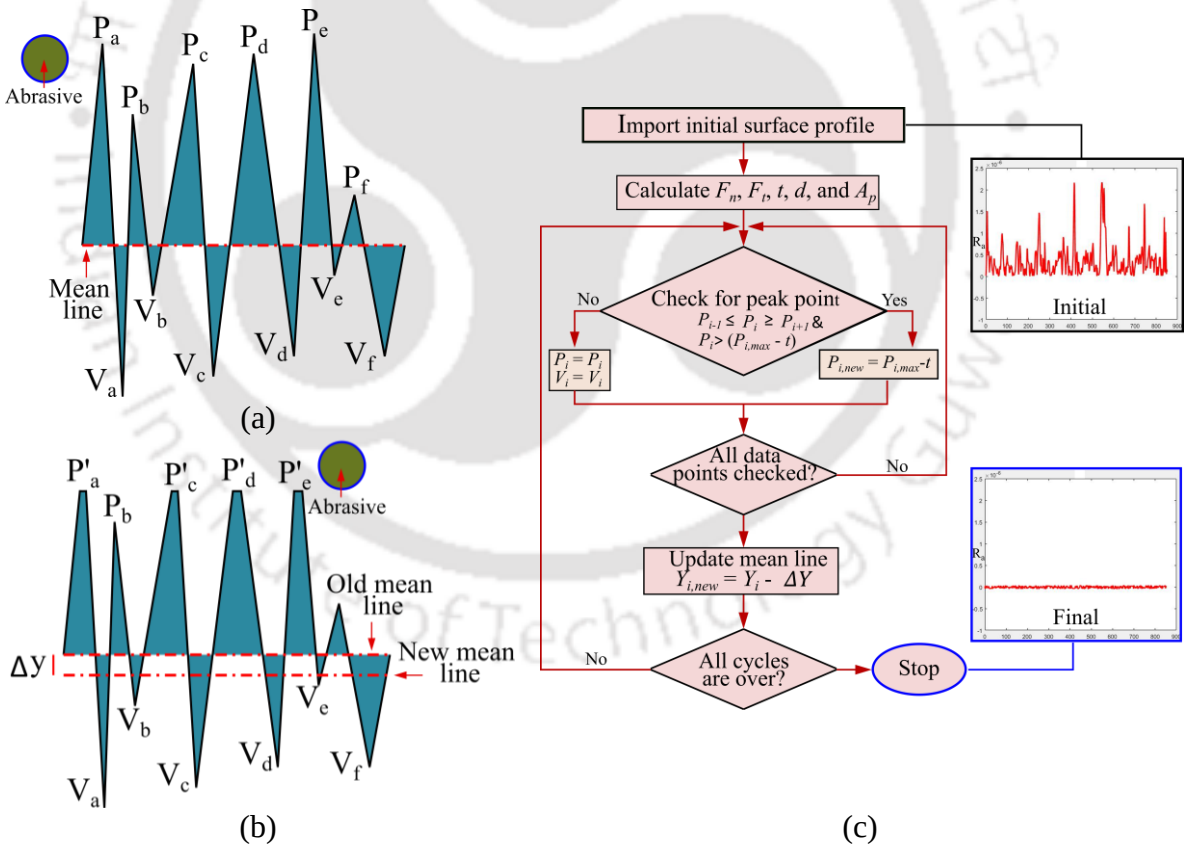

Fig. 2.18 Surface irregularities (a) before and (b) after polishing; (c) Flowchart showing algorithm to calculate final surface roughness profile

After every iteration, the mean line gets updated to calculate the average surface roughness, as illustrated in Fig. 2.18(c) and Eq. (2.45). Where n is the number of data points.

The iteration is repeated for the predefined number of cycles, and the flow chart of the respective algorithm is illustrated in Fig. 2.18(b). Furthermore, the % reduction in R_a is calculated from Eq. (2.46).

$$Y_{i,new} = Y_i - \Delta Y \tag{2.44}$$

$$R_a = \frac{\sum_{i=1}^{n} |Y_i|}{n} \tag{2.45}$$

$$\% \, \Delta R_a = \frac{(R_a)_{before\ polishing} - (R_a)_{after\ polishing}}{(R_a)_{before\ polishing}} \times 100 \tag{2.46}$$

2.8 Results and discussion

The *H-ECMR* enhances biocompatibility and the surface quality of biomaterials; herein, the synergic action of electrochemical reaction along with the mechanical abrasion reduces the finishing time and produces a uniform surface quality. Furthermore, *average surface roughness* (R_a), *kurtosis* (R_{ku}), and *skewness* (R_{sk}) are further analyzed to determine the change in surface characteristics before and after polishing. Moreover, including an electrochemical reaction between the substrate and tool produces a uniform and thick oxide deposit on the substrate of Ti-6Al-4V. SEM, EDX, and XPS are used to analyze characteristics of the oxide layer formed on biomaterial before and after finishing and are discussed in the subsequent sections. Various input parameters' impact on the workpiece's surface quality is also analyzed.

2.8.1 Impact of mu-metal on effectiveness of polishing tool

The magnetic flux circulating through the core's tip is responsible for spreading the MR fluid at the polishing zone, producing nonuniform surface quality on the polished surface. Hence, concentrated magnetic field lines must be created at the polishing spot to overcome limitations. A simulation study of the polishing tool with and without mu-metal is illustrated in Fig. 2.19. The magnetic shield material (i.e., mu-metal) confines the tip of the electromagnet core to restrict the magnetic field's leakage. It provides a uniform and concentrated magnetic field at the polishing spot. Mu-metal, a magnetic shielding material is an alloy of nickel, molybdenum, and iron; its chemical composition is analyzed through the EDX and shown in Fig. 2.20(b). Due to the higher permeability value for mu-metal, a low reluctance path for the magnetic field

provides a shield against a static magnetic field. It further allows the passing of a magnetic field around the shield area, overpassing the protected space.

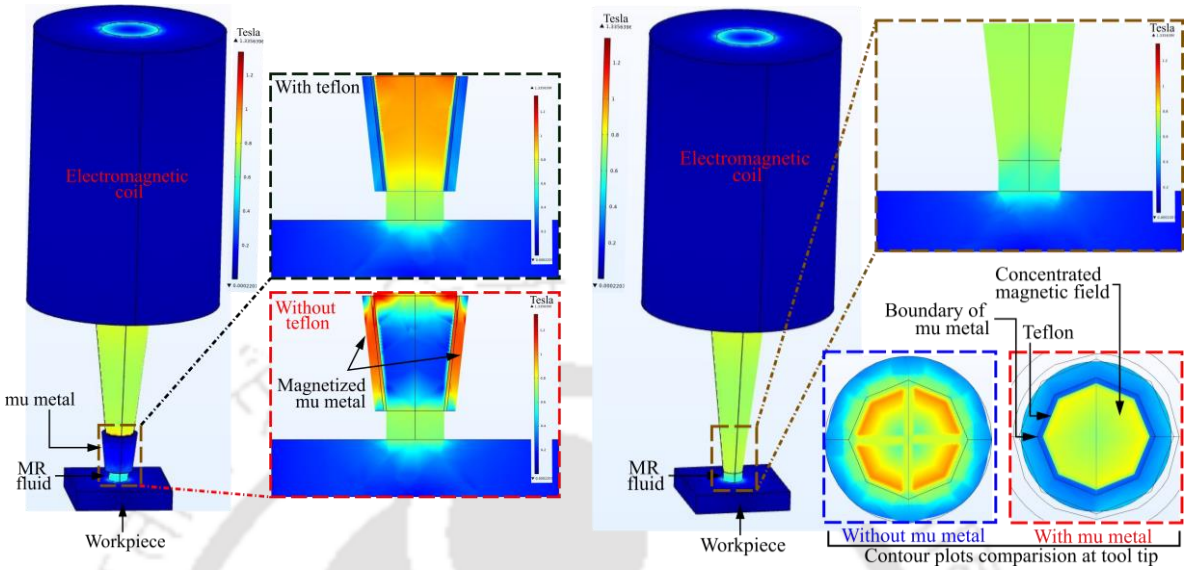

(a) (b)

Fig. 2.19 Simulation study of polishing tool (a) with and (b) without mu-metal

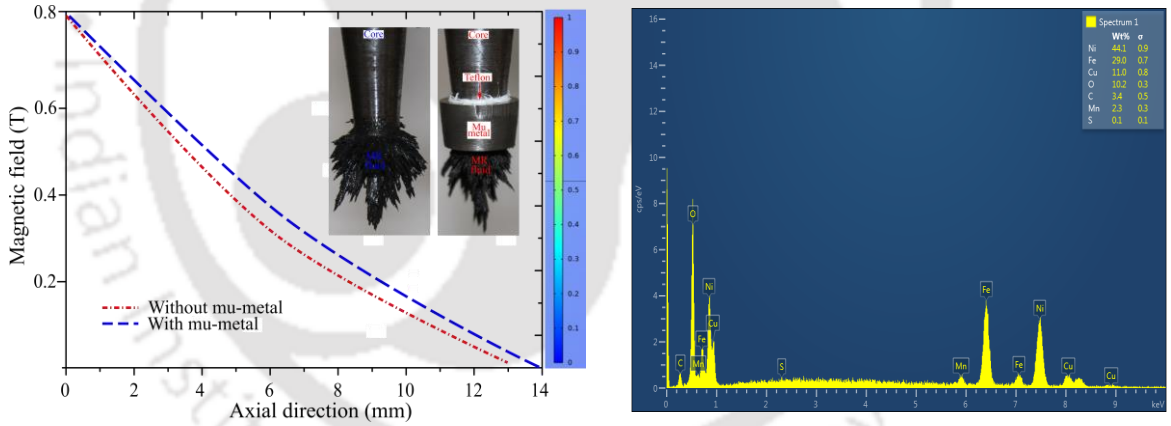

(a) (b)

Fig. 2.20 Variation of magnetic field (a) along axial direction (i.e., Z axis) from tool tip and (b) EDX study for mu-metal composition

Furthermore, simulation analysis is performed to study the magnetic field line generated with the inclusion of mu-metal. It is observed that direct contact with the mu-metal initially leads to the magnetic flux flow through it, as illustrated in Fig. 2.19(a). Hence, a nonmagnetic material (i.e., Teflon) is required between the core material and mu-metal to discontinue the magnetization of the mu-metal. The computational results show that including the mu-metal over the polishing tool's surface restricts the magnetic field's leakage and provides a uniform and concentrated magnetic field at the polishing spot, as shown in 2.19(b). Moreover, concentrated MR fluid is achieved with enclosed mu-metal over the surface of the

electromagnet core, as shown in Fig. 2.20(a). The increase in the magnetic field in the axial direction (red dashed line) of the polishing tool is also observed during experiments.

2.8.2 Impact of process parameters

Analyzing process parameters' impact on the output responses during the H-ECMR finishing is crucial for determining their optimum combinations to achieve maximum surface roughness reduction with uniform surface quality. The influence of different process parameters, namely the polishing tool's rotational speed, the percentage composition of electrolyte in MR fluid, the current applied between the workpiece and polishing tool, and surface finishing time on surface quality, is examined and discussed in the subsequent section.

2.8.2.1 Rotational speed of polishing tool

The rotational motion of the polishing tool is provided to produce the centrifugal forces on the abrasives during the surface finishing. Figure 2.21(a) shows the influence of the polishing tool's rotation speed on the % reduction in R_a while keeping electrolyte's Vol. concentration, applied current, and finishing time constant at 45%, 2 Amp, and 30 mins, respectively. The polishing tool's rotational speed is varied between 400 to 1400 rpm. Initially, it is observed that with increased rotational speed, the % reduction in the R_a rises to 800 rpm. Afterward, the surface quality starts to deteriorate. The maximum surface finish improvement (i.e., % reduction in R_a of 96.23%) is obtained at 800 rpm, as shown in Fig. 2.21(a). The CIPs chains are bonded because of the applied external magnetic field; it is observed that increased rotational speed beyond optimum value leads to the dominance of centrifugal force applied to the CIPs chains over their holding capacity. This phenomenon leads to the detachment of CIPs chains beyond optimum rotational speed, which is responsible for the deterioration in the surface quality of the polished surface.

2.8.2.2 Electrolyte concentration (Vol. %)

Magnesium Chloride ($MgCl_2$) is combined with Ethylene glycol ($C_6H_6O_2$) in distilled water to form an electrolyte to increase the efficiency of the electrochemical reaction. The electrolyte is the MR fluid's transportation medium to enable the electrochemical reaction during the H-ECMR finishing process. The simultaneous action of the mechanical abrasion and electrochemical reaction helps to produce uniform surface quality. Variation of % reduction in R_a with the volume % of electrolyte in MR fluid is illustrated in Fig. 2.21(b). The percentage concentration of electrolyte in MR fluid is varied between 35 to 55% while keeping other

process parameters, i.e., the rotational speed, applied current, and polishing time constant at 800 rpm, 2 Amp, and 30 mins, respectively. An increase in the electrolyte's concentration initially leads to an increased % reduction in R_a. However, after a certain point, the % reduction in R_a decreases with higher electrolyte concentration. The reaction rate of Ti-6Al-4V with $MgCl_2$ and $C_2H_6O_2$ in distilled water is low when the electrolyte's concentration in MR fluid is below 45%. However, with a further increase in the percentage of electrolyte, the reaction rate becomes vigorous, producing pits on the polished surface. Figure 2.21(b) shows the variation of % reduction in R_a with a change in electrolyte concentration. The maximum % reduction in R_a (i.e., 97.23%) is achieved at 45% electrolyte concentration. Furthermore, the vigorous reactions between the substrate and electrolyte produce a steep downward slope of % reduction in R_a between 45 to 55% electrolyte concentration.

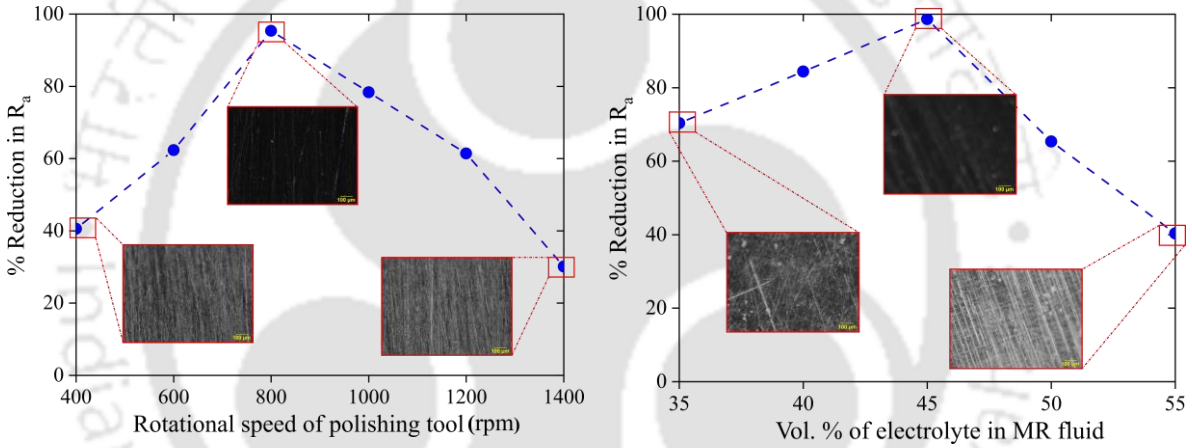

Fig. 2.21 Variation of percentage reduction in % reduction in R_a with (a) rotational speed of polishing tool and (b) electrolyte concentration (Vol. %) in MR fluid

2.8.2.3 Finishing time

The impact of finishing time on the % reduction in R_a is shown in Fig. 2.21 (a). During experiments, the finishing time is varied between 20 to 35 mins, keeping the tool's rotational speed, applied current, and electrolyte concentration fixed at 800 rpm, 2 Amp, and 45%, respectively. Initially, the % reduction in R_a rises with an increased finishing time. After 30 mins of finishing time, the maximum % reduction in R_a is observed (i.e., 97.12%). However, with a further increase in the finishing time, the reduction in average surface roughness decreases because diamond particles generate scratches over the finished part, as illustrated in Fig. 2.22(a).

2.8.2.4 Applied current

The current applied between the substrate and polishing tool triggers the electrochemical reaction, and the reaction rate primarily depends on it during H-ECMR finishing. The analysis of the variation of current applied to the % reduction in R_a was studied (Fig. 2.22(b)) by varying it between 1 to 2.4 Amp while keeping rotational speed, electrolyte concentration, and finishing time constant at 800 rpm, 45%, and 30 mins, respectively. The increased applied current leads to a rise in the percentage reduction in the average surface up to the optimum point (i.e., 2 Amp); beyond that, % reduction in R_a reduces as the reaction rate increases between electrolyte and substrate, which causes the production of pits, as shown in Fig. 2.22(b).

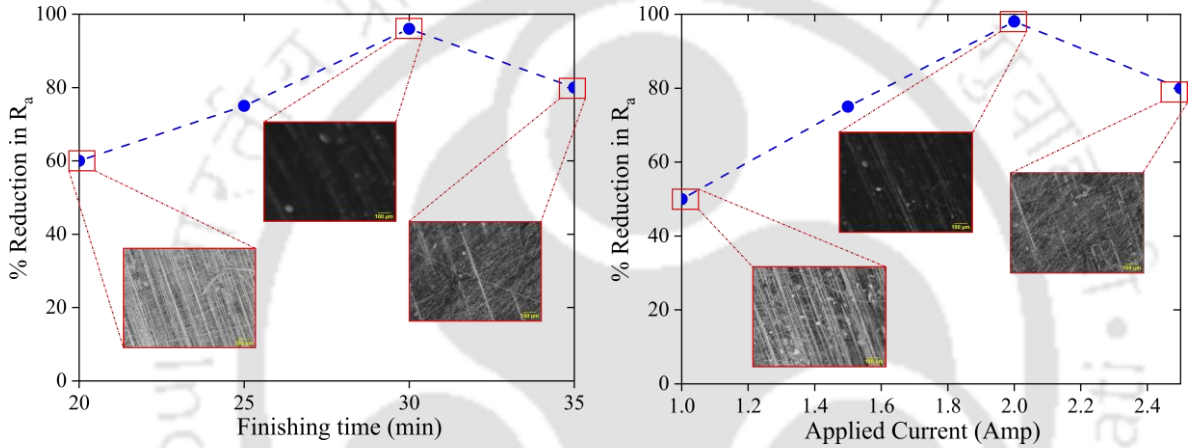

Fig. 2.22 Variation of % reduction in R_a with (a) finishing time and (b) applied current

2.8.3 Characterization of workpiece surface

The *H-ECMR* finishing process produces a uniform polished surface over the Ti-6Al-4V. The initial R_a value of 325.90 nm decreases to 12.90 nm on the polished workpiece surface through optimum parameters, as discussed in the previous section. A mirror-like polished surface is achieved on the biomaterial, as illustrated in Fig. 2.23(a). Furthermore, the 2D surface roughness profiles comparison among pre and post-finishing of the workpiece is shown in Fig. 2.23(a). It is noticed that initially, different scratch marks produced on the biomaterial surface are significantly removed after H-ECMR finishing. Furthermore, a comparison between the linear R_a profiles before and after polishing is shown in Fig. 2.23(b).

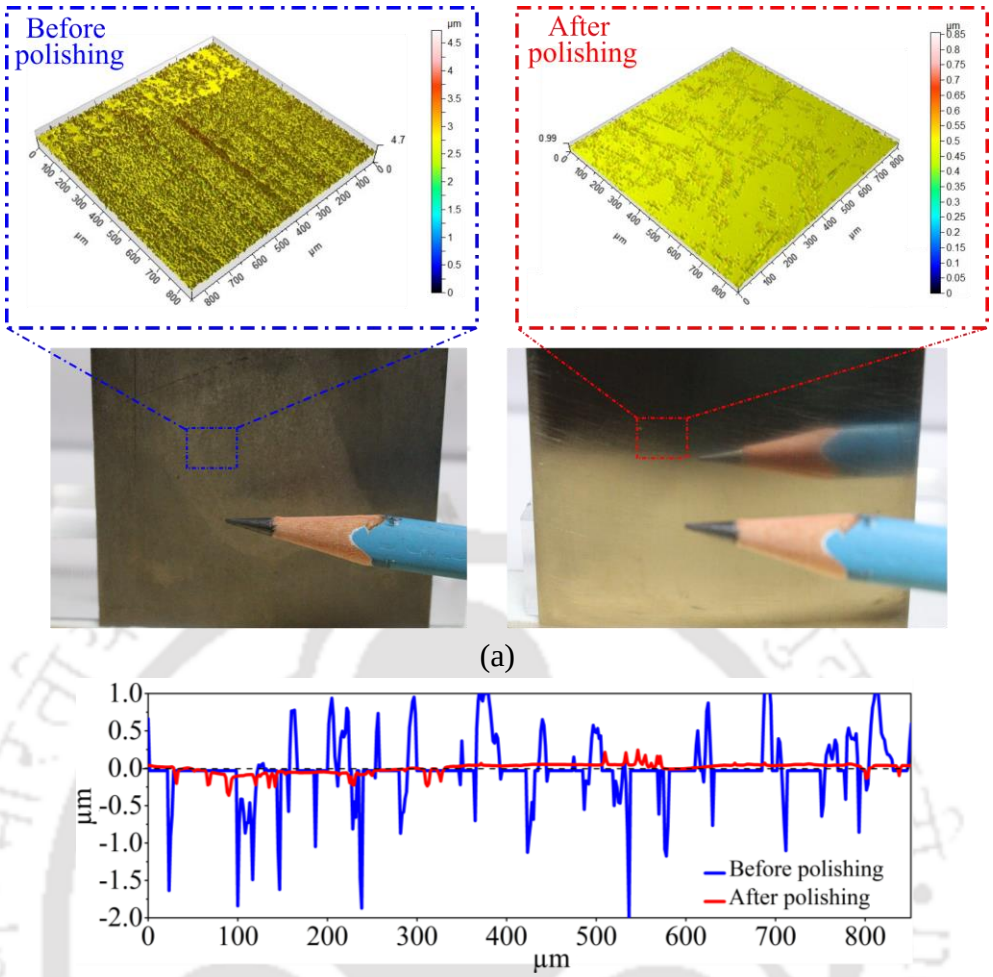

Fig. 2.23 Comparison between (a) area and (b) linear surface roughness profiles before and after finishing

Scanning Electron Microscopic (*SEM*) images, as shown in Fig. 2.24, are used to analyze the surface topography of the workpiece substrate before and after the polishing operation. Initially, pits and scratch marks are easily visible on the Ti-6Al-4V surface (Fig. 2.24). However, after finishing, a smooth and uniform surface is produced on the biomaterial surface. Furthermore, the *Atomic Force Microscopic* (*AFM*) image (Fig. 2.24) also shows a significant improvement in the surface topography of the polished surface. The analysis of R_a only delivers details regarding the mean depth of valleys and altitude of peaks from an average line on the surface irregularities. Hence, a study of kurtosis (R_{ku}) and skewness (R_{sk}) is also performed to get details regarding the surface characteristics of Ti-6Al-4V during H-ECMR finishing. Kurtosis is a statistical tool used to determine the flatness of the peaks generated over the substrate surface; However, skewness analyzes the supremacy of valleys and peaks of the workpiece surface. A kurtosis value higher than three (i.e., R_{ku} = 3.45) is observed before

polishing, representing the pointed peaks observed on the surface irregularities, as shown in Fig. 2.24.

Moreover, the positive value of the skewness (i.e., R_{sk} = 1.13) is observed on the initial workpiece surface, denoting that valley numbers are lower than peaks. However, after H-ECMR finishing, the kurtosis value is reduced below three (i.e., R_{ku} = 1.69), denoting generated flat peaks of surface irregularities after finishing. Similarly, the negative skewness (i.e., R_{sk} = -0.52) represents that the number of peaks is reduced than valleys after the H-ECMR process on the biomaterial surface. The negative skewness and kurtosis value of less than three indicates that the chances of wear out of the surface irregularities from the workpiece surface on their tribological contact are very low as fewer flat peaks are produced than valleys.

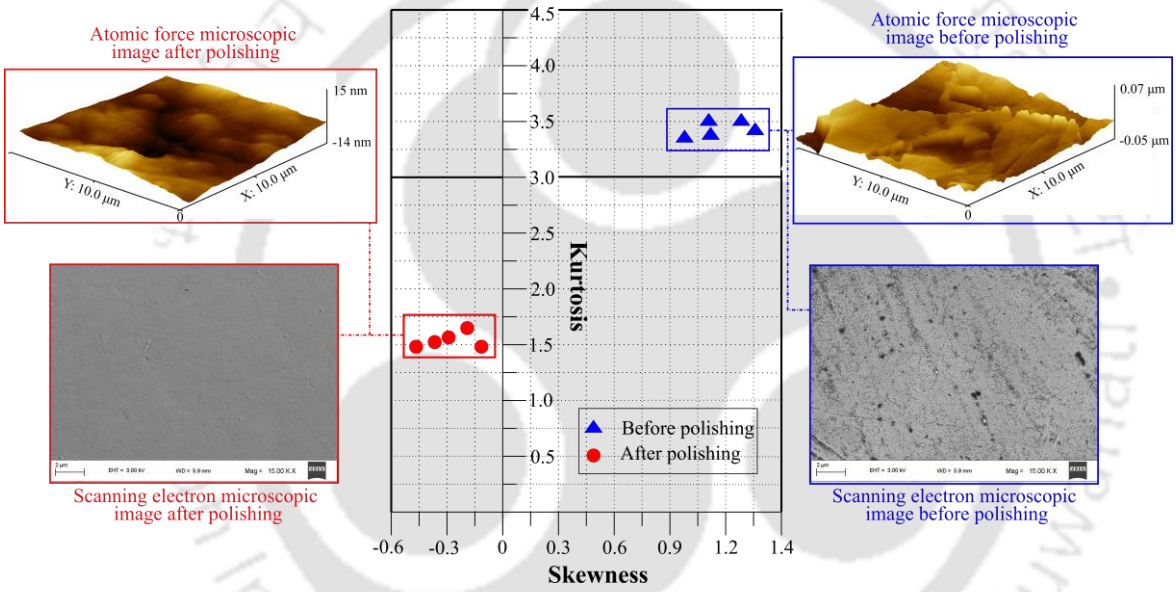

Fig. 2.24 Kurtosis Vs. skewness mapping, and workpiece images from atomic force microscope and scanning electron microscope before and after polishing

The H-ECMR and conventional Magnetorheological Finishing (MRF) efficiency is compared by performing finishing operations at identical process parameters conditions on the substrates having the same mapping area (i.e., 50×50 mm). The % reduction in R_a is measured continuously with an interval of 5 mins, as shown in Fig. 2.25(a). A higher % reduction in R_a value of 96.41% is achieved using H-ECMR compared to a lower value of 49.63% using MRF for 30 min of polishing time. The synergic operation of the electrochemical reaction and the polishing reduces the surface finishing time for the H-ECMR process.

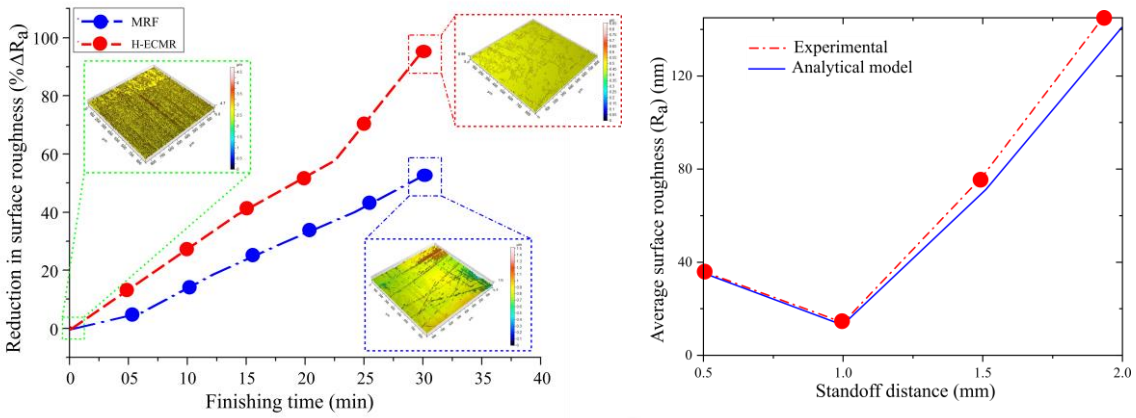

(a) (b)

Fig. 2.25 Comparison of Avg. surface roughness between (a) H-ECMR and MRF at different finishing times and (b) experimental measurement and analytical model at different standoff distances

The standoff distance between the workpiece surface and the polishing tool tip is kept varying, which results in a change in the magnetic force applied to the abrasive particle during finishing. At a 0.5 mm standoff distance, the final average R_a is decreased to 37.56 nm from 317.25 nm; however, a further surge in the standoff distance causes a reduction in the final R_a to 1 mm, as shown in Fig. 2.25(b). Subsequently, as the distance between the tool and the workpiece increases, the value of R_a also increases proportionately. Active abrasive particles number rise with a surge in the standoff distance, which causes a decrease in the R_a value till 1 mm of standoff distance. However, a further rise in the distance between the workpiece and the tool causes a significant decline in the magnetic force generated on the diamond particles during polishing, leading to a higher R_a value of the polished surface.

As discussed in Section 2.7, the developed analytical model for determining average surface roughness is compared with the experimental results (Fig. 2.25(b)). It is observed that with an increase in the standoff distance, the difference (i.e., % error) between the results obtained from the analytical model and experimental data increases. Initially, for a range of standoff distance between 0.5 to 1 mm, the % error varies from 2.35 to 3.69. However, at a 2 mm standoff distance, the % error is increased to 8.96. As the standoff distance increases, the number of active abrasive particles increases, though the magnetic field applied from the electromagnet is still constant for holding the CIPs chain. Hence, there is a higher chance of detachment of a few CIPs chains from the polishing media, which leads to a lower number of active abrasive particles calculated analytically than from the experiment.

2.8.4 Oxide layer thickness

The oxide layer development on the biomaterial's surface is crucial as it increases its corrosion resistance. The Ti-6Al-4V reacts with the environmental oxygen and forms a passive oxide layer of TiO_2. The pH value of the passive oxide layer is the same as the human body and helps to reduce corrosion during their interaction. However, the thickness of the oxide layer on the biomaterial surface is nonuniform, with a layer thickness in the range of a few nanometers (i.e., 5-10 nm); hence, the number of corrosion potential sites on the Ti-6Al-4V surface is higher. The H-ECMR finishing process uses an electrolytic solution of $MgCl_2$ and $C_2H_6O_2$ in distilled water that reacts with the Ti-6Al-4V and forms its oxide on the polished surface, as shown in Eq. (2.18). The polished surfaces of the substrate are analyzed through *Scanning Electron Microscopic* (*SEM*) images before and after polishing. Initially, a nonuniform and thinner oxide layer is easily visible on the surface of Ti-6Al-4V in Fig. 2.26. However, after finishing with H-ECMR, a uniform, thick oxide layer forms on the polished surface. EDX, XPS, and SEM studies are performed to examine the compositions on the biomaterial surface. The weight % of O is increased from its initial value of 0.7 to 8.2 on the polished surface of Ti-6Al-4V, as shown in Fig. 2.26. Furthermore, a uniform atomic concentration of O is observed to be increased from 8 nm to 78 nm on the Ti-6Al-4V surface after finishing, as observed from the depth profiling of XPS and shown in Fig. 2.27. It is because the reaction of $TiCl_4$ (produced from the chemical reaction of $MgCl_2$ with Ti) with $C_2H_6O_2$ leads to the formation of TiO_2. The formation of TiO_2 shows a strong adhesion property with the surface of the Ti alloy and is chemically inactive (i.e., doesn't react) with other ions available in the electrolyte. It forms a uniform and thick passive layer of oxide on the Ti alloy surface.

High-resolution XPS spectra of Ti-6Al-4V detected its constituents like Ti, Al, V, and C. The Al available on the biomaterial surface in Al_2O_3 form before and after polishing (i.e., 5.3 and 5.8 on the unpolished and polished surface, respectively). Hence, a significantly low amount of Al is detected in spectra. Furthermore, the V content in the Ti-6Al-4V remains constant (i.e., 4.2 and 4.1 on the unpolished and polished surfaces, respectively) and is much lower tough to fit the V 2p region for additional information. Hence, the Ti 2p is the primal focus of the high-resolution XPS spectra. A comparatively higher signal is detected for Ti 2p on substrates before and after polishing, as shown in Fig. 2.26. Furthermore, it is also observed that the intensity of O 1s increases on the polished surface compared to the unpolished surface. Ti^{3+} 2p1/2, Ti^{3+} 2p3/2, and Ti^{4+} 2p3/2 are the three subsets of the Ti 2p spectra having a binding energy of 462.06, 459.69 and 455.95 eV, respectively. However, electrochemical reactions

occur between the substrate and workpiece, which increases the intensity of the Ti^{4+} 2p3/2 on the polished surface.

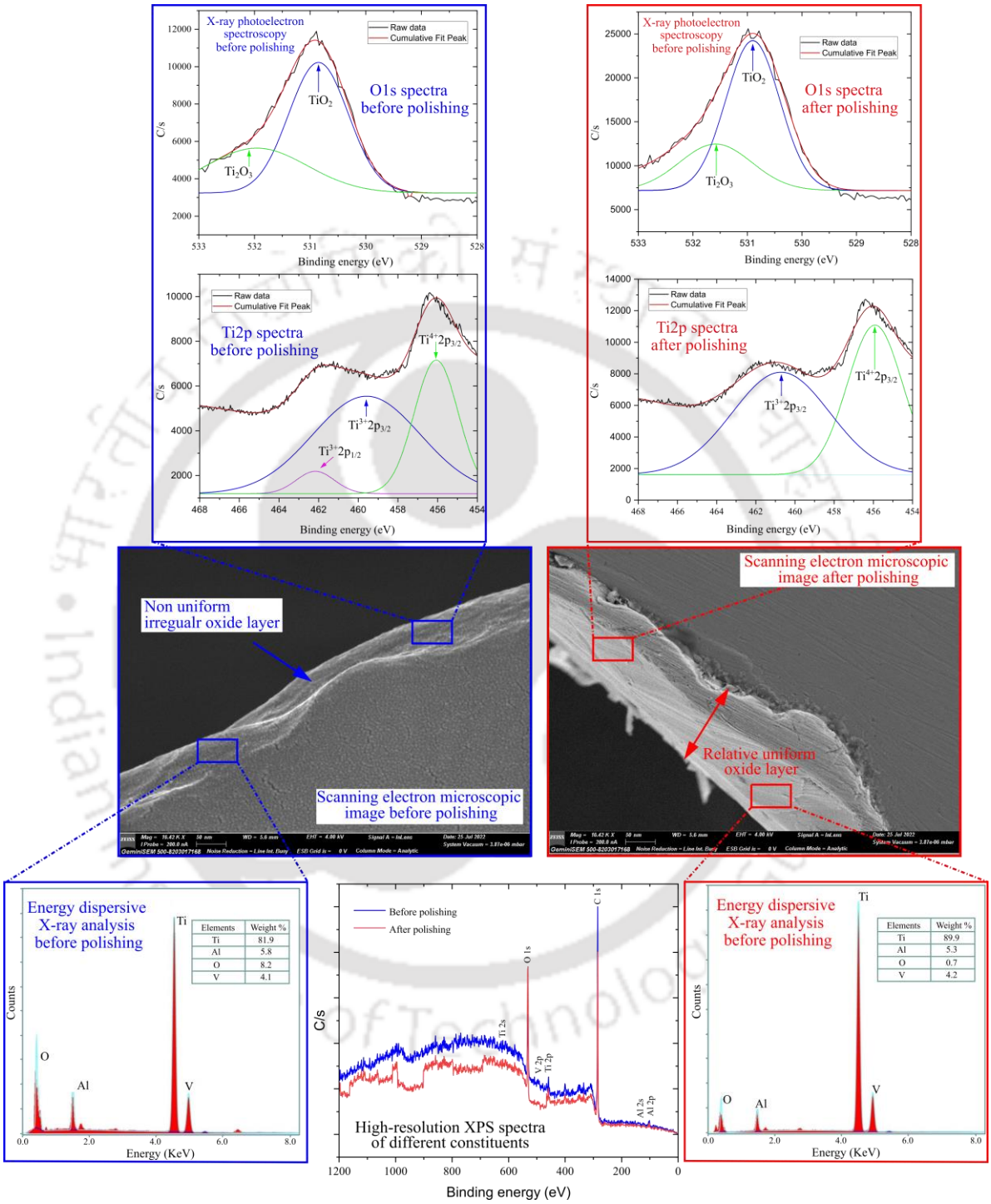

Fig. 2.26 Comparison between oxide layers by EDX, SEM, XPS studies on Ti-6Al-4V biomaterial surface before and after H-ECMR finishing process

Furthermore, the binding energy of the subset mentioned above is close to TiO, Ti_2O_3, and TiO_2, respectively. The unoxidized Ti (i.e., 462.06) was detected on the unpolished surface of the substrate, as shown in Fig. 2.26. It is unattainable after finishing, indicating that a subset

of Ti available on the polished surface is in the form of its oxide, as shown in Fig. 2.26. TiO_2 is the major subset of the passive layer forms on the substrate surface, showing stable properties with an octahedral structure. O 1s spectral region illustrates that the intensity of TiO_2 increases on the Ti-6Al-4V surface after finishing, as shown in Fig 2.26.

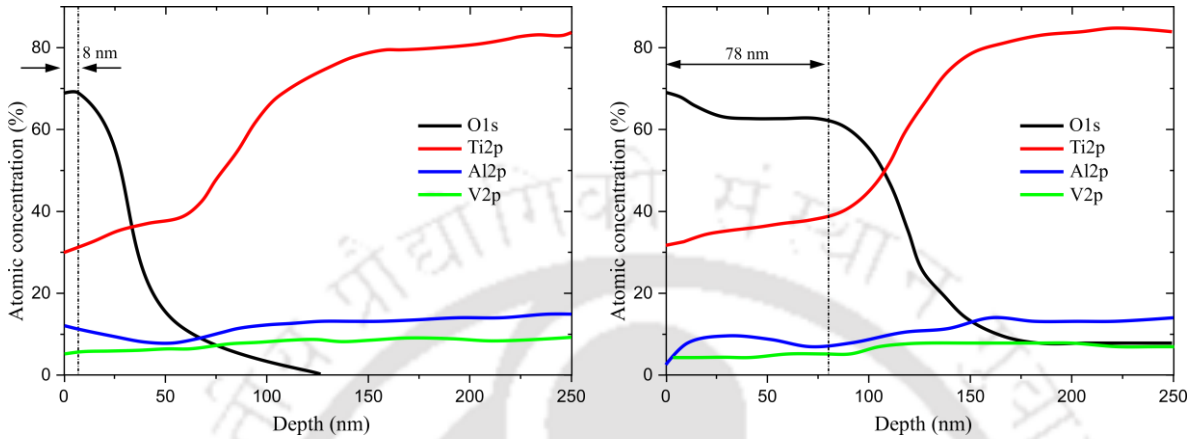

Fig. 2.27 Depth profiles of different constituents on Ti-6Al-4V surface (a) before and (b) after finishing using XPS analysis

2.9 Summary

In this chapter, the study is made for the permanent magnet and electromagnet-based MFAF process. It is observed that the surface finishing time for the conventional MFAF process is very high, and a novel MFAF-based surface finishing is required to improve the process efficiency. Moreover, the electromagnet-based MFAF process provides an advantage of an in-situ variation of the magnetic field and provides better controllability during polishing as compared with the permanent magnet-based MFAF process. Hence, a working principle of the novel electromagnet-based *Hybrid-Electrochemical Magnetorheological Fluid* (*H-ECMF*) finishing process is discussed in the present chapter. Herin, the synergic action electrochemical machining, and Magnetorheological Finishing help to reduce the polishing time during the surface finishing process. Furthermore, an electromagnet-based polishing tool is developed for in-situ magnetic field control during the polishing process, further capable of producing desired surface quality over polished surfaces. The bottom of the polishing tool is covered with the mu-metal to concentrate the magnetic field at the targeted workspace. Moreover, an analytical model is developed to predict the final surface roughness achieved after the H-ECMF finishing process. It is found that the results obtained from the developed analytical model are in excellent agreement with the experimental results. A 96.41% reduction in surface roughness (% ΔRa) is achieved during *Hybrid Electrochemical Magnetorheological* (*H-ECMR*) finishing,

compared to 49.63% using the conventional *Magnetorheological Finishing* (*MRF*) for 30 minutes of polishing time. Instigating an electrochemical reaction along with mechanical abrasion increases the polishing efficiency. The results attained from the developed analytical model to predict the surface roughness agrees with the experimental observations; however, with an increase in standoff distance, the percentage error between analytical and experimental results increase (i.e., 2.35% to 8.96%) due to the lower holding capacity of the *Carbonyl Iron Particles* (*CIPs*) chains by the polishing tool at a higher standoff distance. The impact of different parameters is analyzed on the % reduction of R_a; the values of the optimized process parameters, i.e., the polishing tool's rotational speed, electrolyte concentration (Vol.%), finishing time, and applied current, are 800 rpm, 45%, 30 minutes and 2 Amp, respectively. The mirror-like polished surface is achieved on the Ti-6Al-4V surface after the H-ECMR finishing. The initial average surface roughness (R_a) value of 325.90 nm is reduced to its final value of 12.90 nm. Moreover, the value of *skewness* (R_{sk}) and *kurtosis* (R_{ku}) achieved on the polished surface is -0.52 and 1.69, respectively, indicating that the low probabilities of wearing out of the biomaterial surface on their tribological interactions as flat peaks with a lower number than the valleys are produced on the biomaterial surface. The electrochemical reaction between the Ti-6Al-4V, $MgCl_2$, and $C_2H_6O_2$ produces a uniform and thick TiO_2 passive layer on the Ti-6Al-4V surface. The layer thickness increases to 78 nm from 8 nm, enhancing the biomaterial's corrosion resistance. Based on experimental observations, it can be concluded that the developed H-ECMR finishing process can reduce the surface finishing time with improved oxide layer thickness on the Ti-6Al-4V biomaterial surface for further enhancement in their biocompatibility.

Chapter 3 Computer Aided Process Planning for H-ECMR Finishing

3.1 Introduction

Hybrid-Electrochemical Magnetorheological (H-ECMR) finishing process is an advanced surface finishing operation that provides mirror-like polished surfaces required for the implants, lenses (telescope, microscope, etc.), miniature parts, etc., for enhanced functionality. However, various features (including holes and pockets) on the workpiece surface produce a challenge during their polishing through the H-ECMR finishing process; the *Carbonyl Iron Particles* (*CIPs*) chains get trapped inside the holes during the finishing operation and generate irregular surface quality on the polished surface. Furthermore, Computer-controlled *H-ECMR* finishing is limited by its non-uniformity of surface roughness, which significantly inhibits products' performance. This surface roughness inconsistency primarily depends on how the tool moves over the targeted surface. This chapter outlines a *Feature-based Hybrid MRF Planning System* (*FHMRF-PS*) developed on the geometrical data inputs to produce automated process planning for the paraffin wax deposition into the hole and pocket features of the workpiece before *H-ECMR*. An external module is developed to deposit paraffin wax in the holes and pockets to ensure a uniform finish over the targeted surface. Moreover, an investigation is made over different tool path strategies: Hilbert, Raster, Spiral, Peano, and trochoidal. A comparison is made among these toolpaths on the magnitude of the final *surface roughness* (R_a) and its variation on the finished profile on an identical domain with the same process parameters.

3.2 Feature-based hybrid MRF planning system

A *Feature-based Hybrid MRF Planning System* (*FHMRF-PS*) is developed to enhance the flat plate's surface quality with hole and pocket features through H-ECMR with an appropriate toolpath. The roadmap for the proposed process planning is discussed in the subsequent sections.

3.2.1 Process planning

Xu et al. [124] reviewed CAPP's development and future trends critically. They categorized the CAPP based on the various systems, including knowledge-based systems, feature-based technologies, data-driven algorithms, etc. Moreover, emphasizing the development of energy-

efficient and energy-conscious process planning is crucial to tackle environmental issues. Furthermore, CAPP must be agile, adaptive, integrated, and distributed to overcome the challenge faced during the mass customization of the global manufacturing industries. Newman et al. [125] developed the energy-efficient CAPP for CNC machining and found that the variation in the process plan reduces energy consumption during machining. Furthermore, a comparison between the semi-finishing and finishing cutting based on energy consumption is also carried out. It is observed that it is lower in the case of high-load metal cutting. Today CAPP research is not just focused on subtractive machining processes. It has to consider hybrid manufacturing, where additive and subtractive processes are combined, where both interoperability of the methods are crucial to producing parts right the first time.

3.2.2 FHMRF-PS decision path

The flow chart of FHMMRF-PS is illustrated in Fig. 3.1; the proposed process planning system is divided into two categories, i.e., the deposition of paraffin wax and the H-ECMR finishing process with an appropriate toolpath. The pockets and holes in the *Computer-Aided Design* (*CAD*) model are identified through an automatic feature recognition module [126]–[128]. Identifying the hole feature of the geometry in the STL file is not feasible as it only contains triangles. Figure 3.2(a) shows an STL file of a body with a hole; two neighboring triangles, A and B, are marked [129]. The sharp change in the triangle's normal direction is easily noticeable; the common edge (highlighted by red color) will participate in the closed loop formed by the similar edges to create a hole. Afterward, unsatisfactory loops are removed by checking the triangles of the STL file; Three evenly distributed edges are identified from each loop [130] [126]. The orientation of the holes is determined through the three edges and projected to the perpendicular planes to calculate the hole axis and origin coordinates. The hole centers and diameters of the hole (d) are determined based on the present orientation. Similarly, the difference between the triangles' maximum and minimum z values inside the cavity is used to calculate the *hole depth* (h). Moreover, the volume of the hole is calculated from the diameter and depth of the hole. The flowchart for the algorithm to determine the volume of hole is shown in Fig. 3.3(a). Once the features are recognized, the best orientation is selected to cover maximum features during a single operation. Before finishing, paraffin wax is deposited inside the hole to maintain its height in accordance with local surfaces. MATLAB® is used to develop the algorithm for the feature recognization, development of toolpath for deposition and polishing, and extraction of hole dimension from the STL file of the CAD model [131].

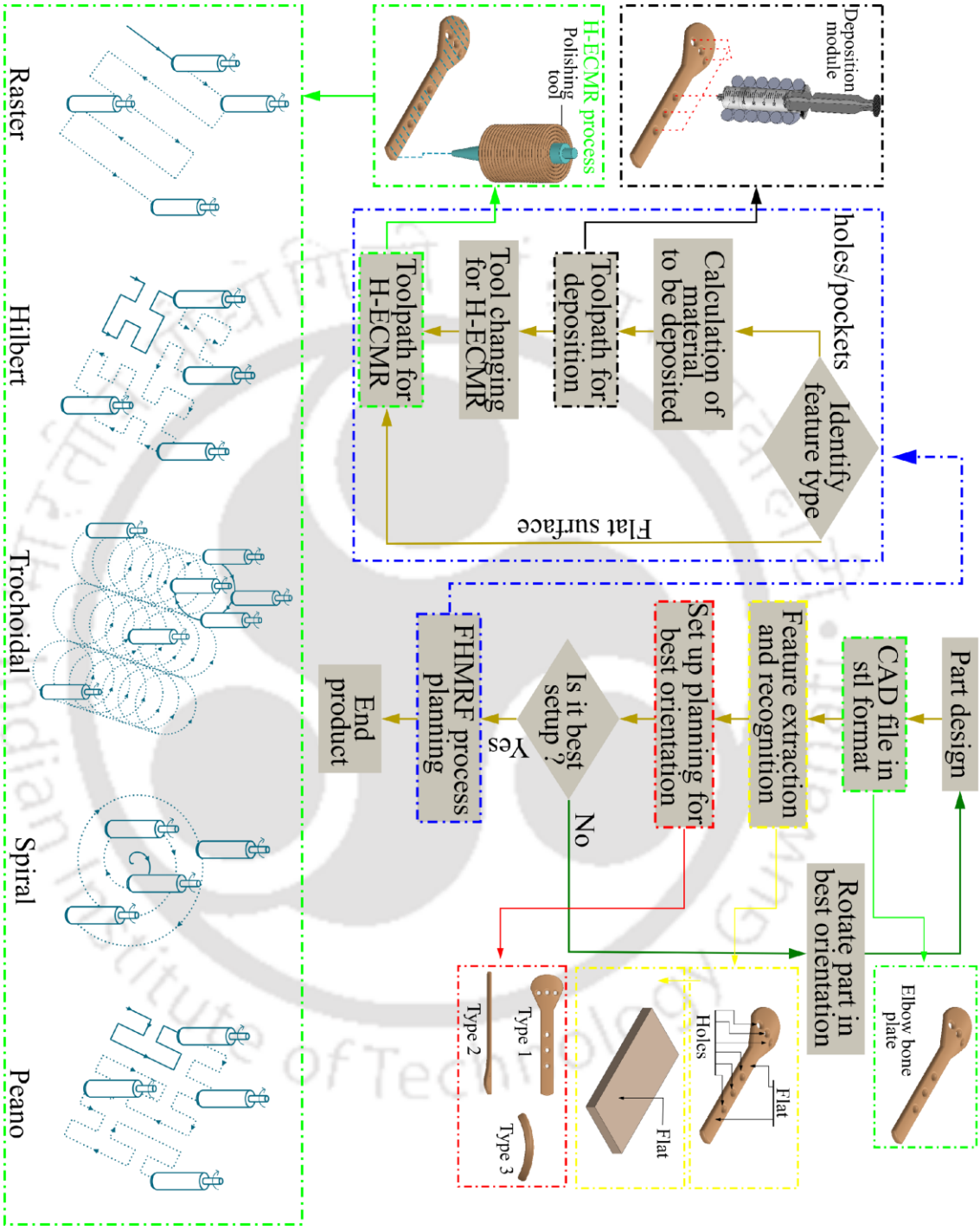

Fig. 3.1 Flow chart of feature-based hybrid MRF planning system (FHMRF-PS)

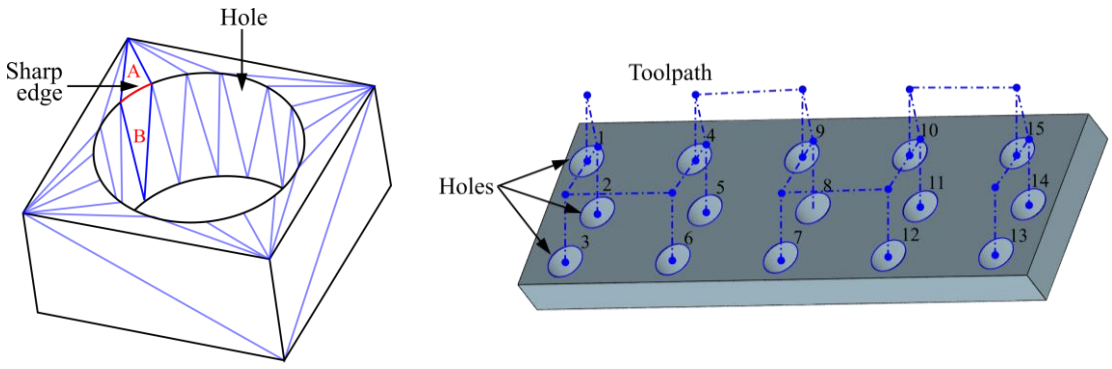

(a) (b)

Fig. 3.2 (a) STL file representation of a hole and (b) toolpath generation for deposition at different holes

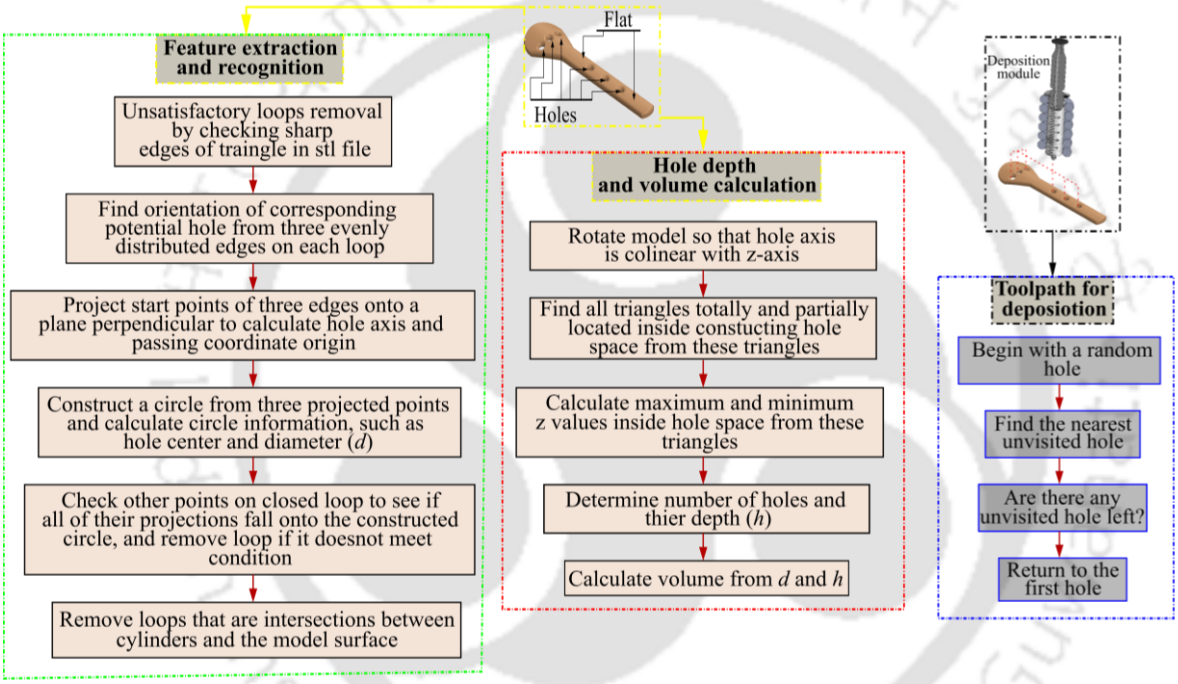

(a) (b)

Fig. 3.3 (a) Flow chart for feature extraction & recognition and hole depth and Vol. calculation, and (b) algorithm for toolpath generation for depositing paraffin wax

3.2.3 External deposition module

The external module is designed and developed to deposit the paraffin wax at the workpiece's targeted location (i.e., pockets and holes), as illustrated in Fig. 3.4. The designed device consists of a metal syringe covered with a heating coil; the increase in the temperature of the metal syringe with using a heating coil leads to the melting of the paraffin wax placed inside it. The variation in applied electric current to the heating coil alters the temperature of the metal syringe. Furthermore, the syringe's plunger is pushed downward to fill the hole with molten paraffin wax. It is required to have a filling material that remains solid during the MRF over the holes and pockets and washes (melts) away easily without affecting the part after

completing the task. Paraffin wax is a very suitable material for this purpose. Also, the lower melting point of the paraffin wax provides the benefit of lower energy consumption during its deposition and not affecting the part quality while melting. Furthermore, the cost efficiency and availability are the primary reasons for its selection as a deposition medium. Moreover, the volume of the pockets and holes is calculated from its STL file, as discussed earlier; accordingly, the plunger is moved downward to deposit the required amount of paraffin wax. A CNC controller regulates the plunger's movement for precise deposition while filling the hole. The displacement of the plunger is calculated from Eq. (3.1).

$$h = \frac{4v}{\pi d^2} \tag{3.1}$$

Where the volume of a pocket or hole is v (calculated from the STL file), the diameter of the plunger is d, and h is the displacement of the plunger. However, an appropriate toolpath is required to avoid repetition while deposition [131].

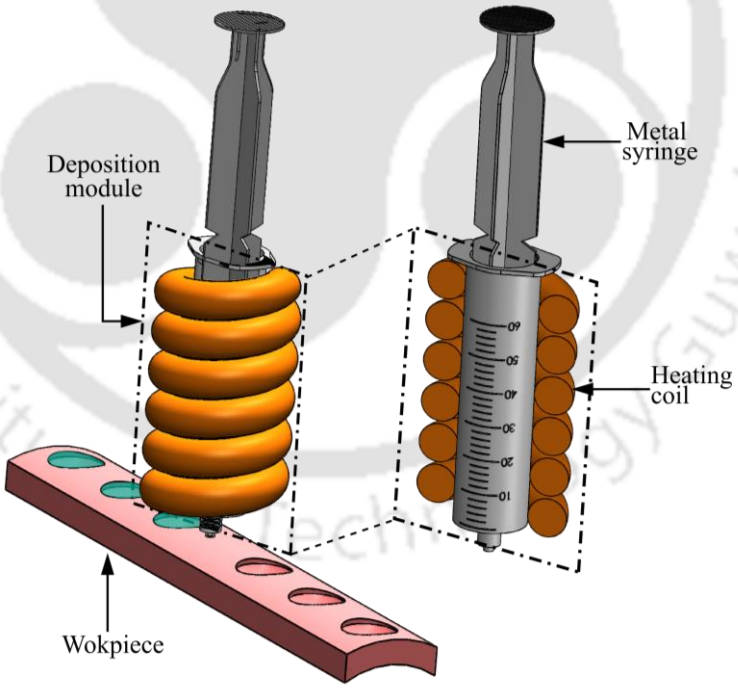

Fig. 3.4 Schematic diagram of external module to deposit paraffin wax

The toolpath for deposition is developed to deposit all the holes on the component in the lowest possible time. The nearest neighbor algorithm for *Travelling Salesman Problem* (*TSP*) has opted to determine the toolpath during the deposition. A few advantages of the TSP

algorithm are its simple implementation and robustness regarding the search space; Herein, holes are assigned to different cities, and a random city is selected first; the distances between the first city and its neighbors are calculated. The city with a minimum distance is selected; the process is repeated until every city is visited. Now, the first city is changed, and based on that, the algorithm is repeated; the algorithm having less travel time is selected for the deposition tool path during FHMMRF-PS, as illustrated in Fig. 3.2(b). The deposition module is attached to the CNC machine for precise movement during the paraffin wax deposition. The plunger of the external deposition module is connected with a *Digital analog converter* (*DAC*) based linear actuator. Based on the volume determined from the.STL file of the CAD model, the displacement value is calculated and transferred to the linear actuator. Moreover, the developed algorithm from MATLAB® for the toolpath of deposition and polishing is implemented with the CNC milling machine.

Furthermore, after the finishing operation is over, the workpiece is placed on a hot plate, and its temperature is increased until the paraffin wax melts down from the workpiece, as shown in Fig. 3.5. The melting point of the paraffin wax is 61ºC. The combination of three phases, i.e., deposition, surface finishing, and dewaxing during FHMRF-PS, enhance the surface quality workpiece having pocket and hole features. A case study is performed on the surface enhancement of additively manufactured bone plates through the developed feature-based hybrid MRF planning system (FHMRF-PS) and discussed in Chapter 4.

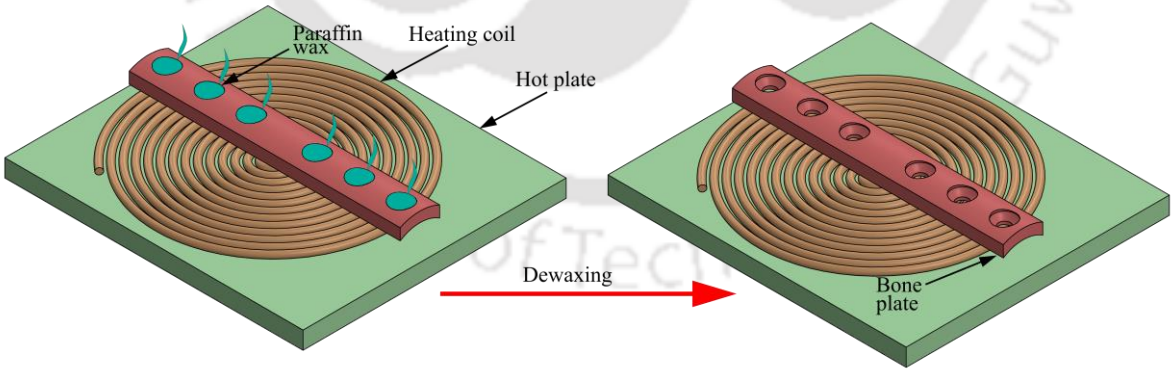

Fig. 3.5 Schematic diagram of dewaxing process

3.2.4 Various area-filling toolpath strategies during H-ECMRF

The regularity in surface roughness can be controlled by the precise movement of the polishing tool over the desired workspace. Hence, toolpath planning is the critical step in the H-ECMR finishing process, influencing the efficiency of the surface finishing process and determining

how the polishing tool moves over the surface to provide uniform surface roughness. In this research, five different toolpaths (i.e., Zig-Zag, Hilbert, Peano, Spiral, Trochoidal) achieve *surface roughness* (R_a) in the range of the nanometers. Zig-Zag is the most commonly used toolpath in surface finishing and machining operations, covering all the regions through parallel lines with the tool, as shown in Fig. 3.6(a) [132]. Zig-zag has been used widely in surface finishing operations [112], [133], [134]. Kim et al. [135] claimed that a smooth zig-zag path (direction parallel) provides better results irrespective of the path interval and the feed rate than the contour-parallel tool path. However, for surface roughness enhancement of irregular shapes (a circle, an octagon, etc.,) a fractal-based toolpath has been developed to increase the finishing operation's efficiency [136].

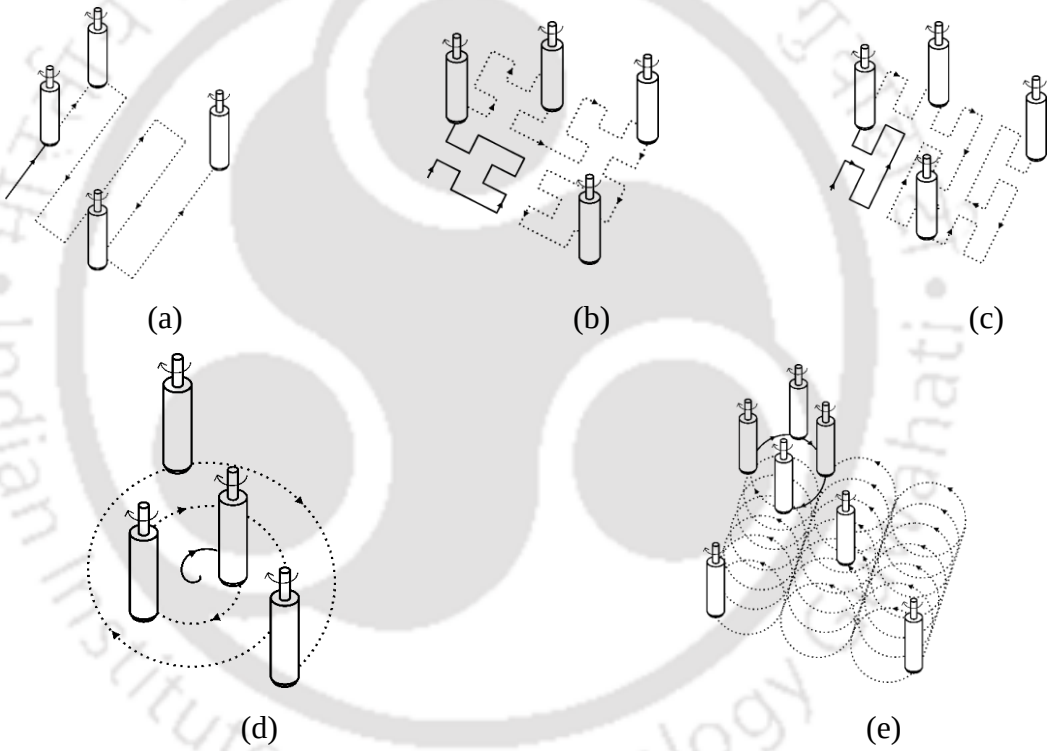

Fig. 3.6 Different toolpaths (a) Zig-Zag, (b) Hilbert, (c) Peano, (d) Spiral, and (e) Trochoidal

Hilbert and Peano are the fractal-based space-filling toolpath strategies, continuous and surjective, with minimum tool retraction, as shown in Fig. 3.6(b) and (c) [137] [138]. Mizugaki et al. [139] have reported that peano (a fractal-based tool path) shows comparatively better results than raster. These paths consist of x-direction short segments as frequently as y-segments. The Spiral toolpath uses a Spiral curve to cover the desired surface with the minimum number of turns, as shown in Fig. 3.6(d) [140]. Trochoidal toolpaths are accomplished using circular cuts, shown in Fig. 3.6(e) [141]. Pessoles et al. [154] mimic the trajectory used in manual finishing on a high-degree milling operation to avoid marks on the

polished parts. Gong et al. [142] implemented a spiral tool path to improve the process accuracy and efficiency of ultra-precision diamond turning. From the studies, it has been observed that the influence of toolpath strategies on surface roughness during H-ECMRF is not often studied. This chapter analyzes the effect of five different toolpaths, namely Hilbert, Peano, Raster, Spiral, and trochoidal, over the magnitude and uniformity of the final surface roughness on the finished profile. A comparison is made among these toolpaths on an identical domain with the same process parameters as the H-ECMRF process. Results attained from *the* optical profilometer and optical microscope are analyzed to study the impacts of these toolpaths.

Increasing productivity with enhanced quality is the primary objective in the manufacturing sector to escalate profitability. In the MFAF process, different techniques have been applied to improve the efficiency of the process [87], [137], [143]–[145]. Preparation of *Magnetorheological* (*MR*) fluid with proper constituents to increase its stability during surface finishing operation, optimization of critical process parameters through various soft computing techniques, such as Neural Networks [146], Genetic Algorithm [93], Fuzzy logic [147], etc., optimization of dwell time algorithm [148] to increase the accuracy of the polished surface, are few of them. However, with the CNC MFAF, different toolpath planning has gained significant momentum to improve process efficiency [132], [137], [149]–[152]. CAM packages provide toolpath strategies such as Zig-Zag and spiral in the surface finishing operation. Prakash et al. [153] analyze the surface roughness obtained through these two toolpath strategies. Zig-Zag ("Raster" term used in the respective paper) provides the best *average surface roughness* (R_a) of 9 nm on the β-TNTZ alloy. However, in the Spiral toolpath, the final surface roughness produced with the large valleys compared to the Zig-Zag has obstacles in removing the debris particles, thus deteriorating the surface quality. Similar efforts were made by Barman et al. [114] analyzed that Zig-Zag ("Parallel" term used in the respective paper) produced better surface topography and roughness as compared with the spiral toolpath. However, the time required to achieve the *average surface roughness* (R_a) of 10 nm on a 15 mm × 15 mm flat workpiece is 6.30 hours. Hence, substitute toolpath strategies such as the Trochoidal toolpath are required to enhance the surface finishing rate for improved MFAF process efficiency.

3.2.5 Zig-Zag Toolpath

The Zig-Zag toolpath pattern is based on planner ray casting along one direction; it is simple, efficient, and robust to cope with any boundary. Scallop height (height of small cusp of material remains on the surface after surface finishing operation) influences the uniformity of R_a on the polished work domain [154]. The stepover value is taken as half of the diameter of the tool

during the surface finishing operation to reduce the scallop height. The trajectory of a single abrasive placed at the circumference of the tool's tip is shown in Fig. 3.7. Equations (3.2) and (3.3) represent the trajectory of the abrasive placed at the periphery of the tool.

$$x = r \times \cos(\dot{\theta}t) \tag{3.2}$$

$$y = r \times \sin(\dot{\theta}t) + v_{feed} \times t \tag{3.3}$$

Where r represents the polishing tool's radius, $\dot{\theta}$ is the tool's rotational speed, v_{feed} denotes the polishing tool's feed, and t is the finishing time.

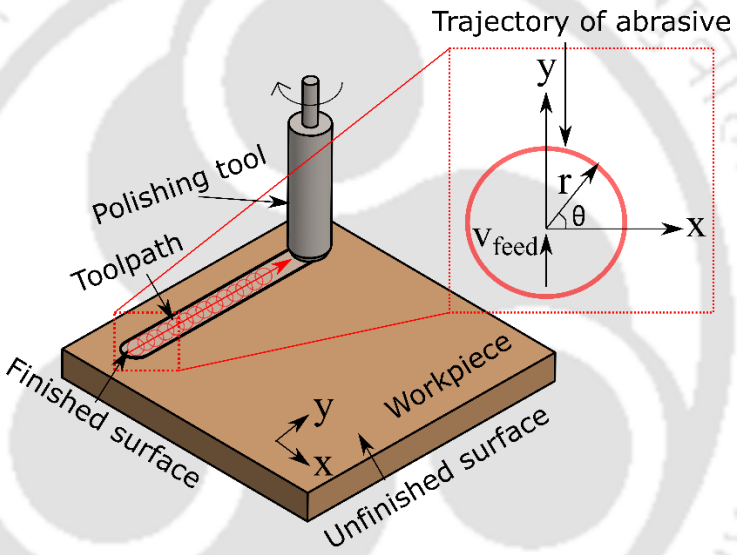

Fig. 3.7 Trajectory of abrasive placed at tool periphery during Zig-Zag toolpath

3.2.6 Fractal curves-based toolpaths

Retraction of the polishing tool during the H-ECMR finishing operation is unfavorable, as the MR fluid's stability gets hindered and produces non-uniformity in the surface roughness. Fractal curves-based toolpaths are the solution to reduce the number of tool retractions; they can map a multi-dimensional space into one-dimensional. Hilbert and Peano, a fractal curve, is utilized to enhance the surface quality of the workpiece through magnetorheological finishing. Hilbert introduces a method of defining a fractal curve as the limit of polygons enclosed in the unit square, using a 4-fold repetition of the successive polygon, corresponding to a base-2 number representation. Peano introduces the idea of a fractal curve based on a continuous mapping of the line segment [0, 1] onto the unit square. The relation between the

curve *distance* (*d*) and *level* (*n*) for Hilbert and Peano is shown in Eq. (3.4) and (3.5), respectively [155].

$$d = \frac{1.0}{\sum_{i=0}^{n}(2)^i} \tag{3.4}$$

$$d = \frac{1.0}{\sum_{i=0}^{n}(3)^i} \tag{3.5}$$

The third level of Hilbert and the second level of Peano curves cover the desired workspace during the surface finishing operation. The abrasive trajectory at the tool's periphery is the same as the Zig-Zag. However, the change in the feed direction from the x-axis to the y-axis is more frequent in Hilbert and Peano than Zig-Zag toolpath.

3.2.7 Spiral toolpath

Spiral curves cover the desired workspace to reduce the number of turns during the finishing operation. The parametric representation for the Spiral curve in the Cartesian plane is represented by Eqs. (3.6) and (3.7).

$$x = r(\varphi)cos\varphi \tag{3.6}$$

$$y = r(\varphi)sin\varphi \tag{3.7}$$

Where r is the monotonic continuous function of the angle, a Spiral curve with the defined center point and stepover are selected to cover the desired workplace. The stepover for the Spiral toolpath is chosen as half of the diameter of the polishing tool for the same reason as discussed earlier in the Zig-Zag toolpath.

3.2.8 Trochoidal toolpath

While manually performing the surface finishing operation on flat surfaces, skilled workers make small circles with the polishing tool having a uniform feed rate, thus attaining a uniform surface roughness covering each area. A replica of the same process can be produced with the assistance of the trochoid curves. The trajectory of a single abrasive placed at the circumference

of the tool's tip is shown in Fig. 3.8. Equations (3.8) and (3.9) represent the trajectory of the abrasive placed at the periphery of the tool.

$$x = R \times \cos(\dot{\phi}t) + r \times \cos(\dot{\theta}t) \tag{3.8}$$

$$y = R \times \sin(\dot{\phi}t) + r \times \sin(\dot{\theta}t) + v_{feed} \times t \tag{3.9}$$

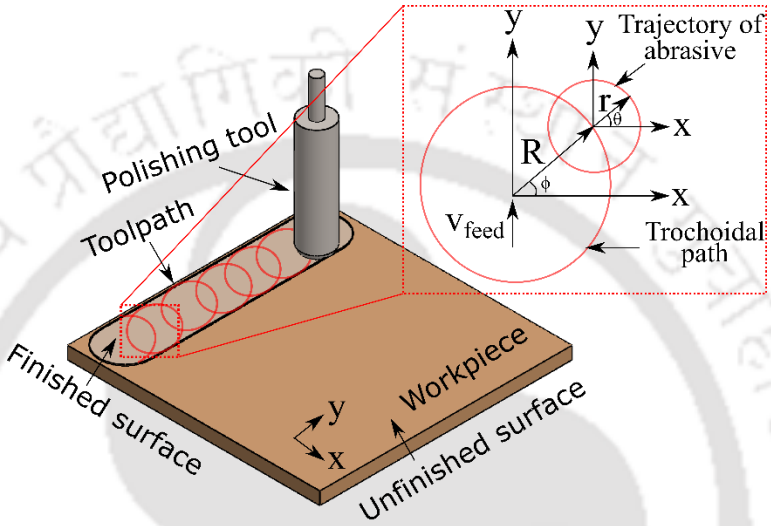

Fig. 3.8 Trajectory of abrasive placed at tool periphery during Trochoidal toolpath

Where, r represents the polishing tool's radius, $\dot{\theta}$ is the tool's rotational speed, v_{feed} is the linear speed of the polishing tool in the y-direction, and R is the radius of the Trochoidal path, $\dot{\phi}$ is the speed at which the tool moves in the Trochoidal path, and t is the finishing time. The force exerted by the abrasive particle on the workpiece can be determined through Eqs. (3.10) and (3.11), where m represents the single abrasive particle mass. The extra component of the force attained by the abrasive particle, as the tool transverse in the Trochoidal arc, assists in increasing the finishing process's efficiency.

$$F_x = m \times \frac{d^2x}{dt^2} = m \times (-R\dot{\phi}^2 \times \cos(\dot{\phi}t) - r\dot{\theta}^2 \times \cos(\dot{\theta}t)) \tag{3.10}$$

$$F_y = m \times \frac{d^2y}{dt^2} = m \times (-R\dot{\phi}^2 \times \sin(\dot{\phi}t) - r\dot{\theta}^2 \times \sin(\dot{\theta}t)) \tag{3.11}$$

3.3 Analytical model

The continuity and momentum equation, as shown in Eqs. (3.12) and (3.13) assist in analyzing the movement of MR fluid during the surface finishing operation.

$$\frac{\partial u_i}{\partial x_i} = 0 \tag{3.12}$$

$$\rho\left[\frac{\partial u_i \partial u_i}{\partial x_i}\right] = \frac{\partial p}{\partial x_i} + \frac{\partial}{\partial x_i}\left[\mu\dot{\gamma}\left(\frac{\partial u_i}{\partial x_j} + \frac{\partial u_j}{\partial x_i}\right)\right] \tag{3.13}$$

Where ρ represents the MR fluid density, p shows the pressure and velocity components in the direction of x_i and x_j are represented by u_i and u_j, respectively, and $\dot{\gamma}$ shows the strain rate. The MR fluid is a non-Newtonian fluid that changes its physical properties under an external magnetic field. Bingham plastic model is opted for the analysis of the MR fluid and its comparison with the Newtonian fluid. The shear stress model for the Bingham plastic is shown in Eq. (3.14).

$$\bar{\bar{\tau}} = \bar{\bar{\tau}}_o + \eta\bar{\bar{D}} \tag{3.14}$$

Where, the yield stress of the Bingham fluid is represented by τ_o and the rate of deformation for the Bingham fluid is denoted by the D in the tensor form. However, the D is further defined by the velocity components (i.e., u_i and u_j) of the MR fluid in the x_i and x_j directions and is shown in Eq. (3.15).

$$\bar{\bar{D}} = \left(\frac{\partial u_i}{\partial x_j} + \frac{\partial u_j}{\partial x_i}\right) \tag{3.15}$$

Bingham fluid's viscosity (η) depends upon the yield stress (τ_o) and strain rate ($\dot{\gamma}$) as shown in Eq. (3.16). Where K is the consistency index with dimension $L^{-1}MT^{-2,}$ and n is a dimensionless quantity known as the flow behavior index. The value of n and K for the Newtonian fluid is one and η, respectively. Furthermore, the strain rate ($\dot{\gamma}$) for the Bingham plastic fluid is represented in terms of the deformation rate tensor, as shown in Eq. (3.17).

$$\eta = \frac{\tau_o}{\dot{\gamma}} + K\dot{\gamma}^{n-1} \tag{3.16}$$

$$\dot{\gamma} = \sqrt{\frac{1}{2}\overline{\overline{D}}:\overline{\overline{D}}} \tag{3.17}$$

Sidpara et al. [156] analyzed the rheological characteristic of the MR fluid and established the regression model for the viscosity (η) and the yield stress (τ_o), correlated with the composition of MR fluid and magnetic field as shown in Eqs. (3.18) and (3.19).

$$\begin{aligned}\tau_o = 18963 - 714.74C - 3673.8A + 104.62D + 16843.45M \\ + 104.61CA + 773.46CM - 21.67AM \\ - 448.89DM + 41491.01M^2\end{aligned} \tag{3.18}$$

$$\begin{aligned}\eta = -31.58 + 0.75C + 4.23A + 0.12D - 10.52M - 0.12CA \\ + 0.61CM - 1.25AM - 0.22DM + 25.46M^2\end{aligned} \tag{3.19}$$

Where *C*, *A*, and *D* are the concentration of CIPs, abrasive, and carrier fluid, respectively. Similarly, M represents the magnetic field intensity. The regression model for the η and τ_o is further used to determine the effect of over-filling of paraffin wax on the rheological characteristics of the MR fluid.

3.4 Methodology

A test specimen (50 mm × 50 mm × 10 mm) made of *Duplex Stainless Steel* (*DSS*) (UNS S32305), a biomaterial, is examined to determine the best surface toolpath strategies to produce uniform surface quality during the H-ECMR finishing process. DSS contains ferrite (BCC lattice) and austenite phases (FCC lattice) at equal proportions. The availability of the ferrite phase in the lattice provides it with magnetic properties suited for the MFAF process. The two-phase alloy provides higher localized corrosion resistance and greater strength than ferrite stainless steel [157]. *Chromium* (*Cr*) and *Nickel* (*Ni*) are major alloy constituents in the range of 20~30% and 5~8%, respectively [158]. The carbon content for the DSS is lower than 0.03%, with enhanced ductility and toughness compared with ferrite stainless steel. Hence, DSS is used as a biomaterial for its improved metallic characteristics [159]. The rotational motion is provided to the polishing tool, and relative motion is delivered between the workpiece and MR

fluid with the translation motion of the CNC bed. However, the H-ECMR finishing process effectively works in the sub-micrometer range only. Hence, a face milling operation is used to reduce the initial surface roughness of the workpiece to the sub-micrometer range (R_a below 1 µm). A face mill tool (diameter = 38 mm) with four carbide inserts is attached to the spindle, as shown in Fig. 3(b). The magnitude of the spindle speed (1000 rpm), feed rate (10 mm/min), and depth of cut (0.25 mm) selected for the operation is based on the literature survey [160].

3.5 Results and discussion

The present section details the limitations of the H-ECMR finishing process during surface enhancement of the workpiece having holes and pockets features. Moreover, the impact of overfilling and underfilling during FHMRF-PS is also discussed in the section. Furthermore, a comparison is made between different toolpath strategies to find an appropriate toolpath during the H-ECMR finishing process to produce uniform surface quality.

3.5.1 Surface improvement of workpiece having holes and pockets

The H-ECMR finishing process is performed on the flat plate with different holes to determine the limiting diameter, facilitating surface finishing. The hole diameter varies from 2 to 3.5 mm, with a regular interval of 0.5 mm. The MR fluid is attached at the tip of the polishing tool; as shown in Fig. 3.9(a), the polishing tool moves downward to squeeze the MR fluid in-between the tool and workpiece as shown in Fig. 3.9(b). Furthermore, the feed is provided as a tool to accomplish the surface finishing operation on the plate. Squeezed MR fluid tries to move inside the hole whenever it passes over it, irrespective of the diameter, as shown in Fig. 3.9(c). Once the polishing tool surpasses the holes, the MR fluid gets trapped inside the holes, as shown in Fig. 3.9(d). Experiments are performed on the different diameter holes, and the MR fluid is held inside the holes every time. The trap of the MR fluid inside holes reduces the amount of MR fluid available to perform the surface finishing operation through the abrasion. Furthermore, reducing the MR fluid quantity decreases the force exerted by the polishing tool on the workpiece; hence an inconsistency in final surface roughness is noticed after the H-ECMR finishing process.

The workpiece's polished surface having holes is further analyzed with the optical microscope. The trapped MR fluid inside holes of diameters 2, 2.5, 3, and 3.5 are easily noticeable in Fig. 3.10. However, apart from the trapping of MR fluid, leaking the carrier medium of the squeezed MR fluid through the holes is also responsible for the varying surface roughness on the polished surface, as shown in Fig 3.11.

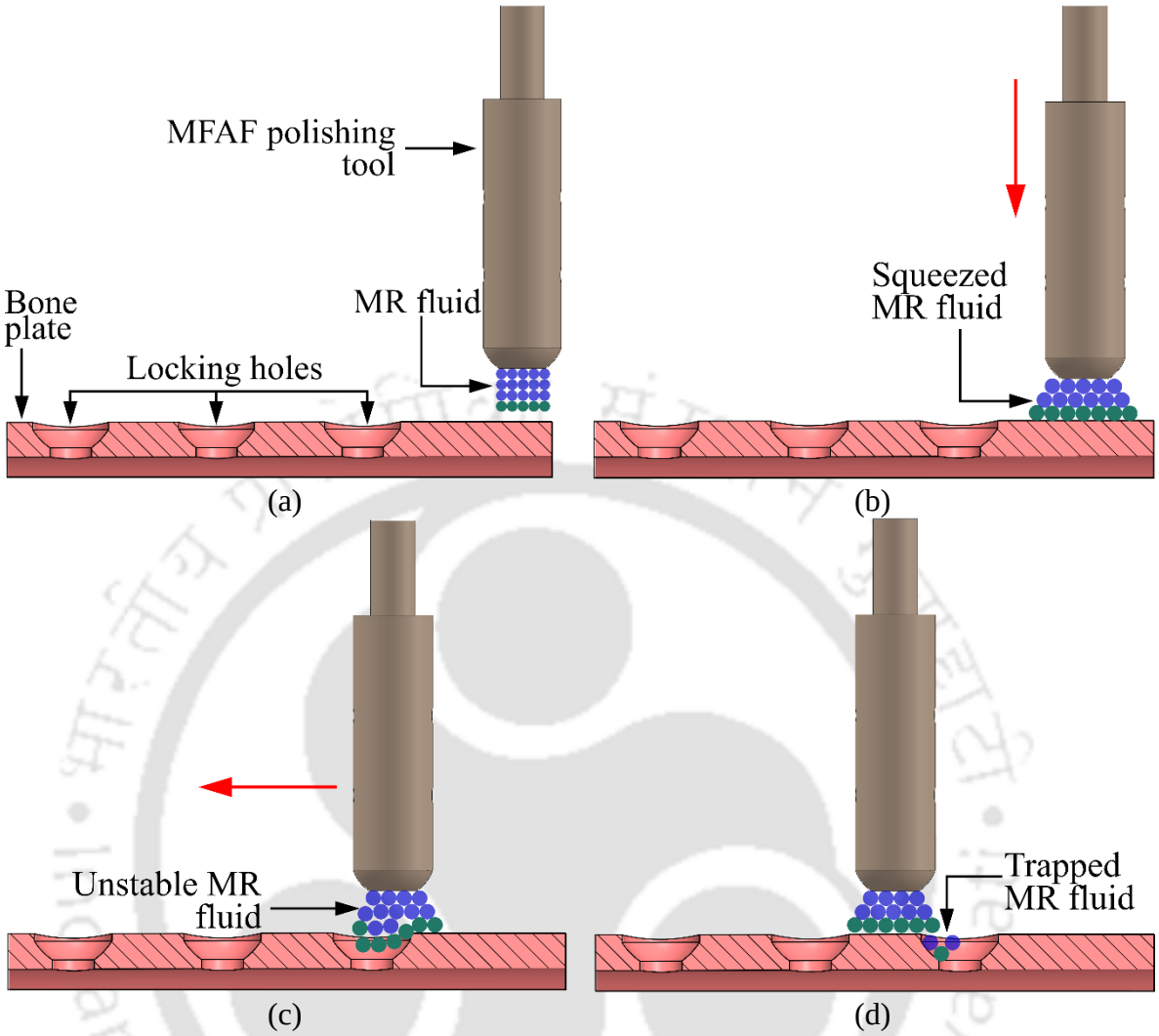

Fig. 3.9 MR fluid under (a) normal, (b) squeezed condition, (c) unstable due to holes, and (d) trapped in hole

A thin layer of the carrier fluid is deposited on the polished surface's opposite face, suggesting the carrier fluid passes through the holes. However, the reduction of carrier medium produces scratch marks on the polished surface, as marked by red lines in Fig. 3.10. The preliminary experiments confirm that the H-ECMR finishing process is incompetent to perform the surface finishing operation on a workpiece with holes or pocket features. Hence, the developed FHMRF-PS is applied to eliminate the previously-mentioned limitations. The H-ECMR finishing process is performed on the bone plates with locking holes. The paraffin wax is deposited in the holes before the surface finishing operation. The amount of deposition is calculated from the CAD model, i.e., 58.75 mm^3; hence the displacement of the plunger is 0.59 mm as calculated from Eq. (3.1).

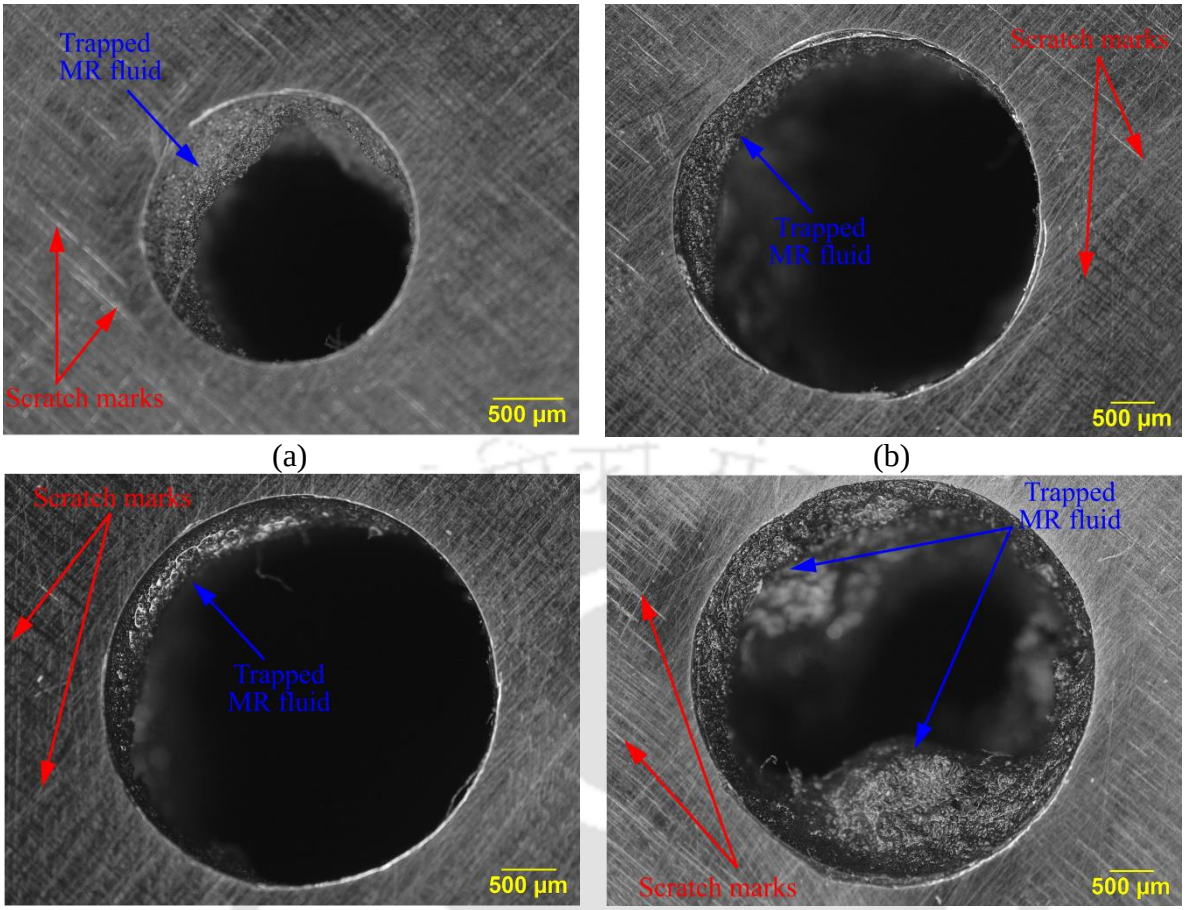

Fig. 3.10 Optical microscopic images of trapped MR fluid inside holes of diameter (a) 2 mm, (b) 2.5 mm, (c) 3 mm, and (d) 3.5 mm

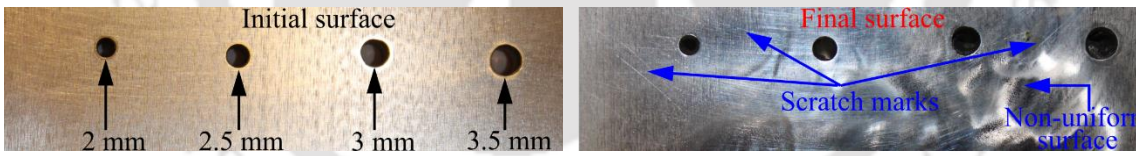

Fig. 3.11 Flat Ti-6Al-4V plates with holes (a) before and (b) after polishing

3.6 Impact of underfilling and overfilling

The impact of under and overfilling the paraffin wax in holes and pockets of the workpiece during the surface finishing process is analyzed. The holes' diameter and the workpiece thickness are 5 mm and 3 mm, respectively. Paraffin wax of 58.75 mm^3 volume is required to fill a single hole in the workpiece. The volume of the deposited paraffin wax varied from 58.75 to 82.42 mm^3 to investigate the impact of its overfilling on the final surface roughness. It is observed from experiments that the extra paraffin wax mixed with the MR fluid leveled the surface, as shown in Fig. 3.12. Mixing paraffin wax increases the volume of carrier fluid of the

MR fluid, the Eqs. (3.18) and (3.19) are used to analyze the change in yield stress and viscosity of MR fluid with the variation of the carrier fluid volume.

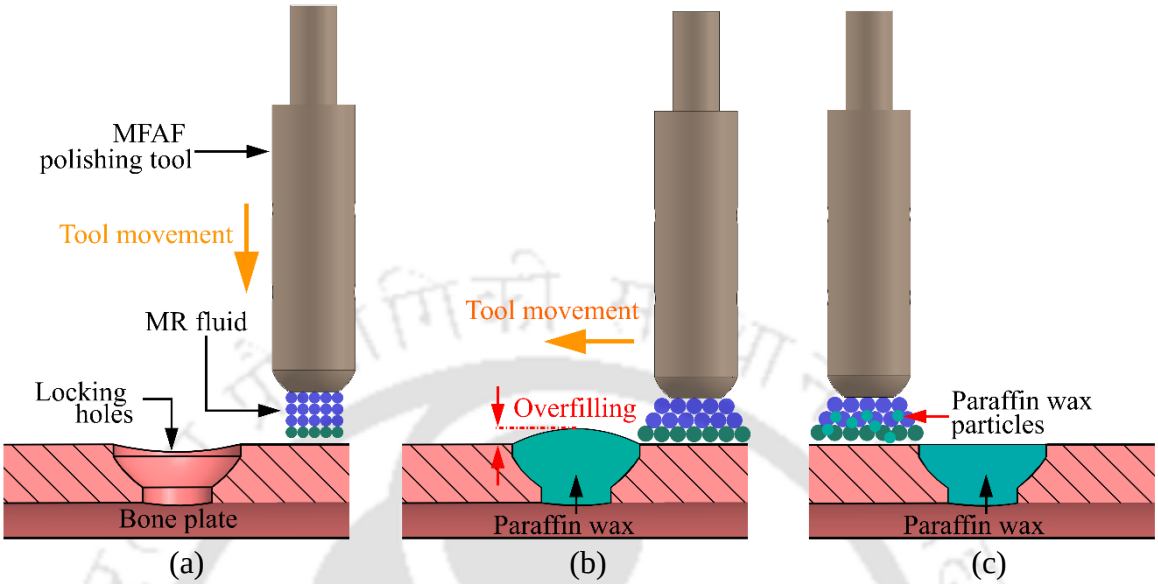

Fig. 3.12 Schematic diagrams showing finishing mechanism of holes in bone plate by MRF (a) without paraffin wax, (b) overfilled with paraffin wax, and (c) paraffin wax trapped in MR fluid while polishing

Figure 3.13(a) shows the impact of %overfilling of the paraffin wax on the yield stress and viscosity of MR fluid. As discussed earlier, an increase in the %overfilling of the paraffin wax leads to increased carrier fluid concentration of MR fluid. The increase in carrier fluid leads to a decrease in MR fluid's yield stress, responsible for deteriorating the surface quality of the polished surface, as shown in Fig. 3.13(b). The impact of the underfilling of the paraffin wax during the surface finishing operation is shown in Fig. 3.14. It is observed from experiments that inconsistency in surface roughness on the polished surface is achieved irrespective of the amount of underfilling. The squeezed MR fluid gets stuck inside the hole resulting in a variation of surface quality on the polished surface. This is because the underfilling provides sites for trapping MR fluid during the surface finishing operation.

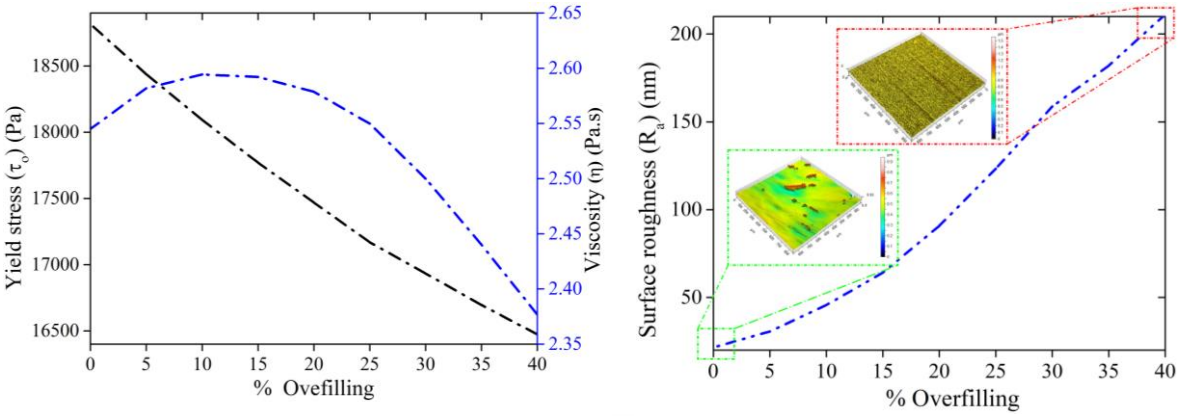

(a) (b)

Fig. 3.13 Impact of % overfilling of paraffin wax on (a) yield stress and viscosity of MR fluid, and (b) surface roughness

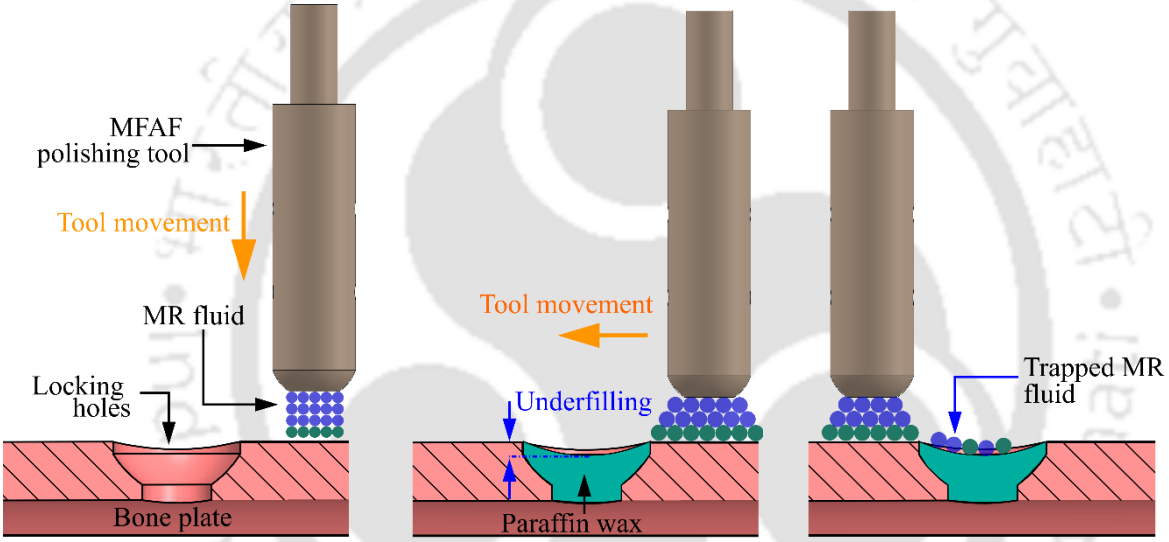

(a) (b) (c)

Fig. 3.14 Schematic diagrams showing finishing mechanism of holes in bone plate by MRF (a) without paraffin wax, (b) underfilled with paraffin wax, and (c) MR fluid trapped in hole while polishing

The proposed FHMRF-PS can perform the H-ECMR finishing process on the workpiece with holes and pockets featured on them. However, the amount of paraffin wax deposited inside those holes and pockets is critical as it affects the surface quality of the polished surface. A case study is performed on the additively manufactured bone plate to improve its surface quality through FHMRF-PS and discussed in Chapter 4.

3.7 Different area-filling toolpath strategies

Autodesk PowerMill software is used to generate the Zig-Zag and Spiral toolpath, and MATLAB is used to produce the Hilbert, Peano, and Trochoidal toolpath. In Zig-Zag, the *surface roughness* (R_a) improvement is 97.84%, as the R_a of the workpiece reduced to 4.81 nm

from 223 nm, as shown in Fig. 3.15. The variation in the R_a over the different parts of the surface is studied, and irregularities are found at the sharp turns. The velocity components of the abrasive particle are the first-order derivative of Eqs. (3.2) and (3.3) w.r.t to time. Now, whenever there is an abrupt change in the direction of the polishing tool (change in direction by 90°), the impulse is generated on the abrasive of the magnitude $m \times 2v_{feed}$, where m denotes the single abrasive particle mass. It is observed that, at the abrupt change in the polishing direction, the surface roughness diminished, as illustrated in Fig. 3.16. The crests produced as the tool passes over the surface are oriented in one direction; this undesired surface orientation is unsuitable for the H-ECMR finishing process.

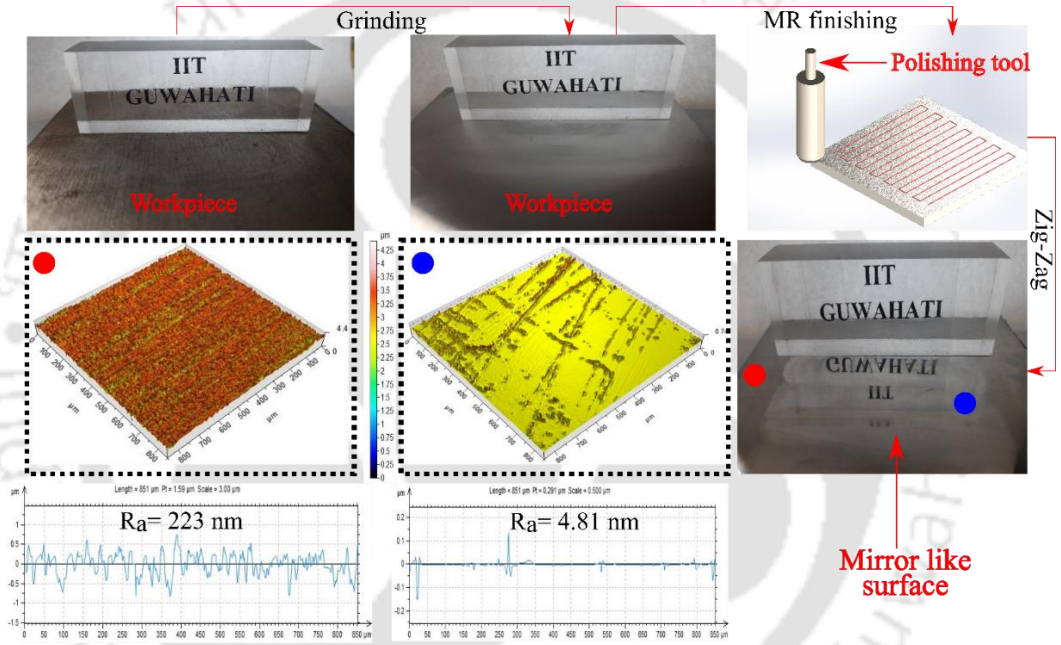

Fig. 3.15 Surface roughness (R_a) obtained through the Zig-Zag toolpath from 223 nm to 4.81 nm

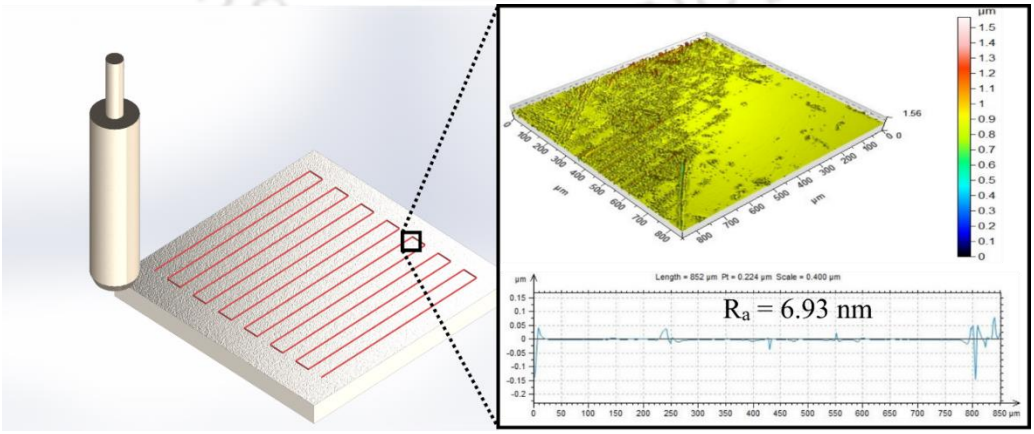

Fig. 3.16 Surface roughness at the change in the direction of polishing tool

The surface roughness (R_a) reduction is 97.12% for the Hilbert toolpath, as R_a reduces to 9.04 nm from 314 nm, as shown in Fig. 3.17. Whereas, for Peano, the reduction is 96.94% with final *surface roughness* (R_a) of 10.23, as shown in Fig. 3.18. The number of turns increases significantly compared to the Zig-Zag; it produces a comparatively non-uniform surface finish.

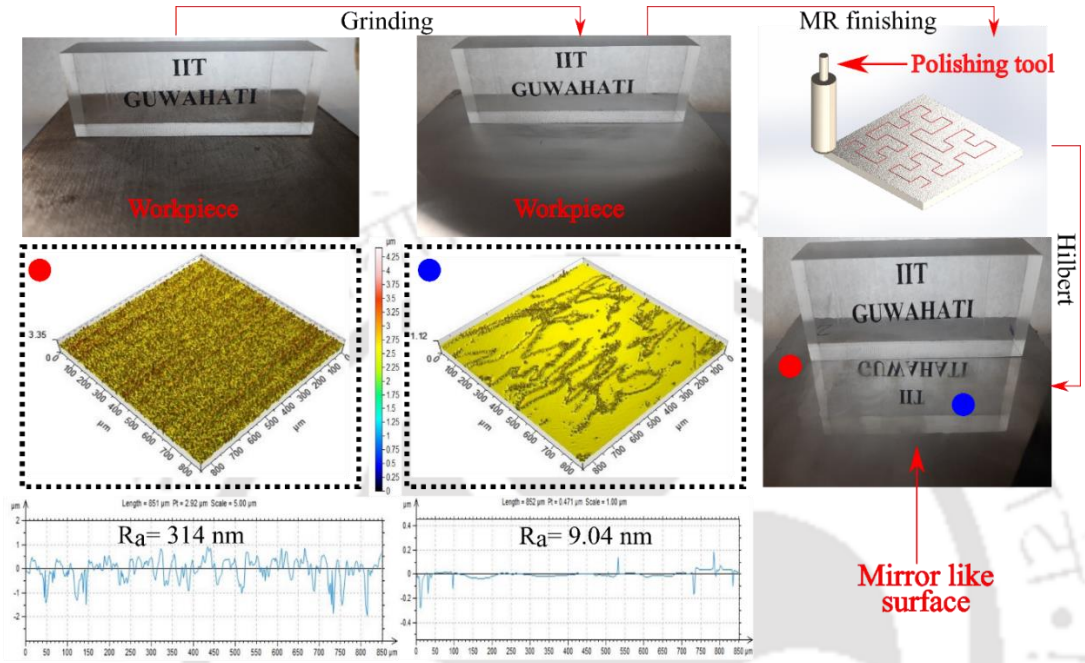

Fig. 3.17 Surface roughness (R_a) obtained through Hilbert toolpath from 314 nm to 9.04 nm

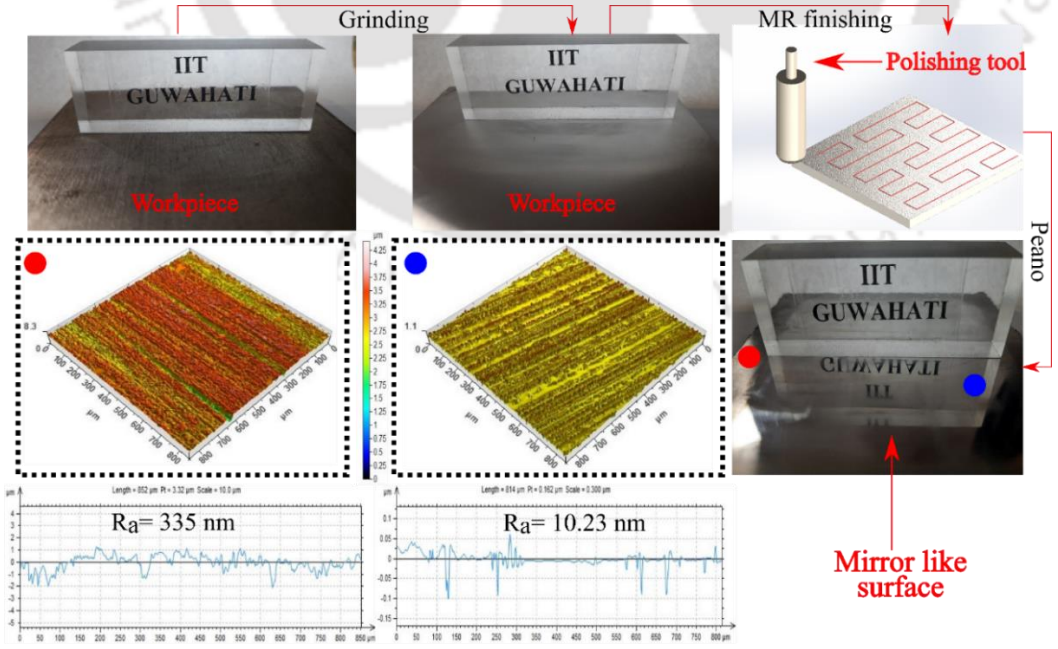

Fig. 3.18 Surface roughness (R_a) obtained through Peano toolpath from 335 to 10.23 nm

The total reduction in the *surface roughness* (R_a) is 97.48% is noticed in the spiral toolpath, as R_a reduces to 6.12 nm from 243 nm, as shown in Fig. 3.19. The circular crest produces along the Spiral curve is responsible for generating the irregularities during the surface finishing.

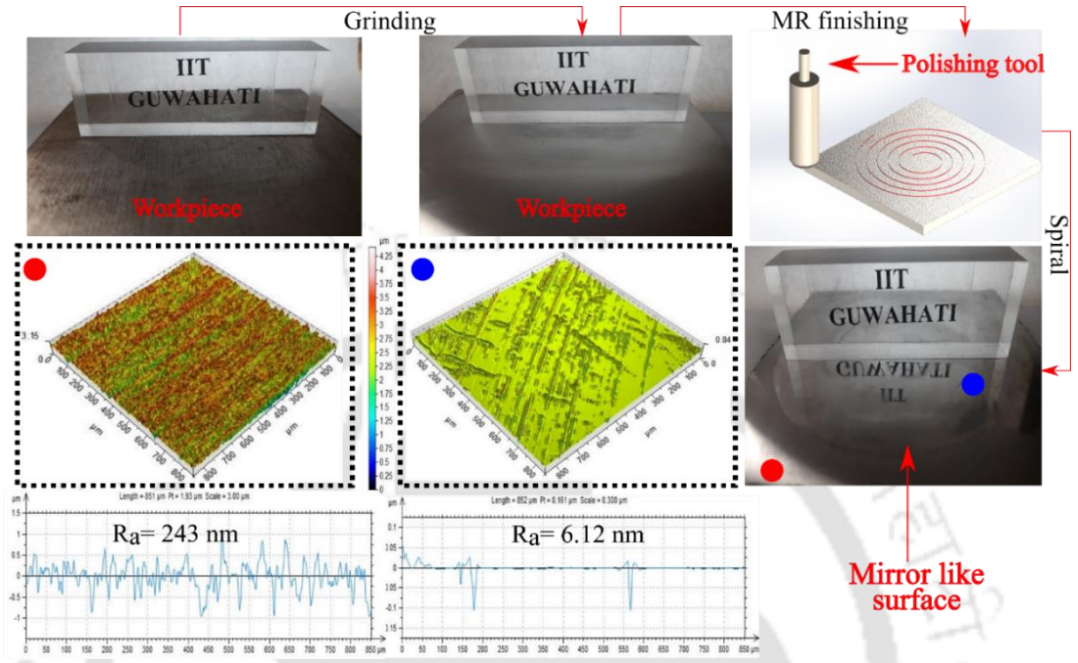

Fig. 3.19 Surface roughness (R_a) obtained through spiral from 243 nm to R_a = 6.12 nm

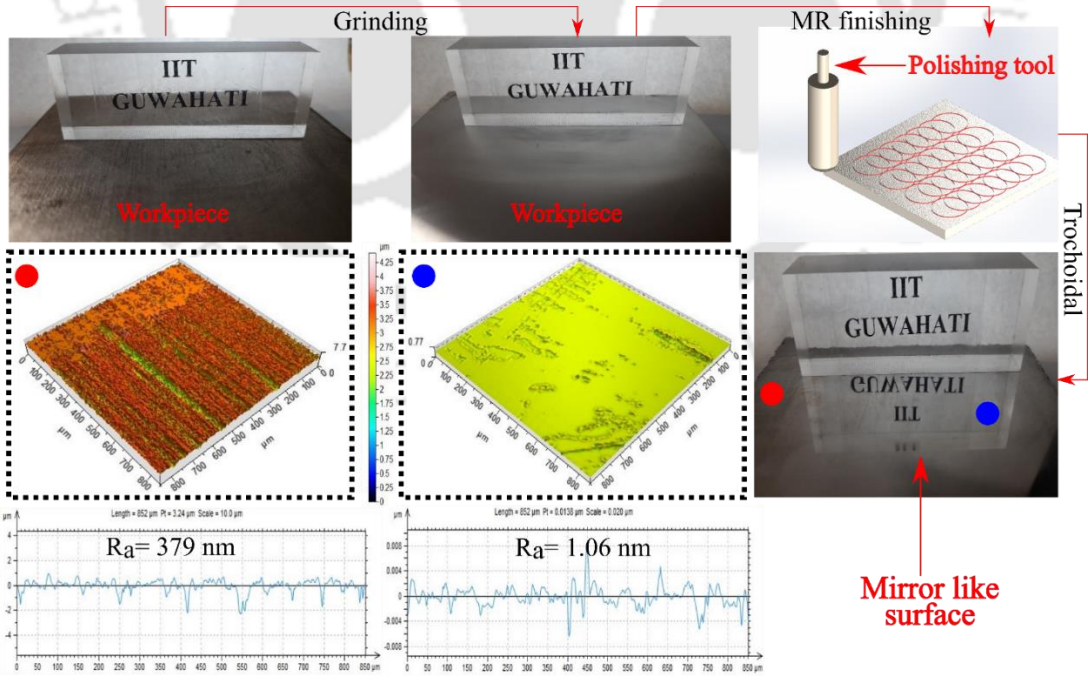

Fig. 3.20 Roughness (R_a) obtained through Trochoidal toolpath from 379 nm to 1.06 nm

The maximum reduction in the *surface roughness* (R_a), i.e., 99.72%, is observed with the best R_a of 1.06 nm in the Trochoidal toolpath. As the polishing tool follows the Trochoidal

path, the repetition of the tool movement over a point increases significantly compared with other toolpaths, as shown in Fig. 3.20. Apart from the additional force discussed earlier, repetition provides uniformity in material removal during the H-ECMR finishing. Moreover, the number of turns also gets reduced during the Trochoidal path. The comparison is made over the different toolpath and listed in Table 3.1. Four corner points (A, B, C, and D) and a center point (E) of the workpiece are selected to investigate the surface roughness. This is considered to analyze the consistency of the surface on the workspace. It is noticed that the standard deviation is the least for the Trochoidal, with maximum uniformity in the surface roughness. Moreover, the best combination of skewness and kurtosis is achieved from the Trochoidal compared to the other toolpaths, as shown in Table 3.2.

Table 3.1 Comparison between the different toolpath techniques

Toolpath	Effective length (mm)	Surface roughness (nm)	% ΔR_a	Standard deviation
Zig-Zag	345	A = 4.81 (best)	97.84	0.7893
		B = 5.78	97.40	
		C = 5.07	97.72	
		D = 6.93 (worst)	96.89	
		E = 6.37	97.14	
Hilbert	504	A = 10.37	96.69	1.6003
		B = 9.04 (best)	97.12	
		C = 9.47	96.98	
		D = 13.55 (worst)	95.68	
		E = 11.26	96.41	
Peano	640	A = 14.55 (worst)	95.65	1.4925
		B = 12.98	96.12	
		C = 10.23 (best)	96.94	
		D = 11.79	96.48	
		E = 13.56	95.95	
Spiral	340	A = 8.54	96.48	1.1548
		B = 9.63 (worst)	96.03	
		C = 6.12 (best)	97.48	
		D = 7.69	96.83	
		E = 7.66	96.84	
Trochoidal	848	A = 1.53	99.59	0.3472
		B = 1.06 (best)	99.67	
		C = 1.24	99.35	
		D = 1.79	99.52	
		E = 2.01 (worst)	99.46	

Table 3.2 Comparison between Skewness and Kurtosis

Toolpath	Skewness (R_{Sk})	Kurtosis (R_{Ku})
Zig-Zag	1.03	6.08
Spiral	-0.08	4.89
Hilbert	0.98	2.41
Peano	1.67	1.76
Trochoidal	-1.23	2.08

The variation in the surface roughness due to the abrupt change in the direction of the polishing tool is the principal challenge during the surface finishing operation. The optical microscopic image of the finished surface is shown in Fig. 3.21 (a) using the Zig-Zag toolpath; scratch marks are produced the sharp turn; the identical phenomenon is observed during Hilbert and Peano as demonstrated in Fig. 3.21 (b) and (c).

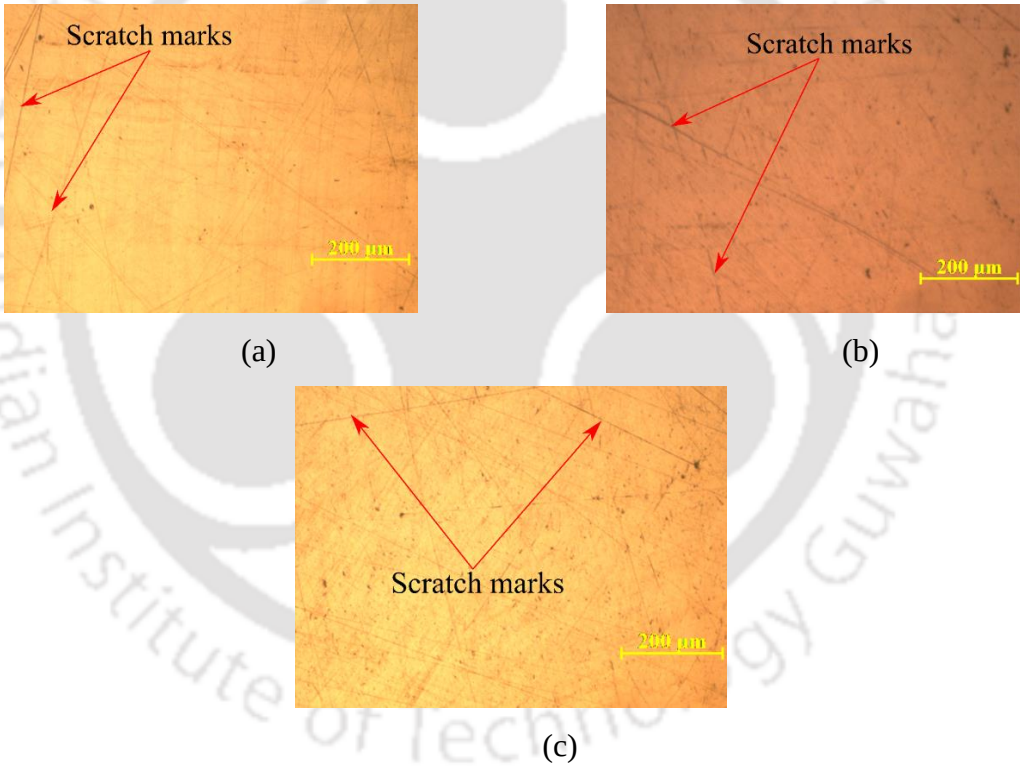

Fig. 3.21 Scratch marks during the abrupt change in the direction of the polishing tool using a) Zig-Zag toolpath b) Hilbert c) Peano

The Trochoidal provides the best surface quality; however, different site on the finished surface is examined through the optical microscope; the unfinished surface shows the marks of the grinding wheel during the surface grinding, as shown in Fig. 3.22(a). The number of these marks reduces but is still observable at the start of the Trochoidal, as the number of repetitions for the first circle is relatively less, as illustrated in Figs. 3.22 (b) and (c). The grinding marks

vanish, and a uniform surface is achieved over the rest of the part on the finished surface, as shown in Fig. 3.22(d).

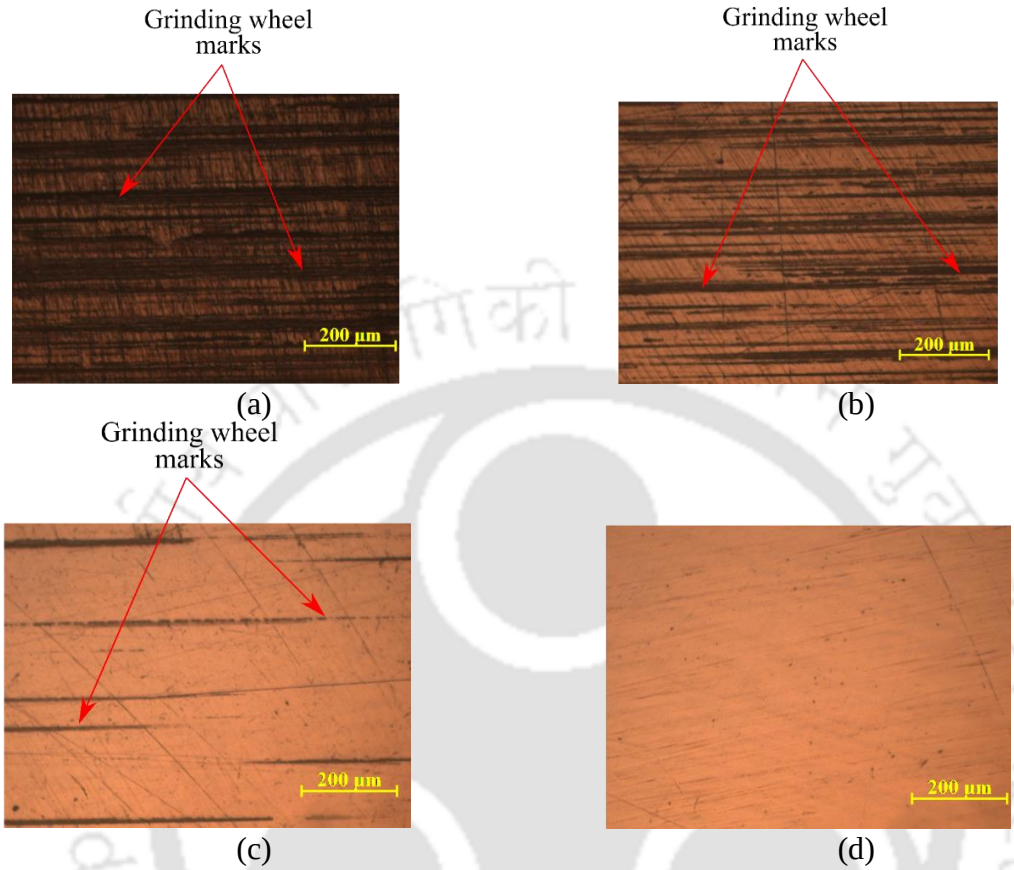

Fig. 3.22 Optical microscopic images of (a) unfinished workpiece, at (b) start, (c) end, and (d) center of Trochoidal toolpath

However, the additional force exerted on the workpiece due to polishing the tool's feed, moving on the Trochoidal curve, is the foremost reason for the enhanced surface quality compared with other toolpaths. To validate this result, the effective length during the Trochoidal toolpath for a single pass (50 mm) is calculated, i.e., 250 mm; the Zig-Zag (selected as it produces the second-best surface roughness) toolpath is repeated five times to achieve the same toolpath length as Trochoidal as shown in Fig. 3.23. A difference of 2.03 nm is noticed between these toolpaths, which shows that the additional force during the Trochoidal toolpath is predominant over the number of repetitions during the surface finishing operation.

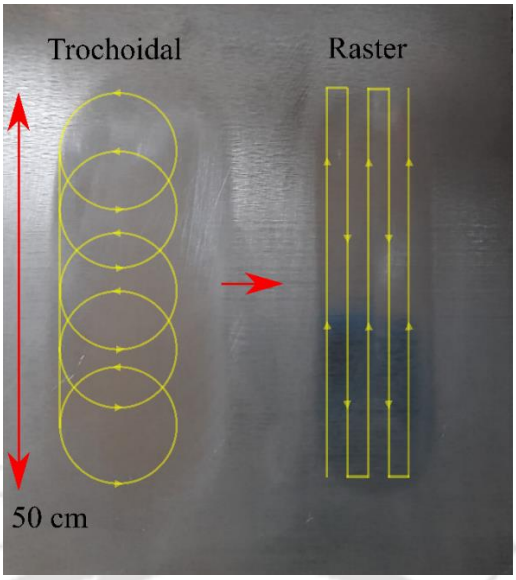

Fig. 3.23 Difference between surface profile for trochoidal and zig-zag with same effective length

3.8 Critical analysis of trochoidal toolpath

In recent years, different models of Trochoidal toolpaths have been proposed for the high-speed milling operation to decrease cutting force with improved tool life. Primarily two models were operated frequently, i.e., a) circular model and b) *trochoidal* (*TR*) model [161]; the prior used successive circular loops to produce the toolpath, straight-line joined tangentially to connect the alternate circles as shown in Fig. 3.24(a). However, the later used a trochoid curve to generate the toolpath, as shown in Fig. 3.24(b). Moreover, Otkur and Lazoglu [162] analyzed the material removal mechanism during the Trochoidal milling and proposed an algorithm for double Trochoidal milling with enhanced functionality. Kardes and Altintas [163] investigated the Trochoidal toolpath's dynamic stability to provide insight into the toolpath during the machining operation. Pleta et al. [164] [165] compared the surface roughness, tool wear, and cutting force generated from the Trochoidal toolpath with the end-milling paths. However, Szaloki et al. [166] developed the empirical model for resultant force, micro-geometrical errors, and surface roughness against each process parameter, i.e., depth of cut, feed rate, stepover, etc. Uhlamann et al. [167] analyzed the effectiveness of the Trochoidal toolpath accompanying energy consumption; a reduction of 35% in machining time is observed with a 6% increase in power consumption. In the H-ECMR finishing process, the prime objective is to enhance the process efficiency by reducing the surface finishing time. Hence, the present aims to develop a Trochoidal toolpath for the H-ECMR finishing process and evaluate the proposed toolpath's performance during the surface finishing operation. A circular model during the Trochoidal

toolpath is opted for the experiment, as symmetrical circular loops provide more uniformity during the H-ECMR finishing process.

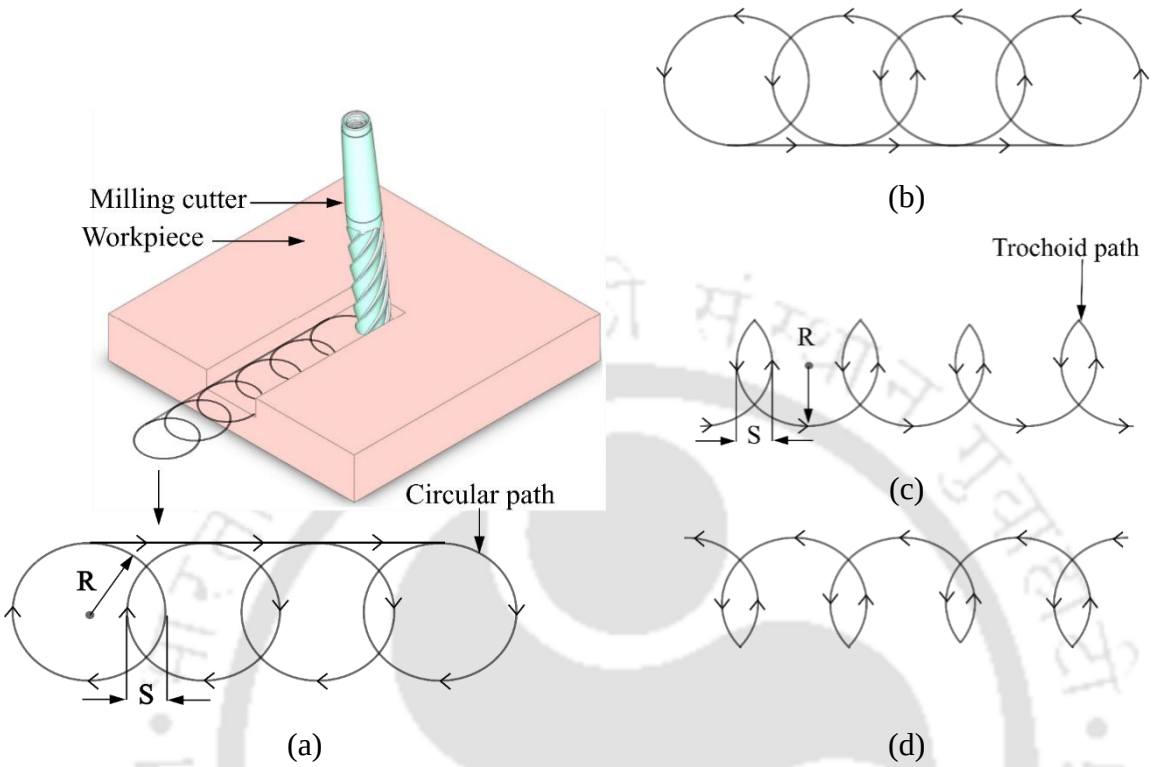

Fig. 3.24 Different models of Trochoidal toolpaths (a) circular with clockwise direction, (b) circular with counterclockwise direction, (c) *TR* model with clockwise direction, and (d) *TR* model with counterclockwise direction

The Trochoidal toolpath, relatively popular in machining operations for enhanced tool life and material removal rate with reduced cycle time, has never been explored for the H-ECMR finishing. A set of experiments is performed to determine the impact of different process parameters of the Trochoidal toolpath, and its relationship with surface quality is evaluated.

3.8.1 Process modeling

The path of the polishing tool during the Zig-Zag and Trochoidal toolpath is shown in Fig. 3.25. The tool engagement angle in the Zig-Zag toolpath (i.e., covers all the workspace through parallel lines with the tool) is 180^{o}, as shown in Fig. 3.25(a). However, the engagement angle of the polishing tool was reduced substantially, as illustrated in Fig. 3.25(b).

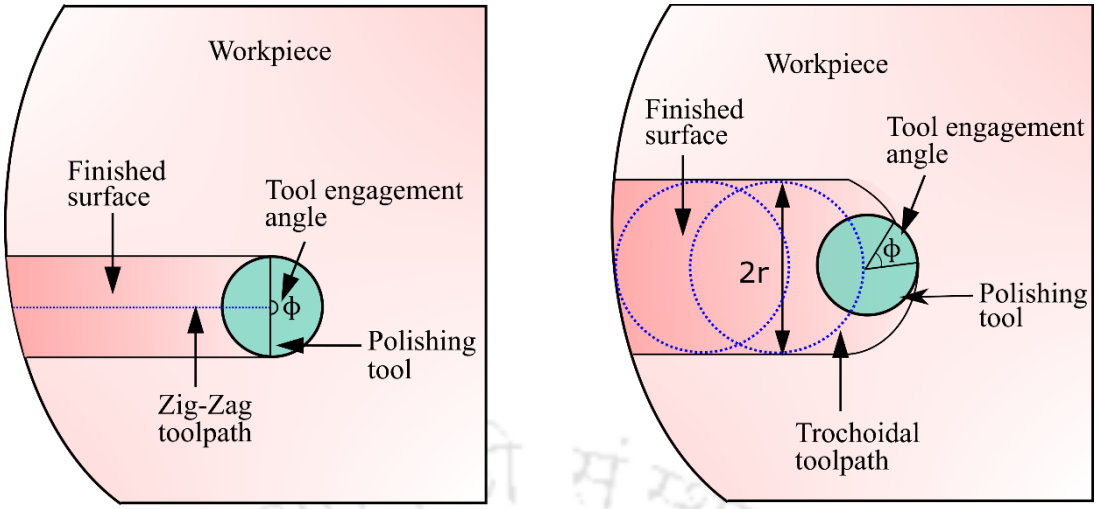

(a) (b)

Fig. 3.25 Tool engagement angle during (a) Zig-Zag and (b) Trochoidal toolpath

The path of the polishing tool traced during the MFAF process is shown in Fig. 3.26, which includes all essential parameters. Where r represents the radius of the Trochoidal toolpath, R is the radius of the polishing tool, V_{feed} means the linear feed velocity in the y-direction, and s represents the distance between the two consecutive circular paths (stepover). Moreover, θ defines the tool's inclination angle from point B while moving on the current toolpath, and ϕ denotes the tool engagement angle. Furthermore, the tool's engagement angle is calculated during the Trochoidal and Zig-Zag toolpath, and a comparative analysis is made on the force applied to the MR fluid chain.

3.8.1.1 Engagement angle

The angle subtended by the remaining workpiece material on the polishing tool is the engagement angle. The periphery of the removed material during the previous and current toolpath is represented by the red and yellow dashed lines, respectively, in Fig. 3.26. Furthermore, at the instant when the angle of inclination of the polishing tool is θ, the engagement angle is represented by angle COD. Point O is the center of the polishing tool defined by Eq. (3.20).

$$(x - r\cos\theta)^2 + (y - r\sin\theta - s)^2 = R^2 \qquad (3.20)$$

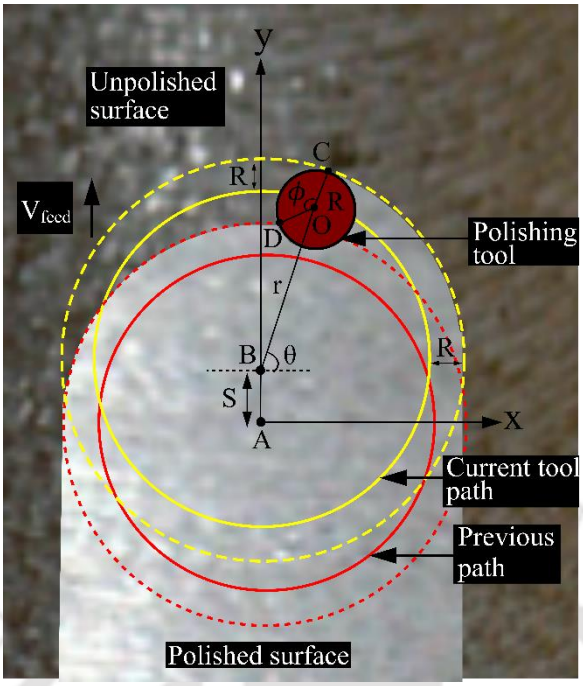

Fig. 3.26 Polishing tool located on the Trochoidal toolpath

The coordinates of the center point are shown in Eq. (3.21). Similarly, point C is the intersection point of the removed material's periphery during the current toolpath (yellow dashed line) and polishing tool. The point is always collinear with the line BO, and the coordinates are shown in Eq. (3.22).

$$x_O = rcos\theta$$
$$y_O = rsin\theta + s \tag{3.21}$$

$$x_C = (r + R)cos\theta$$
$$y_C = (r + R)sin\theta + s \tag{3.22}$$

The periphery of the removed material during the previous toolpath (red dashed line) is represented by Eq. (3.23), and its intersection with the polishing tool produces point D.

$$x^2 + y^2 = (r + R)^2 \tag{3.23}$$

The intersection points (O, C, and D) are used to determine the *engagement angle* (ϕ), as shown in Eq. (3.24). As the number of parameters is higher, making the equation complex, an algorithm in Matlab is developed to generate the *engagement angle* (ϕ).

$$\phi = \cos^{-1}\frac{x_O^2 + y_O^2 - (x_O x_D + x_O x_C + y_O y_D + y_O y_C - x_D x_C - y_D y_C)}{\sqrt{[(x_O - x_D)^2 + (y_O - y_D)^2][(x_O - x_C)^2 + (y_O - y_C)^2]}} \tag{3.24}$$

The impacts of the process parameters are analyzed and shown in Fig. 3.27 for the *tool radius* (*R*) of 5 mm, kept fixed for the observation. Fig 3.27(a) shows the variation of the tool *engagement angle* (ϕ) with *inclination angle* (θ) for different stepovers keeping the radius of the Trochoidal curve as 50 mm. It is observed that the maximum and minimum engagement angle (ϕ) for the stepover 5.0 is 92.86° and 13.33°, respectively, significantly less than the engagement angle (ϕ) of the tool during the Zig-Zag toolpath (i.e., 180°). The engagement angle (ϕ) increases with the inclination angle (θ) up to 90°, then decreases. However, the maximum engagement angle is observed when the inclination angle is 90°, as the material available for the removal is higher at the specified instant, as shown in Fig. 3.27. Similarly, an increase in the stepover leads to an increase in material removal area; hence, the engagement angle (ϕ) increases. As the stepover approaches the diameter of the polishing tool, the engagement angle (ϕ) is 180°. The decrease in the radius of the Trochoidal curve with constant stepover (i.e., 7.5 mm) increases the material removal area; hence the engagement angle (ϕ) increases, as shown in Fig. 3.27(b).

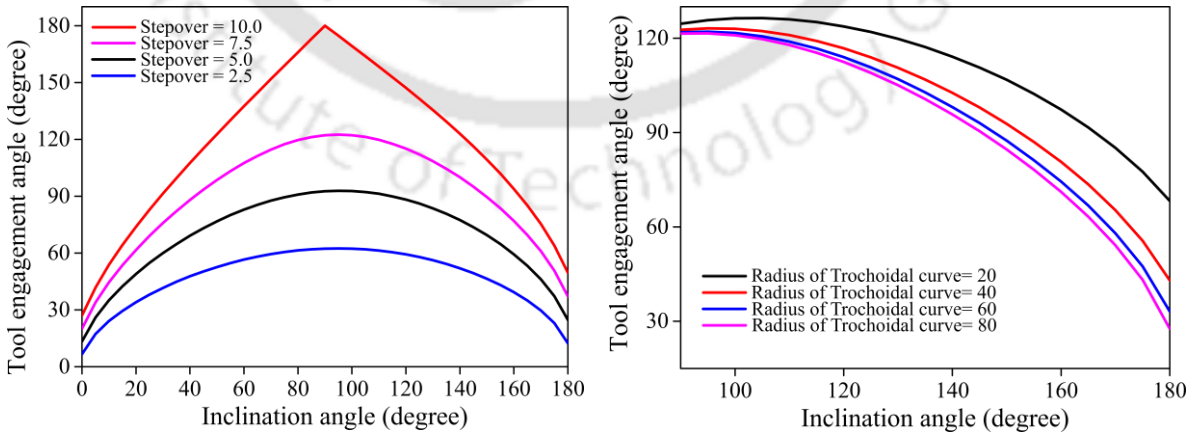

Fig. 3.27 Relation between inclination angle and tool engagement angle for (a) stepover and (b) radius of Trochoidal curve

3.8.1.2 Finishing force modeling for trochoidal toolpath

H-ECMR finishing process utilizes the rheological property of the *Magnetorheological* (*MR*) Fluid [168]; during the surface finishing operation, a chain-like structure is formed by the constituents of the MR fluid (i.e., Abrasive and *Carbonyl Iron particles* (*CIPs*)) [87]. Moreover, the normal force exerted on the MR fluid indents the abrasive particle (diamond) into the workpiece, and the shear force helps to remove the material from the workpiece. Several assumptions have been made while developing the force model, including that the power consumption during the surface finishing operation is only due to the material removal [169]. Abrasive particles are assumed to be spherical and aligned perpendicular to the polishing tool. Also, the MR fluid chain is treated as a beam to analyze its deflection during the surface finishing operation. The *power* (P) consumption in terms of *specific energy* (u) during the surface finishing operation is evaluated from Eq. (3.25).

$$P = uM_r \tag{3.25}$$

Where, M_r is the *Material Removal Rate (MRR)*. Now, power consumption depends upon the *force* (F) applied during the surface finishing and the *peripheral velocity* (V) of the polishing tool, as shown in Eq. (3.26). Furthermore, the combined effect of the workpiece velocity (v), depth of cut (d), and width of the cut (b) can define the MRR.

$$FV = uvdb \tag{3.26}$$

The width of the cut during the surface finishing process is calculated with the help of the tool engagement angle, as shown in Eq. (3.27).

$$l = R\phi \tag{3.27}$$

Hence, the F is correlated with the ϕ and is shown in Eq. (3.28).

$$F = \frac{uvdR\phi}{V} \tag{3.28}$$

The force applied on the MR fluid chain during the Trochoidal and Zig-Zag toolpath is compared based on Eq. (3.28). A comparison is made between the force applied on the MR

fluid during the Trochoidal and Zig-Zag toolpath at the instant when point A is at the origin (Ref. Fig. 3.26), the center of the tool is at the y-axis, and the radius of the Trochoidal curve and tool is 30 mm and 9 mm, respectively. It has been found that the force applied on the MR fluid chain during the Zig-Zag is 2.21 times higher than the Trochoidal toolpath, as shown in Eq. (3.29)

$$\frac{F_{Zig-Zag}}{F_{Trochoidal}} = \frac{\Phi_{Zig-Zag}}{\Phi_{Trochoidal}} = 2.21 \tag{3.29}$$

The force applied on the bottom of the MR fluid chain leads to its deflection, and each MR fluid chain is treated as a cantilever beam. One end of the MR fluid chain connected to the electromagnet acts as the fixed end, and the other is free. Deflection (δ) due to the force applied in the transverse direction of the MR fluid chain is calculated from Eq. (3.30).

$$\delta \propto \frac{Fl^3}{3I} \tag{3.30}$$

Where l and I are the lengths and moment inertia of the MR fluid chain. Analytically, it is observed that the deflection caused by the MR fluid chain during the Zig-Zag toolpath is 2.21 times higher than the Trochoidal toolpath, as shown in Fig. 3.28.

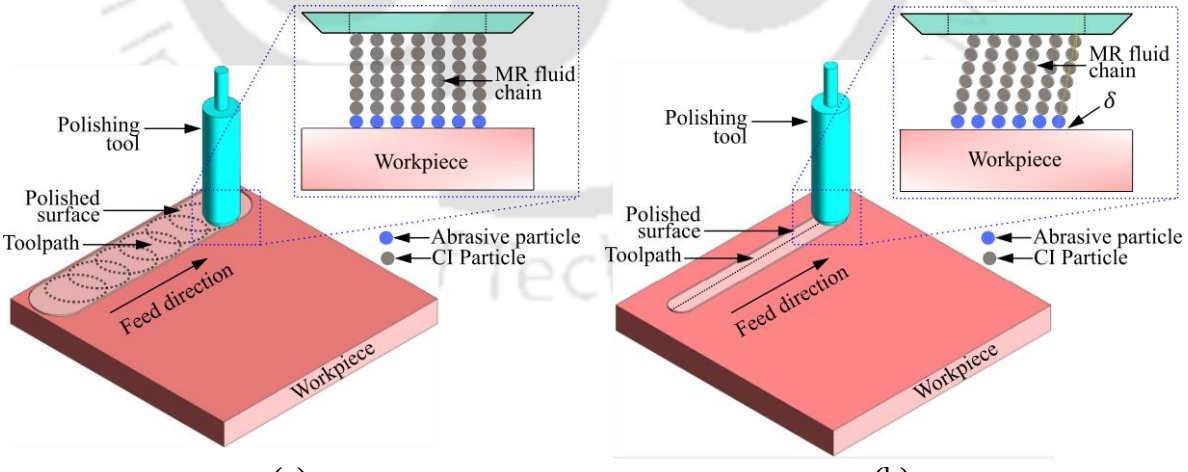

Fig. 3.28 Deflection in MR fluid chain during (a) Trochoidal and (b) Zig-Zag toolpaths

3.8.1.3 Stepover

The distance between the two consecutive circles (i.e., stepover) of the Trochoidal toolpath is crucial to determine the uniformity in the surface roughness. The overlapping of the circles characterizes the uncovered area during the surface finishing operation. These exposed region leads to produce variation in the surface quality. For calculating the uncovered area corresponding to a single pass, different regions during the overlap of the circles (namely *P* and *Q*) are shown in Fig. 3.29. The area of impact of the polishing tool for the Trochoidal toolpath (indicated by green dashed line) for circles *P* and *Q* covers are represented by 1 and 1', respectively. The shared region between the circles is denoted by 3. For calculation of the uncovered area indicated by 2, a rectangle is drawn (represented by a blue line) with the circle's diameter as its side. Eq. (3.31) is used to calculate the area of the *uncovered region* (A_u).

$$A_u = (A_2 + A_{2'}) = Area\ of\ rectangle - (A_1 + A_{1'} - A_3) \tag{3.31}$$

Where, A_1 and $A_{1'}$ represents the area of impact for circles *P* and *Q*, respectively, and calculated from Eq. (3.32). A_3 denotes the area shared by the circles and can be determined from Eq. (3.33).

$$A_1 = A_{1'} = \pi(r+R)^2 \tag{3.32}$$

$$A_3 = 2\left((r+R)^2 Cos^{-1}\left(\frac{(r+R)-s}{r}\right) - ((r+R)-s)\left(\sqrt{((r+R)^2-((r+R)-s)^2)}\right)\right) \tag{3.33}$$

Where *r* represents the radius of the trochoidal curve, *R* denotes the radius of the polishing tool, and *s* denotes the stepover, after simplifications the area of the *uncovered region* (A_u) can be represented by Eq. (3.34).

$$A_u = 0.858(r+R)^2 - (4s(r+R)) + r^2 Cos^{-1}\left(\frac{(r+R)-s}{(r+R)}\right) + 2((r+R)-s)\left(\sqrt{((r+R)^2-((r+R)-s)^2)}\right) \tag{3.34}$$

The A_u is a function of the stepover and submission radius of the Trochoidal curve and polishing tool radius, and its three-dimensional surface plot is shown in Fig. 3.30. It is observed that the lower radius of the Trochoidal curve is favorable with the higher stepover distance. However, with the decrease in the stepover, the uncovered region's area increases, which is unsuitable for the process. The sensitivity analysis observed the impact of $r+R$ and s over the uncovered region area is 12.46% and 21%, respectively, showing that the stepover is significant while determining the consistency in the surface roughness.

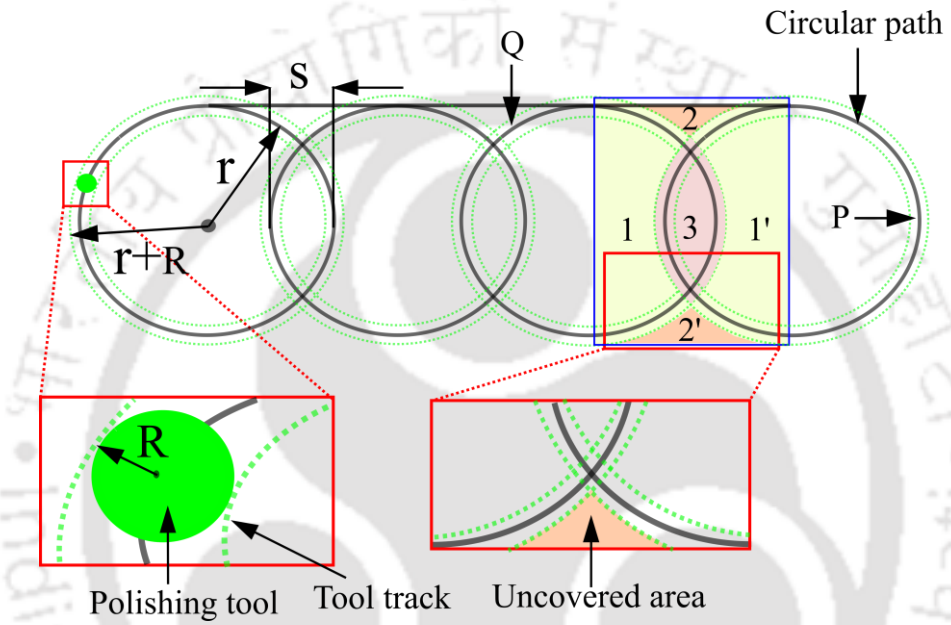

Fig. 3.29 Impact of step over during the Trochoidal toolpath

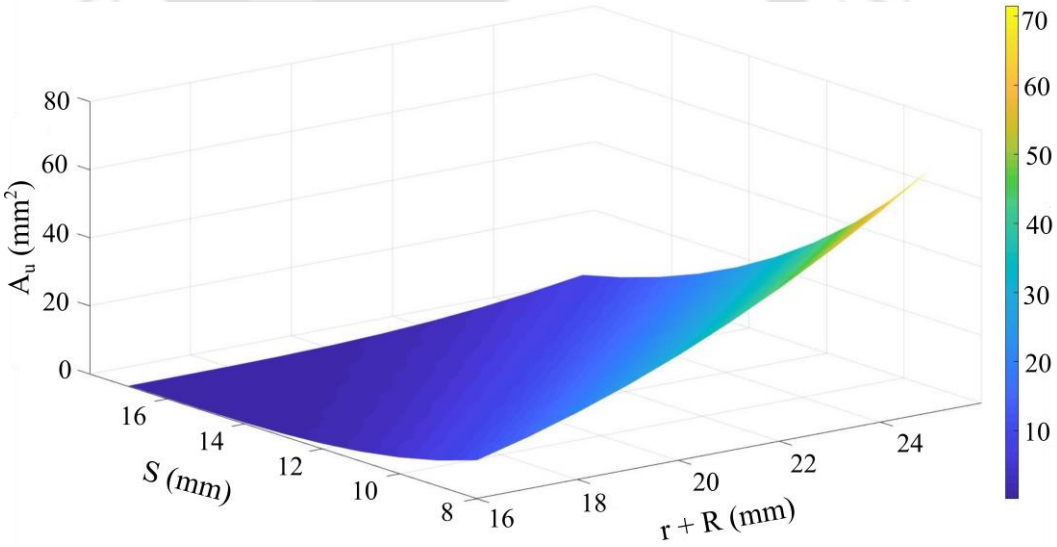

Fig. 3.30 Three-dimensional surface plot for area of uncovered region (A_u)

3.8.2 Comparison between Trochoidal and zig-zag toolpath

Autodesk PowerMill® software is used to generate the Zig-Zag toolpath. At the same time, an algorithm in MATLAB® is developed to create the Trochoidal toolpath. The polishing tool traces the toolpaths to cover the entire workspace. The instantaneous snapshot of the polishing tool is taken during the experiment, as shown in Figs. 3.31 and 3.32. The image is further analyzed in ImageJ software, and the ratio of deflection in the CIP chain during the Zig-Zag to the Trochoidal toolpath observed is 2.52. It is observed that the experimental results are in good agreement with the analytical model, as discussed earlier. The higher force in the case of the Zig-Zag toolpath leads to deflecting the CIP chain more than the Trochoidal toolpath. This phenomenon changes the orientation of the *normal force* (F_n) applied on the workpiece by the abrasive during the Zig-Zag toolpath, as shown in Fig. 3.31. Hence, the reduced normal force during the Zig-Zag toolpath decreases the finishing time. Compared with Zig-Zag, *surface roughness* (ΔR_a) reduction is achieved with a reduced polishing time during the Trochoidal toolpath.

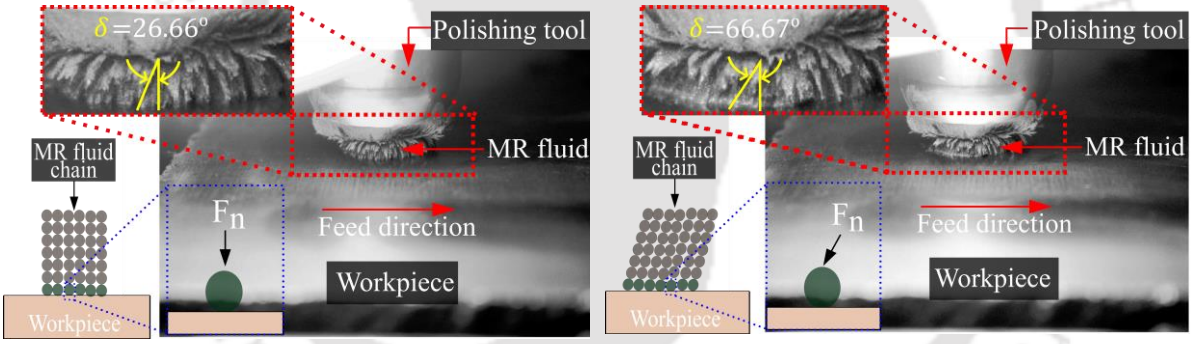

(a) (b)

Fig. 3.31 Comparison between chain deflection between (a) Trochoidal and (b) Zig-Zag toolpaths

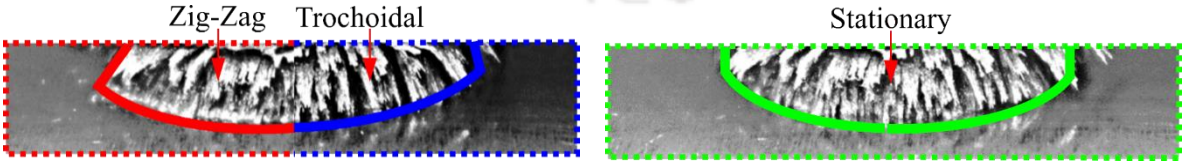

(a) (b)

Fig. 3.32 Comparison between angle of deflection during (a) finishing operation and (b) stationary condition

Experiments have been performed on the DSS with identical process parameters on the specified work domain. Comparison is made between the Zig-Zag and Trochoidal toolpath accompanying the different surface roughness parameters. The *average surface roughness* (R_a) achieved during the Zig-Zag toolpath is inferior to the Trochoidal toolpath, as the deflection in the CIP chain of the MR fluid reduces the impact of the *normal force* (F_n) during the surface finishing operation. The study and modeling of skewness and kurtosis are also required for a better surface description and proper functioning of the polished surface. The *skewness* (R_{sk}) and *Kurtosis* (R_{ku}) are analyzed at different feed rates, as shown in Fig. 3.33, during the Trochoidal and Zig-Zag toolpath. Removing peaks from the surface irregularities is performed with the H-ECMR finishing process; however, during the Zig-Zag toolpath, the number of peaks on the polished surface is higher than the valley at higher feed rates. Hence, a positive *skewness* (R_{sk}) is observed, increasing the chance of wearing during the tribology contact. Higher feed rates (3~6 mm/min) reduce the interaction time between the CIP chain and the workpiece, resulting in lower peak removal. However, at lower feed rates (< 1 mm/min), the interaction time increases, leading to removing a higher number of peaks, and negative skewness is noticed. In the case of the Trochoidal toolpath, repetition of the toolpath at a specified point increases the contact time between the workpiece and the CIP chain. Hence, fewer peaks than the valleys are produced (i.e., negative R_{sk}), retain the fluid and provide good lubricating properties suited for the biomaterials. *Kurtosis* (R_{ku}) greater than 3 is observed during the Zig-zag toolpath, meaning pointed peaks increase the chances of wear-off during the tribological contact. However, in the case of the Trochoidal toolpath, R_{ku} less than 3 is observed, i.e., flat peaks are produced during the surface finishing operation. Hence, the best combinations of kurtosis and skewness suited for the biomaterial are achieved with the Trochoidal toolpath. The implant type, including dental, acetabular cup, spinal fusion cages, etc., requires positive skewness and kurtosis greater than 3. The surface parameters necessary to improve the osseointegration, which enhances the interaction between the implant and bone, are needed. On the contrary, a few implants (knee, femoral head, bone plates, etc.) need negative skewness and kurtosis of less than 3 to reduce the wear rate and minimize the aseptic loosening.

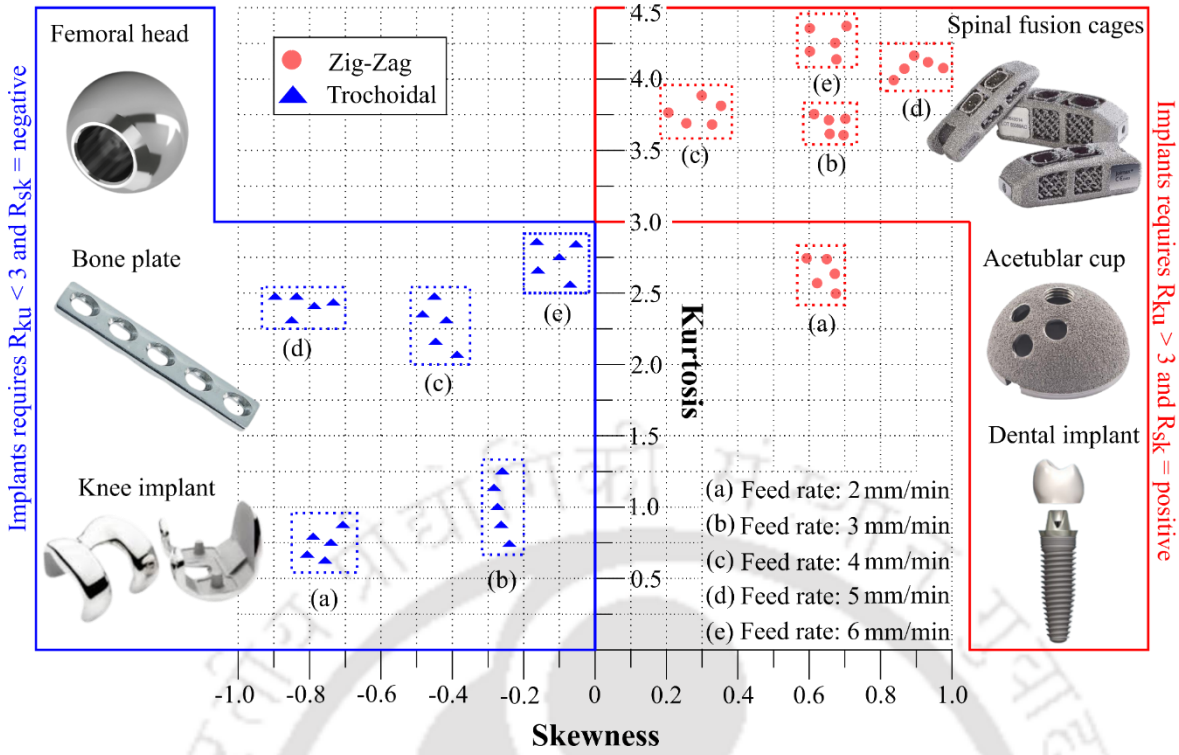

Fig. 3.33 Comparison between the Skewness and Kurtosis for Trochoidal and Zig-Zag toolpath at different stepovers

3.8.3 Experimental investigation on Trochoidal toolpath process parameters on surface roughness

Five measurements are taken for single output to reduce the noise associated with the experimental result. The mean value of the recorded reading is used to develop the empirical formula for the Trochoidal toolpath during the H-ECMR finishing process. The statistical design of experiments is utilized to plan, perform and analyze the experiments. Statistical software is used to implement the *Central Composite Design* (*CCD*) to produce the combination of experimental process parameters. The CCD technique is effective for the analyze the interaction of the parameters. Compared with the other methods, a minimum set of experiments is required in the case of CCD. The number of experiments is calculated from Eq. (3.35).

$$N = 2^n + 2n + n_c \tag{3.35}$$

Where the N represents the number of experiments, 2^n represents the factorial part, $2n$ denotes the starts parts and n_c represents the center part of the experiments. Based on the preliminary investigations, the magnitude of different parameters is assigned and listed in Table 3.3. The

experiments were performed on a rectangular workspace of 100 mm length and 30 mm width, made of DSS.

Table 3.3 Coded levels and actual values of the process parameters

Sr. No.	Parameter	Unit	Levels		
			-1	0	1
1.	Radius of Trochoidal curve (r)	mm	25	30	35
2.	Feed (F)	mm/min	4	5	6
3.	Stepover (s)	mm	12.5	15	17.5

3.8.3.1 Regression analysis

Response Surface Methodology (RSM) is applied to develop a relationship between the output variable and process parameters using mathematical and statistical techniques. The order of influence of the input variable on the measured responses is characterized by the RSM approach [170]. The regression model shows an empirical relation between the output variable and the input factor [171]. This study uses the *Central Composite Design* (*CCD*) method to develop the regression model based on the experimental responses [172]. The *average surface roughness* (R_a) model as the function of process parameters is represented by Eq. (3.36).

$$R_a = 891 - 42.6r + 28.8F - 21.9s + 0.708r^2 - 0.57F^2 + 0.459s^2 + 0.171rF - 0.062rs + 2.04sF \quad (3.36)$$

Analysis of Variance (*ANOVA*) is used to determine the significance of the process parameters on the output. The developed regression model is analyzed through the ANOVA, and required modification is performed to get the best-suited combination [173]. The ANOVA result corresponding to the *average surface roughness* (R_a) is listed in Table 3.5. The compatibility of the regression equation is improved by identifying and removing the non-significant terms. The standard tabular F-value and predicted F-value ratio are compared at a 95% confidence interval. It is observed that the developed model failed in the F-test as the ratio of the F-value is greater than 1. Hence the non-significant terms are removed to improve the developed regression model. Figure 3.34 shows that the F-value corresponds to combinations of different parameters; terms with a value less than 1.5 are eliminated from the regression model [7].

Table 3.4 Details of design of experiments

Std. order	Run order	Factors			Responses			
		Radius of Trochoidal curve (r)	Feed (F)	Stepover (s)	Surface roughness (R_a, nm)	Kurtosis (R_{ku})	Skewness (R_{sk})	Finishing time (T, min)
16	1	30	6	17.5	30.14	4.26	-0.16	59.62
17	2	30	5	12.5	19.02	2.98	-0.47	66.69
14	3	35	5	15	37.98	5.71	-0.12	69.99
13	4	25	5	15	40.69	7.36	-0.04	80.51
19	5	30	5	15	10.40	1.03	-0.86	68.33
18	6	30	5	17.5	25.95	4.25	-0.27	71.54
15	7	30	4	15	20.26	2.56	-0.36	85.41
20	8	30	5	15	36.89	2.98	-0.19	68.47
7	9	25	6	17.5	40.39	6.39	-0.11	65.41
4	10	35	6	12.5	33.56	5.78	-0.21	57.46
6	11	35	4	17.5	25.95	4.25	-0.26	88.81
12	12	30	5	15	10.96	1.45	-0.78	68.39
10	13	30	5	15	11.08	0.89	-0.81	68.26
11	14	30	5	15	10.38	1.96	-0.70	68.34
5	15	25	4	17.5	32.85	8.90	-0.39	98.12
3	16	25	6	12.5	33.96	7.26	-0.42	67.09
9	17	30	5	15	10.36	1.30	-0.82	68.51
1	18	25	4	12.5	39.96	6.85	-0.29	100.63
8	19	35	6	17.5	41.71	4.36	-0.56	59.13
2	20	35	4	12.5	40.96	5.96	-0.48	86.19

Table 3.5 ANOVA for surface roughness

Source	DF	SS	MS	F-Value	P-Value	R^2	
Regression	9	1991.91	221.324	2.95	0.053	72.66%	$F_{(0.05,9,10)}^{Standard} = 3.0204$
Linear	3	875.3					
Square	3	775.42					$F^{Regression} < F_{(0.05,9,10)}^{Standard}$
Interaction	3	232.33					
Residual Error	10	749.62	74.962				The regression model is not accepted
Lack-of-Fit	5	174.73	34.945	0.30	0.891		
Pure Error	5	574.89	114.979				
Total	19	2741.54					

The modified equation is developed by neglecting the insignificant combination of process parameters shown in Eq. (3.37). The ANOVA is again performed on the modified regression equation, and the results are listed in Table 3.6. The F-value corresponds to the regression equation, and the standard tabular is 5.93 and 2.05, respectively. As the ratio of the F-value is less than 1, the empirical equation for the average surface roughness is passed in the

test of adequacy. Similar efforts are made to develop the empirical equation for the skewness, kurtosis, and finishing time are shown in Eqs. (3.38), (3.39), and (3.40). The number of experiments obtained for three process parameters is 20, with 8 factorial parts, 6 centers, and 6 start points, as listed in Table 3.4.

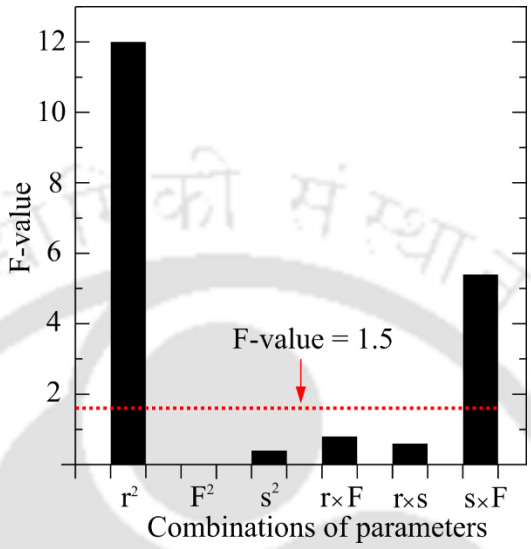

Fig. 3.34 F-value corresponds to different process parameters combination

$$R_a = 669 - 44.17r + 1.89F + 0.33s + 0.734r^2 \quad (3.37)$$

Table 3.6 ANOVA for surface roughness

Source	**DF**	**SS**	**MS**	**F-Value**	**P-Value**	
Regression	4	1719.14	429.79	6.31	0.003	$F_{(0.05,4,14)}^{Standard} = 2.3947$
Linear	3	1723.08				
Square	1	1674.10				$F^{Regression} > F_{(0.05,9,10)}^{Standard}$
Residual Error	15	1022.39	68.16			
Lack-of-Fit	10	447.50	44.75	0.39	0.904	The regression model is accepted
Pure Error	5	574.89	114.979			
Total	19	2741.54				

$$R_{ku} = 155.1 - 8.09r + 1.92F - 4.41s + 0.1378r^2 - 0.273F^2 + 0.201s^2 + 0.0508rF - 0.0431rs - 0.058sF \quad (3.38)$$

$$R_{sk} = 12.83 - 0.916r - 0.0104F + 0.0216s + 0.01526r^2 \quad (3.39)$$

$$T = 562.1 - 17.95r - 46.73F - 7.54s + 0.2448r^2 + 2.419F^2 + 0.16s^2 + 0.196rF + 0.0848rs + 0.095sF \quad (3.40)$$

The experimental output and the results obtained from the regression model for its validation are compared in Fig. 3.35. The variation of experimental measurement of different surface roughness parameters is shown by the error bar. Furthermore, the difference between the experiment and predicted data is primarily due to the curve fitting of the developed regression model. The R-square value concerning the developed regression model is the maximum and minimum for *finishing time* (t) and *average Surface Roughness* (R_a). Hence, the variation of the predicted data with the experimental data is more for the R_a and less for the finishing time. The result suggests that the expected values agree with the experimental data.

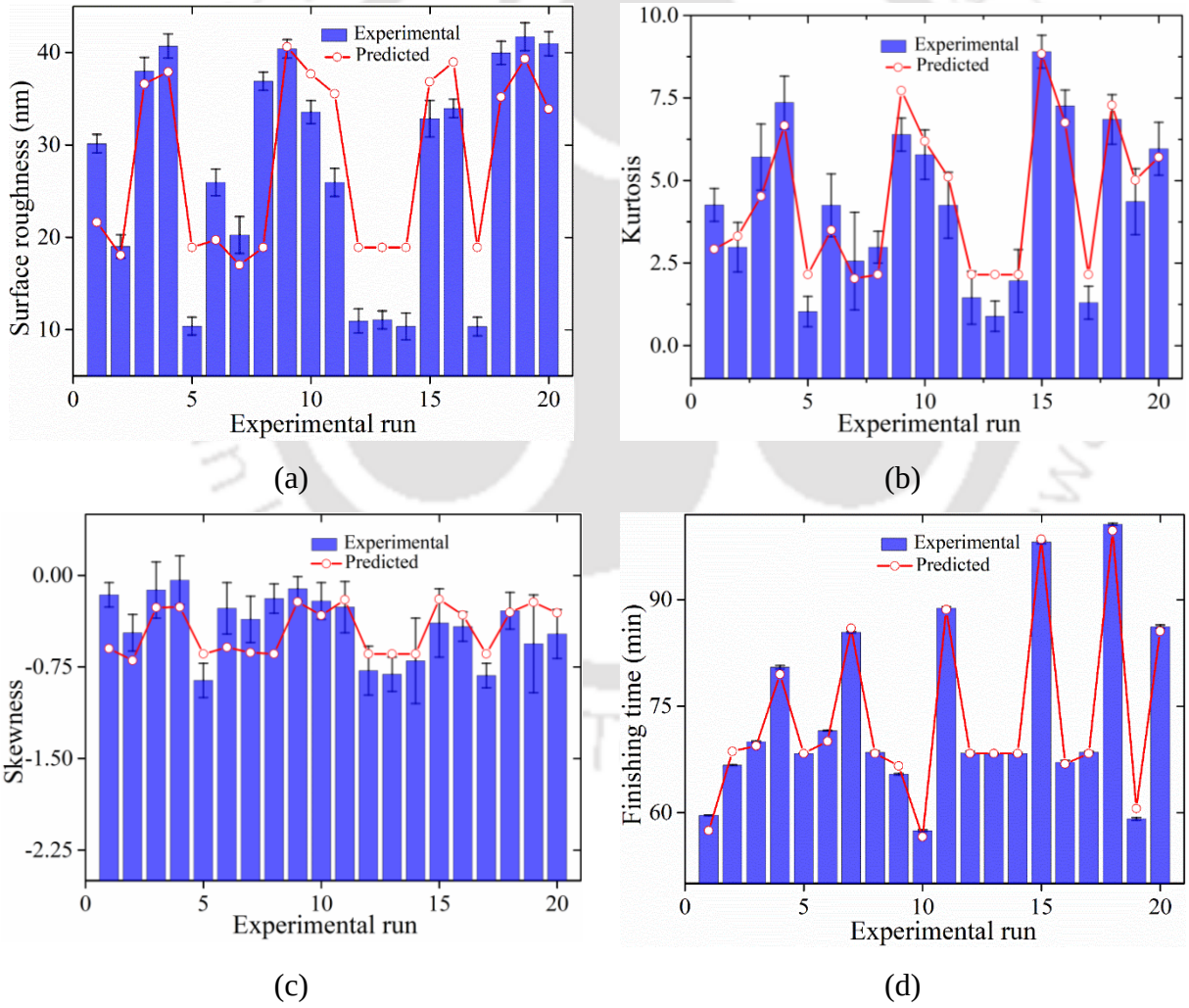

Fig. 3.35 Comparison between the experimental and predicted results for (a) surface roughness (R_a), (b) kurtosis (R_{ku}), (c) Skewness (R_{sk}), and (d) finishing time (T)

The surface roughness of the DSS biomaterial is enhanced with the H-ECMR finishing process up to a few nanometers. The developed Trochoidal toolpath can produce uniform surface roughness compared with the zig-zag toolpath. As discussed earlier, the Trochoidal toolpath creates a better-polished surface than the Zig-Zag toolpath. However, the different process parameters (i.e., stepover, the radius of the Trochoidal curve, and feet rate) affect its effectiveness and efficiency. An analysis is made to determine these process parameters' impact on the workpiece's surface quality.

3.8.3.2 Stepover

Stepover is defined by the overlap between the two consecutive circles of the Trochoidal toolpath. The stepover gets reduced with the increase in the percentage of overlap between the two circles. The increased amount of overlap always enhances the surface quality of the polished surface; on the contrary, it increases the finishing time. Fig. 3.36(a) shows the impact of the percentage of overlap on the *finishing time* (T) and the *uncovered area* (A_u) as discussed in Eq. (3.34). The *radius of the Trochoidal curve* (r) and feed rate is constant for the experiment, i.e., 30 mm and 4 mm/min, respectively, for the rectangular workspace of 30 mm width and 50 mm length. It is observed that with an increased percentage of overlapping, the finishing time increases, whereas the uncovered area decreases. Furthermore, to cover the 50 mm length, two circular curves require up to 30% of overlap (i.e., stepover is 9 mm); however, the number of required circles increases with further overlap. Hence a steep slope is observed after 30% of overlapping. The impact of the percentage of overlapping over the different surface roughness parameters is illustrated in Fig. 3.36(b).

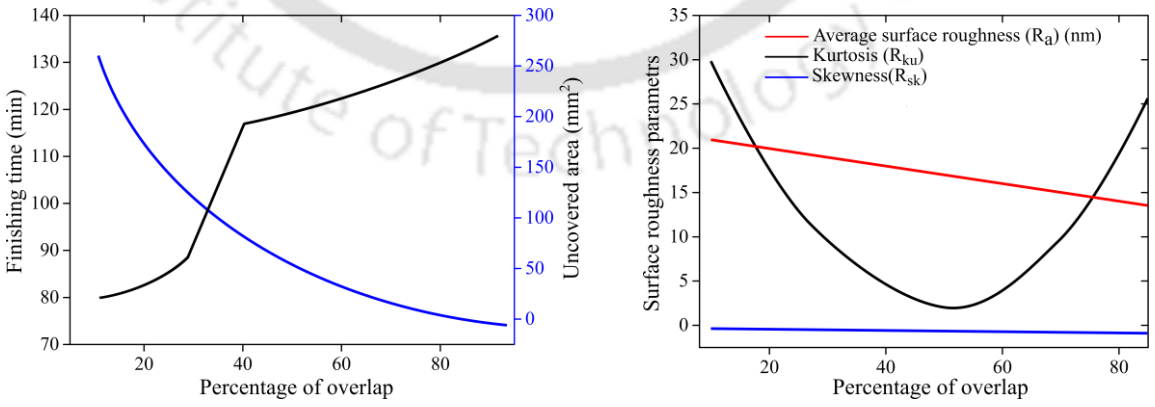

(a) (b)

Fig. 3.36 Impact of stepover on the (a) uncovered area, finishing time, and (b) surface roughness parameters

The radius of trochoidal (30 mm) and feed rate (4 mm/min) is kept fixed for the analysis. The *average surface roughness* (R_a) of the polished surface reduces with the increase in the percentage of the overlap of the Trochoidal curves as the uncovered area reduces. A slight reduction in peaks is noticed with increased overlap of the Trochoidal curves as *skewness* (R_{sk}) decreases. After the 15 mm stepover (50% of the overlap for the 30 mm Trochoidal curve), the value of Kurtosis (Rku) starts increasing and producing the pointed peaks.

3.8.3.3 Curve radius

The impact of the radius of the Trochoidal curve on the different surface roughness parameters (i.e., R_a, R_{ku}, and R_{sk}) for the H-ECMR finishing process is shown in Fig. 3.37(a). The impact of the radius of the Trochoidal toolpath is significant on the surface roughness parameters. Experiments are performed for a single pass of length 50 mm. 50% of the overlap has opted for each radius of Trochoidal cure to map the entire workpiece. *Average surface roughness* (R_a) increases with the increase in the radius of the Trochoidal curve. It is because the uncovered region's area increases with the radius of the Trochoidal curve for 50% of the overlapping. An identical trend is noticed for the *kurtosis* (R_{ku}); however, after 35 mm, the line gets steeper, leading to more pointed peaks. *Skewness* (R_{sk}) almost remains independent from the variance of the radius of the Trochoidal curve.

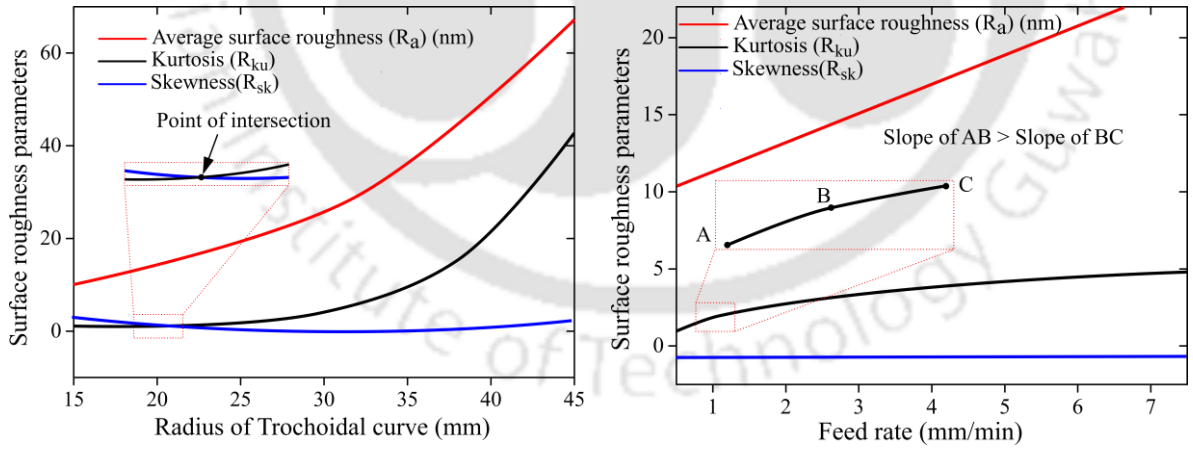

(a) (b)

Fig. 3.37 Variation of surface roughness parameters with (a) radius of Trochoidal curve (b) feed rate

3.8.3.4 Feed rate

The influence of the feed rate on surface roughness parameters is shown in Fig. 3.37(b). The duration of interaction between the CIP chain and the workpiece depends upon the feed rate. The experiments are performed to analyze the feed rate effect by keeping the radius of the

Trochoidal curve (30 mm) and stepover (15 mm) constant while mapping the workspace. The *average surface roughness* (R_a) increases with an increase in the feed rate, as a low feed rate provides high interaction time and vice versa. However, the increase in the interaction time beyond a specific limit deteriorates the polished surface and produces scratch marks. Initially, up to 1 mm/min, the higher *kurtosis* (R_{ku}) value leads to pointed peaks because of the scratches. Furthermore, the *kurtosis* (R_{ku}) increases with the feed rate. However, the number of peaks increases with the increase in the feed rate as the *Skewness* (R_{sk}) is reduced.

Based on the combination of the process parameters during the Trochoidal toolpath, the surface enhancement is performed on the powder bed fusion fabricated plate. The biomaterial samples (SS316L) with a specification of 50×50×10 mm are fabricated using SLM for surface enhancement and further wear resistance. The size 15–45 µm powder particles are used to manufacture the final product, as shown in Fig. 3.38. A fiber laser of wavelength 1070 nm with a power of 400 W is used to melt the powder particles. The maximum exposure time of around 1 µs is fixed with a focal point diameter and feed rate of 70 µm and 5 m/s, respectively. The surface defects, including unmelted powder particles and pores, are easily visible in Fig. 3.39. The H-ECMR finishing process enhances the surface quality of the SLM fabricated parts. However, the H-ECMR finishing process is limited to the workpiece's surface roughness in the sub-micron range, necessitating an intermediate approach to reduce the R_a in the submicron range. Hence, milling is executed on SLM-fabricated parts before the H-ECMR finishing. A face milling tool is used, and the depth of cut, feed rate, and spindle speed during the milling operation were 0.25 mm, 10 mm/min, and 1000 rpm, respectively [26]. Afterward, the H-ECMR finishing process is performed to decrease the R_a of the milled surface in the range of a few micrometers.

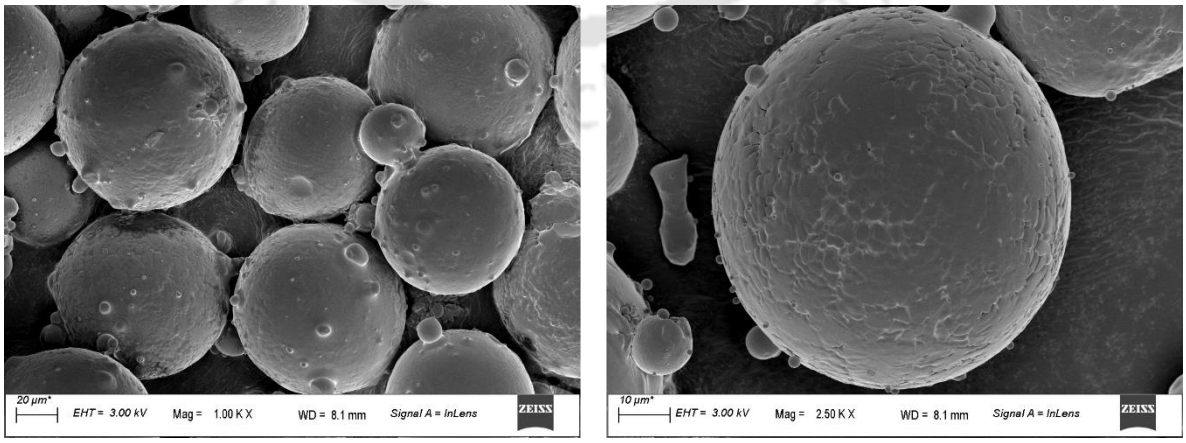

Fig. 3.38 Scanning electron microscopic images of SS316L (a) powder particles and (b) enlarged view of a single particle

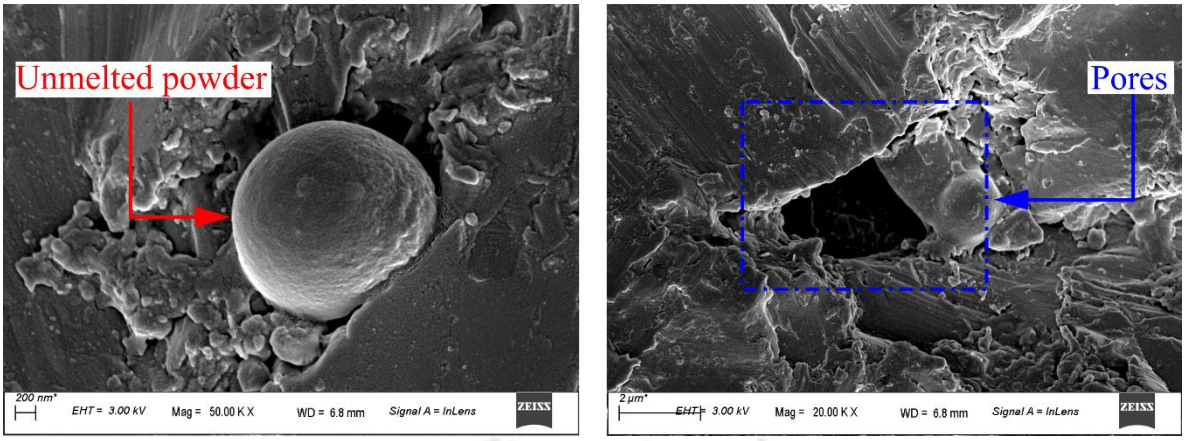

(a) (b)

Fig. 3.39 Surface defects showing (a) unmelted powder and (b) pores on SLM fabricated workpiece surface using SS316L powder

The initial surface defects on the surface of SLM fabricated parts, as shown in Fig. 3.39, produce a poor surface quality of the workpiece. However, the milling operation reduces the initial R_a value of 8.32 µm to 0.89 µm with an 89.30% decrease in average surface roughness. Afterward, the H-ECMR finishing process is carried out on the biomaterial to reduce further its surface roughness in the range of a few nanometers. The normal force is generated on abrasive particles due to the action of magnetic force produced from the electromagnet, helping to indent the materials into the workpiece. The feed and centrifugal force, along with the electrochemical reaction, help to remove material by the indented abrasive from the workpiece, which reduces the workpiece's surface irregularities. The combined action of forces minimizes the value of average surface roughness from 0.89 µm to 34.26 nm with a 96.15% reduction in R_a. The 1D and 2D average surface profiles and surface texture comparison of the biomaterial after operating by different processes are shown in Fig. 3.40.

The surfaces during different post-processing phases are analyzed through the optical profilometer to analyze the changes in the surface topology. Initially, unmelted powders are easily visible on the SLM-fabricated biomaterial surface, as illustrated in Fig. 3.41(a). However, the surface defects from the additively manufactured biomaterial surface are significantly removed after milling, as shown in Fig. 3.41(b). Furthermore, the scratch marks produced by the milling cutter are noticeable on the milled surface (Fig. 3.41(b)). However, the H-ECMR finishing process significantly reduces the scratch marks generated from the milled biomaterial surface, as illustrated in Fig. 3.41(c).

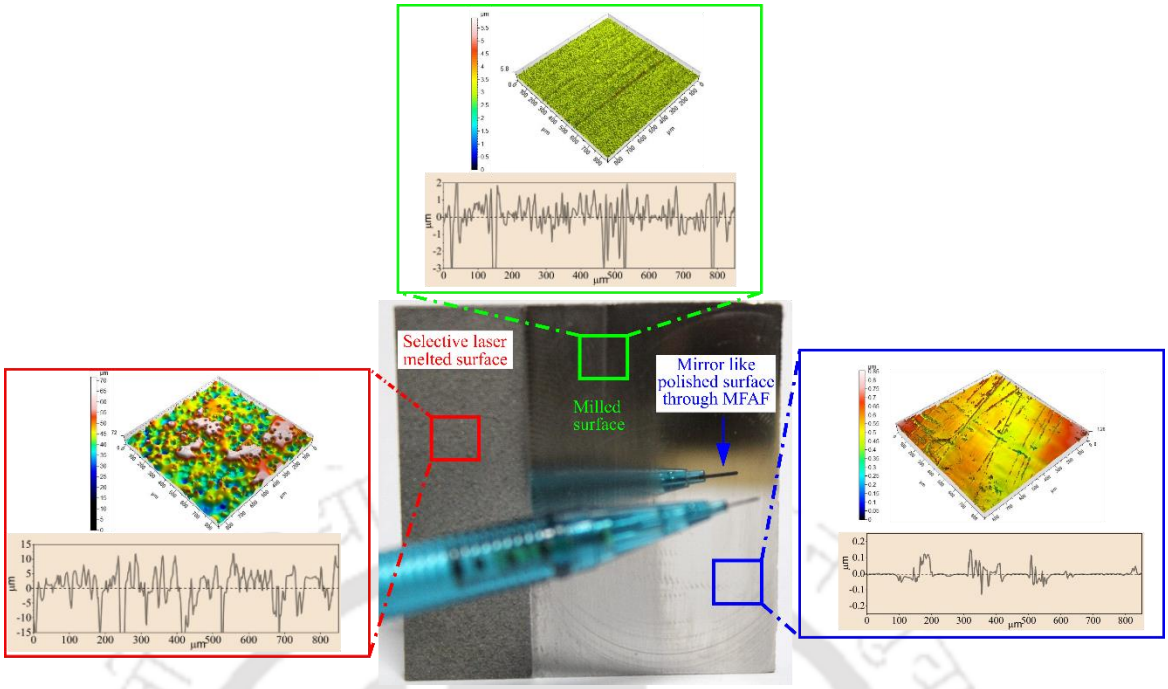

Fig. 3.40 1D and 2D surface roughness profiles on selective laser melted, milled, and H-ECMR polished surfaces

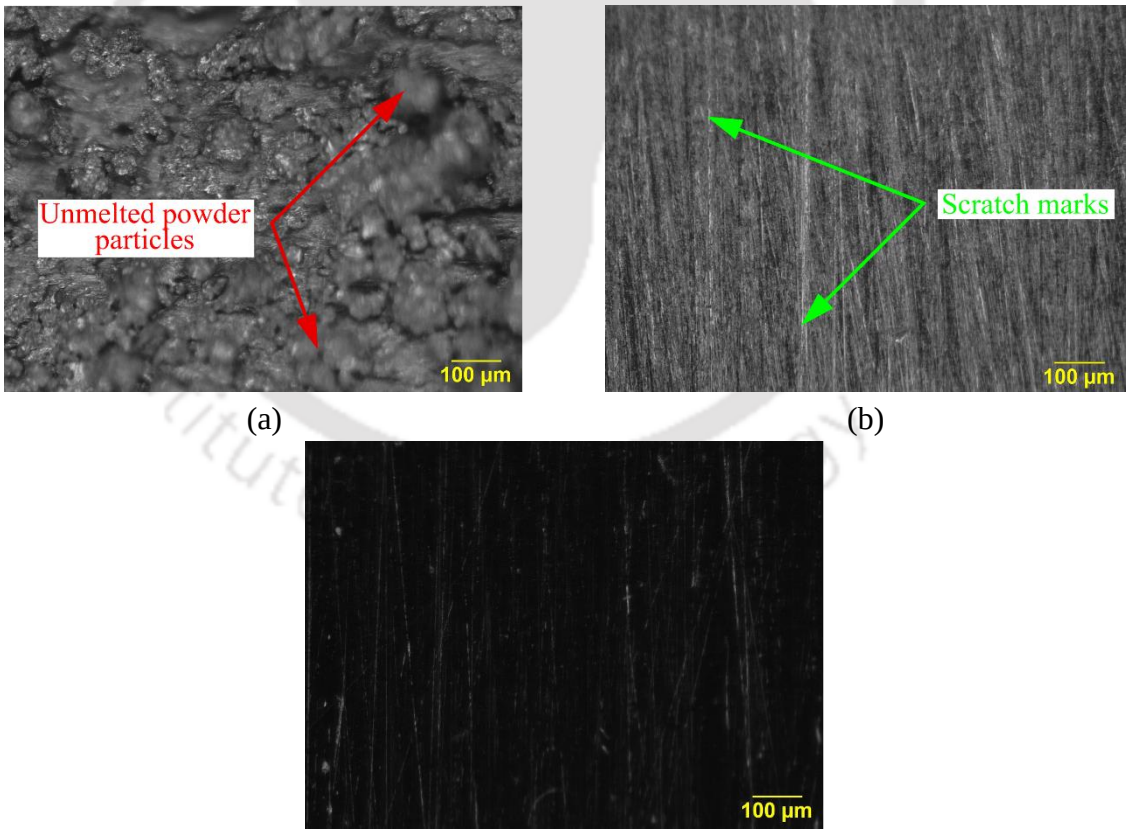

(a) (b)

(c)

Fig. 3.41 Optical microscopic images of (a) SLM fabricated, (b) milled, (c) H-ECMR polished surfaces

3.9 Summary

This chapter focuses on the development of a *Computer-Aided Process Planning* (*CAPP*) for super-finishing through the *H-ECMR* finishing process. The inconsistency in the surface roughness on the polished surface of the workpiece having holes is observed during the *H-ECMR* process irrespective of their size (i.e., hole diameter). Trapping of *Magnetorheological* (*MR*) fluid and leakage of carrier medium from the holes are the primary reasons for the irregularities in the polished surface quality. *FHMRF-PS* is developed with an external deposition module, which helps deposit paraffin wax over the pockets or holes with the nearest neighbor algorithm of the *Travelling Salesman Problem* (*TSP*) to avoid repetition during deposition. The underfilling and overfilling of paraffin wax are critical as they affect the surface quality of the polished surface. An increase in the % overfilling leads to a decrease in MR fluid's yield stress, which is further responsible for surface quality deterioration. However, inconsistent surface quality is produced on the polished surface irrespective of the amount of underfilling, as trapping of MR fluid reduces the polishing efficiency. Moreover, a comparison is made between the different toolpath strategies, such as Zig-Zag, Hilbert, Peano, Spiral, and Trochoidal. In Zig-Zag and Spiral toolpaths, unidirectional crests are produced as tools pass over the surface; this undesired orientation generates a non-uniform finished surface. The Fractal curves such as Hilbert and Peano consisted of significantly high numbers of sharp turns, making them unsuitable for the process. The Trochoidal toolpath, which is conventionally used for high-speed milling operation, is the most suitable for the H-ECMR finishing process. The investigation shows that the Trochoidal toolpath can enhance a duplex stainless steel plate's surface roughness (R_a) from 379 nm to 1.06 nm. For the studied Trochoidal toolpath, the *Carbonyl Iron Particles* (*CIPs*) chain deflection is less compared to Zig-Zag toolpath which increases the effective force acting on the workpiece, thereby reducing the polishing time. The key finding of the research is mentioned below. Furthermore, the increase in stepover and radius of the Trochoidal curve increases the uncovered area; also, an increase in feed rate lowers the interaction time between the CIPs chain and workpiece, which leads to a decrease in average surface roughness. *Skewness* (R_{sk}) is negative, and *Kurtosis* (R_{ku}) is less than three during the Trochoidal toolpath indicating the number of valleys is higher than the peaks, and the peaks are flat.

Chapter 4 Post-processing of Additively Manufactured Implants

4.1 Introduction

Additive Manufacturing (*AM*) provides ample advantages compared with the conventional manufacturing process, including fabricating complex structures with minimal material waste [174][175]. In the biomaterial field, AM can produce implants per patient standards with improved functionality [176]. However, apart from its several advantages, the surface quality of additively manufactured biomaterial is rough. However, poor surface quality can result in inaccurate or inconsistent measurements, leading to errors in the fit and function of the implant and providing a favorable environment for bacterial growth and colonization, increasing the risk of infection [177], [178]. A rough surface on an implant can cause inflammation and irritation in the surrounding tissue, leading to complications such as implant rejection or failure. Furthermore, poor surface quality can result in increased wear and tear of the implant, leading to a shorter lifespan and the need for replacement surgery. Hence an appropriate surface finishing operation is required to reduce the surface roughness of the additively manufactured biomaterial to provide a uniform surface quality on the polished surface. The present chapter aims to improve the surface quality of the bone plate and femoral head fabricated through powder bed fusion as shown in Fig. 4.1.

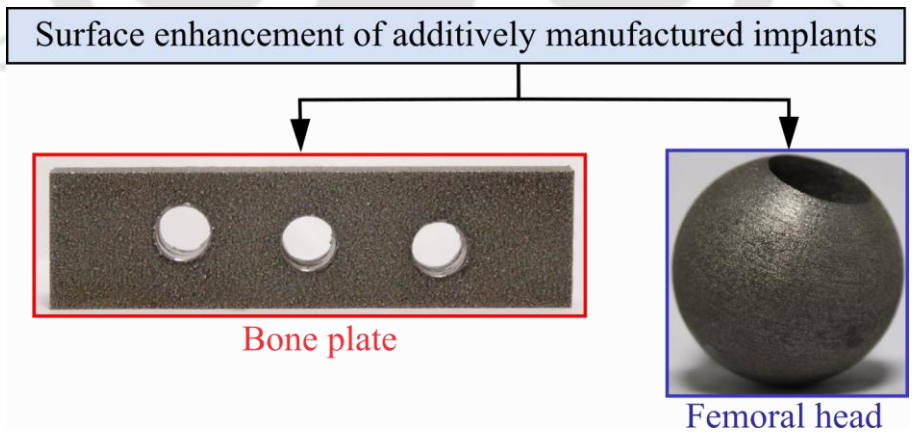

Fig. 4.1 Case study on surface enhancement of bone plate and femoral head fabricated through powder bed fusion

The femoral head is a critical component in *Total Hip Arthroplasty* (*THA*), a surgical procedure to replace a damaged or diseased hip joint with an artificial implant. The femoral head is an essential part of the hip implant system and serves several crucial functions. It forms

the ball-shaped portion of the hip joint. It articulates with the acetabular cup, which is the socket-shaped component of the hip implant. This articulation allows for smooth and frictionless hip joint movement, enabling patients to regain mobility and perform daily activities with reduced pain and improved function. Furthermore, it bears a significant portion of the body's weight, transmitting forces from the femur to the hip joint. When properly implanted, the femoral head distributes the load evenly across the acetabular cup, ensuring optimal load transmission and minimizing stress on the surrounding bone and tissues. This load distribution is crucial to prevent bone resorption and ensure the implant's long-term stability. Furthermore, the bone plate, used to support broken bones during healing, is the specific type of implant being studied in this research. Bone plates are medical devices used in orthopedic surgery to stabilize and support fractured bones during healing. It is essential in treating complex fractures, non-unions, and malunions, where traditional immobilization methods, like casts, may not provide sufficient stability for proper bone healing. Bone plates are used to hold fractured bone segments together, providing stable support and immobilization to allow the bone to heal correctly. The plates are attached to the bone using screws, which anchor the plate securely to the bone fragments. Moreover, it is beneficial in fractures of weight-bearing bones like the femur, tibia, and humerus. They help to restore and maintain the bone's mechanical integrity, allowing patients to bear weight and start early rehabilitation exercises. It also provides internal fixation, meaning they are placed directly on the bone surface and remain inside the body after healing. This reduces the risk of external infections and allows patients to begin early mobility and rehabilitation. However, *Laser Pwder Bed Fusion* (*LPBF*) or *Selective Laser Melting* (*SLM*) is a 3D printing technique that builds the final product layer by layer, but the surface quality of the bone plate produced by this method is inadequate and requires post-processing to improve it.

Laser Pwder Bed Fusion (*LPBF*) or *Selective Laser Melting* (*SLM*) is a 3D printing process capable of fabricating a wide range of materials: steels, Ti alloys, and Ni-based superalloys with a layer thickness between 20-50 µm. Compared to the other metal-based AM, the lower order of the layer thickness during the SLM process provides an advantage of fabricating near net shape with near full density [179]. Herein, the CAD model of the parts to be produced is initially sliced, and the contour of each slice is mapped through a laser source on the powder bed. The heat from the laser source helps to melt and fuse the powder particles, and the final product is fabricated by repeating the same for each layer, as shown in Fig. 4.2 [180]. The powder size used during the SLM process varies from 15-63 µm [181][182]. However, the various defects produced on the surface increase the fabricated part's surface

roughness value, which is still a significant challenge during SLM. The defects produced on the surface are because of the loosely bonded powders, partially melted powders, balling melts, semi-welds, staircase effects, etc. Loosely bonded powders are produced because of the adhesion of the raw particle on the surface. In contrast, partially melted powders are made under the influence of heat diffused from a molten pool [3] [4]. Moreover, the balling melts are caused by the wetting problem of liquid metal and solid surface, and the staircase effect is caused by the layer's high thickness of the deposited material [7] [6]. Furthermore, insufficient melting of metal powder produces a semi-weld defect [6]. However, different post-processing methods have been proposed in recent years to eliminate the surface defects of the SLM fabricated parts and further improve their surface quality.

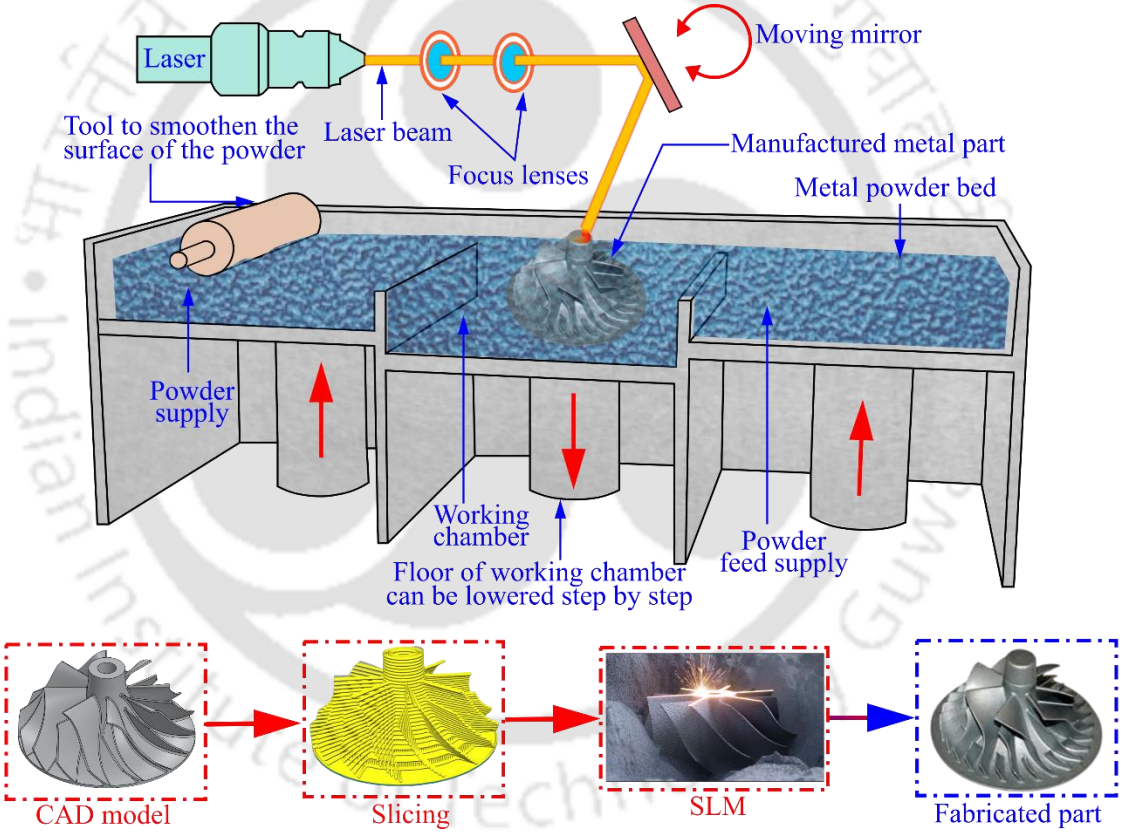

Fig. 4.2 Schematic diagram explaining working principle of selective laser melting (SLM)

Laser Polishing utilizes heat to remelt and reflow the surface irregularities to enhance the surface quality of SLM fabricated parts [183]. Marimuthu et al. [184] performed the laser polishing on Ti-6Al-4V, reducing the R_a value from 10.2 µm to 2.4 µm. It was also concluded that the minimum melt pool velocity achieves a wider laser track and enhanced surface quality. Similarly, Bhaduri et al. [185] conducted experiments to improve the surface quality of the aluminum parts fabricated from SLM. A thermal insulating alumina ceramic plate is used

beneath the workpiece to enhance the remelting. An 88% reduction in R_a is achieved on the parts. However, the residual stress generation during surface finishing is a significant challenge. Moreover, chemical etching is used as the post-processing technology to improve the surface quality of the SLM fabricated parts. Herein, the chemical reaction with the etchant and the surface irregularities assists in enhancing the parts' surface quality [186]. Farber et al. [187] use a combination of different etchants, namely, NH_4OH/H_2O, H_2SO_4/H_2O_2, and H_2SO_4/HCl, during the chemical etching of the Ti alloy. They have observed that the NH_4OH/H_2O produces promising results compared to the other combinations of etchants. Surmeneva et al. [188] carried out chemical etching on the scaffolds made of Ti alloy. HF/HNO_3-based chemical etchant is used with multiple immersions of the polishing tool in the etchant during the chemical etching and observed that more immersion stages are required to remove entrapped powders from the fabricated parts. The present chapter details the surface enhancement of the Ti-6Al-4V femoral head and bone plate fabricated through powder bed fusion. Moreover, the *average surface roughness* (R_a) is a metric that quantifies the mean deviation of the peaks and valleys on a surface from the central line. Yet, it fails to encapsulate the topographical characteristics of peaks and valleys. To supplement this limitation, statistical measures such as *skewness* (R_{sk}) and *kurtosis* (R_{ku}) are employed to characterize the asymmetry and peaks flatness of the surface profile, respectively. However, to gain a more holistic understanding of the distribution of the surface material, the Abbott-Firestone curve, or material ratio curve, is utilized. This curve is separated through three distinct regions, namely *valley area* (S_{vk}), hill (S_{pk}), and *core* (S_k). It provides insight into the relative availability of the material in each of these regions. It also enables the analysis of the wear rate of biomaterials in tribological interactions by providing a comprehensive view of the surface irregularities. Moreover, the biocompatibility of biomedical implants is examined through the wettability, wear, and corrosion test before and after post-processing. Furthermore, laser scanning is performed to study the dimensional accuracy of the femoral achieved during the H-ECMR finishing process.

4.1.1 Post-processing of femoral head

The *Hybrid-Electrochemical Magnetorheological* (*H-ECMR*) polishing process reduces the surface irregularities of the biomedical implants manufactured using additive techniques, such as *Selective Laser Melting* (*SLM*). This process combines an electrochemical reaction with mechanical abrasion to produce a uniform R_a in the order of a few nanometers. The H-ECMR finishing process utilizes the unique properties of the *Magnetorheological* (*MR*) fluid to

improve the surface irregularities of the workpiece surface without altering its topographical characteristics [94][189].

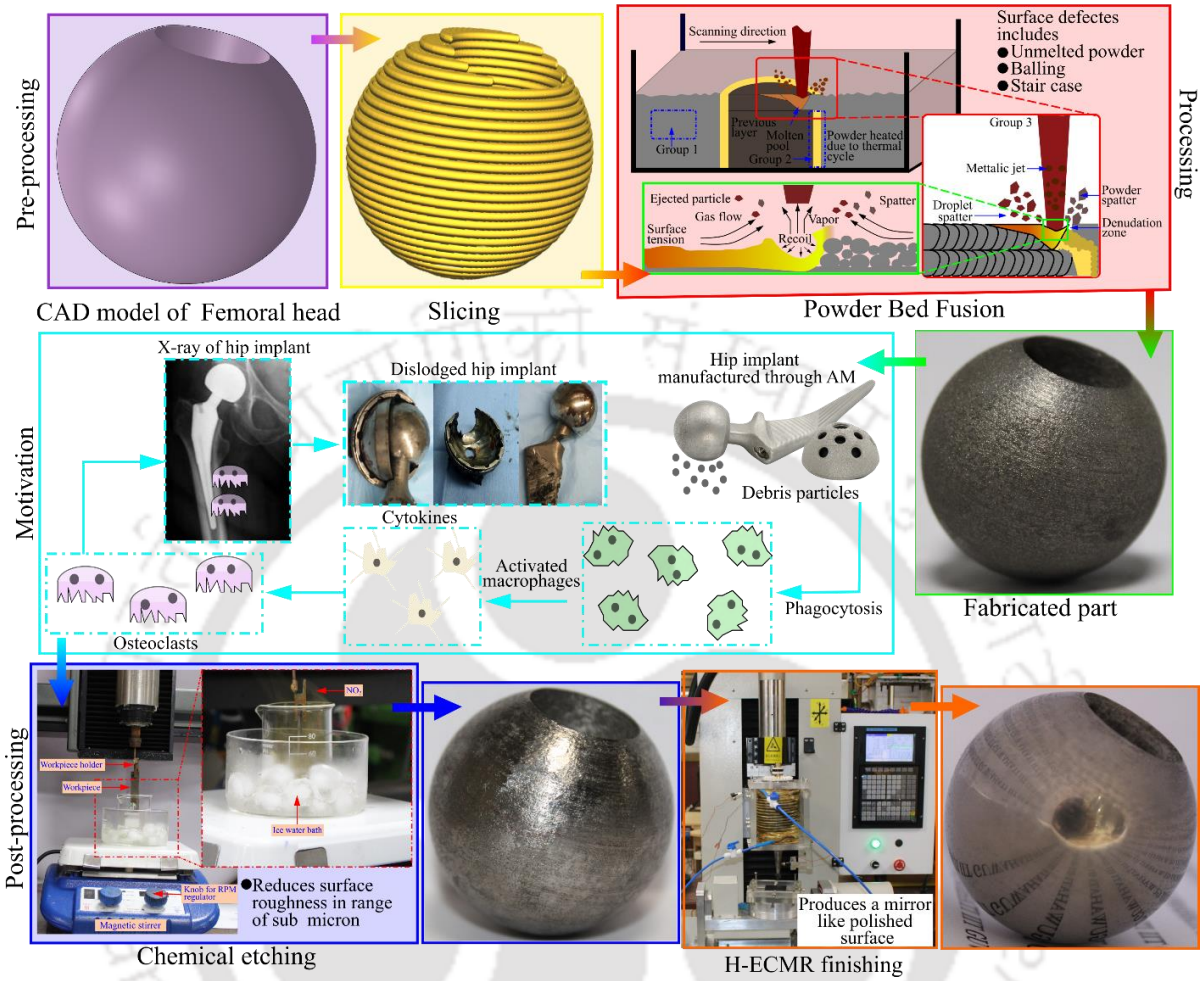

Fig. 4.3 Flowchart of present work, including pre-processing, motivation, and post-processing of the femoral head surface

The surface defects produce irregularities on the surface of the LPBF fabricated biomaterials, necessitating post-processing to enhance their surface quality functionality. *Hybrid-Electrochemical Magnetorheological* (*H-ECMR*) finishing process is an advanced surface finishing method that produces a mirror liked polished surface with high dimensional accuracy. However, the initial surface roughness must be in the sub-micron range to implement the H-ECMR finishing process. Hence an intermediate surface finishing process is required surface roughness reduction of the additively manufactured product in the sub-micron range. Based on the various literature surveys, chemical etching is the best-suited polishing operation for Ti alloys. The working principle of the H-ECMR finishing and chemical etching is elaborated in the subsequent sections. The present work is broadly classified into three categories, i.e., fabrication of product through the LPBF, chemical etching followed by H-

ECMR finishing process to reduce the surface roughness in the range of nanometers, as illustrated in Fig. 4.3. Moreover, an optical profilometer, *Scanning Electron Microscope* (*SEM*), and *Atomic Force Microscope* (*AFM*) is used to examine the impact of the post-processing on the surface of the additively manufactured femoral head made of Ti-6Al-4V. Furthermore, the biocompatibility of biomedical implants is reviewed through the wettability, wear, and corrosion test before and after post-processing. Laser scanning is also performed to study the dimensional accuracy of the femoral head achieved during the H-ECMR finishing process.

4.1.1.1 Methodology

The metal-on-metal bearing couple in *Total Hip Arthroplasty* (*THA*) glides smoothly during physical activity of the human body, with reduced wear rate compared with metal on polyethylene. However, the poor surface quality of the femoral head of THA fabricated through the LPBF surface leads to an increase in its wear rate on their tribological interaction, which is a function of *average surface roughness* (R_a) as represented in Eq. (4.1) [2].

$$k = a(R_a)^b \tag{4.1}$$

Where material-dependent constants are denoted by a and b that can be evaluated experimentally. The increased wear rate of the femoral head produces a higher number of debris particles, each having size of nanometres. The interaction of debris particles (or foreign particles) with the human body leads to phagocytosis, a cellular process for removing these foreign particles from the human body having sizes larger than 0.5 µm [10]. The phagocytosis-activated macrophages lead to the generation of the cell responsible for the destruction of foreign particles. Furthermore, the potential cells release small proteins, namely cytokines, to maintain the activity of the immune system, further accountable for the generation of the osteoclasts, multinucleated giant cells which absorb foreign particles [11]. The generation of osteoclasts in higher numbers starts to absorb the different components of the THA, leading to its dislodge, as shown in Fig. 4.3. Moreover, the debris particles are spread inside the human body through blood circulation, responsible for the systematic toxicity of various organs, including kidneys, eyes, levers, etc. [12]. Furthermore, these small metal particles cause Aseptic loosening or *Adverse Reactions to Metal Debris* (*ARMD*), which may instigate *Aseptic Lymphocytic Vasculitis and Associated Lesions* (*ALVAL*) or Pseudotumours, inflammatory masses, and metal hypersensitivity [13]. During the LPBF, Ti-6Al-4V powder particles of 15–

45 µm size are used to fabricate the femoral head. A fiber laser of wavelength 1070 nm with a power of 400 W is used to melt the powder particles. The maximum exposure time of around 1 µs is fixed with a focal point diameter and feed rate of 70 µm and 5 m/s, respectively. The H-ECMR finishing process follows chemical etching to enhance the surface quality and biocompatibility of the femoral head.

4.1.1.2 Chemical etching

Hybrid-Electrochemical Magnetorheological (*H-ECMR*) finishing uses the synergic action of the electrochemical reaction and mechanical abrasion to produce a mirror liked polished surface on the workpiece. Herein, *Carbonyl Iron Particles* (*CIPs*) grasped in-between abrasive particles are used as an unbonded form of the polishing tool and performed efficiently on the workpiece having initial surface roughness in the range of sub-micron range [190]. However, the surface roughness of the LPBF fabricated femoral head lies between 6-40 µm, necessitating an intermediate process to reduce its surface roughness in the sub-micron range. Chemical etching, a surface finishing operation, is used to accomplish the above-mentioned challenges. Henein, fabricated parts are dipped in a chemical solution to initiate chemical reactions. The constituents and compositions of chemical solutions primarily depend on the material of the manufactured parts and the value of the final surface roughness required to achieve. Chemical etching provides precise, uniform parts independent of the complexities of workpiece geometrics. Furthermore, the finishing rate of chemical etching is higher than the other finishing processes, namely, laser polishing, abrasive flow finishing, electron beam irradiation, etc. It reduces surface roughness at different workpiece features (holes, ducts, etc.) unattainable through other finishing processes. Lee et al. [191] perform the surface finishing operation on the Ti-6Al-4V fabricated through LPBF, and a maximum reduction of 57.8% in R_a is achieved on the polished surface of the workpiece through laser polishing. Similarly, Ma et al. [192] compared the impact of laser polishing on the two different grades of Ti alloy, namely, TC11 and Ti-6Al-4V, fabricated through the LPBF, and the value of R_a is reduced to 0.375 µm from 5.226 µm for Ti-6Al-4V. Similarly, for TC11, the value of R_a is reduced from 7.21 µm to 0.73 µm. However, including residual stress during laser polishing reduces the fatigue strength of the fabricated parts. Furthermore, the small spot diameter of the laser polishing tool increases the polishing time for a complex structure. Urlea and Brailovski [193] performed the post-processing on the Ti-6Al-4V fabricated at different orientations ranging from 0^o to 135^o with powder bed assistance and further post-processed the workpiece through the electropolishing

to improve the surface quality of the manufactured part. For all differently oriented workpieces, uniform surface roughness in the 1-3 µm range is achieved on the polished surface.

Tsoeunyane et al. [194] performed the electropolishing, and a five times reduction in the waviness was detected on the polished surface compared with the initial fabricated surface. However, the adverse effect of the electrolyte during electropolishing is a significant challenge. Moreover, chemical etching utilizes the chemical reaction between an acidic solution and Ti-6Al-4V to reduce the surface roughness of the LPBF fabricated part. A solution of *Hydrofluoric acid* (*HF*) and *Nitric acid* (HNO_3) in an appropriate ratio is used during chemical etching to enhance the surface quality of the femoral head fabricated through the LPBF. In the present work, an apparatus is developed to enable the chemical etching process to reduce the surface roughness of the LPBF-manufactured femoral head in the sub-micron range. Herein the femoral head is attached to the spindle of the 3-axis *Computer Numerical Control* (*CNC*) machine with the assistance of the workpiece fixture. The femoral head having a hole to place the femoral stem during the *Total Hip Arthroplasty* (*THA*), is used to fix one end of the workpiece fixture. The other end of the workpiece is attached to the 3-axis CNC spindle. The acid-based chemical solution is placed in the beaker, at the top of the magnetic stirrer, and over the CNC machine's bed. *HF* is utilized to remove material of Ti-6Al-4V during chemical etching, whereas HNO_3 is used to absorb Hydrogen gas produced during the interaction of *HF* with Ti-6Al-4V. The hydrogen gas makes pits on the polished surface of the workpiece; hence, the HNO_3 is used to minimize its effect. Moreover, the passive oxide layer (TiO_2) on the Ti alloy surface reacts with *HF* and produces hexafluoride titanate, as shown in Eqs. (4.2) and (4.3) [195].

$$TiO_2 + 6HF = [TiF_6]^{2-} + 2H^+ + 2H_2O \tag{4.2}$$

$$2Ti + 6HF = 2Ti^{3+} + 2H_2(g) + 6F^- \tag{4.3}$$

Ti^{3+} produced during the 2nd reaction further oxidized and formed TiF_6^{2-} while interacting with F^-. As discussed earlier, the hydrogen gas produced during the reaction is further developed into *Dihydrogen monoxide* (H_2O) and *Nitric oxide* (*NO*) while reacting with HNO_3, as shown in Eq. (4.4) [196].

$$2H_2(g) + 2HNO_3 = 4H_2O + 2NO \tag{4.4}$$

The combined action of *HF* and HNO_3 on *Ti* is shown in Eq (4.5).

$$Ti + 6HF + 2HNO_3 = [TiF_6]^{2-} + 2H^+ + 2H_2O + 2HNO_2 \quad (4.5)$$

Nitrous acid produced during the reaction mentioned above is unstable; however, experimentally, it has been observed that the NO_2 brown-colored gas is evaluated through the chemical etching of the Ti-6Al-4V. The reaction during the chemical etching is shown in Eq. (4.6) [197].

$$Ti + 6HF + 2HNO_3 = [TiF_6]^{2-} + NO_2 + NO + 3H_2O + 2HNO_2 \quad (4.6)$$

Maintaining a mole ratio of 6:1 between the HF and Ti-6Al-4V is required to restrict the further dissolution caused by HF to produce an irregular surface over the polished surface. However, the inclusion of *Aluminium* (*Al*) and *Vanadium* (*V*) in the Ti alloy leads to a slight increase in HF's mole fraction; however, if insufficient mole fraction of the HF in the chemical solution causes passivation of the Ti-6Al-4V surface as per the reaction shown in Eq. (4.7) [198]. The interaction of different constituents with a chemical solution is illustrated in Fig. 4.4

$$Ti^{3+} + 2HNO_3 + 3H_2O = TiO_2 + 6H^+ + HNO_2 \quad (4.7)$$

The combination of chemical solutions for surface enhancement Ti-6Al-4V is not explored extensively in research. Pyka et al. [199] experimentally improved the surface quality of the open porous Ti-6Al-4V structures through chemical etching. The combination of hydrofluoric acid with water is used as the chemical solution. However, the study does not discuss the mechanism involved in dissipating the hydrogen gas impact during the process. Wysoci et al. [200] used different hydrofluoric and nitric acid combinations to enhance the titanium scaffolds' surface quality. They observed that uniform surface quality is achieved when the chemical solution contains 2.2% hydrofluoric acid and 20% nitric acid by volume. Similarly, Balyakin et al. [201] performed experiments to reduce the surface roughness of the Ti-6Al-4V and reported that 10% of hydrofluoric acid and 10% nitric acid by volume produced a maximum reduction in surface roughness. In the present work, preliminary experiments are performed to evaluate the best combination of hydrofluoric acid and nitric acid in the chemical solution over the flat workpiece as shown in Fig. 4.4. Moreover, the interaction of the Ti-6Al-4V with the chemical solution produces the hydrogen gas (Fig. 4.4) on the workpiece's surface

responsible for the pits' generation on the polished surface. Hence, magnetic stirrer is used to removes the hydrogen gas from the workpiece surface. The magnetic needle is place in the solution and rotates at specified speed to remove the settling of hydrogen gas on the workpiece surface. Moreover, the chemical reaction is exothermic, hence frozen water is placed at the outside chamber of the beaker to reduce the increased temperature during the chemical etching.

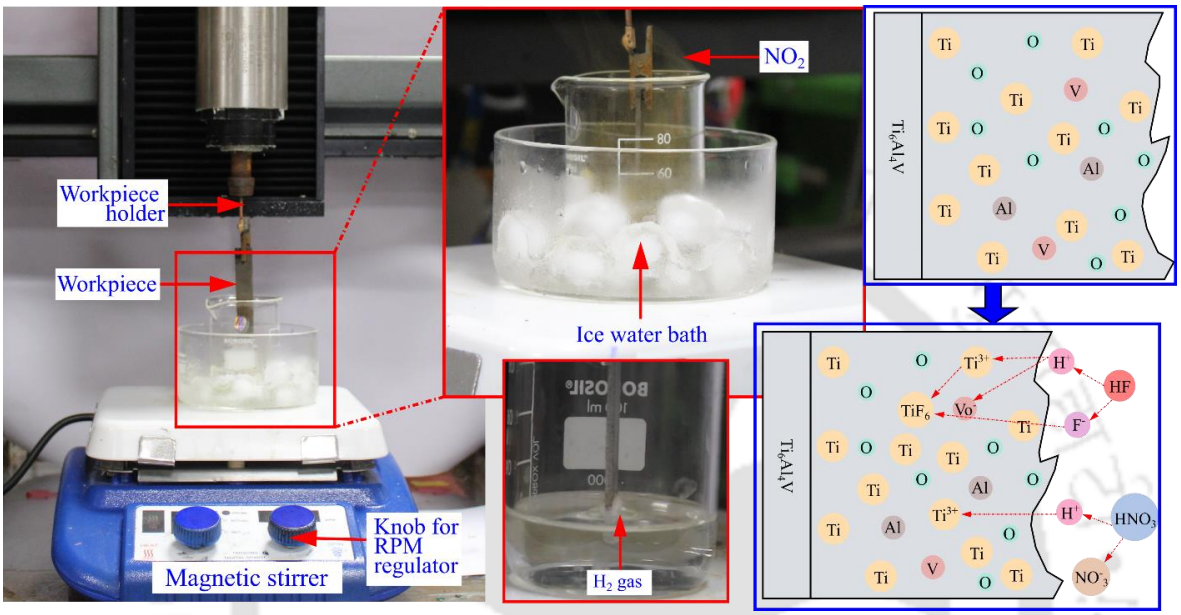

Fig. 4.4 Experimental setup and chemical reactions at Ti-6Al-4V surface during chemical etching

4.1.1.3 Hybrid-electrochemical magnetorheological finishing

Chemical etching assists in reducing the surface roughness of the specimen in the sub-micron range; however, further improvement in the surface roughness is unattainable by the process as the increased chemical rate between the solution and the workpiece leads to produce pits on the polished surface. Hence, chemical etching follows the H-ECMR finishing process for further reduction in average surface roughness of LPBF fabricated femoral head to improve its biocompatibility. The synergic action of the mechanical abrasion and electrochemical reaction during H-ECMRF generates a uniform surface roughness on the femoral head in the range of a few nanometers. Herein, the abrasive embedded *Magnetorheological* (*MR*) fluid in the impact of the external magnetic flux acts as a polishing media to facilitate mechanical abrasion on the femoral head surface [202]. The MR fluid comprises the carrier medium, abrasive, ferromagnetic particles, and stabilizer. Furthermore, the workpiece fixture is fabricated with the *Stereolithographic Apparatus* (*SLA*) to hold the femoral on the bed of the 5-axis CNC, as

illustrated in Fig. 4.5(a). The relative motion of MR fluid with the femoral head generates the required forces to improve the surface quality, as shown in Fig. 4.5(b).

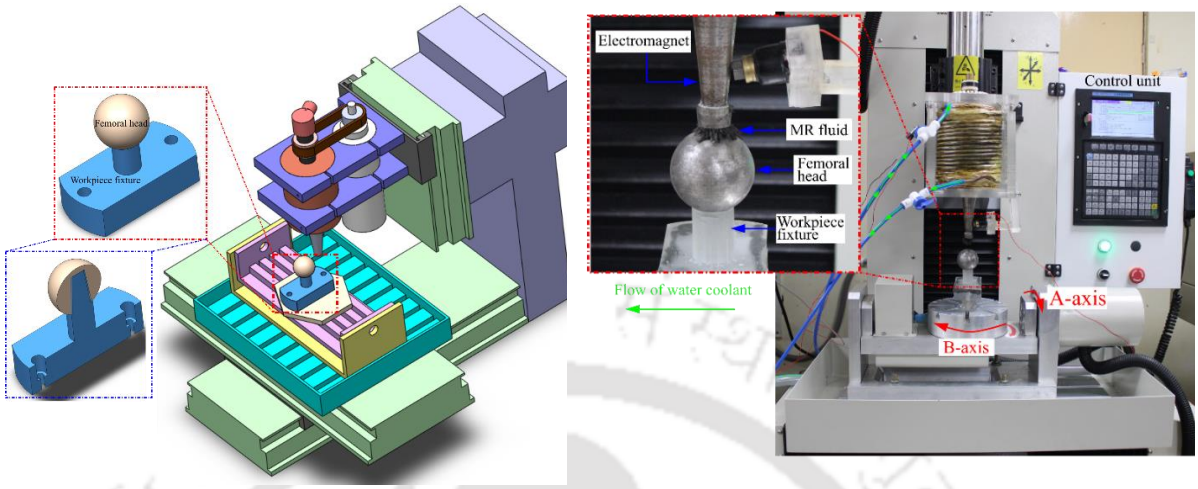

(a) (b)

Fig. 4.5 (a) CAD model and (b) experimental setup for H-ECMR finishing process of femoral head

An electromagnet-based Magnetorheological finishing is used during surface finishing operation on the Ti-6Al-4V. The non-varying magnetic field generated with the assistance of the electromagnet magnet affects process efficiency during the surface finishing process. In situ variation in the rheological properties of MR fluid, as required in different biomedical implants, is unattainable with a permanent magnet-based magnetorheological finishing process. The pure iron core of the electromagnetic coil provides a concentrated magnetic field at the polishing zone. Furthermore, the cooling coils are wrapped over the electromagnet, and coolant is circulated through these coils to reduce resistive heating. Four mounting plates provide housing for the electromagnet and ensure its fixed position. Provision for threaded joints in each mounting plate can be used to lock their respective positions once adjusted. This electromagnet-based polishing tool setup is retrofitted over a 5-axis *Computer Numerical Control* (*CNC*) milling machine to provide an appropriate *Degree of Freedom* (*DOF*) required between the polishing tool and the workpiece. The potential difference is applied between the polishing tool and workpiece; a carbon brush is connected to the electromagnet's core for the desired purpose. The different process parameters and composition of MR fluid during the polishing are listed in Table 4.1 during the H-ECMR finishing process of the femoral head.

Table 4.1 MR fluid compositions and process parameters values during H-ECMR finishing

Constituents / Parameters	Composition (% by Vol.) / Magnitude
Carbonyl Iron Particles (CIPs)	40 %
Diamond	7%
Magnesium chloride	16.35%
Ethylene glycol	6.15%
Distilled water	22.5%
Glycerol	8 %
Feed rate	1 mm/min
Polishing tool's rotational speed	800 rpm
Standoff distance	1 mm
Applied current	2 Amp

4.1.1.4 Results and discussion

The present work is broadly classified into three categories, i.e., product fabrication through the laser powder bed fusion process, chemical etching, and H-ECMR finishing process to enhance the biocompatibility and surface quality of the femoral head. The subsequent section discusses the surface quality and biocompatibility achieved on the femoral head surface after the post-processing.

Surface quality

Chemical etching is performed on the surface of the LPBF fabricated femoral head to reduce its surface roughness in the range of the sub-micron. However, preliminary experiments were performed on the LPBF-manufactured Ti-6Al-4V flat workpiece to determine the optimum process parameters. Workpieces are cleaned with ethanol before the chemical etching to remove the impact of any foreign material during the chemical reaction. The concentration of nitric acid is kept fixed at 3.17 M as per the literature survey, and the HF's concentration varies from 1 to 4 M [203] to determine the best-suited molar concentration combination of solutions during chemical etching. The chemical solutions are placed in the glass beaker, as discussed earlier. The magnetic needle of the magnetic stirrer is rotated at the speed of 400 rpm. Experiments are performed for 30 min, and the surface roughness of the workpiece is measured every 5 min during the chemical etching. The experiments are conducted three times to reduce the noise associated with the results. Ice cubes are placed in the external chamber to provide the ice bath during the chemical etching to reduce the temperature raised during exothermic chemical reactions.

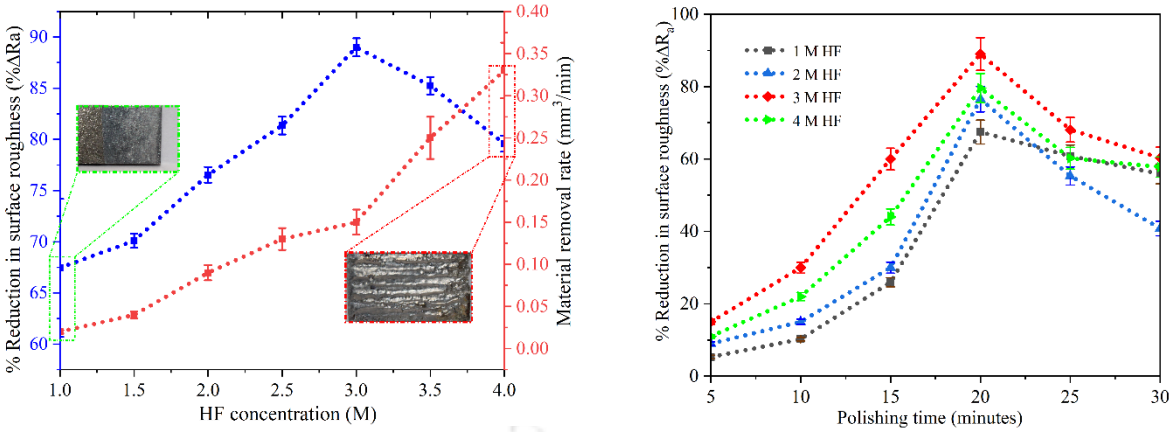

(a) (b)

Fig. 4.6 Impact of (a) HF concentration and (b) polishing time during chemical etching

The mean and standard deviation of the material removal rate (*MRR*) and % reduction in R_a with respect to the concentration of HF for the LPBF fabricated workpiece is illustrated in Fig. 4.6(a). Within the range investigated, *MRR* and % reduction in surface roughness increased with increasing molar concentration of HF in the solution. The increase in MRR after HF concentration reaches the value of 3 moles is more pronounced, and representative control of chemical etching becomes difficult at higher concentrations of the HF. On the contrary, the % reduction in surface roughness decrease with an increase in the concentration of HF after 3.0 M. The maximum reduction in R_a, i.e., 93.25%, is achieved at 3.0 M of HF. Furthermore, the maximum MRR of 0.34 mm^3/min is reached at 4 M of HF in a chemical solution. However, the number of pits on the polished surface increases at 4 M of HF, leading to the deterioration of the polished surface. A decreased value of 77.26% reduction in average surface roughness is observed at the same concentration of HF.

Moreover, the impact of etching time on the % reduction in surface roughness is also studied and shown in Fig. 4.6(b). During the study, concentrations of the HNO_3 were kept fixed at 3.17 moles, and the HF concentration varied from 1 mole to 4 moles. Furthermore, with increased etching time, the % reduction in surface roughness increases to 3.0 M; afterward, it starts to decrease. The maximum reduction in R_a, 92.76%, is observed for 3.0 M of HF compared to the other chemical solution. Moreover, an increase in the polishing time leads to a decrease in the irregularities on the workpiece surface initially; However, after an optimum polishing time (i.e., 20 min), the rate of reaction increases and starts to produce pits, the phenomenon decreases the value of the reduction in average surface roughness, i.e., 63.27%. Moreover, an increasing number of HF moles increases the evolution of gases responsible for the generation of pits. Moreover, the lower chemical reaction rate at values of molar concentration less than 3.0 M is responsible for the decreased value of percentage reduction in

average surface roughness. However, the further increase in molar concentration (> 3.0 M) of HF in the chemical solution increases the reaction rate vigorously, responsible for deteriorating the surface quality. Hence, the concentration of HF opted as 3 M with 20 min of polishing time during the flat workpiece's chemical etching, and the final surface roughness (R_a) value is reduced to 0.94 µm from its initial value of 14.89 µm. A significant reduction in the undulation on the workpiece surface is observed and illustrated in Fig. 6. Hence, the same combination of process parameters is used to enhance the femoral head surface quality manufactured through the LPBF.

The final surface roughness (R_a) is reduced to 0.98 µm from its initial value of 14.67 µm on the surface of the femoral head after the chemical etching. The comparison between the 1D and 2D surface roughness before and after chemical etching is illustrated in Fig. 4.7.

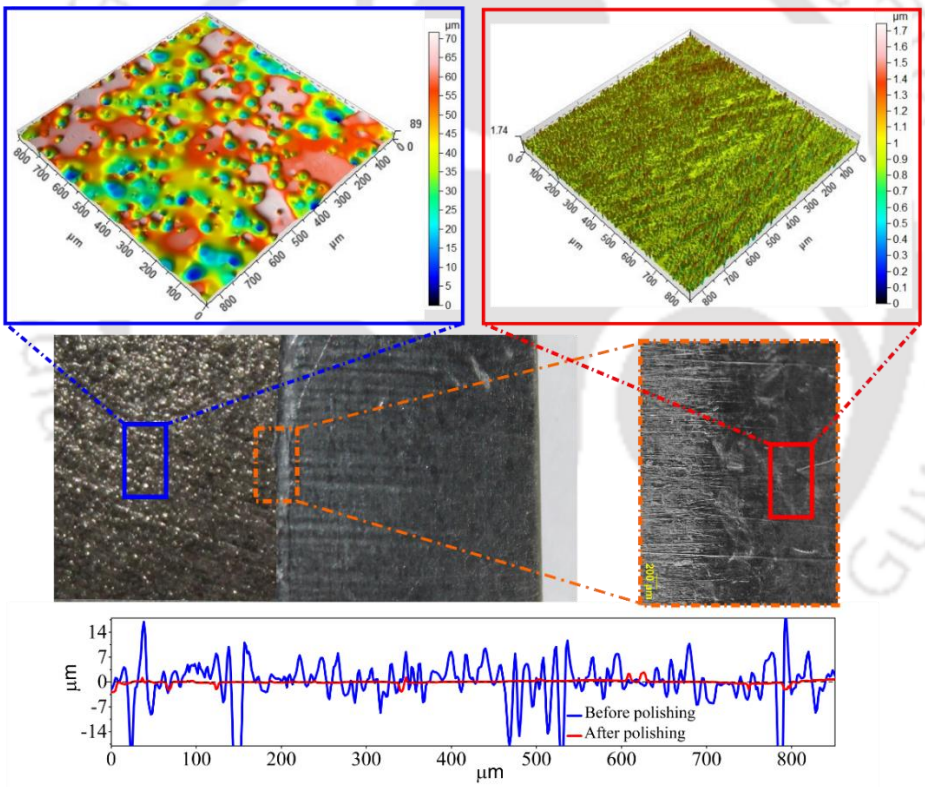

Fig. 4.7 1D and 2D surface profile before and after chemical etching

The surface defects produced during the fabrication of the femoral head, including loosely bonded powders, partially melted powders, balling melts, etc., are removed after the chemical etching as observed through the *Scanning Electron Microscope* (*SEM*) as shown in Fig. 4.7. Moreover, *Atomic Force Microscope* (*AFM*) shows that a significant reduction in surface undulation is achieved through the chemical etching on the femoral head surface.

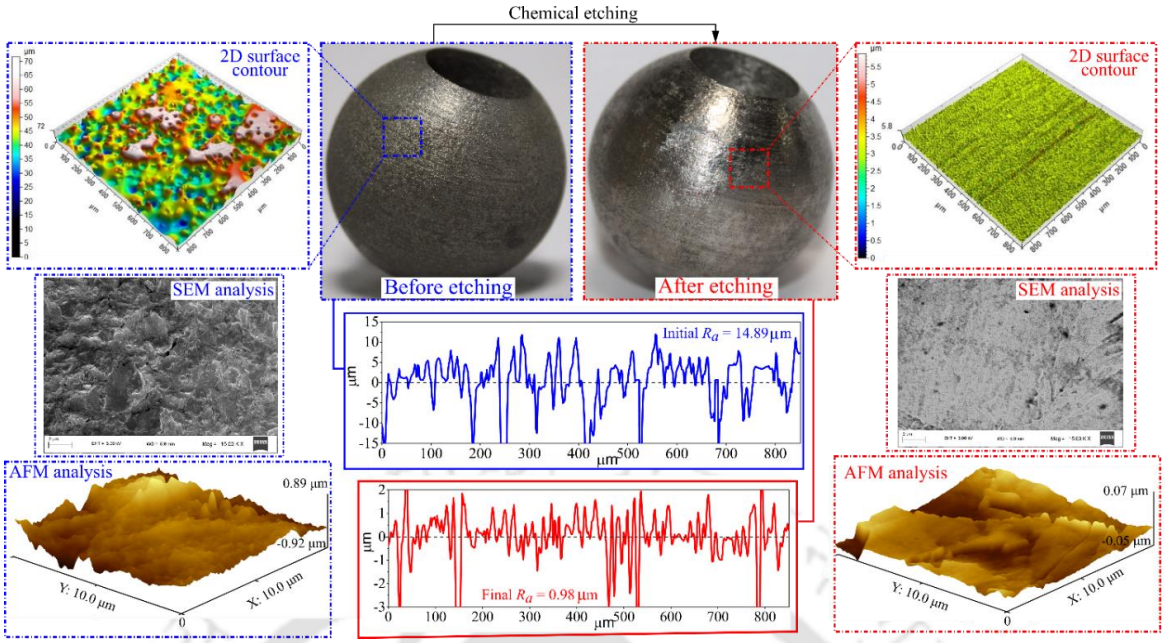

Fig. 4.8 1D and 2D surface roughness profiles, atomic force microscopic, scanning electron microscopic images of femoral head surface before and after chemical etching

The H-ECMR finishing process reduces the surface roughness of the chemically etched femoral head surface in the range of nanometers. As discussed earlier, the 5-axis CNC milling is retrofitted with the H-ECMR finishing tool to increase the degree of freedom during the finishing operation. The chemical composition of the MR fluid and the process parameters combination during the H-ECMR finishing process of the femoral head are listed in Table 2. It is observed that the R_a of the femoral head was reduced to 33.14 nm from 0.98 µm. The comparison between the 1D and 2D surface roughness profiles is shown in Fig. 4.8. Initially, few pits were produced on the chemically etched surface of the femoral head, as observed through the SEM; however, after the H-ECMR finishing process, uniform surface quality is observed on the femoral head surface, as shown in Fig. 4.9. Moreover, AFM analysis shows a smooth and uniform surface after the polishing.

The kurtosis (R_{ku}) and skewness (R_{sk}) analysis is also studied before and after post-processing on the biomaterial surfaces. Initially, a kurtosis value higher than three (i.e., R_{ku} = 4.01) is obtained on the LPBF fabricated femoral head, representing the pointed peaks produced over surface irregularities, as shown in Fig. 4.10. Moreover, the positive value of the skewness (i.e., R_{sk} = 0.96) is built on the surface, denoting that the quantity of peaks is higher than valleys. However, after chemical etching on LPBF fabricated part, the kurtosis value is reduced below three (i.e., R_{ku} = 2.31), denoting that flat peaks are generated on the workpiece surface irregularities. However, the positive value of skewness (i.e., R_{sk} = 0.76) signifies that the quantity of peaks is still greater than valleys. Moreover, after the H-ECMR finishing, the

kurtosis value reduces further to 0.54, indicating flat peaks produced on surface irregularities. Similarly, the negative skewness (i.e., R_{sk} = -0.19) represents that the quantity of peaks is reduced below valleys after H-ECMR finishing on LPBF fabricated biomaterial.

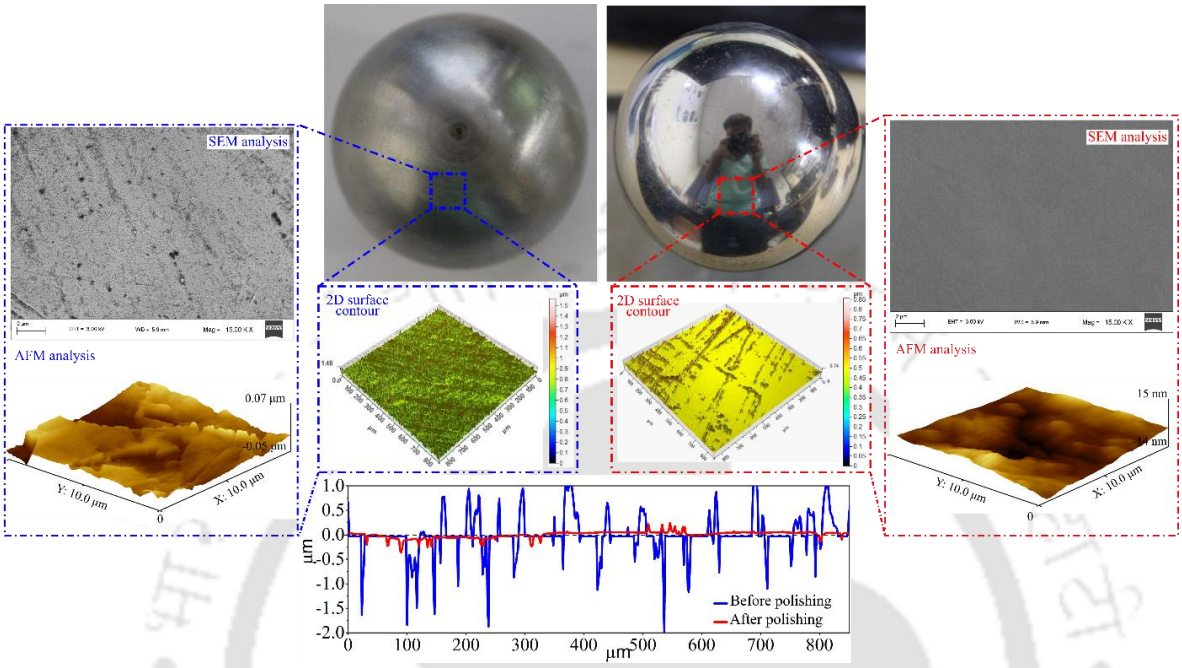

Fig. 4.9 1D and 2D surface roughness profiles, atomic force microscopic, scanning electron microscopic images of femoral head surface before and after H-ECMR finishing

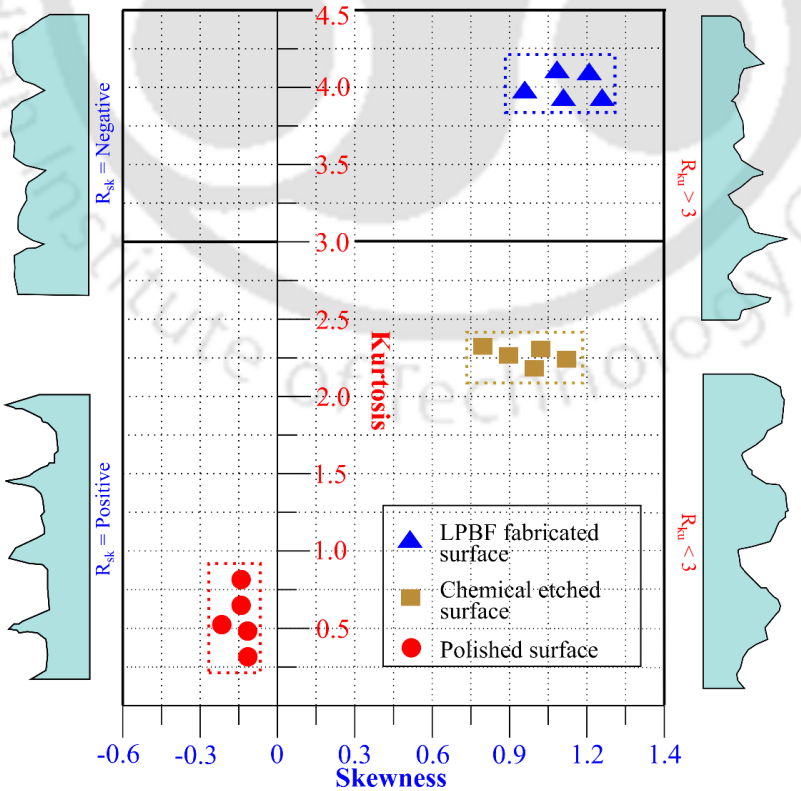

Fig. 4.10 Kurtosis Vs. skewness plot for LPBF fabricated, chemically etched, and H-ECMR finished surfaces

The variation in the femoral head surface topography before and after the H-ECMR finishing process is analyzed to validate the polishing process capabilities. The H-ECMR finishing process utilizes the MR fluid's rheological properties during the workpiece's surface enhancement. The constituent of MR fluid was discussed earlier, comprised of distilled water. The mechanical abrasion of the bonded abrasive particle with the workpiece surface generates the friction force, which further converts into heat energy. The conventional polishing methods, like grinding, lapping, etc., change the topography of the polished surface due to the inclusion of a head during the polishing operation. However, in the case of the H-ECMR finishing process, the carrier fluid (i.e., distilled water) dissipates the heat generated during the mechanical abrasion, eliminating the chance of variation in the surface topography of the workpiece surface. The infrared-based thermal camera is used to analyze temperature distribution during the H-ECMR finishing process, as illustrated in Fig. 4.11(a). The temperature variation along the green line from point A to B is shown in Fig. 4.11(b). The maximum temperature of 35^{o}C is observed at the point of interaction of the MR fluid and the workpiece. Furthermore, laser scanning of the femoral head is used before and after the H-ECMR finishing process to determine the change in its surface topography, as illustrated in Figs. 4.11(c) and (d). The same contour of the femoral head is achieved with a reduction of 280 µm in its maximum height. The reduction is observed due to material removal during the H-ECMR finishing process. Hence, the H-ECMR finishing process reduces the R_a of the femoral head in the range of a few nanometers without altering its surface topography.

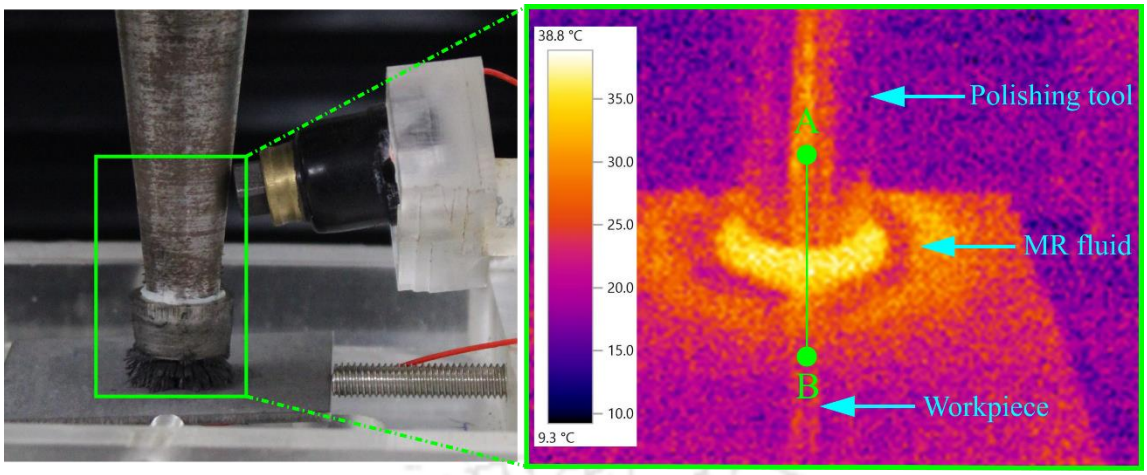

(a)

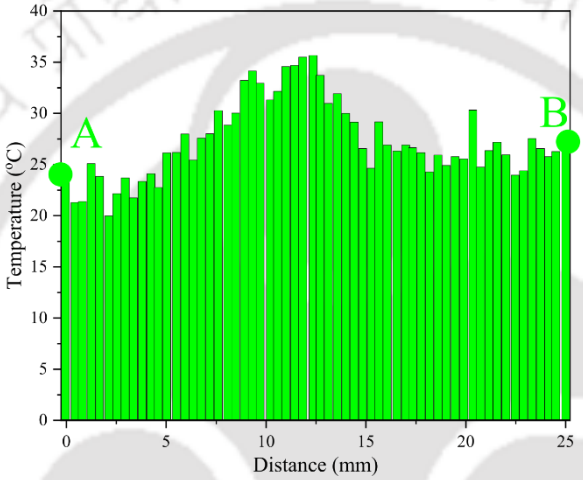

(b)

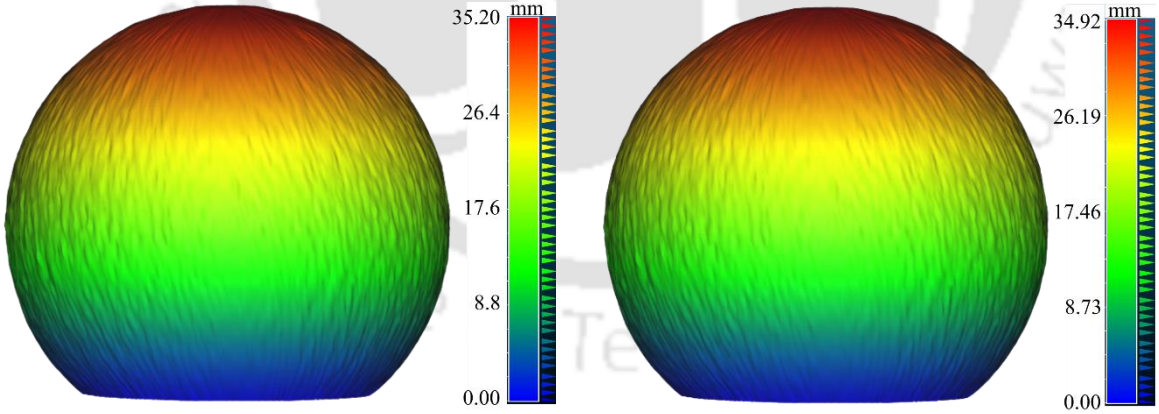

(c) (d)

Fig. 4.11 (a) Thermal analysis and (b) temperature variation along line AB during H-ECMR finishing process; Comparison between femoral heads surface topography (c) before and (d) after H-ECMR finishing

4.1.2 Post-processing of bone plate

Bone plates in orthopedic surgery have significantly improved patient outcomes, as they provide strong and stable fixation, enabling early rehabilitation and restoring the function of fractured bones. Bone plates are used to immobilize and hold fractured bone segments together.

They are applied to the surface of the bone and held in place with screws that pass through the plate and into the bone. This fixation method provides stability and prevents movement at the fracture site, allowing the bone to heal properly. Moreover, it is advantageous in fractures of weight-bearing bones, such as the femur, tibia, and humerus. They provide the necessary strength and support to bear weight and withstand the forces applied during movement and weight-bearing activities. Bone plates offer internal fixation, meaning they remain inside the body after healing. Unlike external fixation methods (e.g., casts), internal fixation with bone plates eliminates the need for external devices and allows for early mobilization and rehabilitation. Furthermore, bridge plating is employed in bone fractures with significant gaps or bone defects. The bone plate spans the gap between the fractured bone ends, acting as a bridge to promote stability and facilitate bone healing across the fault. The present study performs the surface finishing operation on the SLM-fabricated Ti-6Al-4V bone plate through the developed FHMRF-PS. Ti-alloy is widely used as a biomaterial for its improved mechanical properties, high corrosion resistance, and biocompatibility. The acceptance of the Ti-alloy with human tissue is far better than other biomaterials, making it ideal for implant material.

The development of a passive oxide layer (TiO_2) over the surface of Ti-6Al-4V restricts the parent material's direct contact with the body fluid when placed inside a human body, enhancing corrosion resistance. However, polishing workpieces with pockets and holes feature through the H-ECMR finishing process is still unattainable. Locking holes are provisioned on the bone plate to fix the broken bones through the tightened mechanism. The stability of MR fluid during the surface finishing of the locking holes is a significant challenge. Trapping of MR fluid inside the pockets and holes reduces the MRF process efficiency and further degrades the surface quality. Hence, the current study used a *Feature-based hybrid MRF planning system* (*FHMRF-PS*), as discussed in Chapter 3, to improve the surface quality of the bone plate. The workflow of the present work is shown in Fig. 4.12.

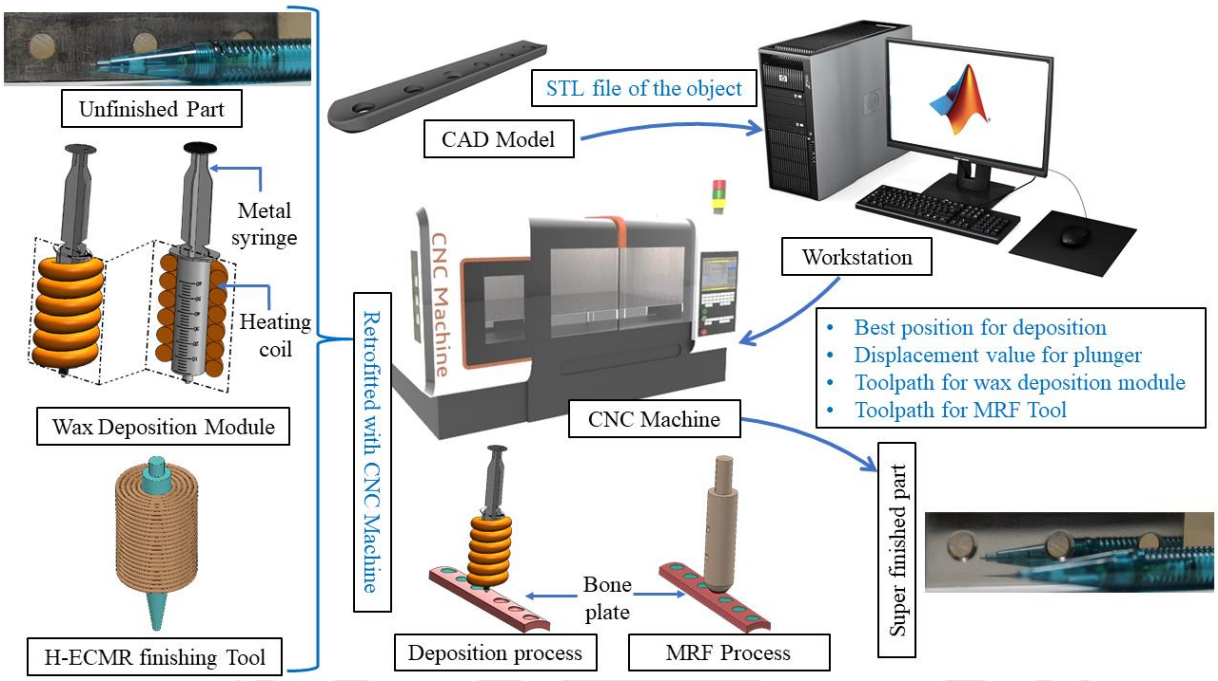

Fig. 4.12 Workflow of feature-based hybrid MRF planning system (FHMRF-PS)

The proposed *Computer Aided Process Planning* (*CAPP*) determines pockets and holes features from the *Standard Tessellation Language* (*STL*) format of the workpiece CAD model. An external deposition module deposits the paraffin wax in the holes or pockets of the workpiece up to the level of the nearby flat surfaces, as shown in Fig. 4.13. Afterward, the H-ECMRF finishing process is performed on the paraffin wax deposited bone plate to unvarying surface quality on the polished surface. Once the surface finishing operation is completed, dewaxing removes the paraffin wax from the workpiece. Herein, the bone plate is placed on the hot plate, and the temperature is increased to the melting points of paraffin wax till it is removed from the locking holes. The standoff distance, polishing tool's rotational speed, and feed rate are kept fixed during the H-ECMR finishing at 800 rpm, 1 mm, and 1 mm/min, respectively. Before undergoing an H-ECMR finishing technique, the average surface roughness of the bone plate is decreased to a submicron range. This is necessary as the H-ECMR finishing process is productive only when the initial surface roughness value is less than 1 micrometer. The milling operation is conducted on the SLM fabricated bone plate to attain the R_a below 1 µm. A face milling tool is used, and the spindle speed, feed rate, and depth of cut during the milling operation were 1000 rpm, 10 mm/min, and 0.25 mm, respectively, based on the literature survey.

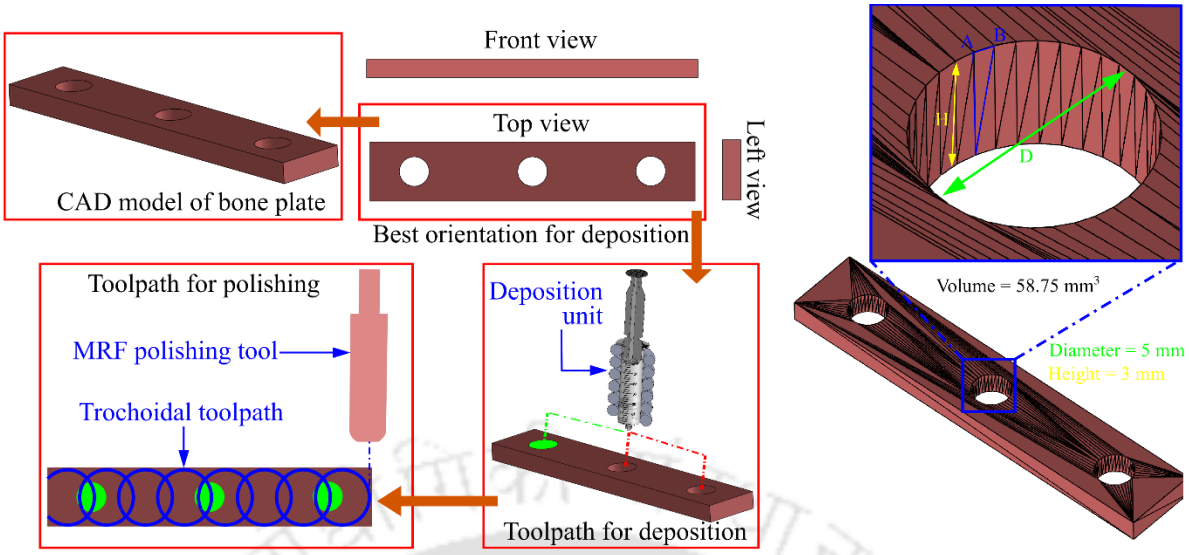

Fig. 4.13 (a) Flow chart of FHMRF-PS for bone plate and (b) determination of hole dimension from STL file

Using the Trochoidal toolpath strategy in H-ECMRF results in more homogeneous and uniform surface roughness and an augmented finishing rate than toolpath strategies such as zig-zag, spiral, and fractal curved-based approaches. This is because the trochoidal toolpath strategy produces an extra component of force while mapping the targeted surface through circular patterns compared to conventional toolpath strategies. The overview of FHMRF-PS during the H-ECMR finishing process for the surface enactment of the bone plate is shown in Fig. 4.14.

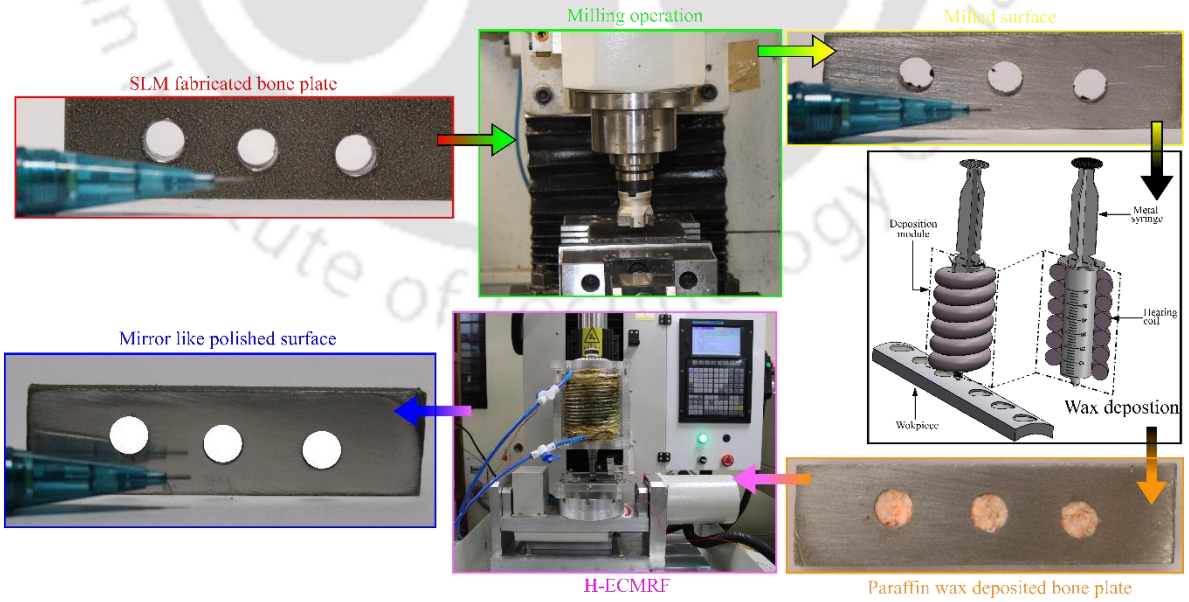

Fig. 4.14 Overview of feature-based hybrid MRF planning system (FHMRF-PS) for H-ECMR finishing of bone plate

4.1.2.1 Surface quality

The *H-ECMR* finishing process reduces the surface irregularities of a bone plate fabricated through SLM. The initial topographical imperfections on the surface of SLM fabricated parts, as depicted in Fig. 4.15(a), resulted in the poor surface quality of the workpiece. However, the milling operation effectively mitigates the initial R_a value of 9.36 µm to 0.98 µm, resulting in a decrease of 89.53% in average surface roughness. The defects produced on the surface because of the loosely bonded powders, partially melted powders, balling melts, semi-welds, and staircase effects are significantly removed from the SLM fabricated surface after the milling operation. Subsequently, the biomaterial undergoes the H-ECMRF process, further enhancing its surface roughness to a few nanometers. An external magnetic field facilitates the indentation of abrasive particles into the workpiece. The normal force is generated on abrasive particles owing to the action of magnetic force produced from the electromagnet, thus inducing indentations on the abrasive into the workpiece. While the feed and rotational motion of the polishing tool aid in removing the indented material from the surface. The combined action of these forces results in the improvement of surface quality. Furthermore, the electrochemical reaction of electrolyte and Ti alloy produces a uniform surface quality on the post-processed bone plate. The synergistic action of mechanical abrasion and the electrochemical reaction reduces average surface roughness from 0.98 µm to 21.37 nm, resulting in a 97.81% decrease in R_a. The 1D and 2D average surface profiles and surface texture comparison of the biomaterial after undergoing different processes are depicted in Figs. 4.15(b) and 4.15(c).

A comprehensive analysis of the *kurtosis* (R_{ku}) and *skewness* (R_{sk}) of the biomaterial surfaces is conducted before implementing the H-ECMR finishing process. Initially, the kurtosis value is observed to be higher than three (i.e., R_{ku} = 4.1) on the surface of the SLM fabricated bone plate, indicative of the presence of acute peaks on the surface irregularity. Furthermore, the skewness value is positive (i.e., R_{sk} = 0.76), denoting that the quantity of peaks exceeds that of valleys. However, post-milling on the SLM fabricated component, the kurtosis value is still higher than three (i.e., R_{ku} = 3.3), indicating that after the milling operation, the pointed peaks are still generated on the milled surface. Moreover, the positive skewness value (i.e., R_{sk} = 0.48) persists, signifying that the prevalence of peaks is still more significant than that of valleys. Subsequently, upon implementing the H-ECMR finishing process, the kurtosis value further decreases to 0.47, signifying the emergence of flat peaks on the surface irregularity. Similarly, the skewness value transforms to a negative value (i.e., R_{sk} = -0.84) post-H-ECMR finishing process on the SLM fabricated biomaterial, signifying that the quantity of peaks is less than that of valleys.

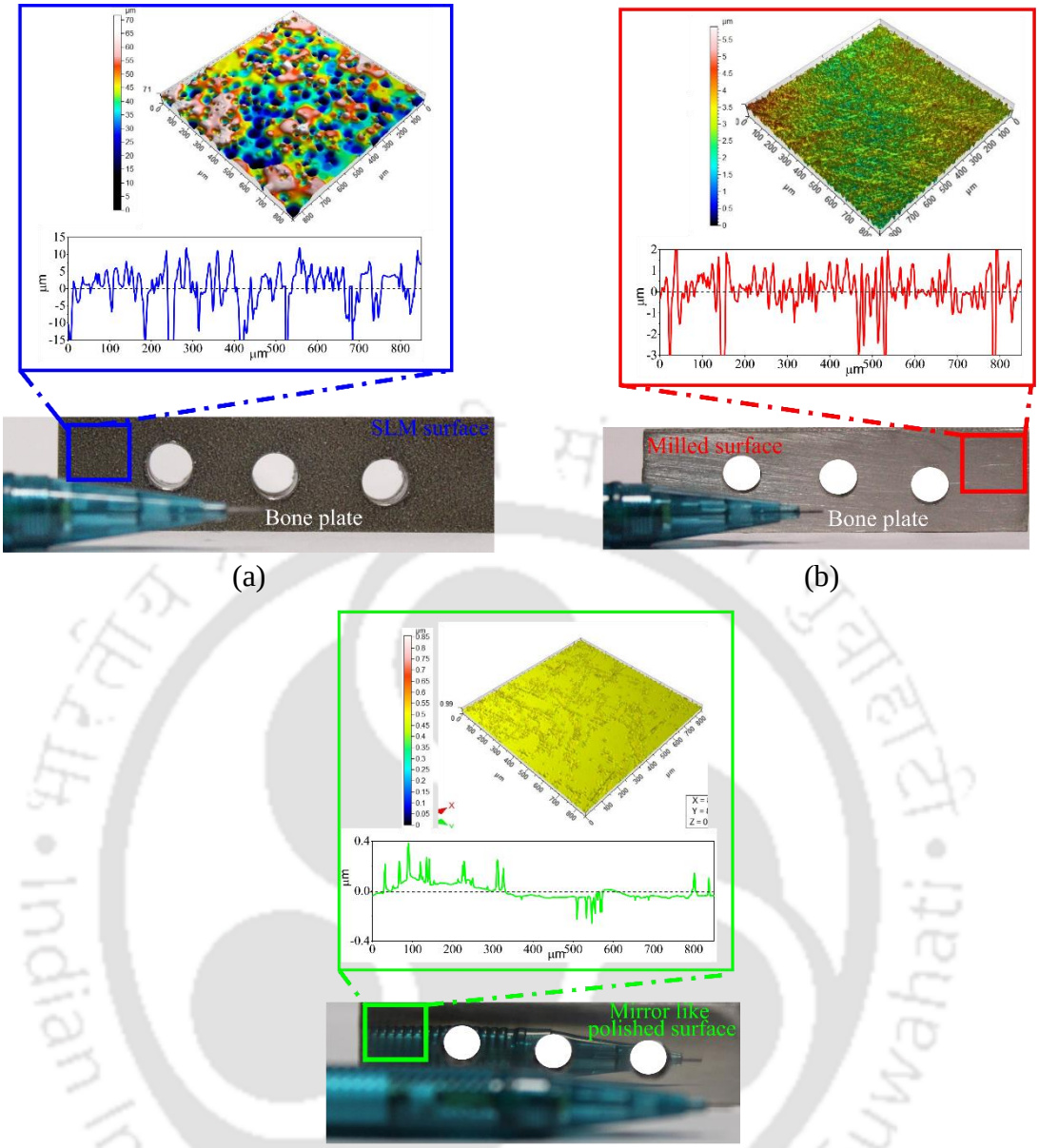

Fig. 4.15 Surface profiles of bone plate (a) initial surface, after (b) milling and (c) H-ECMRF process

4.1.2.2 Abbott-Firestone curve

The Abbott-Firestone curve, also known as the material ratio curve, is a graphical representation of the relationship between the area of peaks and valleys on the surface, is analyzed before and after polishing using data obtained from an optical profilometer. The surface irregularities' quantitative analysis reveals that the material under the peaks of the surface irregularities is drastically reduced (i.e., from 18.61 to 3.69 $\mu m^2/\mu m$) post-milling on the workpiece surface. The H-ECMR finishing process further reduces the areas covered by the peaks from 3.69 to 0.27 $\mu m^2/\mu m$. This decrease in the area beneath peaks signifies that the wear rate of the polished surface will reduce as the available material during the tribological

interaction reduces. Moreover, the area beneath the valleys is decreased to 7.56 µm^2/ µm from 110.79 µm^2/ µm post milling and further reduced to 1.07 µm^2/ µm after H-ECMR finishing. The unmelted powder particles on the workpiece surface are responsible for the high material values available at peaks and void areas in the valleys. Furthermore, the material ratio curve's peak thickness is reduced to 1.07 µm from 8.02 µm after milling and further reduced to 0.76 µm after the H-ECMR finishing process. Moreover, the valley thickness was initially 19.12 µm after SLM, which decreased to 2.32 µm after milling and further reduced to 0.12 µm after the H-ECMR finishing process. The Abbott firestone curves on the SLM fabricated, milled, and H-ECMR polished surfaces are illustrated in Fig. 4.16.

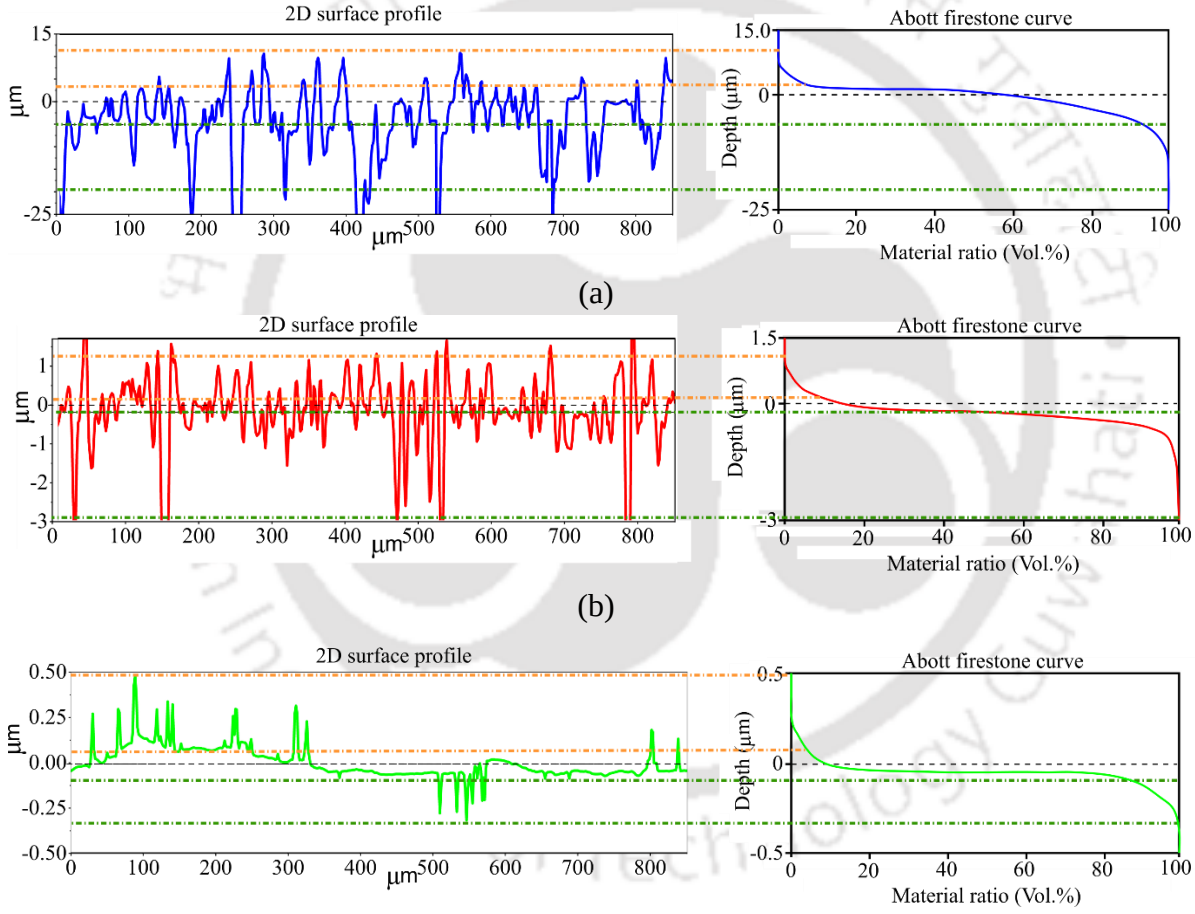

Fig. 4.16 Abbott-Firestone curves for (a) SLM fabricated, (b) milled, and (c) H-ECMR polished surfaces

Figure 4.17 illustrates the surface reflectance of different surfaces, including the SLM, fabricated, milled, and H-ECMR polished surfaces. The surface reflectance is measured compared to a highly polished silver surface that has 100% reflectivity as a reference. The wavelength of the incident light varied from 0 to 1000 nm. The reflectance of the SLM

fabricated part is 6.32% which further increases to 32.69% after the milling operation. However, after the H-ECMR finishing, the reflectivity of the bone plate is increased to 61.23%. Reducing surface irregularities from the SLM fabricated bone plate helps improve the polished surface's reflectivity.

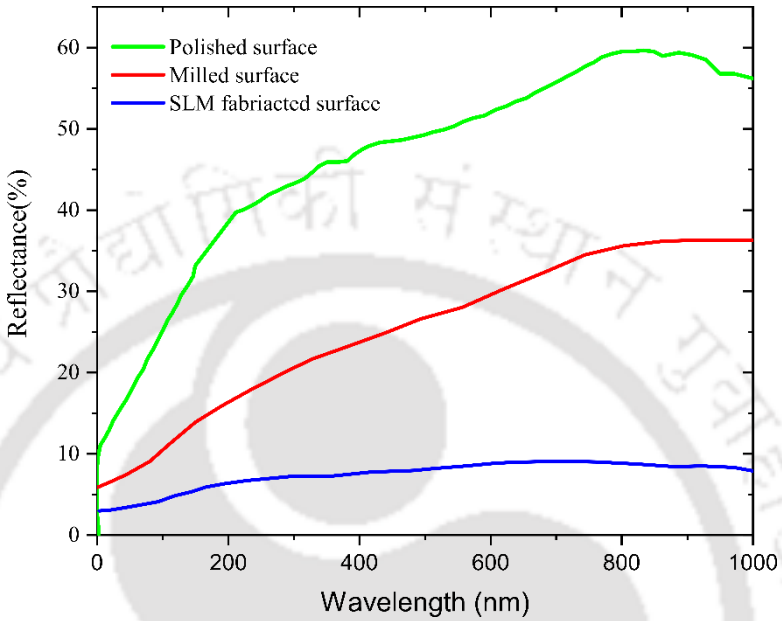

Fig. 4.17 Surface reflectance for (a) SLM fabricated, (b) milled, and (c) H-ECMR polished surfaces

4.1.3 Metallurgical analysis

The variations in the topographical characteristics of the surfaces during different post-processing phases are systematically examined via an optical profilometer. Initially, the presence of unmelted powders on the surface of SLM-fabricated biomaterial is discernible, as depicted in Fig. 4.18(a). However, the surface defects from the additively manufactured biomaterial surface are significantly mitigated post-milling, as illustrated in Fig. 4.18(b). Nevertheless, the scratch marks imparted by the milling cutter are exposed on the milled surface, as depicted in Fig. 4.18(b). However, implementing the H-ECMR finishing process reduces the scratch marks on the milled biomaterial surface, as described in Fig. 4.18(c).

An examination of the cross-sectional profile of the SLM-fabricated Ti-6Al-4V workpiece is conducted to assess the enhancement in surface quality achieved post the implementation of different post-processing techniques. Figure 4.19 illustrates the cross-sectional view of the selective laser melted surface, wherein the surface irregularities, including various surface defects, are clearly observable. Post-milling, a marked reduction in surface defects is visible on the milled surface (Fig. 4.19).

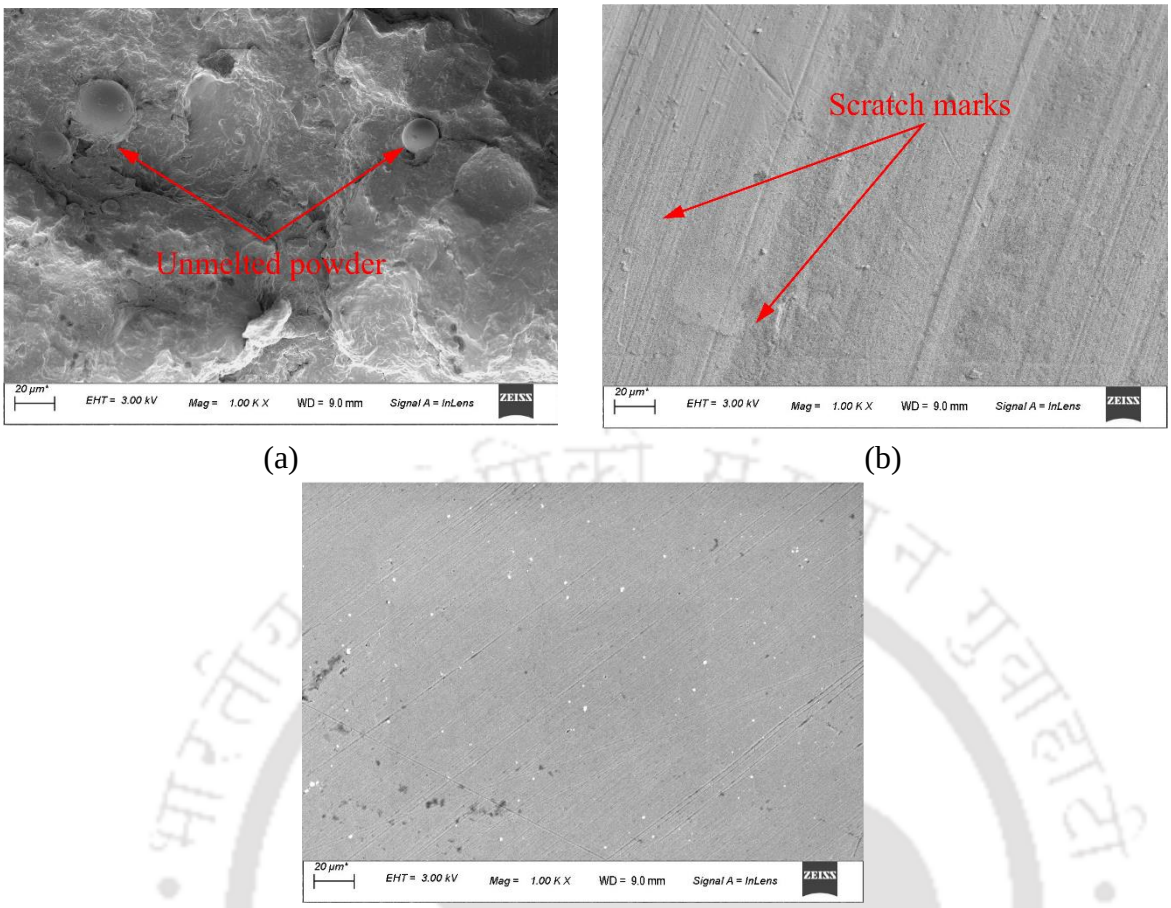

Fig. 4.18 Optical microscopic images of (a) SLM fabricated, (b) milled, (c) H-ECMR polished surfaces

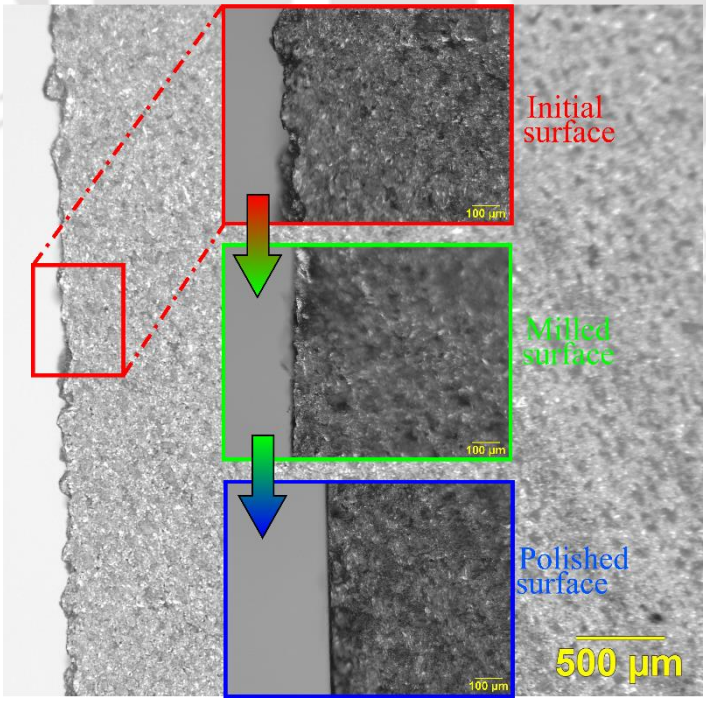

Fig. 4.19 Optical microscopic images of workpiece cross-section and zoomed view on a spot for (a) SLM fabricated, (b) milled, and (c) H-ECMR polished surfaces

Nevertheless, the presence of burrs, which are the small, raised edges left by the milling process, is still evident on the milled surface in Fig. 4.19. However, upon implementing the H-ECMR finishing process, a homogenous surface free from any burrs is observed in the cross-sectional view of the additively manufactured biomaterial, as depicted in Fig. 4.19.

4.1.4 Biocompatibility test

The biocompatibility tests are conducted on the Ti-6Al-4V workpiece fabricated through LPBF, including wettability, wear, and corrosion test, to analyze its functionality before and after surface finishing and discussed in the subsequent section.

4.1.4.1 Wettability test

The impact of post-processing on the wettability of the femoral head is analyzed through a goniometer (Apex instrument MMC-8C). The hydrophilic nature of the TI-6Al-4V is required for orthopedic implants, including hip, knee, bone plates, etc., as it reduces platelet adhesion and coagulation. Moreover, it also demotes the sheltering of bacteria, fungi, and various viruses responsible for the implants' short or long-term infection under adverse conditions [90]. The wettability of an implant surface is defined as the contact angle between the solid and liquid surfaces. The value of a contact angle greater than 90^{o} denotes the hydrophilic nature of the implant surface with high wettability. However, The value of a contact angle less than 90^{o} indicates the hydrophobic nature and is responsible for low wettability [65]. Figure 4.20 illustrates the contact angle of the different surfaces with the water droplet. The water droplet takes time while coming into a steady state as the average surface roughness is very high, i.e., 14.89 µm on the LPBF fabricated surface. The initial value of the contact angle is 84.45^{o}, further decreased to 64.36^{o} at steady state as shown in Fig 4.20. The lower value of the contact angle increases plate adhesion and coagulation. The contact angle on the chemically etched surface is increased to $86.81^{o,}$ and the water droplet is stable as the surface irregularities are reduced significantly. The hydrophilic nature of the additively manufactured surface is observed after the H-ECMR finishing process as the contact angle increases (i.e., 112.16^{o}) between the polished surface and water droplet. The hydrophilic nature of the biomaterial surface demotes platelet adhesion and coagulation and reduces the sheltering of bacteria, fungi, and viruses.

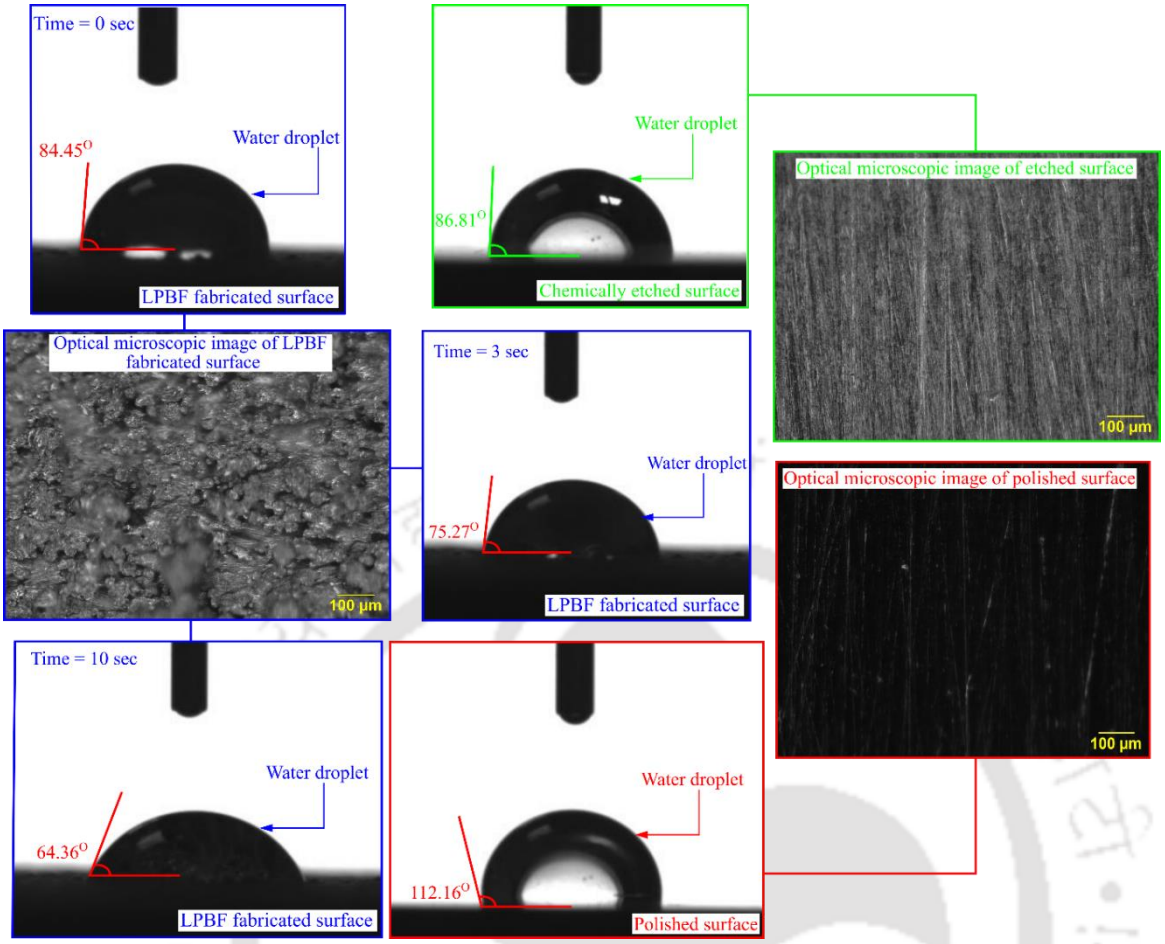

Fig. 4.20 Contact angle on LPBF fabricated, chemically etched, and H-ECMR finished surfaces

4.1.4.2 Corrosion test

When placed inside the body, an implant's sustainability primarily depends on its functionality. Failure of the biomaterial during its operation produces adverse effects on the human body. The degradation of the biomaterial surface in the corrosive environment due to body fluid (contains sodium, water, chloride, etc.) and blood leads to the circulation of debris inside the human body through blood circulation, responsible for the systematic toxicity of various organs, including kidneys, eyes, levers, etc. [53]. Furthermore, allergens and carcinogens are caused because of the ions generated during the corrosion. The studies suggest that most of the failures of the implant are due to its dissolution in body fluid [56]. Corrosion resistance on the post-processing of the biomaterials is analyzed through a three-electrode-based corrosion test, as shown in Fig. 4.21(a). Herein, three different electrodes, namely, reference, working, and counter electrodes, are used with a scan rate of 0.25 Mv/S. 0.5 mole of NaCl (pH value as human blood, i.e., 7.41) at ambient temperature is used as the solution during the corrosion test. The Isopropanol and *Deionized* (*DI*) water are used to remove the foreign material from the workpiece surface and kept in an electric dryer to remove moisture before the corrosion

test. The Tafel plot generated after the three-electrode-based test is used to determine the corrosion rate of the surface before and after post-processing, as illustrated in Fig. 4.21(b).

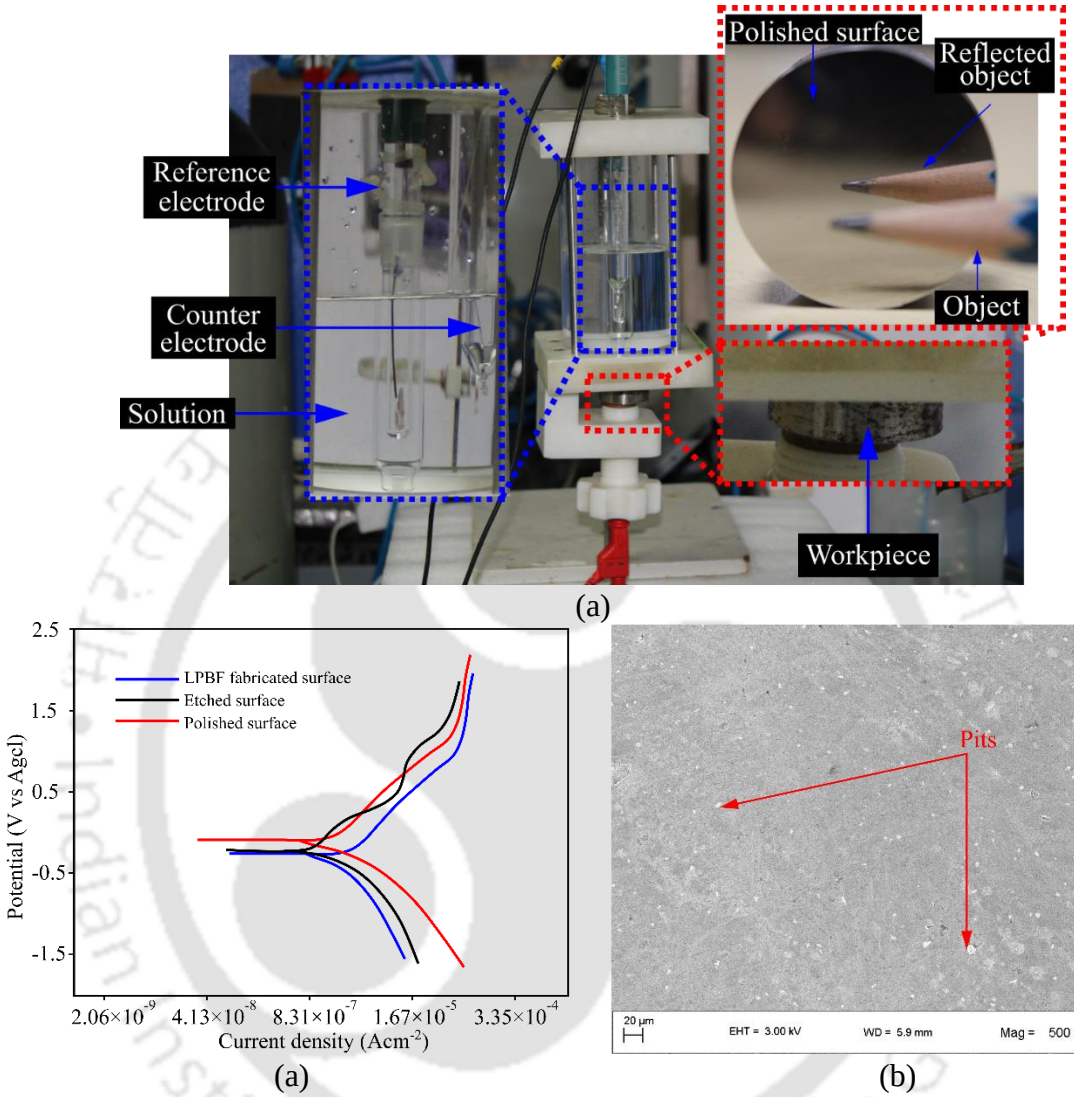

Fig. 4.21 (a) Experimental setup for corrosion test, (b) potentiodynamic polarization behavior of LPBF fabricated, chemically etched, and H-ECMR finished surfaces, and (c) pits on polished surface of biomaterial after corrosion test

The corrosion rate for the LPBF fabricated Ti-6Al-4V is 0.081 mm/year, further reduced to 0.0103 mm/year after the chemical etching. Meanwhile, the biomaterials' enhanced surface quality has been found to boost their corrosion resistance. Surface irregularities of LPBF fabricated surface are very high, creating the grooves for confined corrosion products, which leads to the lodgment of positive charges and contributes to pit development. The corrosion rate value on the final polished surface is 0.0046 mm/year. Very little to no positive charges accumulate on the polished surface. This selected biomaterial is less prone to corrode since many smaller metastable hole spots are generated after polishing, as shown in Fig. 4.21(c).

Moreover, the electrochemical reaction during the H-ECMR finishing process provides a uniform and thick passive oxide layer on Ti-6Al-4V surface responsible for enhancing its corrosion resistance.

4.1.4.3 Wear test

Pin-on-disc experiment is implemented to evaluate the wear rate to determine the sustainability of the post-processed biomaterials under adverse conditions [204][98]. The interaction between the biomaterials is observed with the *Ultra High Molecular Weight Polyethylene* (*UHMWPE*), as illustrated in Fig. 4.22(a). UHMWPE simulates the bone material during the wear test. Its physical properties are identical to the human bone, with density, hardness, and tensile strength of 940 kg m^{-3}, 45 HRB, and 40 MPa, respectively. The pins during the wear tests were printed using LPBF. Afterward, the surfaces of the pins are improved through chemical etching, followed by the H-ECMR finishing process. Moreover, Fig. 4.22(b) shows the comparison of friction coefficient during the tribological interaction of Ti-6Al-4V pins with UHMWPE. The friction coefficient is higher for the LPBF fabricated surface compared with the chemical etched and H-ECMR processed surfaces. It is because unmelted powders get detached from the surface and increase the magnitude of the coefficient of friction.

Moreover, the "stick-slip" phenomenon happens throughout the first 0 to 100 seconds during biomaterial interaction with UHMWPE. The dynamic interaction phenomenon among the UHMWPE and LPBF fabricated Ti-6Al-4V surfaces is responsible for an unsteady movement next to the sliding track. The tribological pairs' higher contact force is initially noticed because of the generated debris particles. These debris particles' size is significantly smaller. Hence, the higher contact pressure is imposed due to the lower contact area. The action of the high contact pressure causes the elimination of soft asperities, leading to the eradication of wear particles from the sliding track. Hence, the coefficient of friction increases during the initial phase of the pin-on-disc experiments for all the surfaces. However, as the R_a of the LPBF fabricated workpiece reduces after post-processing, it decreases the coefficient of friction during its tribological interaction with the UHMWPE, as discussed in Eq. (4.1). The wear rate corresponding to the LPBF fabricated, chemically etched, and polished surfaces are 18.86×10^{-5}, 6.36×10^{-5}, and 0.96×10^{-5} mm^3/min, respectively, as shown in Fig. 4.22(c). The significant reduction in surface irregularities after the post-processing of the LPBF fabricated Ti-6Al-4V is the primal reason for the enhancement in the wear resistance. Furthermore, a negative skewness and the kurtosis value of less than three measured on the H-ECMR polished surface indicates that the wear out of the surface irregularities from the workpiece after their

tribological contact is significantly less compared with the LPBF fabricated parts and the chemically etched surfaces.

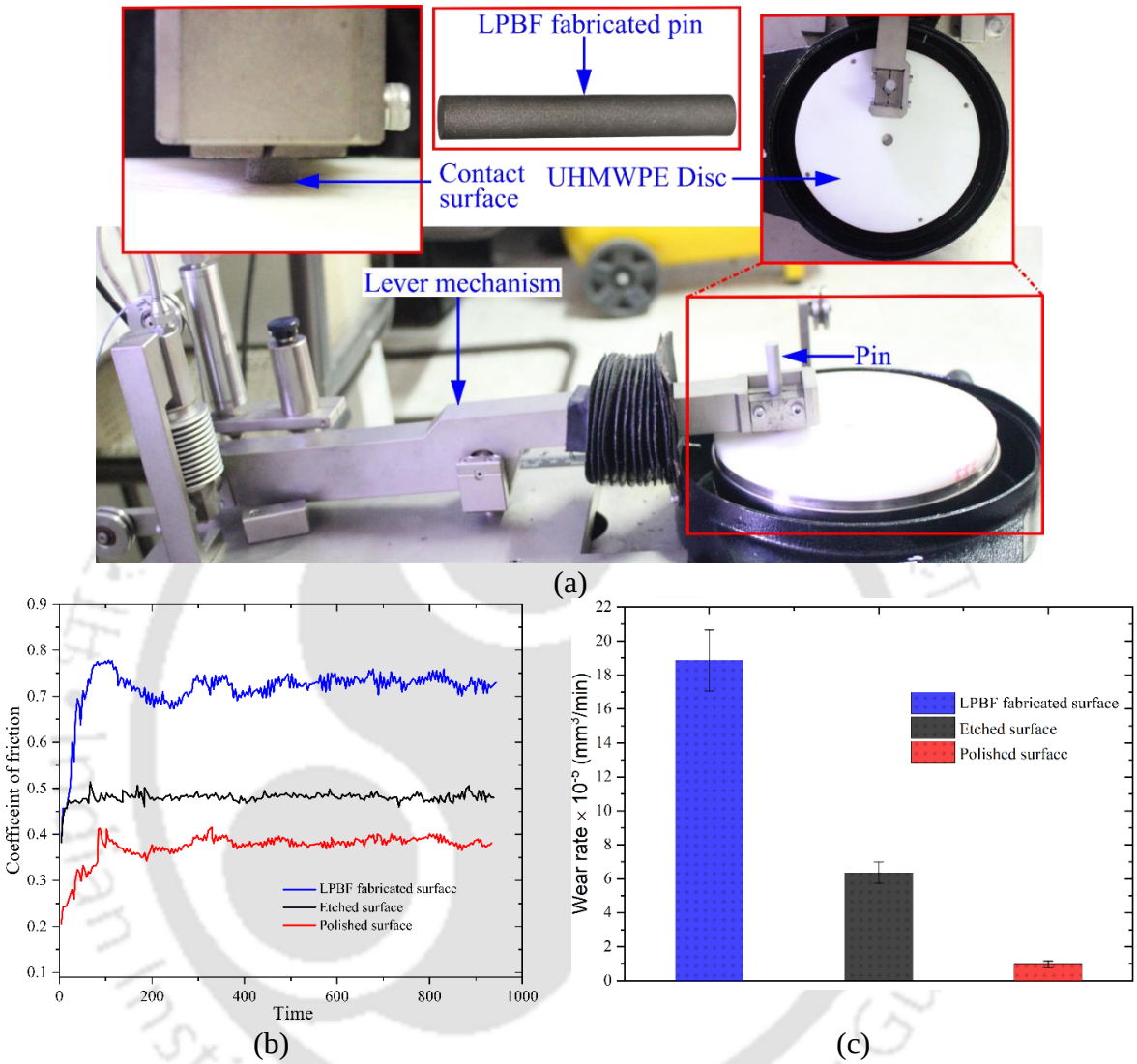

Fig. 4.22 (a) Wear experimental test set up, (b) coefficient of friction, and (c) wear rate for LPBF fabricated, chemically etched, and H-ECMR finished surfaces

The present study further investigates the consequences of surface characteristics on the wear rate of biomaterials. The results of the H-ECMR polished surfaces, characterized by negative skewness and kurtosis values of less than three, suggest a low probability of wear on the surface irregularities during tribological contact. The finished surface exhibits flat peaks with a lower frequency than valleys. The wear resistance is augmented on surfaces showing a lower magnitude of kurtosis (< 3) and negative skewness. The wear mechanism during H-ECMR finishing while polishing the Ti-6Al-4V workpiece is examined through *Scanning Electron Microscopy* (*SEM*) images. The forces applied to the abrasive particles are illustrated in Fig. 4.23(a); the interaction of abrasive particles with surface irregularities generates the

reaction force (F_r). Compared to the reaction force, the higher *finishing force* (F_n) results in two-body abrasive wear. The external magnetic field is responsible for the generation of the normal force. In contrast, the polishing tool feed leads to the production of the shear force during the surface finishing process. However, when the reaction force surpasses the finishing force, the abrasive particles roll and slide over the surface, resulting in three-body abrasion wear, as depicted in Fig. 4.23(b). This results in plowing and discernible abrasion marks on the finished surface, as illustrated in Fig. 4.23(d).

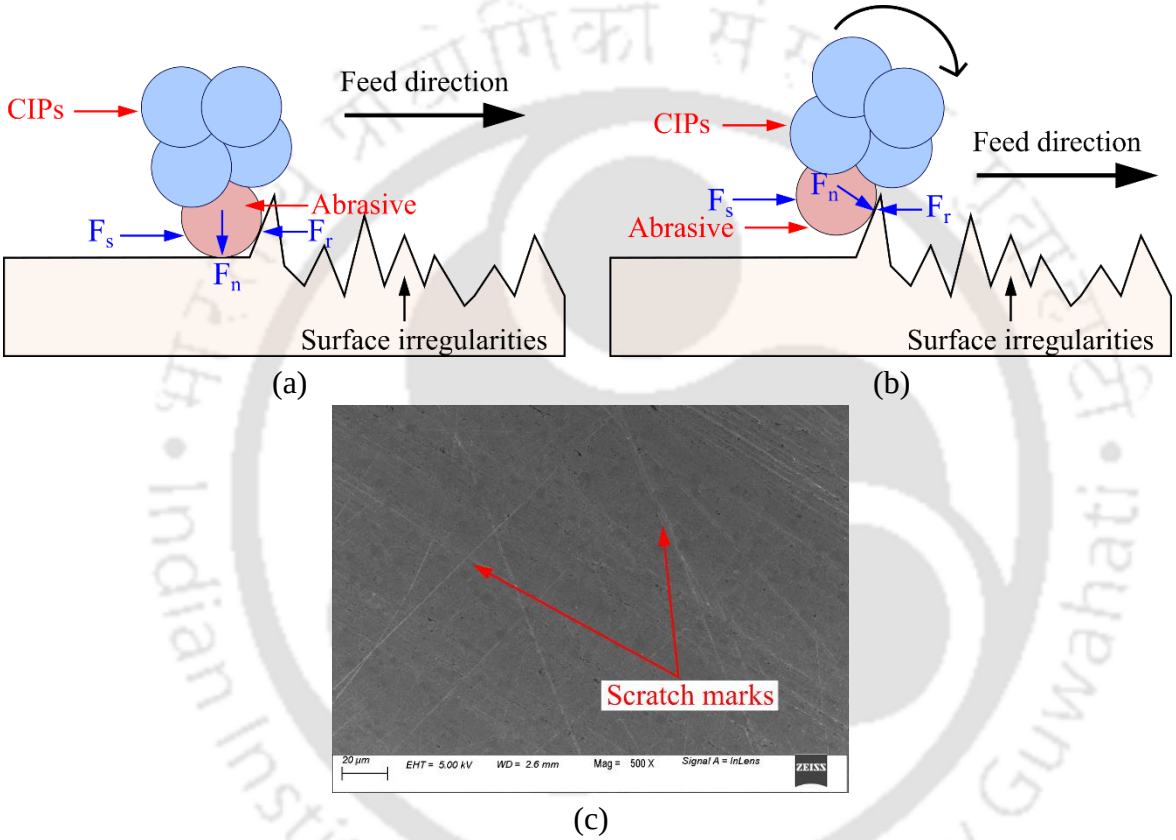

Fig. 4.23 Schematic diagram explaining mechanism of (a) two-body, (b) three-body abrasive wear during H-ECMR process, and (c) scanning electron microscopic image of polished surface

4.2 Summary

The present study aims to enhance the biocompatibility of the post-processed *Laser Powder Based Fusion* (LPBF) Ti-6Al-4V femoral head of the *Total Hip Arthroplasty* (*THA*) and boned plate. The poor surface quality and defects of the LPBF fabricated femoral heads lead to Aseptic loosening or *Adverse Reactions to Metal Debris* (*ARMD*), further causing systematic toxicity of various organs, including kidneys, eyes, levers, etc., during their tribological interaction. The *Hybrid-Electrochemical Magnetorheological* (*H-ECMR*) finishing process is

used to reduce the surface roughness of the femoral head in the range of a few nanometers. However, the *H-ECMR* finishing process effectively applies to biomaterials with initial surface roughness (R_a) in the sub-micron range. Hence, chemical etching is used as an intermediated finishing process to reduce the average surface roughness (R_a) of the femoral head to 0.98 µm from its initial value of 14.67 µm. The average surface roughness (R_a) is reduced to 33.14 nm from 0.98 µm after chemical etching to produce a mirror-like polished surface during the H-ECMR finishing process. The synergic action of the mechanical abrasion and electrochemical reaction generates uniform surface quality on the femoral head surface. The carrier fluid (i.e., distilled water) of the *Magnetorheological* (*MR*) fluid dissipates the heat generated during the mechanical abrasion and enhances the surface quality without affecting the surface topography.

Furthermore, the *Feature-based hybrid MRF planning system* (*FHMRF-PS*) is used to improve the surface quality of the additively manufactured Ti-6Al-4V bone plate. The H-ECMR finishing process generated a mirror-like surface on the biomaterial after polishing. The final Ra value of 21.37 nm is attained from 9.36 µm through FHMRF-PS. Moreover, Post-processing of the Ti-6Al-4V provides a hydrophilic nature of the biomaterial surface, demotes platelet adhesion and coagulation, and reduces the sheltering of bacteria, fungi, and viruses. The corrosion rate for the LPBF fabricated Ti-6Al-4V is 0.081 mm/year, further reduced to 0.0103 mm/year after chemical etching as surface irregularities of LPBF manufactured surface are very high, creating the grooves for confined corrosion products. The wear rate value on the final polished surface is further reduced to 0.0046 mm/year as an electrochemical reaction during the H-ECMR finishing process provides a uniform and thick passive oxide layer on the surface of Ti-6Al-4V. The wear rate corresponding to the LPBF fabricated, chemically etched, and polished surfaces are 18.86×10^{-5}, 6.36×10^{-5}, and 0.96×10^{-5} mm^3/min, respectively. A negative skewness and the kurtosis value of less than three after the post-processing of the LPBF fabricated Ti-6Al-4V is a primal reason for the enhancement in the wear resistance of the biomaterial. Based on the experimental results, it can be concluded that the surface quality and biocompatibility of the LPBF fabricated workpiece are enhanced after the post-processing through chemical etching followed by H-ECMR finishing.

Chapter 5 Conclusions and Future Plan

5.1 Conclusions

In the present work, a novel *Hybrid-Electrochemical Magnetorheological* (*H-ECMR*) finishing process is developed to enhance the biocompatibility of the post-processed additively manufactured biomedical implants. The poor surface quality and defects of the additively manufactured implants lead to Aseptic Loosening or *Adverse Reactions to Metal Debris* (*ARMD*), further causing systematic toxicity of various organs, including kidneys, eyes, levers, etc., during their tribological interaction. Herein, the synergic action of electrochemical reaction and mechanical abrasion reduces the surface roughness value of the polished surfaces in the few nanometers range. The electrolyte as a carrier medium in MR fluid enables the electrochemical reaction by providing the potential difference across the workpiece and polishing tool. After polishing, the developed process improves the passive oxide layer thickness and uniformity of the Ti-6Al-4V surface. The key outcomes of the present work are discussed in the subsequent sections.

5.1.1 Development of Magnetorheological Fluid Assisted Finishing process

This work aims to design and develop a novel *Hybrid Electrochemical Magnetorheological (H-ECMR)* finishing to enhance the surface quality of the Ti-6Al-4V biomaterial with reduced polishing time. The critical points of the work are summarized below.

- A 96.41% reduction in surface roughness ($\%\Delta R_a$) is achieved during *Hybrid Electrochemical Magnetorheological* (*H-ECMR*) finishing, compared to 49.63% using the conventional *Magnetorheological Finishing* (*MRF*) for 30 minutes of polishing time. Instigating an electrochemical reaction along with mechanical abrasion increases the polishing efficiency.
- The mirror-like polished surface is achieved on the Ti-6Al-4V surface after the H-ECMR finishing. The initial *average surface roughness* (R_a) value of 325.90 nm is reduced to its final value of 12.90 nm. Moreover, the value of *skewness* (R_{sk}) and *kurtosis* (R_{ku}) achieved on the polished surface is -0.52 and 1.69, respectively, indicating that the low probabilities of wearing out of the biomaterial surface on their tribological interactions as flat peaks with a lower number than the valleys are produced on the biomaterial surface.

- The electrochemical reaction between the Ti-6Al-4V, $MgCl_2$, and $C_2H_6O_2$ produces a uniform and thick TiO_2 passive layer on the Ti-6Al-4V surface. The layer thickness increases to 78 nm from 8 nm, enhancing the biomaterial's corrosion resistance.

5.1.2 Computer-aided process planning of H-ECMR finishing process

This work aims to develop a *Computer-Aided Process Planning* (*CAPP*) for super-finishing flat surfaces with pockets through the *H-ECMR* finishing process. The significant finding from the research is summarized below.

- The inconsistency in the surface roughness on the polished surface of the workpiece having holes is observed during the *H-ECMR* process irrespective of their size (i.e., hole diameter). Trapping of *Magnetorheological* (*MR*) fluid and leakage of carrier medium from the holes are the primary reasons for the irregularities in the polished surface quality.
- *FHMRF-PS* is developed with an external deposition module, which helps deposit paraffin wax over the pockets or holes with the nearest neighbor algorithm of the *Travelling Salesman Problem* (*TSP*) to avoid repetition during deposition.
- The underfilling and overfilling of paraffin wax are critical as they affect the surface quality of the polished surface. An increase in the % overfilling leads to a decrease in MR fluid's yield stress, which is further responsible for surface quality deterioration. However, inconsistent surface quality is produced on the polished surface irrespective of the amount of underfilling, as trapping of MR fluid reduces the polishing efficiency.

Moreover, a comparison is made between the different toolpath strategies, and the significant findings are summarized below.

- The average percentage reduction in surface roughness (% ΔR_a) for Zig-Zag, Hilbert, Peano, Spiral, and Trochoidal toolpaths are 97.39%, 96.57%, 96.22%, 96.73%, and 99.51%, respectively. The repetition of the tool movement over a point reduces surface roughness significantly for the Trochoidal toolpath compared with other toolpaths.
- The 96.82% *reduction in surface roughness* (ΔR_a) is achieved during the Trochoidal toolpath in 70 minutes. In contrast, only a 45.36% reduction in R_a is noticed during the Zig-Zag toolpath for the same finishing time. It is because The *Carbonyl Iron Particles (CIPs)* chain deflection is less in the Trochoidal toolpath than in the Zig-Zag toolpath.

- The increase in stepover and radius of the Trochoidal curve leads to a decrease in average surface roughness and skewness as the uncovered area is increased based on the regression analysis.

5.1.3 Surface enhancement of additively manufactured implants

The present study aims to enhance the biocompatibility of the post-processed *Laser Powder Based Fusion* (LPBF) Ti-6Al-4V femoral head of the *Total Hip Arthroplasty* (*THA*) and bone plate. The significant finding of the current research is stated below.

- The average surface roughness (R_a) is reduced to 33.14 nm from 0.98 µm after chemical etching to produce a mirror-like polished surface on the Ti-6Al-4V femoral head of the THA during the H-ECMR finishing process. The synergic action of the mechanical abrasion and electrochemical reaction produces uniform surface quality on the femoral head surface.
- The finishing process generated a mirror-like surface on the biomaterial after polishing on the Ti-6Al-4V bone plate. The final R_a value of 21.37 nm is attained from 9.36 µm.
- Post-processing of the femoral head provides a hydrophilic nature of the biomaterial surface, demotes platelet adhesion and coagulation, and reduces the sheltering of bacteria, fungi, and viruses.
- The corrosion rate for the LPBF fabricated Ti-6Al-4V is 0.081 mm/year, further reduced to 0.0103 mm/year after the chemical etching as surface irregularities of LPBF manufactured surface are very high, creating the grooves for confined corrosion products. The wear rate value on the final polished surface is further reduced to 0.0046 mm/year as an electrochemical reaction during the H-ECMR finishing process provides a uniform and thick passive oxide layer on the surface of Ti-6Al-4V.
- The wear rate corresponding to the LPBF fabricated, chemically etched, and polished surfaces are 18.86×10^{-5}, 6.36×10^{-5}, and 0.96×10^{-5} mm^3/min, respectively. A negative skewness and the kurtosis value of less than three after the post-processing of the LPBF fabricated Ti-6Al-4V is a primal reason for the enhancement in the wear resistance of the biomaterial.

5.2 Scope for future work

In-Vitro and In-Vivo analysis can be conducted on biomaterials polished through proposed polishing methods.

The symbiotic relationship between in-vitro and in-vivo analyses is essential for comprehensively assessing the performance of biomaterials with polished surfaces. In-vitro experiments provide controlled conditions for initial screening, enabling rapid evaluations of various formulations and treatments. Meanwhile, in-vivo studies offer a more realistic understanding of biomaterial behavior within living organisms, considering complex interactions and long-term effects. Synthesis of insights from both realms equips researchers with a holistic perspective, guiding the development of effective biomaterials in controlled settings and demonstrating safety and efficacy in natural physiological environments. It is essential to determine the behavior of the polished surface under controlled conditions.

Analysis of cell seeding can be studied over polished surfaces to analyze its biocompatibility.

The alteration of biomaterial performance within living tissues is influenced by the inherent nature of the biomaterial surface as well as the diverse range of bioactive agents and biomolecules employed for functionalization. To emulate the intricate tissue microenvironment more effectively, surface finishing methodologies combined with bioactive agents and biomolecules are commonly used. Essential parameters, including surface chemistry, topography, chemical composition, wettability, stiffness, and dimensionality must all be carefully considered while designing substitutes for medical applications. By manipulating implant surface properties, such as surface charge, functional groups, and topography, precise control over the initial attachment of cells can be achieved. This strategic manipulation of surface attributes is pivotal in guiding and regulating how cells initially adhere to the implant, offering opportunities for tailored and controlled outcomes.

A toolpath strategy compatible with H-ECMR finishing can be developed to produce uniform surface quality with reduced finishing time.

Toolpath planning is a crucial element in modern manufacturing, guiding the precise movement of cutting tools during machining operations. Toolpaths ensure accuracy, efficiency, and quality in the production process by determining the optimal path for material removal. They minimize waste, reduce machining time, and enhance surface finish, contributing to cost-effective and high-quality manufacturing. Additionally, well-designed toolpaths extend the lifespan of cutting tools and promote safe operations by preventing collisions. Toolpath planning is the linchpin that transforms design concepts into tangible, precisely crafted products. A Trochoidal toolpath for a freeform surface can be developed, as shown in Fig. 5.1.

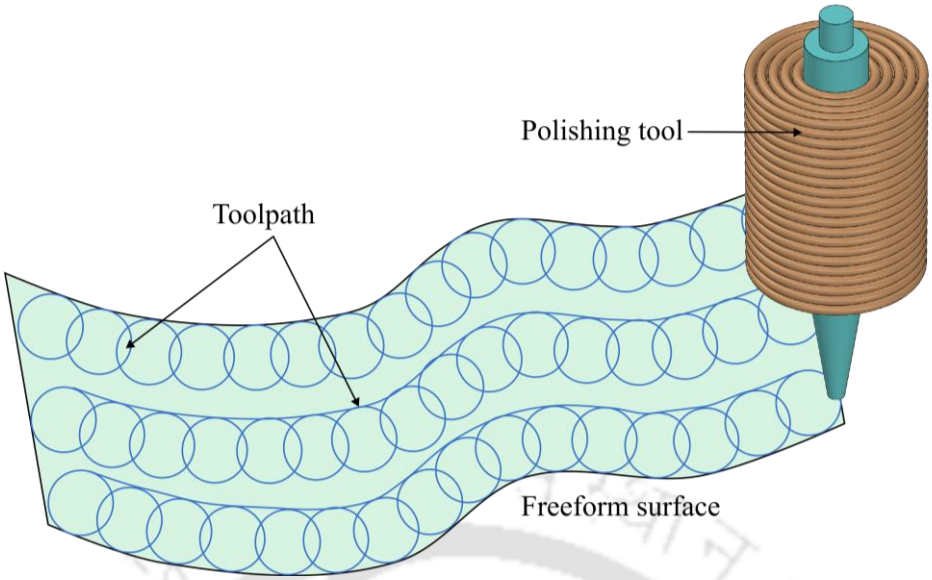

Fig. 5.1 Toolpath for freeform surfaces

Developing a workstation for simultaneous fabrication and nanofinishing of additively manufactured biomedical implants can be considered.

A workstation enabling the fabrication of biomedical implants and their post-processing will improve the dimensional accuracy and efficiency of the manufacturing process.

Appendix A Magnetorheological Fluid Assisted Finishing (MFAF) Process

A.1 Introduction

In today's manufacturing sector, it is required to manufacture products that have an exceptionally low tolerance. The desired high precision (or low tolerance) can be obtained through various finishing processes, which consist of bonded (honing, grinding, lapping, etc.) or unbonded (Abrasive flow finishing) forms of the tool. An unbonded tool is more reliable and beneficial because it helps achieve a highly polished surface without affecting the material topography of the product. From the different literature surveys, it has been emphasized that an effective unbonded finishing tool can be produced through the assistance of *Magnetorheological* (*MR*) Fluid, as it has in-situ control on its rheological properties. The MR fluid mainly comprises abrasives and metal powder mixed in the viscoelastic solid base. Over the last few decades, several MR fluid-assisted finishing processes have been developed, such as *Magnetorheological Finishing* (*MRF*), *Magnetorheological Honing* (*MRAH*), *Rotational Magnetorheological Flow Finishing* (*R-MRAFF*), *Ball End Magnetorheological Finishing* (*BEMRF*), *Magnetorheological Abrasive Flow Finishing* (*MRAFF*), *Chemo-Mechanical Magnetorheological Finishing* (*CMMRF*) and *Magnetorheological jet finishing* (*MR Jet Finishing*). The following section explores the evolution of MR fluid-assisted finishing processes, their development, applications, influencing process parameters, the composition of MR fluids, and governing analytical models. The key capabilities & limitations of different MR fluid-assisted finishing processes are also discussed, and a comparison was made to provide an overview at a glance.

A.2 Magnetorheological fluid (MR fluid)

In 1963, a scientist from the National Aeronautics and Space Administration (NASA) utilized the MR fluid for the first time [6]. He has used the MR fluid to control the motion of liquid fuel in the space shuttles. However, in the field of surface finishing, MR fluid's stiffness helps to enhance the surface quality, as discussed earlier. Conventionally, an MR fluid consists of abrasives (i.e., silicon carbide, boron carbide, diamonds, etc.) and metal powder (powder iron, carbonyl iron particles, or iron/cobalt alloys) circulated in the viscoelastic solid base (grease, hydrocarbon oils, etc.) of carrier fluid (mineral oils, silicon oils, etc.) [205]–[209]. A high concentration of solid particles (metal powder and abrasives) in MR fluid reduces its fluidity,

increases sedimentaion, and promotes inhomogeneous mixing. Hence, optimality in the concentration of constituents is always required to achieve enhanced surface finishing. The potential features of an MR fluid suitable for surface finishing application are shown in Fig. A.1.

In an MR fluid, the metal particles tend to sediment (due to heavy metal particles) and agglomerate (due to the remnant magnetization). These particles form very stiff structures that are difficult to remove later. Therefore, different MR fluid compositions with low sedimentation properties were proposed by several researchers, as shown in Table A.1. The rheological properties of MR fluid, i.e., viscosity and yield stress, are vital parameters for surface finishing. High yield stress leads to better surface finishing but produces scratches on the surfaces beyond a specific limit. Similarly, high viscosity also creates a similar difficulty. During the operation, the viscosity and the yield stress of the MR fluid get reduced, as devastating and breaking of metal particles & abrasives. Therefore, it is very challenging to maintain a consistent value of viscosity and yield stress throughout the operation. However, corrosion of metal particles, as they oxidized quickly in the base fluid, may also decrease the finishing efficiency with a non-uniform surface finish.

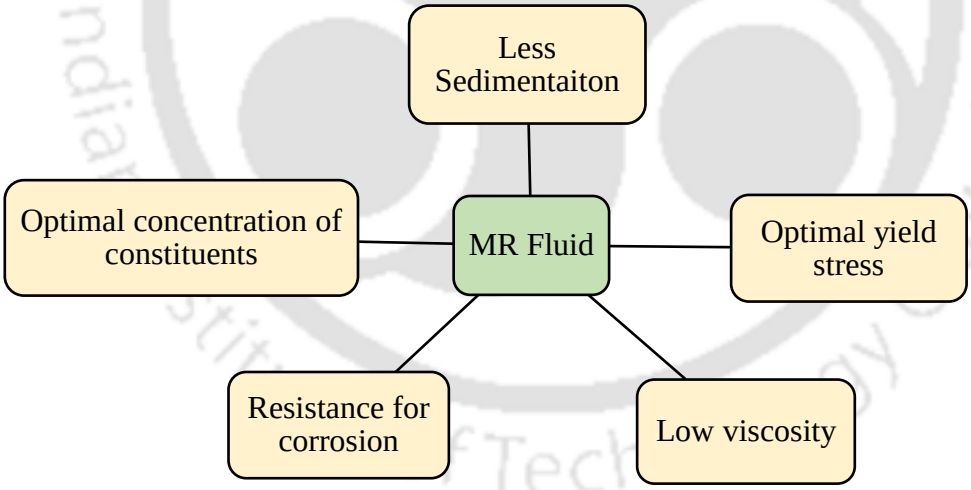

Fig. A.1 Features of MR fluid

Appropriate chemistry is required between the workpiece and MR fluid to achieve the desired surface finish. Initially, MR fluid-assisted finishing operations were found to be limited to only ceramics, quartz, and glasses. However, with the continuous development in MR fluid compositions, the process is now equally available for metallic objects. A list of suitable MR fluids & their compatible material is provided in Table A.2.

Table A.1 Composition of MR fluid to reduce particle agglomeration

Sl. No.	MR fluid composition to reduce particle agglomeration	Ref.
1	Coated iron particles with AlSt with the carrier fluid	[210]
2	Coated iron particles with lecithin or SDS	[211]
3	Oleic acid with MR fluid	[212]
4	Grease With MR fluid	[213]
5	Tetramethylammonium oxides with MR fluid	[214]
6	Thixotropic agents like carbon fibers, nanoparticles of silica with MR fluid	[215] [216]
7	Surfactants like Oleic acid or stearic acid with MR fluid	[217]
8	The viscoplastic base medium as a continuous phase with MR fluid	[218]
9	Water in oil emulsions as carrier liquid with MR fluid	[219]
10	Adding magnetic nanoparticles to MR fluid with MR fluid	[220] [221]
11	Reduced iron powder with SiC, water, and PEG with MR fluid	[222]
12	Sintered magnetic abrasives 45 vol% and 55 vol% carrier fluid	[223]
13	CIP with Nonvolatile hydrocarbon and deionized water (4.5 wt. %)	[224]
14	CIP 4% with deionized water 88%, and 4% stabilizer	[225]
15	CIP 30% (CL grade) with 10% SiC abrasive, 12% grease, and 48% paraffin oil	[226]
16	Fluid containing cubic Fe_3O_4 nanoparticles	[227]
17	CIP with Deionized water, stabilizer, cerium oxide, and additives	[228]
18	CIP with polishing abrasive particles, water, and stabilizers	[229]
19	CIP 38.2% , deionized water 58.4 %, glycerol 2.6%, CeO_2 5 % (% by volume)	[230]
20	CIP 36%, water 57%, CeO_2 6%, stabilizing agent 1% (% by volume)	[231]

Analysis of the quantitative behavior of MR fluid during the finishing processes is essential to optimize its effects on surface quality. Seok et al. [232] proposed an analytical model based on the dual characteristics (solid and liquid) of MR fluid to analyze the material removal rate of the workpiece, as shown in Eq. (A.1).

$$\frac{dz}{dt} = \alpha\left(\mu_s P V_p + \frac{\eta}{H} V_p^2\right) \tag{A.1}$$

Where $\frac{dz}{dt}$ is the rate of change in the workpiece height, α is proportionality constant, μ_s is the coefficient of static friction, P is pressure applied over MR fluid, V_p is workpiece velocity, η is apparent viscosity, and H is MR fluid ribbon height. Apart from this, various analytical models have been developed to analyze the relationship between the shear stress and shear strain of

MR fluid, as listed in Table A.3. However, a detailed discussion of the different MR fluid-assisted finishing processes is provided in the following section.

Table A.2 Compositions of MR fluid for different materials

Sl. No.	Material		Compositions (Vol. %)	Reference
1.	Infrared (IR)	LiF, AMTIR-1, MgF_2	36% CIP, 2.7% alumina, 58% water and 3% stabilizer	[233]
		CaF_2, ZnS, BK7	36% CIP, 5.1% alumina, 55.9% water and 3% stabilizer	
		ZnSe	36% CIP, 5.4% 9220 nanoalumina, 55.6% water and 3% stabilizer	
		Al_2O_3	36% CIP, 5.7% CeO_2, 55.3% water and 3% stabilizer	
		CVD diamond	36% CIP, 2.5% 9220 nanoalumina, 58.5% water and 3% stabilizer	
2.	Brass		15% CIP, 18% alumina, 65% paraffin oil and 2% AP3 grease	[234]
	Stainless steel			
3.	Ti alloy		30% CIP, 10% diamond, 52% deionized water and 8% glycerol	[235]
4.	Co-Cr alloy		25 vol.% CIP, 20% SiC, 59% paraffin oil and 6% AP3 grease	[236]
5.	Borosilicate glass		36% CIP, 5% diamond, 60.9% water and 3% stabilizer	[237]
6.	Mild steel		20 vol.% CIP, 25%SiC, 44% paraffin oil and 11% AP3 grease	[238]
7.	Al alloy		36% CIP, 5% Al_2O_3 and fumed SiO_2, 60% paraffin oil, 3% glycine and 2% glycerol	[239]
8.	Silicon		20% CIP, 6% CeO_2 and 74% deionized water	[240]
9.	K9 mirror		33.84% CIP, 2.82% stabilizing agent, 57.34% silicone oil, and 6% CeO_2	[150]

Table A.3 Mathematical models to analyze relationship between shear stress and shear strain of MR fluid

Sl. No.	Model Name	Equation	Reference
1.	Bingham plasticity	$\tau = \tau_0(H)sgn(\dot{\gamma}) + \eta\gamma; \lvert\tau\rvert > \lvert\dot{\tau}\rvert$ $\tau = 0; \lvert\tau\rvert < \lvert\dot{\tau}\rvert$	[241]
2.	Herschel-Bulkley	$\tau = \tau_0 + k\gamma^n$	[242]–[246]
3.	Robertson-stiff [R-S]	$\tau = k(\dot{\gamma}_0 + \dot{\gamma})^n$	[247][248]
4.	Mizrahi-berk	$\tau^{0.5} = \tau_0^{0.5} + k(\dot{\gamma})^n$	[249]–[251]
5.	Casson	$\sqrt{\tau} = \sqrt{\tau_0} + \sqrt{\mu_p\gamma}$	[156], [252], [253]
6.	Sisko	$\mu = \mu_\infty + k(\dot{\gamma})^{n-1}$	[254]
7.	Williamson	$\mu = \mu_0 + k(\dot{\gamma})^n$	[255]

τ: Shear stress; η/μ: Apparent viscosity; μ_∞: Sisko viscosity
τ_0: Yield stress; k: Consistency factor; μ_0:Williamson viscosity
H: Magnitude of magnetic field; n: Flow index
$\dot{\gamma}$: Shear strain rate; μ_p: Plastic viscosity

A.3 MR fluid assisted finishing processes

Numerous efforts were made in the last few decades to develop MR fluid-assisted finishing processes such as *Magnetorheological Finishing* (*MRF*), *Rotational Magnetorheological Flow Finishing* (*R-MRAFF*), *Ball End Magnetorheological Finishing* (*BEMRF*), *Magnetorheological Abrasive Flow Finishing* (*MRAFF*), *Chemo-Mechanical Magnetorheological Finishing* (*CMMRF*) and *Magnetorheological jet finishing* (*MR Jet Finishing*), *Magnetorheological Honing* (*MRAH*) [6]–[10]. The timeline of these processes' development is shown in Fig. A.2, and their comprehensive study is discussed in the subsequent sections.

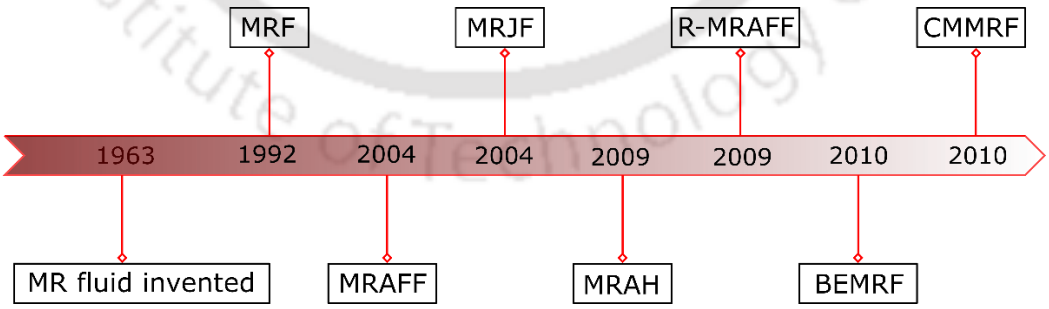

Fig. A.2 Features of an MR fluid timeline of the development of magnetorheological fluid-assisted finishing process

Magnetorheological finishing (MRF)

In 1992, Kordonski et al. developed the MRF process at nskthe Luikov Institute of Heat and Mass Transfer in Minsk, [256][257]. Afterward, several efforts were made to enhance its efficiency [258]–[260], and the first enhanced automated MRF process was developed by QED Technologies Inc. [261]. Herein a workpiece is mounted at a fixed distance from a rotating carrier wheel, which carries MR fluid in the shape of a ribbon, as shown in Fig. A.3. An electromagnet is placed underneath the wheel surface, creating a magnetic flux in the gap between the workpiece and the rotating wheel. A nozzle delivers a stable and uniform ribbon of MR fluid over the wheel. However, the MR fluid ribbon pulled against the wheel surface by the magnetic field generates the normal and tangential forces at the contact zone with the workpiece, as shown in Fig. A.4 (a) and (b). Furthermore, normal force assists the indentation of abrasives in the workpiece, whereas tangential (drag) force generates the shear action. The forces' combined effort helps plow out material from the workpiece. Meanwhile, normal force primarily depends on the workpiece's immersion depth, regulated through the ribbon height. Although to generate a stable and uniform MR fluid, height of ribbon must be above 0.4 mm [262]. Apart from ribbon height, key process parameters of the MRF process is shown in Fig. A.5.

Although constant carrier wheel speed is obligatory during the finishing of isotropic materials, for anisotropic materials, it engenders lopping defects, as different crystallographic orientation causes non-uniform hardness of anisotropic materials to overcome this; optimized dwell time algorithms are depleted, which maps the surface and accordingly provides more finishing time to finish hard crystals as compared to the soft ones. [263].

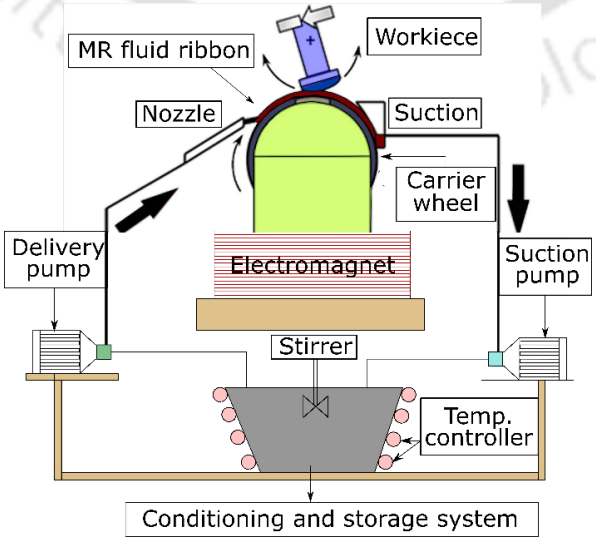

Fig. A.3 Schematic diagram of MRF process

Initially, MRF was developed to finish ceramics, glass, and quartz materials to achieve a mirror-like finished surface (R_a value up to nanometers). However, with further improvement in the process, soft optical polymers like polymethyl methacrylate (PMMA), polycrystalline zinc sulfide (ZnS), water-soluble single crystals like potassium dihydrogen phosphate (KDP), and chemical-vapor-deposited (CVD) can also be finished without taking out the nodule texture on the surface [264]. The major challenge in the preexisting technique is to finish freeform surfaces. To overcome this, Seok et al. [265] developed a disc-type permanent magnet-based tool, herein rotary motion is provided to the tool to activate the shear action of MR fluid, as shown in Fig. A.6. However, a convex surface of stainless steel is given over the disc's curved surface on which a layer of MR fluid is provided to finish the freeform workpiece. A freeform surface of silicon was finished to analyze its effectiveness, and a surface roughness (R_a) of 40 nm was achieved.

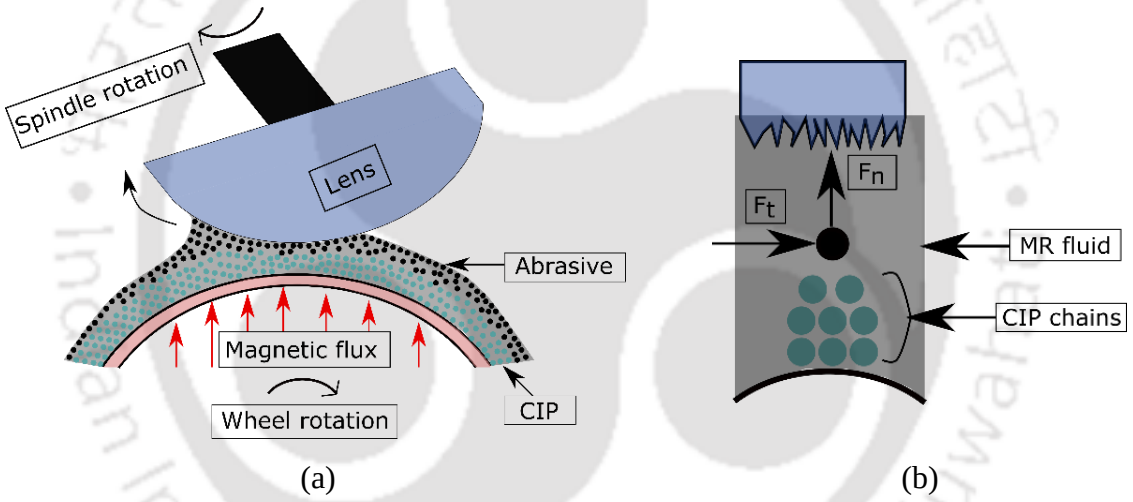

Fig. A.4 (a) Detailed view of MRF process and (b) forces acting on abrasive

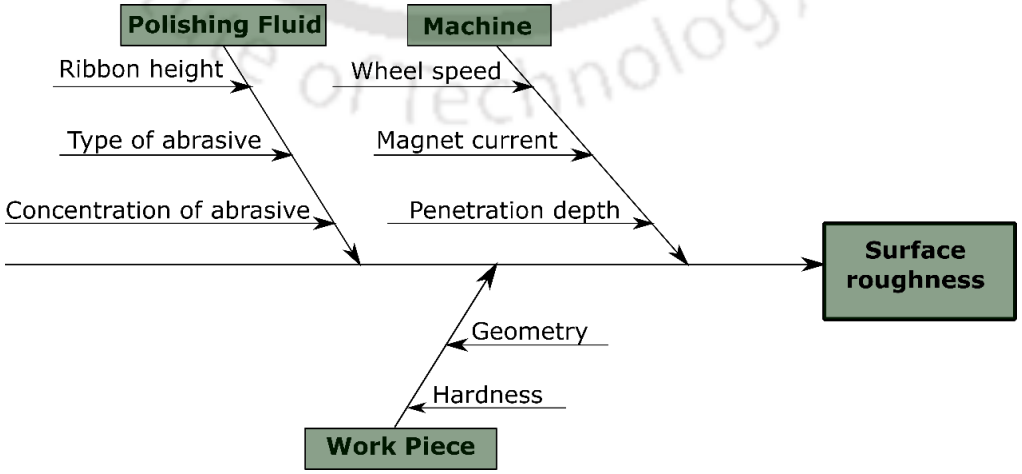

Fig. A.5 Ishikawa cause and effect diagram of MRF process

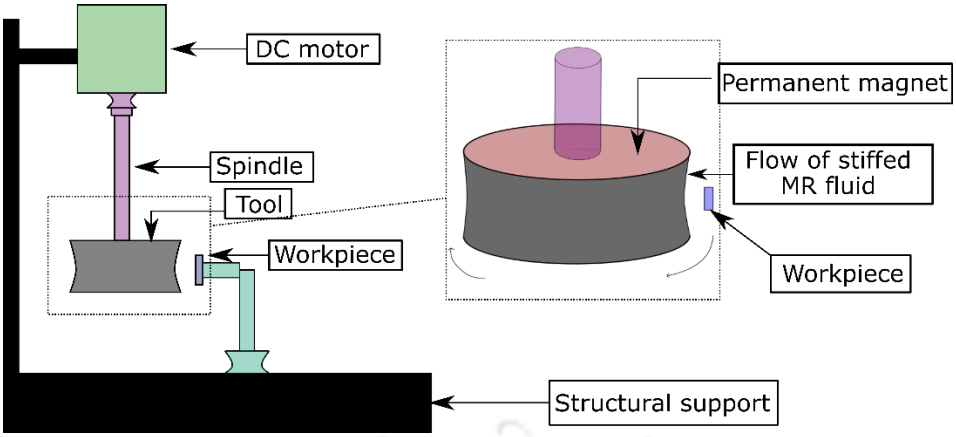

Fig. A.6 Tool design of disc-based magnetorheological finishing

Ball end magnetorheological finishing process (BEMRF)

In 2010, to achieve a precise surface finish of flat, three-dimensional, intricately shaped surfaces such as grooves, overhangs/undercuts, with better control over the forces, Singh et al. [108] developed BEMRF. Herein, pressurized MR fluid is allowed to enter the channel provided in the tool through a rotary union, as shown in Fig. A.7 [266]. However, with the assistance of an electromagnet, the concentrated magnetic field is generated at the bottom of the tool. Therefore, a ball-end-shaped MR fluid structure with very high viscosity is formed at the tool's tip [231]. Meanwhile, the metal particle present in the MR fluid arranged themselves alongside the path of the external magnetic field, with the non-magnetic abrasive particles having cutting edges grasped in between.

However, the normal forces and shear force, generated due to relative motion between the tool and workpiece, help in indenting abrasives and facilitates the abrading action to plough out the unevenness from the workpiece surface. However, these forces are precisely controlled by varying external magnetic fields according to the necessities [267]. Furthermore, tool rotation is provided to achieve a high shear rate at the tool-workpiece interface, as shown in Fig. A.8 [268] [269]. However, a precision workstation and sophisticated computer algorithms ensure this process is automated and robust [270].

Meanwhile, the magnetic field's magnitude determines the mechanism of wear, i.e., in a higher magnetic field, metal particles hold abrasives tightly and eliminate any chance of its rolling during the finishing operation. Hence, two body finishing mechanism is firmed with the workpiece. Whereas, with the lower magnetic field, abrasive rolled from metal particles over the workpiece, and three bodies finishing mechanism is firmed. However, the latter case is unfavorable, generating abrasion, plowing, and indentation marks over the finished surfaces.

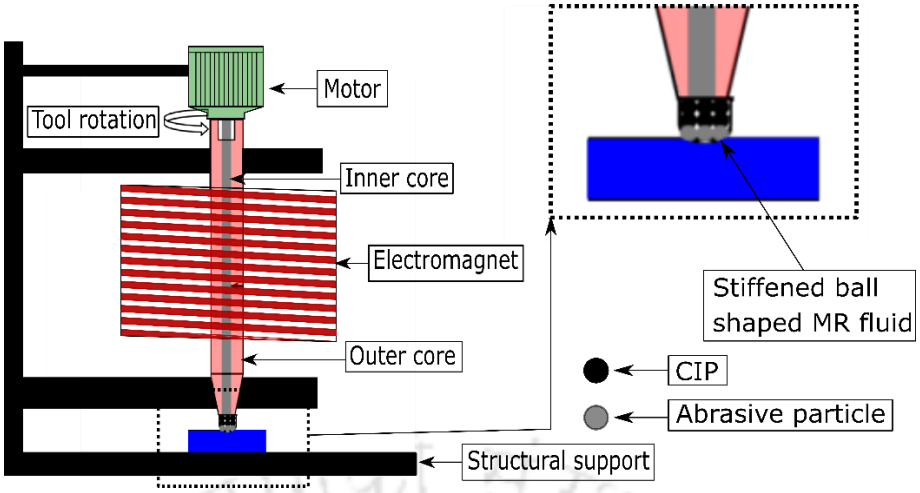

Fig. A.7 BEMRF tool with different components

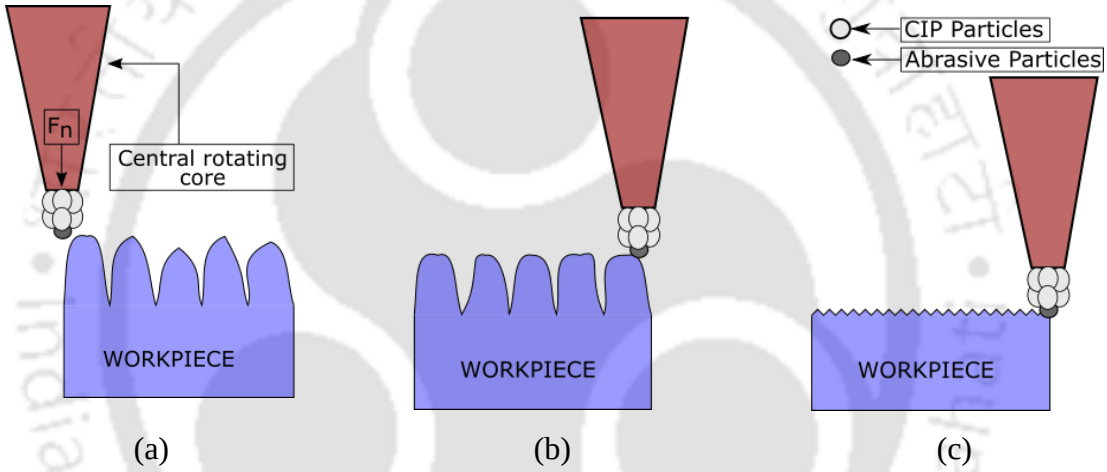

Fig. A.8 Material removal in BEMRF process (a) tip of tool embedded with MR fluid approaching for finishing process, (b) enhanced surface roughness after removing some workpiece material, and (c) final surface roughness after removing undulations from workpiece surface

Although while finishing non-ferromagnetic material, the magnetic field distribution is not uniform through the workpiece, reducing the finishing forces. To overcome this problem, Khan et al. [271] used a permanent magnet beneath the workpiece, which generates a uniform magnetic field. Hence, copper (non-ferromagnetic) was finished with 60 minutes of finishing time, and surface roughness (R_a) of 102 nm was obtained. Achieving a subtle surface finish for fused silica glass (used in high-energy laser pulses) is challenging. Therefore, exploiting oxide cerox 1663 powder as an abrasive in the MR fluid generates a surface roughness (R_a) of 0.14 nm with a magnetizing current of 2.4 A through BEMRF [78]. However, magnetizing current above 2.4 A produced deep scratch marks on the finished surface, as high normal force is engendered. Along with magnetizing current, different process parameters of the BEMRF process are shown in Fig. A.9.

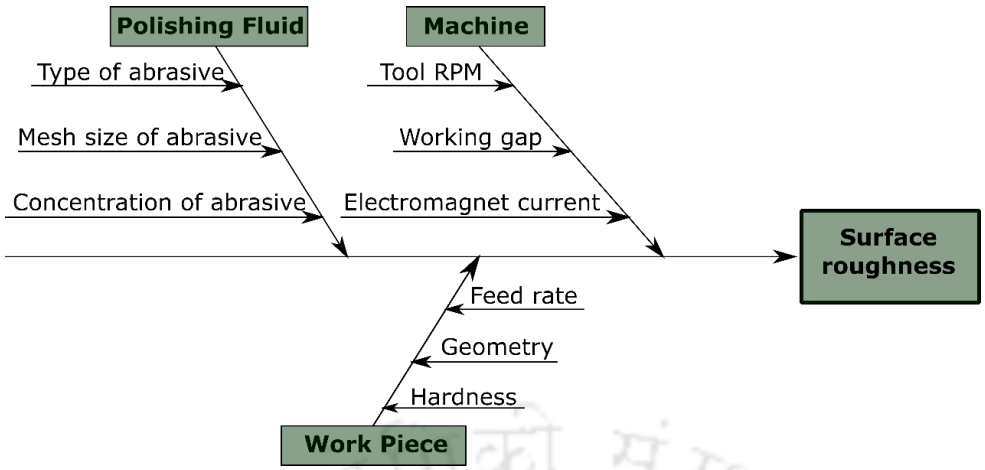

Fig. A.9 Ishikawa cause and effect diagram of BEMRF

Magnetorheological abrasive flow finishing (MRAFF)

In 2004 to produce a uniform surface finish with a constant velocity flow of MR fluid, Jha and Jain developed MRAFF at IIT Kanpur [272]. However, MRAFF is a hybrid process that utilizes synergy between two methods, i.e., magnetorheological finishing (MRF) and abrasive flow machining (AFM). Herein the synchronized motion of two in-lined opposite-placed pistons helps to produce the reciprocating motion of MR fluid. Though, the hydraulic system drives these pistons. However, the workpiece is positioned correctly in the fixture, and the MR fluid flows over it, as illustrated in Fig. A.10. The magnetic field is provided where the workpiece is placed to get MR fluid assistance, and other areas are kept unaffected. Hence, MR fluid's reciprocating motion generates the shear stress required to plow out the materials from the workpiece and provide better surface roughness. However, the magnitude of the magnetic field defines the material removal rate during the finishing operation, i.e., when the low magnetic field is applied, abrasive particle roll over the surface as shown in Fig. A.11 (a), with further increase in the magnetic field, the material gets removed as shown in Fig. A.11 (b) and (c). Hence the surface of the workpiece enhance with an increase in the magnetic field. However, to control the surface finish precisely, different process parameters of the MRAFF process are shown in Fig. A.12.

The appropriate composition of the MR fluid is crucial to accommodate the finishing processes. Therefore, 20% CIP (Grade CS from BASF, 18-micrometer average particle size), 20 % abrasive of 400 mesh size, and 60% of carrier fluid with additive (Vol. %) are the required constituents in MR fluid for MRAFF. However, to achieve surface roughness (R_a) of 340 nm, a magnetic field of 0.574 T is needed with 200 finishing cycles. Meanwhile, an analytical analysis is proposed to analyze MR fluid behavior during the MRAFF process. Thus, It was

noticed that MR fluid viscosity (μ) changes in a third-order logarithmic function of the magnetic field (B) and also yields strength (τ_y) of the MR fluid increases with an increase in the magnetic field, as shown in Eqs. (A.2) and (A.3) [273].

$$\mu = 5918.57 + 10191.33\ln(B) + 6110.52(\ln(B))^2 + 1222.70(\ln(B))^3 \quad \text{(A.2)}$$

$$\tau_y = -33.10 + \frac{67.09\ln(B)}{B} + \frac{51.4}{B^{1.5}} \quad \text{(A.3)}$$

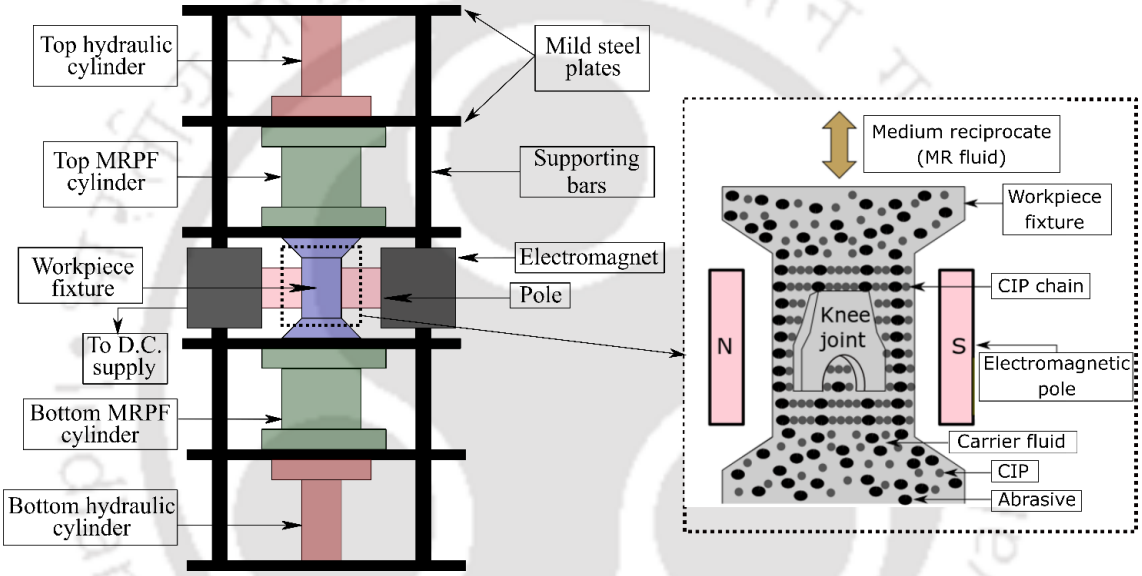

Fig. A.10 Experimental setup of MRAFF with different components

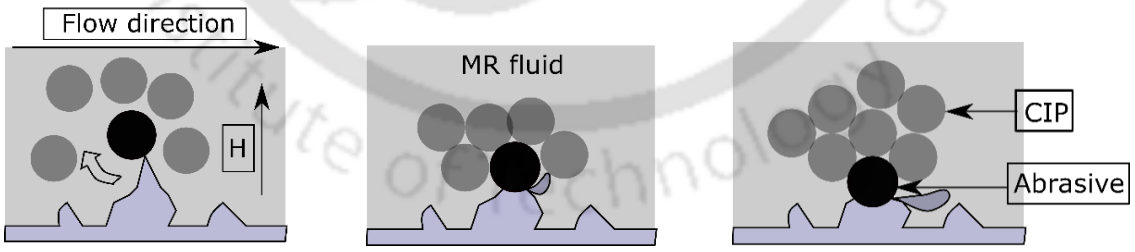

Fig. A.11 Finishing action of an abrasive on a single peak: (a) abrasive particle rolling over roughness peak, (b) abrasive particle takes a small cut on roughness peak, and (c) abrasive grain takes a big cut on roughness peak

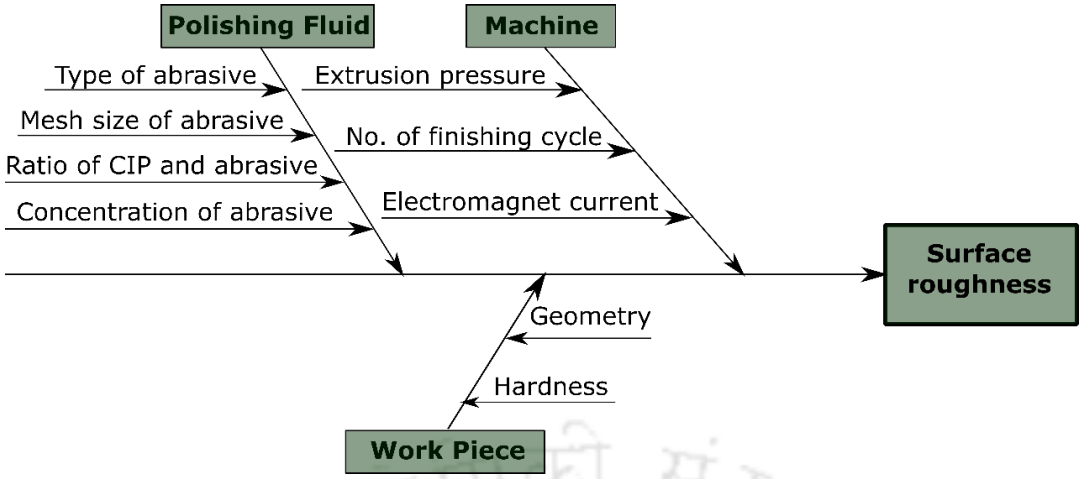

Fig. A.12 Ishikawa cause and effect diagram of MRAFF process

Rotational-magnetorheological abrasive flow finishing (R- MRAFF)

In 2009, to enhance MRAFF process efficiency, Das et al. developed R-MRAFF, as shown in Fig. A.13. Herein, rotational motion is provided to magnets, Instead of keeping them fixed (as in the case of MRAFF) to increase abrasive particles' effectiveness. It is because the rotational motion generates a centrifugal force on the abrasive, and its resultant action with axial (generated because of reciprocation of MR fluid) helps to move the abrasive in the helical path shown in Fig. A.14 (a) [274]. Whereas, in the case of MRAFF, abrasives follow a straight path, as shown in Fig. A.14 (b). Now, in the helical path, the effective length traveled by an abrasive increases compared with the straight path; hence, its effectiveness is improved. To validate this, surface finishing on a knee joint implant is conducted [275], and it is found that the finishing rate in R-MRAFF was 0.104 nm per hour, which is greater than MRAFF 0.052 nm per hour, with a better surface finish. However, three different forces were responsible for performing surface enhancement, i.e., magnetic force (F_m), centrifugal force (F_{cen}), and axial force (F_a), as shown in Fig. A.14 (c). Furthermore, F_m and F_{cen} assist in indenting abrasive in the workpiece, whereas F_a helps to generate the shearing action, and the combined effort of all the forces aids in removing material [276].

Parametric analysis of various process parameters shown in Fig. A.15 is examined with their effects on surface finish [277]. However, it was noticed that the magnet's rotation speed has the highest contribution to the surface finish among all the process parameters. Although, with an increment in the magnet's rotational speed, the surface quality of the material improved, after a specific limit, the surface quality deteriorated because the CIP's holding capacity to hold abrasive gets vanished, and the disorderly action of abrasive generated scratch marks on the surface [278].

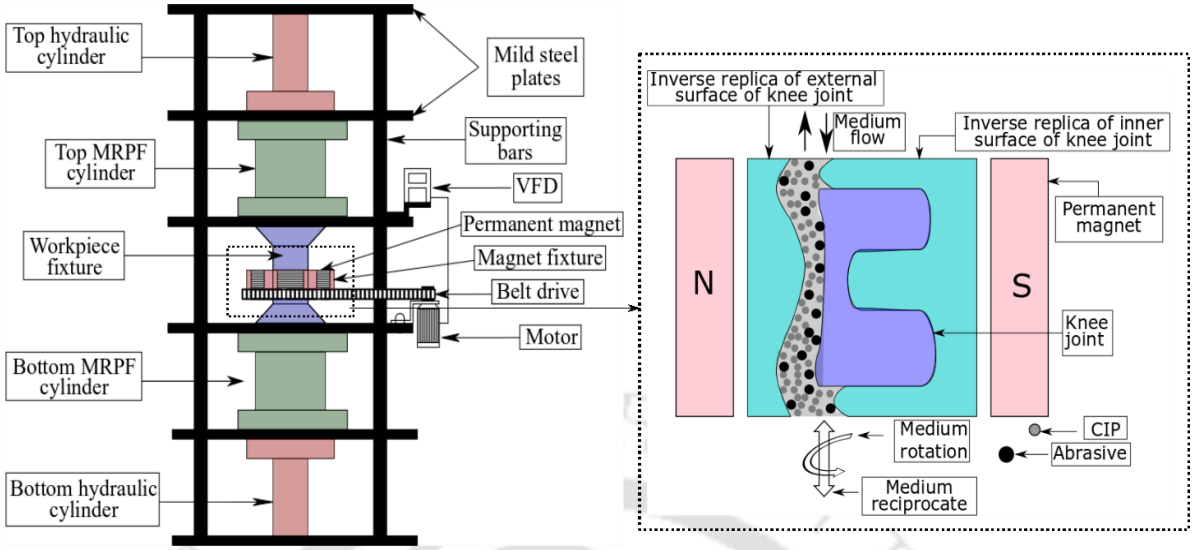

Fig. A.13 Experimental setup of R-MRAFF

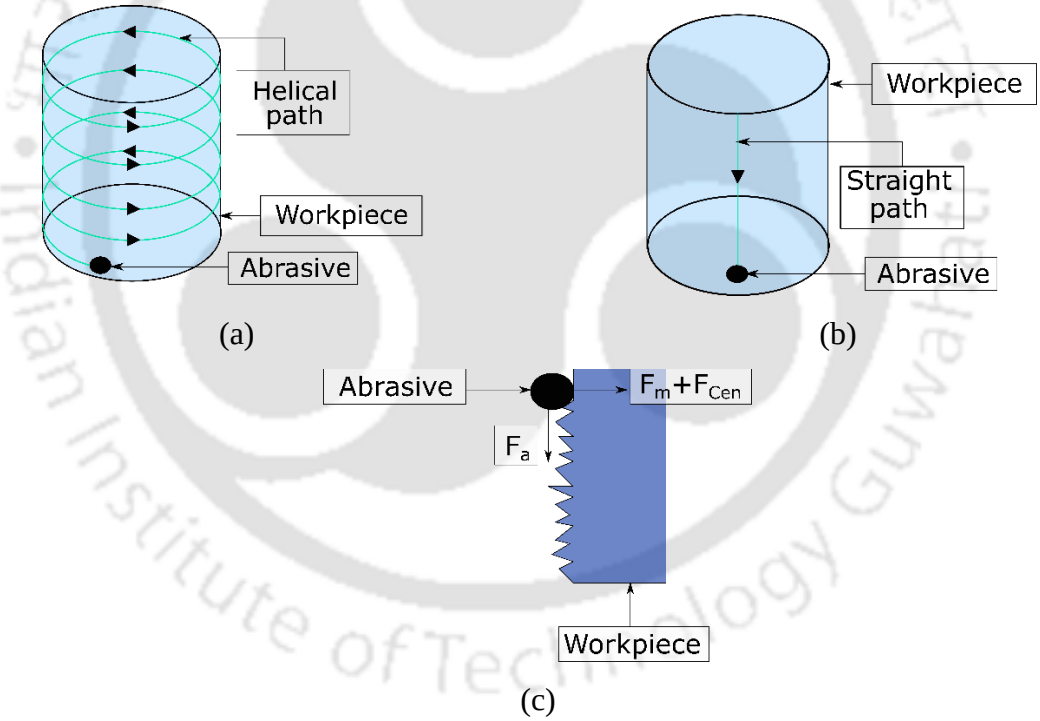

Fig. A.14 Traced path of a single abrasive particle on cylindrical workpiece during (a) R-MRAFF, (b) MRAFF, and (d) different forces acting during R-MRAFF

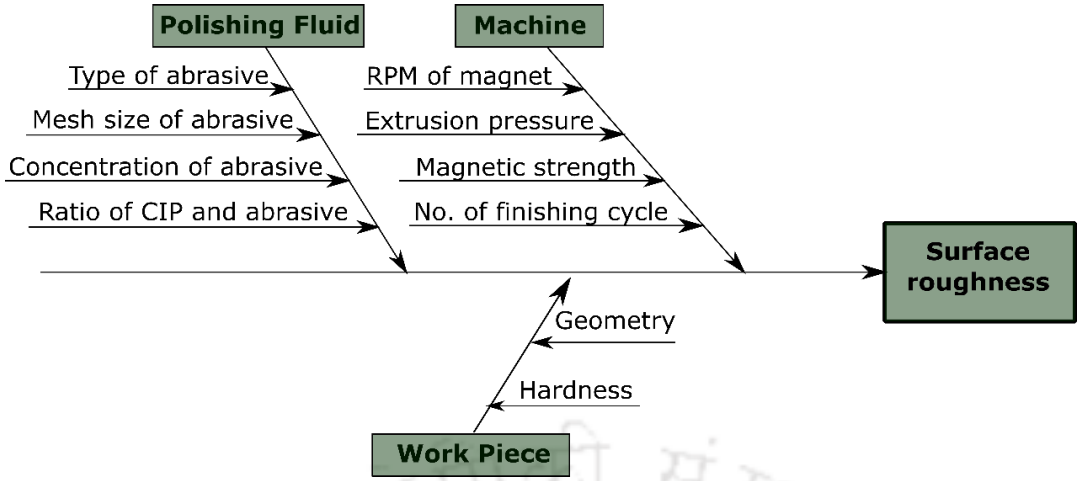

Fig. A.15 Ishikawa cause and effect diagram of R-MRAFF

A.4 Critical analysis

The MR fluid-assisted finishing process review provides insight into a broad area of this Nano finishing technology. Therefore, by analyzing, it is found that MRF is best suited to finish optical components, whereas, to finish ductile materials, BEMRF is proficient among the MR fluid-assisted finishing processes, as shown in Fig. A.16. However, there are some challenges allied with these advanced finishing processes. Hence, the limitations associated with MR fluid-assisted finishing techniques and their benefits are listed in Table A.4.

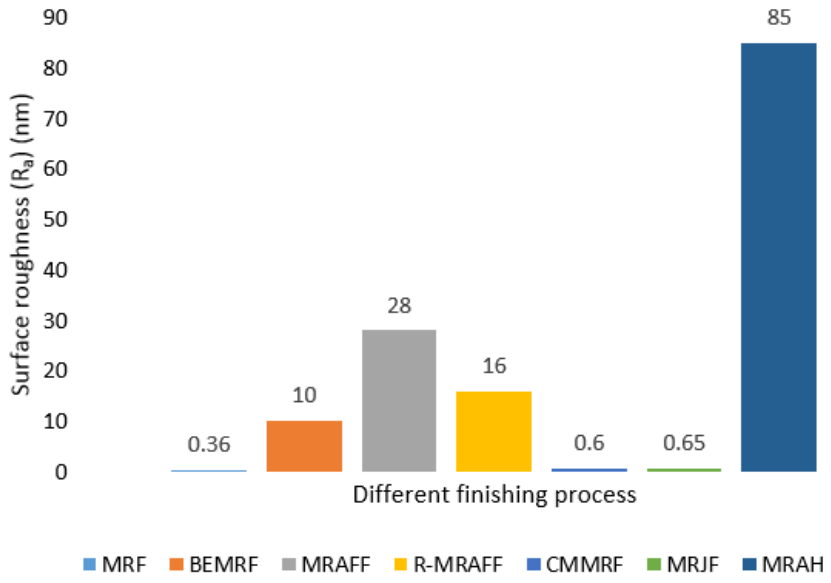

Fig. A.16 Surface roughness achieved by different finishing processes

However, lots of development is required to improve the efficiency and effectiveness of these finishing processes. Hence, the unstable areas where improvisation is needed to improve

its process capability are listed in Table A.5. Moreover, MR fluid-assisted finishing processes are utilized in different sectors to attain better surface quality, such as in optical industries, MRF is exploited to enhance the surface quality of the lens, mirrors, etc.; in biomedical, R-MRAFF and BEMRF are used to finish prostheses implants (hip, knee prosthesis, etc.), in the electronics industry, CMMRF is applied to finish silicon crystals; however, the surface quality of industrial components such as micro gears, nozzles, etc. also get enhanced.

Table A.4 Key capabilities and limitations of various MR-fluid-based finishing processes

Process	Benefits	Limitations
MRF	In a fully automated system, surface roughness up to atomic level can be achieved.	Only applicable for optical materials and ceramics.
BEMRF	Freeform surfaces can be finished.	Low productivity.
MRAFF	Almost uniform surface quality can be achieved.	Every time a change in the workpiece fixture is required with a slight change in the workpiece design.
R-MRAFF	Surface accuracy is high.	Low productivity.
CMMRF	the surface roughness up to atomic level can be achieved.	Not applicable for materials having high hardness like Ti alloy, Co-Cr alloy, etc.
MRJF	Stabilizes the fluid to finish steep cavities and concave surfaces.	Not applicable for freeform surfaces.
MRAH	Reduction in the finishing time because of the rotation of the workpiece.	Not applicable for freeform surfaces.

Table A.5 Critical research area of MR fluid-assisted finishing processes

Unstable	Process	Stable
Well developed.	**MRF**	In situ surface metrology, Ribbon height, workpiece position, tool position, wheel speed, magnetic flux, and penetration depth.
Working gap, the height of the MR fluid brush.	**BEMRF**	Tool rpm, magnetic flux workpiece position, and tool position
In situ surface metrology, the velocity of flowing fluid.	**MRAFF**	Number of finishing cycles, magnetic flux, and extrusion pressure.
In situ surface metrology, the velocity of flowing fluid.	**R-MRAFF**	Number of finishing cycles, magnetic flux, extrusion pressure, and magnet rpm.
In situ surface metrology, working gap, and height of MR fluid brush.	**CMMRF**	Tool rpm, magnetic flux workpiece position, and tool position.
In situ surface metrology and working gap.	**MRJF**	Jet velocity, magnetic flux workpiece position, and tool position.
In situ surface metrology and working gap.	**MRAH**	Workpiece rpm, magnetic flux workpiece position, and tool position.

Appendix B Nanofinishing of Directed Energy Deposited Topologically Optimized Bone Plates

B.1 Introduction

Bone can heal itself without leaving a scar through natural processes such as inflammation, cartilage growth, and bone remodeling [300]. However, in cases of severe or pathological fractures, the bone's ability to heal can be limited, resulting in delays or non-union problems that need additional treatments, such as bone fixation implants [301]. In the United States, it is assessed that there are 15×10^6 fractures each year, costing over 60×10^9 dollars [302][303]. Bone fixation is a common surgical procedure used to treat broken bones. The procedure involves pins, screws, plates, and rods to stabilize and immobilize the broken bone [304]. This helps to hold the bone in place while it heals. The bone fixation implants that are commercially available are usually made of metallic materials such as stainless steel, titanium, cobalt, and its alloys [305]. However, in many cases, the body permanently contains these implants, leading to several long-term problems [306], including releasing metal ions, which can cause inflammation and infection and lead to screw loosening. One of the most significant concerns is the effect of these metallic implants on the bone itself. The stiffness of these metallic materials is much higher than that of natural bone [307]. The significant difference in mechanical characteristics between bone and metal materials may result in bone stress shielding, when the implant bears the load instead of the bone, and can cause bone instability and loss. The modulus of elasticity of the cortical bone ranges between 3-30 GPa; however, the modulus of elasticity of commonly used biomaterial, i.e., Ti6Al4V, CoCrMo alloys, and stainless steel are 110 GPa, 210 GPa, and 190 GPa, respectively [308].The high rigidity of metal implants can cause stress to accumulate in the fixation device, resulting in plate cracking or screw pullout. Topological optimization is a solution to reduce the stress shielding effect [309]. It is a computational method for finding the optimal distribution of the material in a design to meet certain design objectives, such as minimum weight, maximum strength, or minimum stress concentrations [310]. The method uses mathematical algorithms to adjust the shape and distribution of the material in a design, considering material properties, manufacturing constraints, and loading conditions. Topological optimization can be applied to various design problems, including mechanical, aerospace, and biomedical engineering [311]. In each case, the goal is to create a lightweight and efficient design while meeting other desired

mechanical properties such as strength, stiffness, or fatigue resistance [312]. The outcome of a topological optimization is often a design with a unique, non-uniform material distribution optimized for the specific design objectives. This can result in significant improvements in design performance compared to more traditional, uniform designs, leading to significant material and weight savings. Solid material with penalization is a mathematical model that describes the behavior of solid objects under various conditions, such as stress and strain caused by external loads [313]. It considers the material's elastic and plastic properties, which is how it reacts when stretched or compressed. The model includes a penalty term, a mathematical formula that helps maintain the conditions or constraints imposed on the material. This is important for providing accurate predictions about how the material will behave in different situations. The term "penalty" comes from the idea that if the constraints are not satisfied, the model will apply a stronger force when the constraints are violated [314]. This helps to keep the simulation accurate and helps it converge to the correct solution. This model type is commonly used in engineering to predict the behavior of structures and mechanical components. Tamimi et al. [315] investigated the utilization of 3D topology optimization to produce lightweight metallic implants that have reduced stiffness. This approach aims to mitigate the issues of stress shielding and bone loss. Advanced manufacturing technology can be used to create porous metals that mimic the properties of bones by designing their structures digitally. *Evolutionary Structural Optimization* (*ESO*) and the *Solid Isotropic Material with Penalization* (*SIMP*) methods are examples of analytical models for performing topological optimization. Naichao Wu et al. [316] comprehensively analyzed the advances in topology optimization of orthopedic implants. Here, stainless steel has been replaced by Titanium alloys to fabricate orthopedic implants. Topology optimization has been used on orthopedic implants to reduce stress shielding, a source of serious complications like peri-prosthetic fractures, aseptic loosening, etc. Bone scaffolds, which are 3D matrices that enable and stimulate the attachment and proliferation of osteo-inducible cells on their surfaces, can now be fabricated with mechanical and biological properties more similar to those of trabecular bone. However, fabrication of the topologically optimized through a conventional manufacturing process is unattainable. Although, with the advancement of *Additive Manufacturing* (*AM*) techniques, limitations such as printing precision, structural anisotropy, and pore connectivity of porous structures have been gradually overcome [317]. Hence, in the present work, *Directed Energy Deposition* (*DED*), an AM technique, is used to fabricate the topologically optimized fixation plate. DED is a 3D printing method depositing layer over layer to fabricate the final product. Herein, materials are deposited by melting them using focused thermal energy, such as plasma,

laser or electron beam [318]. DED employs a laser or electron beam as the energy source, which generates a molten pool of feedstock material (powder or wire) directed by the system command to create the desired shape, as shown in Fig. B.1 [319]. This technique has been used to deposit materials such as titanium alloy, steel, stainless steel, and nickel-based alloy [320].

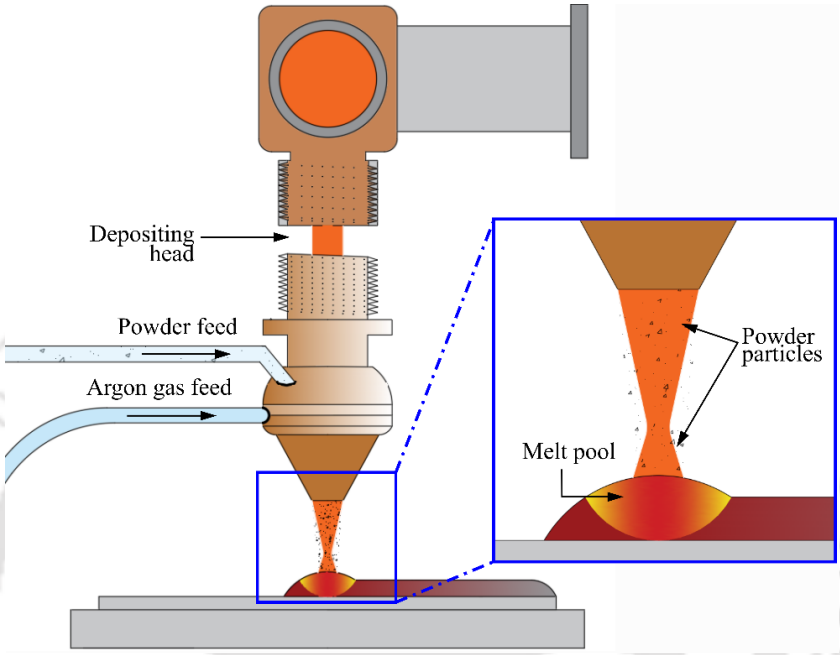

Fig. B.1 Schematic representation of Directed Energy Deposition

However, the DED fabricated part surface requires a post-processing method to improve its surface quality. Hybrid-Electrochemcial Magnetorheological Fluid (H-ECMR) finishing process, an advanced super polishing method, is used to improve the surface quality of the DED fabricated part. Herein, the synergic action of magnetorheological finishing and electrochemical reaction help to produce a uniform surface quality. However, the initial surface roughness of the fabricated part must lie in the submicron range to effectively perform the H-ECMR finishing process. Hence, milling is accomplished on the DED fabricated part before the H-ECMR finishing process. The present work aims to achieve the topological optimization of the fixation plate to reduce the stress shielding effect. The topologically optimized fixation plate is fabricated with the DED, followed by the H-ECMR finishing process to produce a uniform surface quality. Moreover, a Scanning Electron Microscope (SEM) and optical profilometer are used to evaluate the variation in the surface characteristics of the DED fabricated part. The overview of the present work is summarized in Fig. B.2.

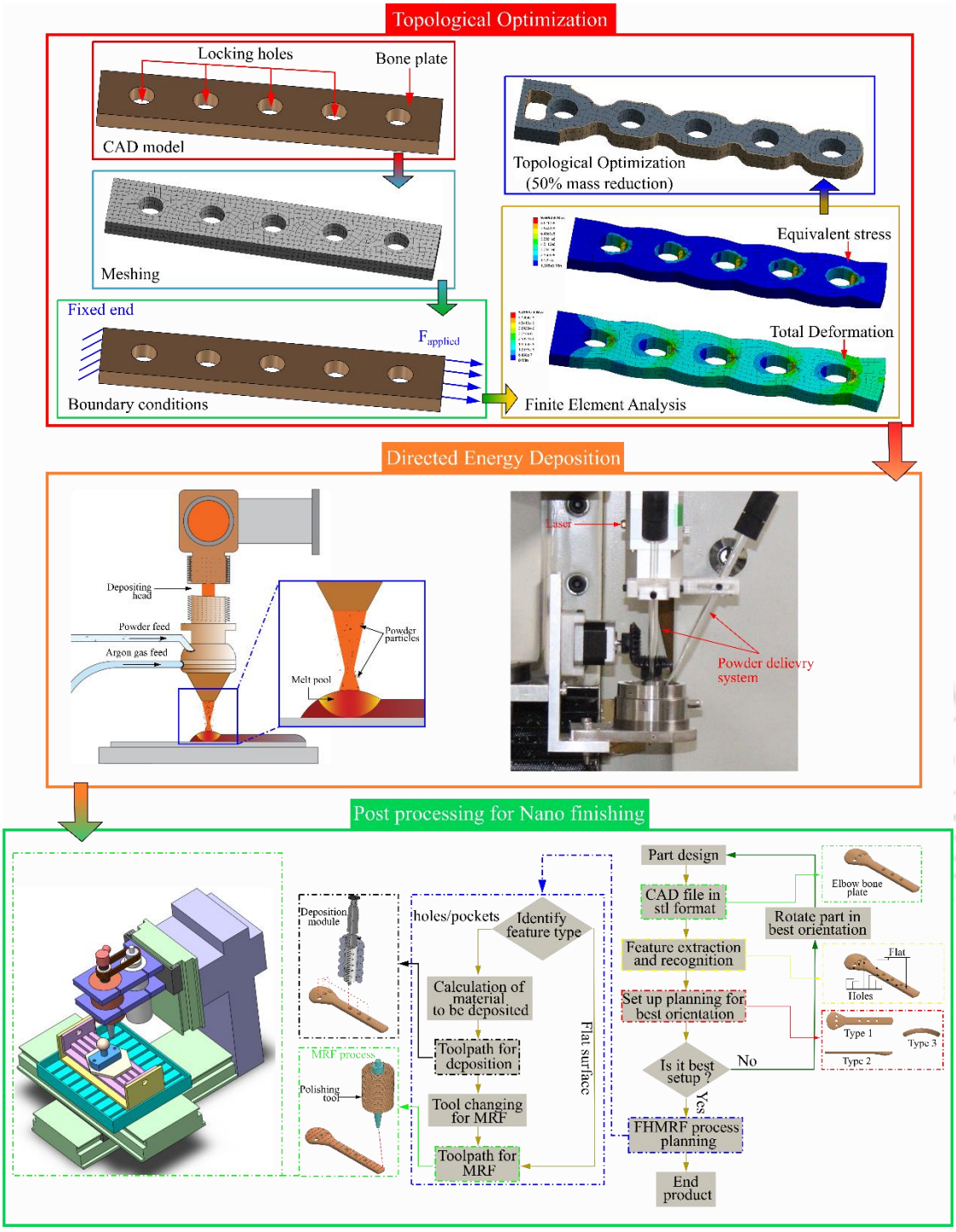

Fig. B.2 Overview of the surface enhancement of the directed energy deposited part

B.2 Methods and materials

Topology Optimization (TO) is a method used to determine the most efficient distribution of materials within a structure. It starts with a *computer-aided design* (*CAD*) model of the structure and divides it into small discrete sections, known as elements, using the *Finite Element* (*FE*) method. Each element is analyzed, and its stiffness or strain is determined, which

helps predict the structure's stress and displacement. Then, each structure component is regarded as a design variable (such as density ρe), and the allocation of materials throughout the structure is adjusted accordingly, according to topological optimization. This is done using a binary strategy, where the material is kept (i.e., solid) or removed (i.e., void) in different structure sections. For the TO calculations in this study, the widely used *Solid Isotropic Microstructure with Penalization* (*SIMP*) method is employed, which aims to minimize the strain energy, constrain the total volume and specify the density of each element. The goal of this process is to create a structure that is robust, efficient, and optimized for specific loads and conditions. Topological optimization is performed through the finite element-based software Ansys. The load is applied at one end of the fixation plate, and the other is kept fixed during the computational analysis. The details regarding the algorithm are discussed in the subsequent section.

Simple evolutionary procedure

The optimal shape and structure of entities available in nature, such as bones, shells, and trees, evolve to adapt to their surroundings over a long period. Topological optimization is a finite element analysis and an evolutionary approach [279]. After analyzing stress distribution using finite element analysis, a *Rejection Criterion* (*RC*) eliminates unused material. If the von Mises stress in an element is below a *Rejection Ratio* (*RR*) multiplied by the highest Von Mises stress over the structure, that element is eliminated. This process is repeated until a steady state is achieved; at this point, an *Evolution Rate* (*ER*) is added to the RR, which is repeated until the desired optimum is reached. The SIMP technique is currently the most widely used mathematical technique for topology optimization [280]. This methodology forecasts the ideal material distribution within a designated area, accounting for load cases, production limitations, performance criteria, and boundary conditions [281]. Broadly defined, optimization consists of determining the occurrence or absence of material at each point within the specified space. To achieve this, the domain is discretized by a finite element mesh comprising isotropic solid microstructures. Each microstructure is assigned either a binary value of ρ_e=1 (black color), signifying the presence of material where required, or a value of ρ_e=0 (grey color), representing material removal where feasible. The SIMP design is grounded on a continuous problem, whereby the objective is to minimize the C (total compliance) parameterized by a coordinates vector $\xi \in \Omega$ with V_c (volume constraint) as shown in Eq. (B.1).

$$min: C \tag{B.1}$$

$$subject\ to: V \leq V_c$$

Within the finite element framework, a designated set of n elements across the vector coordinates $\xi \in \Omega$ represents a given structure. The design variable, x(ξ), represents the discrete availability of material and is subsequently relaxed to yield continuous values within the interval (0,1]. Intermediary values are penalized by utilizing a power law to facilitate convergence toward a discrete topology. The optimization problem is subject to constraints that ensure the elastic equilibrium (Eq. (B.2)) satisfaction with a load vector f and global stiffness matrix K.

$$Ku = f \tag{B.2}$$

The element stiffness K_i can be expressed as a function of the design variable $x = \{x_1, x_2, ..., x_n\}$ as shown in Eq. (B.3).

$$K_i = x_i^P K_0 \tag{B.3}$$

The design variable x_i is bound within the interval (0, 1], while K_0 represents the constant element stiffness when x_i equals 1. With the notation mentioned above for symmetric K, the total compliance can be expressed as presented in Equation (B.4).

$$C_P(X) = f^T u = u^T K u = \sum_i x_i^P u_i^T K_0 u_i \tag{B.4}$$

Furthermore, the optimization statement can be defined through Eqs. (B.5) and (B.6).

$$\min_x : C_P(X) = \sum_i x_i^P u_i^T K_0 u_i \tag{B.5}$$

$$\begin{gathered} subject\ to: V \leq V_c \\ : 0 < x(\xi)_{min} \leq x(\xi) \leq 1 \end{gathered} \tag{B.6}$$

The vector $x(\xi)_{min}$ represents the smallest densities required to prevent singularities, while $V(x)$ denotes the entire material volume at present. The SIMP approach utilizes a penalization

scheme that renders the design space non-convex, potentially leading to local minima. In cases where a higher magnitude of p is used, local minima are frequently encountered instead of the global minima. To overcome this issue, a continuation method is employed. SIMP is initially executed with a penalization of $p_{init} = 1$ until a solution converges. The penalization value is then incremented by 1/2, and the present solution is treated as the initial problem. This process continues until the penalization magnitudes generate a discrete solution while avoiding an ill-conditioned stiffness matrix K.

B.3 Experimental details

SS316L powder particles of 46-106 µm size are used during the fabrication of the DED parts, as shown in Fig. B.3. A ytterbium laser is used to melt the powder particles to produce a robust and focused beam of light. This laser works by using a high-power laser diode to excite the ytterbium atoms in the fiber, which causes them to release light in a very narrow and consistent wavelength. This light is amplified as it travels through the fiber, resulting in a highly efficient and compact laser that can be used for various applications, such as cutting and welding materials, telecommunications, and scientific research. A 1040 nm continuous laser wavelength with a Gaussian profile is generated to fabricate the part. After the fabrication of the DED parts, the milling operation is performed to reduce the surface roughness of the manufactured part in the range of micrometers to operate the H-ECMR process effectively. A face milling cutter (35 mm diameter) removes the unmelted and unbonded powder particles from the substrate. The H-ECMR finishing process is further used to achieve a mirror-like polished surface on the DED fabricated part [282].

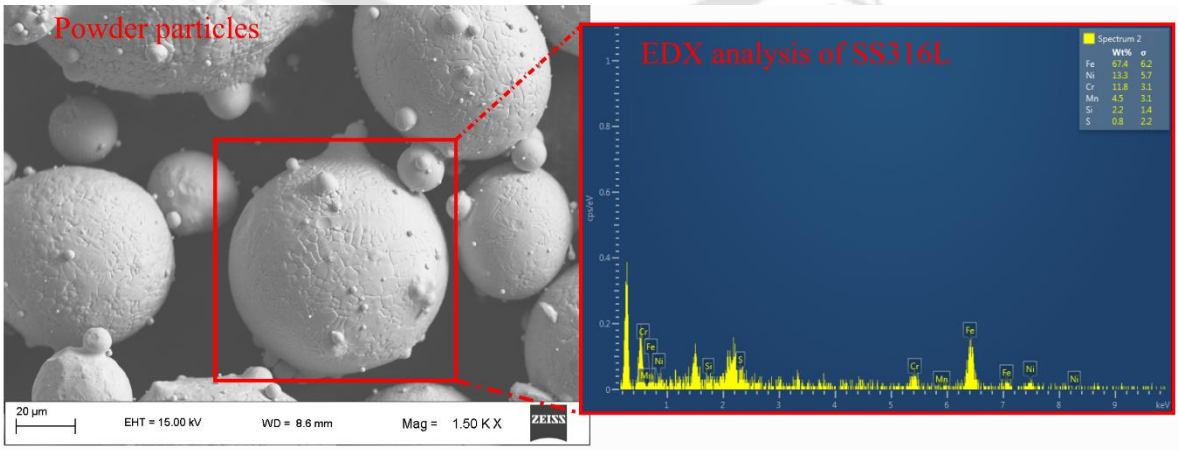

Fig. B.3 SEM and EDX analysis of SS316L powder particles

Herein, the electrochemical reaction combines with mechanical polishing to reduce the surface finishing time and produce unvarying surface roughness on the fixation plate. Mechanical polishing is accomplished with the assistance of *Magnetorheological* (*MR*) fluid. This fluid has tiny magnetic particles suspended in a liquid. When a magnetic field is applied, the particles align and create a semi-solid material that can be used to polish the surface. During the polishing, the material to be polished is placed on a bed of 5 axis CNC milling machine, as shown in Fig. B.4.

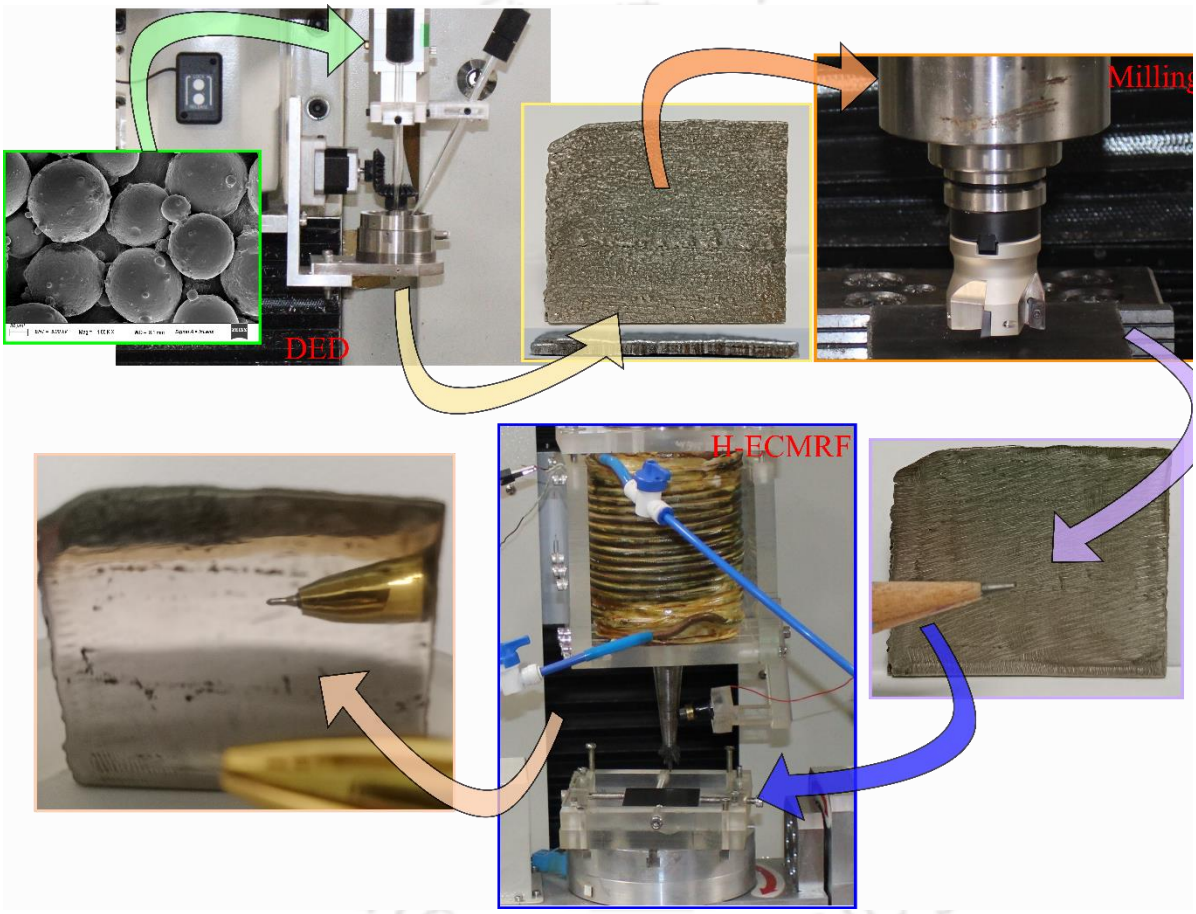

Fig. B.4 Overview of surface enhancement of the directed energy deposited part

The magnetorheological fluid is applied to the bottom of the polishing tool, and a magnetic field is used to create the semi-solid material. The polishing tool is then moved over the material's surface, polishing it to a high degree of precision. The strength of the magnetic field can be adjusted to control the stiffness of the magnetorheological fluid, allowing for precise control over the polishing process [123]. The constituents of the MR fluids are glycerol, phosphoric acid, carbonyl iron particles, diamond abrasive particles, and distilled water. The potential difference between the polishing tool and the workpiece is applied to trigger the electrochemical reaction. Electrochemical reactions remove a thin material layer from a metal

surface to improve its finish and smoothness. The process involves using an electrolyte solution and a cathode (tip of the electromagnet) that is in contact with the metal surface to be polished (anode). When a voltage is applied between the cathode and the anode, a current flow is established through the electrolyte solution (Carrier medium of MR fluid). This current causes an oxidation reaction to occur at the surface of the anode, which results in the formation of a thin layer of metal oxide. The metal oxide is then dissolved by the electrolyte, which removes the roughness and imperfections from the surface of the anode. Combining electrochemical reactions with mechanical abrasion is an effective method for achieving a high-quality surface finish on metal parts and components. Furthermore, a *Feature-based Hybrid MRF Planning System* (*FHMRF-PS*) is used to improve the surface quality of the fixation plate, as it has holes and produces unitability of (*Magnetorheological*) MR fluid during the polishing [283].

B.4 Results and discussion

The present work aims to develop a topologically optimized fixation plate through directed energy deposition. Afterward, a novel *Hybrid-Eelctrochemcial Magnetorheological* (*H-ECMR*) finishing process is developed to improve the surface quality of the fabricated part.

Topological optimization

Structural analysis of the fixation plate for different mass reductions from 40% to 100% is performed to analyze the impact of topological optimization on its mechanical property. The optimized fixation plate for different values of mass retention is shown in Fig. B.5. The total deflection in the fixation plate with 100% mass retention is 1.76×10^{-6} m as its stiffness (5.69×10^{10} N/m) is higher as compared with the other topologically optimized fixation plate. However, the total deflection value in the fixation plate with 50% mass retention is increased by 18.86% as its value rises to 2.09×10^{-6}. The increase in the total deflection for the fixation plate with 50% mass retention is because of its lower stiffness (i.e., 4.79×10^{10} N/m). However, further decrease in the mass retention of the fixation plate leads to produce a discontinuity in its model, as shown in Fig. 4. The stiffness value corresponds to mass retention of 90%, 80%, 70%, and 60% are 5.55×10^{10}, 5.54×10^{10}, 5.25×10^{10}, and 4.99×10^{10} N/m respectively and shown in Fig. B.6(a). However, The energy stored inside the fixation plate under loading, termed strain energy, increased with a decrease in the mass retention of the fixation plate, as shown in Fig. B.6(b). The reduction in stiffness further reduces the stress shielding responsible for bone loss and instability.

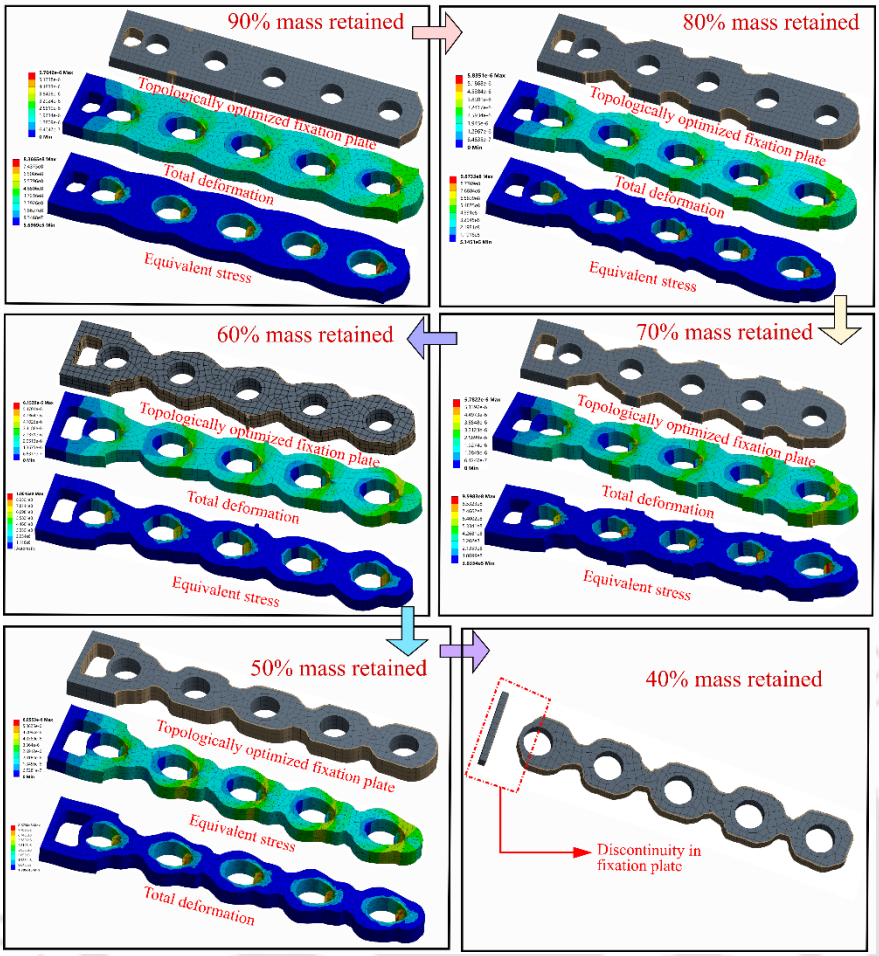

Fig. B.5 Total deformation and stiffness of fixation plates at different mass retention

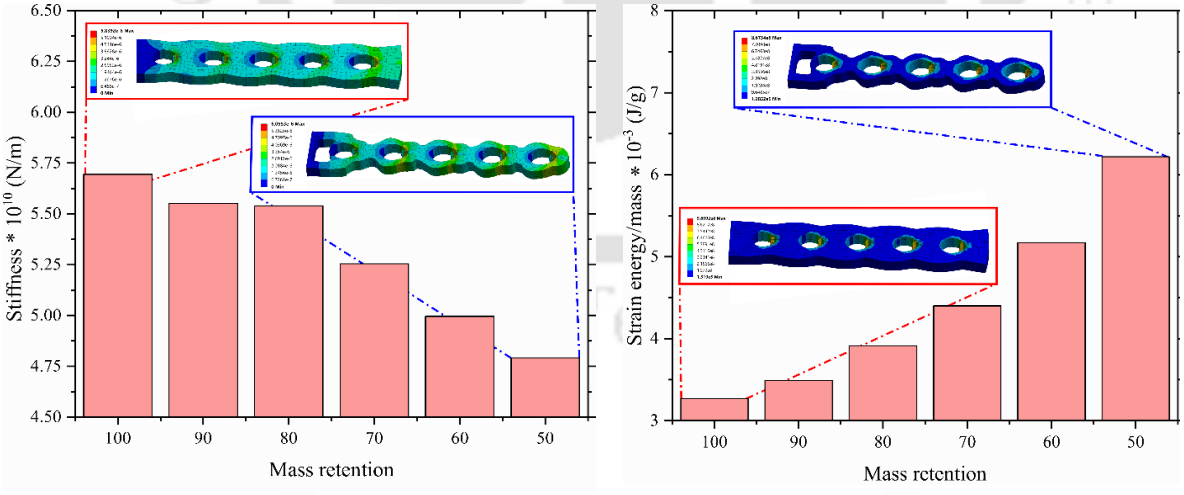

(a) (b)

Fig. B.6 Variation of (a) stiffness and (b) strain rate with mass retention

Table B.1 Mechanical strength of different mass retention of fixation plate

Mass retention (%)	Total deformation (m)	Equivalent stress (Pa)	Equivalent strain
100	1.76×10^{-6}	8.30×10^{7}	4.53×10^{-4}
90	1.80×10^{-6}	7.06×10^{7}	3.81×10^{-4}
80	1.81×10^{-6}	8.78×10^{7}	4.77×10^{-4}
70	1.90×10^{-6}	9.17×10^{7}	4.98×10^{-4}
60	2.0×10^{-6}	1.01×10^{8}	5.52×10^{-4}
50	2.1×10^{-6}	1.03×10^{8}	5.60×10^{-4}

Surface quality

The fixation plate with 50% mass retention is fabricated with the assistance of Directed energy deposition. The SS316L powder particle is fed into the laser to melt to fabricate the fixation plate, as shown in Fig. B.7; the surface quality of the manufactured part is inferior due to the unfused particles and pores, as shown in Fig. B.8. The average surface roughness (R_a) value on the DED fabricated surface is 14.23 µm. The 2D and 1D surface profiles of the DED fabricated part are shown in Fig. B.7.

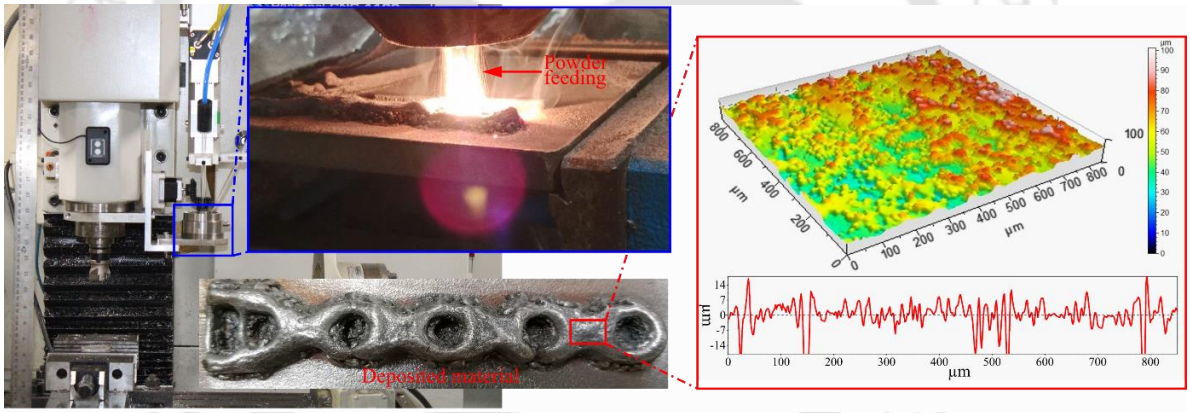

Fig. B.7 Surface profile of DED fabricated part

A milling operation was performed over the fixation plate before the H-ECMR finishing process to reduce the R_a value in a few micrometers range. After the milling operation, the R_a value is reduced to 0.91 µm, and the milled surface's 2d and 1D surface profile is shown in Fig. B.9. However, a few scratched marks are easily visible SEM image of the milled surface as shown in Fig. B.10(a). After the milling operation, the surface defects, including the unmelted, unbonded powder particles and pores, are removed from the additively manufactured bone plate.

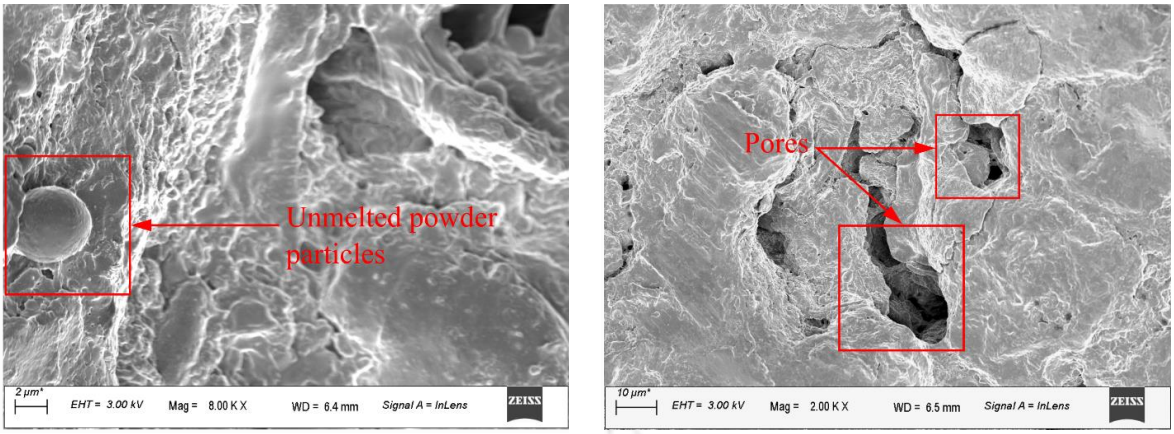

(a) (b)

Fig. B.8 Surface defects on DED fabricated fixation plate (a) unmelted powder particle and (b) pores

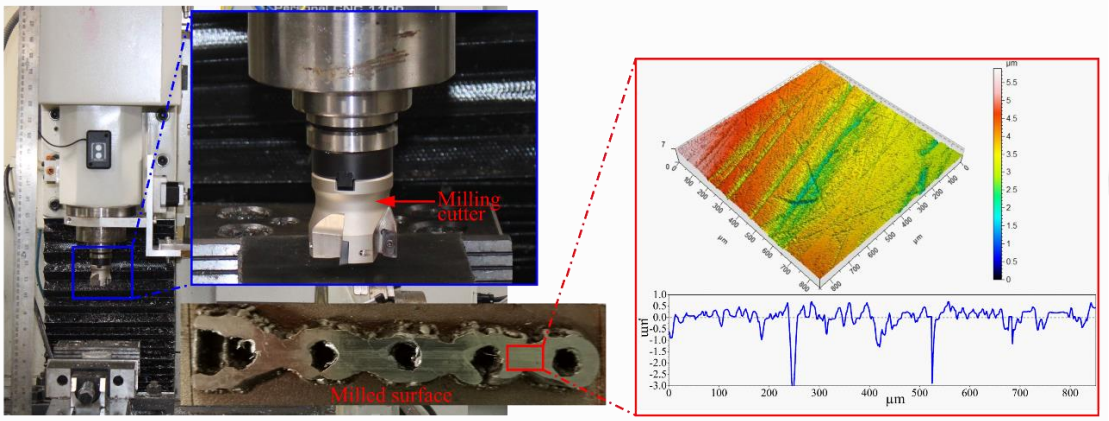

Fig. B.9 Surface profile of milled surface of fixation plate

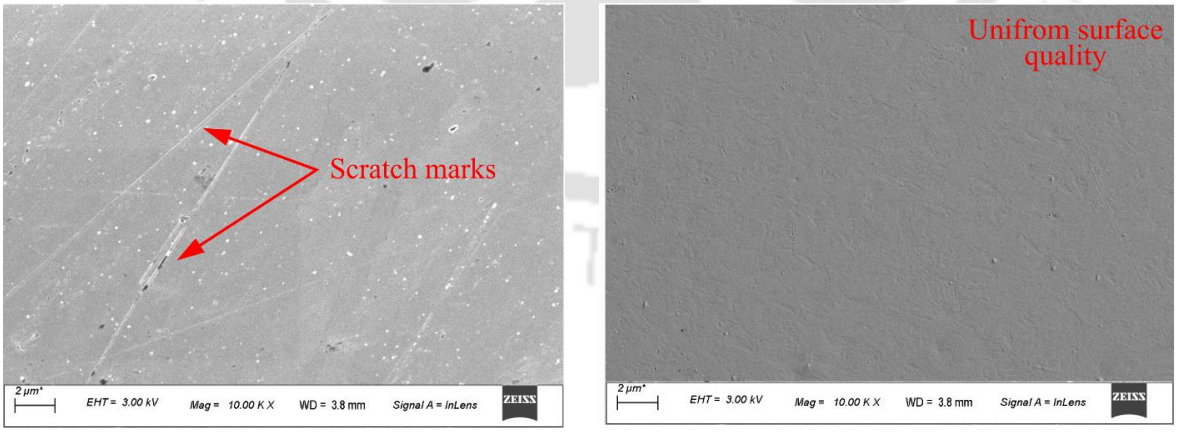

(a) (b)

Fig. B.10 SEM image of (a) milled surface and (b) polished surface

The H-ECMR finishing process is applied after the milling operation as the surface roughness value of the additively manufactured surface is reduced in the submicron range. The unbonded form of the polishing media assists in lowering the value of R_a in a few nanometers

range; the combined action of the magnetorheological finishing along with the electrochemical reaction provides an unvarying surface quality on the fixation plate surface after polishing. The areal and linear representation of the surface profile after the H-ECMR finishing process is shown in Fig. B.11. The value of the R_a is reduced to 29.26 nm from 0.91 µm, and a mirror liked polished surface is achieved. The improved surface quality leads to improve fixation plate functionality during its operation.

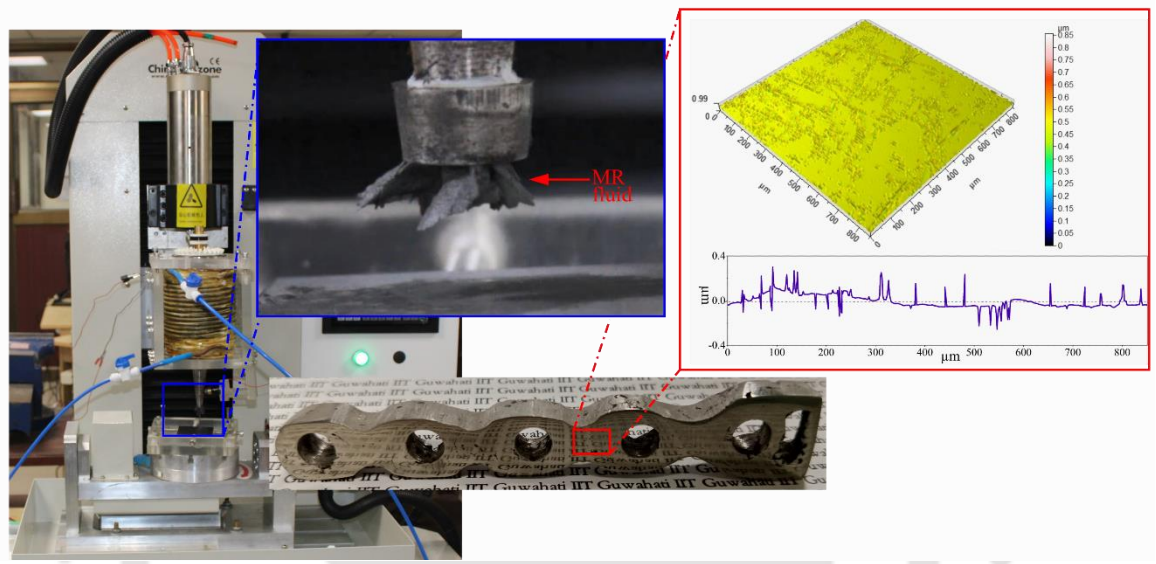

Fig. B.11 Surface analysis of fixation plate polished surface

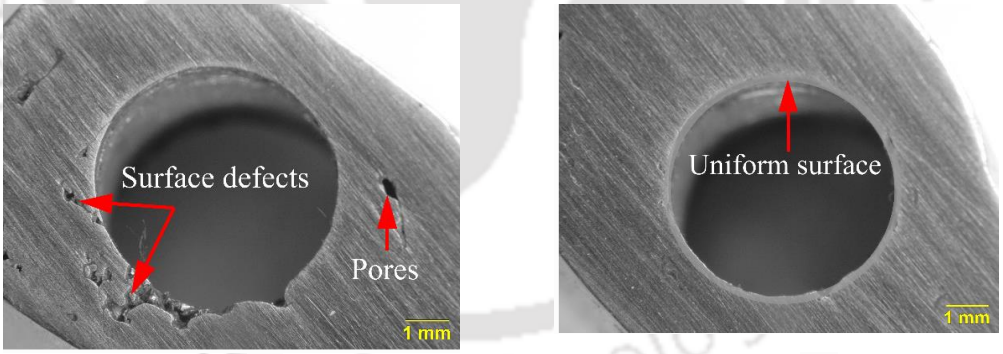

(a) (b)

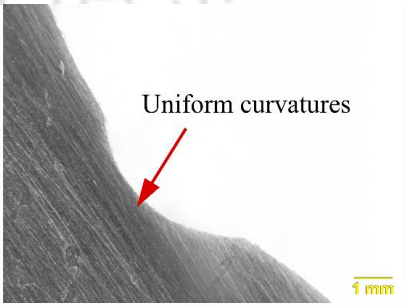

(c)

Fig. B.12 (a) Surface defects on holes edge, uniform (b) hole, and (c) curvatures on the polished surface after H-ECMR finishing process

The surface topography is also analyzed through the optical microscope to study the impact of the H-ECMR finishing process. Before the surface finishing operation, irregularities and pores on the holes are clearly visible in Fig. B.12(a). However, after implementing the H-ECMR finishing process, a uniform edge of the circular hole is achieved, as shown in Fig. B.12(b). Similarly, a uniform curvature was produced on the bone plate after the H-ECMR finishing process, as shown in Fig. B.12(c).

The present study aims to perform nanofinishing on the topologically optimized fixation plate fabricated through *Laser-Directed Energy Deposition* (*L-DED*). Finite element-based computational analysis is performed on the conventional fixation plate for its topological optimization to reduce stress shielding. Afterward, *L-DED* is used to fabricate the topologically optimized fixation plate. Furthermore, the milling operation followed by the *Hybrid-Electrochemical Magnetorheological* (*H-ECMR*) finishing process to eliminate the surface defects from the fabricated part and produce a mirror-like polished surface. The key finding of the present work is summarized below.

- The stiffness of the fixation plate is reduced from 5.69×10^{10} N/m to 4.79×10^{10} N/m for mass retention of 50% and 100% during the topological optimization of the fixation plate, further helping to reduce the stress shielding during its operation.
- The *average surface roughness* (R_a) value on the *L-DED* fabricated surface is 14.23 µm with unbonded powder particles and pores on the surface, further leading to an increase in the release of metal ions, which can cause inflammation and infection and lead to screw loosening.
- Milling operation eliminates the surface defects and reduces the Ra value in the submicron range (i.e., 0.91 µm) from 14.23 µm.
- The *H-ECMR* finishing process is further used to produce a mirror-like polished surface, reduce the surface roughness value to 29.26 nm, and produce a uniform surface quality. The improved surface quality leads to improve fixation plate functionality.

The experimental and computation results suggest that the nanofinishing is achievable on the topologically optimized *L-DED* fabricated fixation plate to reduce stress shielding during operation.

References

[1] K. H. E. Kroemer, "Anthropometry and biomechanics: Anthromechanics," in *Biomechanics in Ergonomics*, CRC Press, 2007, pp. 59–106.

[2] D. Dowson, M. Diab, B. Gillis, and J. Atkinson, "Influence of countersurface topography on the wear of UHMWPE under wet or dry conditions: polymer wear and its control." Washington DC: American Chemical Society, 1985.

[3] Ivántabernero, A. Paskual, P. Álvarez, and A. Suárez, "Study on Arc Welding Processes for High Deposition Rate Additive Manufacturing," *Procedia CIRP*, vol. 68, pp. 358–362, Jan. 2018, doi: 10.1016/J.PROCIR.2017.12.095.

[4] S. Han, M. Zielewski, D. M. Holguin, M. M. Parra, and N. Kim, "Optimization of AZ91D Process and Corrosion Resistance Using Wire Arc Additive Manufacturing," *Appl. Sci. 2018, Vol. 8, Page 1306*, vol. 8, no. 8, p. 1306, Aug. 2018, doi: 10.3390/APP8081306.

[5] U. S. Kim and J. W. Park, "High-Quality Surface Finishing of Industrial Three-Dimensional Metal Additive Manufacturing Using Electrochemical Polishing," *Int. J. Precis. Eng. Manuf. - Green Technol.*, vol. 6, no. 1, pp. 11–21, 2019, doi: 10.1007/s40684-019-00019-2.

[6] R. Chou, J. Milligan, M. Paliwal, and M. Brochu, "Additive Manufacturing of Al-12Si Alloy Via Pulsed Selective Laser Melting," *JOM*, vol. 67, no. 3, pp. 590–596, Mar. 2015, doi: 10.1007/S11837-014-1272-9/TABLES/3.

[7] P. B. Bacchewar, S. K. Singhal, and P. M. Pandey, "Statistical modelling and optimization of surface roughness in the selective laser sintering process:," *http://dx.doi.org/10.1243/09544054JEM670*, vol. 221, no. 1, pp. 35–52, Apr. 2007, doi: 10.1243/09544054JEM670.

[8] P. K. Jain, P. M. Pandey, and P. V. M. Rao, "Experimental investigations for improving part strength in selective laser sintering," *Virtual Phys. Prototyp.*, vol. 3, no. 3, pp. 177–188, 2008, doi: 10.1080/17452750802065893.

[9] A. Wang, D. C. Sun, C. Stark, Dumbleton, and JH, "Wear mechanisms of UHMWPE in total joint replacements," *Wear*, vol. 181, pp. 241–249, 1995.

[10] C. Rosales and E. Uribe-Querol, "Phagocytosis: A Fundamental Process in Immunity," *Biomed Res. Int.*, vol. 2017, 2017, doi: 10.1155/2017/9042851.

[11] J. W. Mesko, J. A. D'Antonio, W. N. Capello, B. E. Bierbaum, and M. Naughton, "Ceramic-on-ceramic hip outcome at a 5-to 10-year interval: has it lived up to its expectations?," *J. Arthroplasty*, vol. 26, no. 2, pp. 172–177, 2011.

[12] H.-G. Willert *et al.*, "Metal-on-metal bearings and hypersensitivity in patients with artificial hip joints: a clinical and histomorphological study," *JBJS*, vol. 87, no. 1, pp. 28–36, 2005.

[13] H. Pandit *et al.*, "Pseudotumours associated with metal-on-metal hip resurfacings," *J. Bone Joint Surg. Br.*, vol. 90, no. 7, pp. 847–851, 2008.

[14] L. J. Rhoades and T. A. Kohut, "Reversible Unidirectional AFM." Google Patents, 1991.

[15] N. Suppression and C. For, "United States Patent [19]," no. 16, pp. 2–6, 2000.

[16] S. S. Kumar and S. S. Hiremath, "A Review on Abrasive Flow Machining (AFM)," *Procedia Technol.*, vol. 25, pp. 1297–1304, Jan. 2016, doi: 10.1016/j.protcy.2016.08.224.

[17] M. R. Sankar, V. K. Jain, and J. Ramkumar, "Abrasive flow machining (AFM): An overview," *Dep. Mech. Eng. Indian Inst. Technol. Kanpur, India*, no. September, pp. 1–8, 2011.

[18] M. Sarkar and V. K. Jain, "Nanofinishing of freeform surfaces using abrasive flow

finishing process," *Proc. Inst. Mech. Eng. Part B J. Eng. Manuf.*, vol. 231, no. 9, pp. 1501–1515, 2017, doi: 10.1177/0954405415599913.
[19] G. Rajeshwar, J. Kozak, and K. P. Rajurkar, "Modeling and computer simulation of media flow in abrasive flow machining process," in *Proceedings of the 1994 International Mechanical Engineering Congress and Exposition*, 1994, pp. 965–971.
[20] A. J. Fletcher, J. B. Hull, J. Mackie, and S. A. Trengove, "Computer modelling of the abrasive flow machining process," in *Surface Engineering*, Springer, 1990, pp. 592–601.
[21] K. L. Petri, R. E. Billo, and B. Bidanda, "A neural network process model for abrasive flow machining operations," *J. Manuf. Syst.*, vol. 17, no. 1, pp. 52–64, 1998.
[22] S. S. Y. Lam and A. E. Smith, "Process monitoring of abrasive flow machining using a neural network predictive model," *Ind. Eng. Res. - Conf. Proc.*, pp. 477–482, 1997.
[23] W. S. Slaughter and A. E. Smith, "Neural Network Modeling of Abrasive Flow Machining."
[24] M. R. Sankar, V. K. Jain, J. Ramkumar, and Y. M. Joshi, "Rheological characterization of styrene-butadiene based medium and its finishing performance using rotational abrasive flow finishing process," *Int. J. Mach. Tools Manuf.*, vol. 51, no. 12, pp. 947–957, 2011, doi: https://doi.org/10.1016/j.ijmachtools.2011.08.012.
[25] M. R. Sankar, V. K. Jain, and J. Ramkumar, "Rotational abrasive flow finishing (R-AFF) process and its effects on finished surface topography," *Int. J. Mach. tools Manuf.*, vol. 50, no. 7, pp. 637–650, 2010.
[26] M. R. Sankar, V. K. Jain, and J. Ramkumar, "Nano-finishing of cylindrical hard steel tubes using rotational abrasive flow finishing (R-AFF) process," *Int. J. Adv. Manuf. Technol.*, vol. 85, no. 9–12, pp. 2179–2187, 2016.
[27] M. R. Sankar, V. K. Jain, and J. Ramkumar, "Experimental investigations into rotating workpiece abrasive flow finishing," *Wear*, vol. 267, no. 1–4, pp. 43–51, 2009.
[28] A. Okada *et al.*, "Surface finishing of stainless steels for orthopedic surgical tools by large-area electron beam irradiation," *CIRP Ann.*, vol. 57, no. 1, pp. 223–226, Jan. 2008, doi: 10.1016/J.CIRP.2008.03.062.
[29] Y. Uno, A. Okada, K. Uemura, P. Raharjo, T. Furukawa, and K. Karato, "High-efficiency finishing process for metal mold by large-area electron beam irradiation," *Precis. Eng.*, vol. 29, no. 4, pp. 449–455, 2005.
[30] Y. Kimura, T. Shinonaga, and A. Okada, "Study on Clarification of Large-Area EB Irradiation Phenomenon by Electron Track Analysis," *Key Eng. Mater.*, vol. 749, pp. 118–123, 2017, doi: 10.4028/WWW.SCIENTIFIC.NET/KEM.749.118.
[31] M. Heckele and W. K. Schomburg, "Review on micro molding of thermoplastic polymers," *J. Micromechanics Microengineering*, vol. 14, no. 3, p. R1, 2003.
[32] D. I. Proskurovsky, V. P. Rotshtein, and G. E. Ozur, "Use of low-energy, high-current electron beams for surface treatment of materials," *Surf. Coatings Technol.*, vol. 96, no. 1, pp. 117–122, 1997, doi: 10.1016/S0257-8972(97)00093-5.
[33] D. I. Proskurovsky, V. P. Rotshtein, G. E. Ozur, Y. F. Ivanov, and A. B. Markov, "Physical foundations for surface treatment of materials with low energy, high current electron beams," *Surf. Coatings Technol.*, vol. 125, no. 1–3, pp. 49–56, 2000, doi: 10.1016/S0257-8972(99)00604-0.
[34] A. Okada, Y. Uno, P. Rahario, and T. Furukawa, "Surface modification of EDMed surface by wide-area electron beam irradiation," in *Proc. ASPE Annual Conf*, 2003, vol. 18, pp. 172–175.
[35] J. W. Murray, P. K. Kinnell, A. H. Cannon, B. Bailey, and A. T. Clare, "Surface finishing of intricate metal mould structures by large-area electron beam irradiation," *Precis. Eng.*, vol. 37, no. 2, pp. 443–450, 2013, doi: 10.1016/j.precisioneng.2012.11.007.
[36] A. Okada *et al.*, "Surface finishing of stainless steels for orthopedic surgical tools by

large-area electron beam irradiation," *CIRP Ann. - Manuf. Technol.*, vol. 57, no. 1, pp. 223–226, 2008, doi: 10.1016/j.cirp.2008.03.062.
[37] A. Okada, Y. Uno, N. Yabushita, K. Uemura, and P. Raharjo, "High efficient surface finishing of bio-titanium alloy by large-area electron beam irradiation," *J. Mater. Process. Technol.*, vol. 149, no. 1–3, pp. 506–511, 2004, doi: 10.1016/j.jmatprotec.2004.02.017.
[38] D. Landolt, "Fundamental aspects of electropolishing," *Electrochim. Acta*, vol. 32, no. 1, pp. 1–11, 1987.
[39] L. Carlsson, T. Röstlund, B. Albrektsson, and T. Albrektsson, "Removal torques for polished and rough titanium implants.," *Int. J. Oral Maxillofac. Implants*, vol. 3, no. 1, 1988.
[40] A. Andreacchi, "Apparatus for electropolishing a stent." Google Patents, 2004.
[41] K. Tajima, M. Hironaka, K.-K. Chen, Y. Nagamatsu, H. Kakigawa, and Y. Kozono, "Electropolishing of CP titanium and its alloys in an alcoholic solution-based electrolyte," *Dent. Mater. J.*, vol. 27, no. 2, pp. 258–265, 2008.
[42] O. Piotrowski, C. Madore, and D. Landolt, "Electropolishing of Titanium & Titanium Alloys in Perchlorate-free Electrolytes," *Plat. Surf. Finish.*, vol. 85, no. 5, pp. 115–119, 1998.
[43] W. Han and F. Fang, "Fundamental aspects and recent developments in electropolishing," *Int. J. Mach. Tools Manuf.*, vol. 139, pp. 1–23, 2019.
[44] J. Lausmaa, B. Kasemo, H. Mattsson, and H. Odelius, "Multi-technique surface charaterization of oxide films on electropolished and anodically oxidized titanium," *Appl. Surf. Sci.*, vol. 45, no. 3, pp. 189–200, 1990.
[45] O. Piotrowski, "The Mechanism of Electropolishing of Titanium in Methanol-Sulfuric Acid Electrolytes," *J. Electrochem. Soc.*, vol. 145, no. 7, p. 2362, 1998, doi: 10.1149/1.1838644.
[46] N. S. Peighambardoust and F. Nasirpouri, "Electropolishing behaviour of pure titanium in perchloric acid--methanol--ethylene glycol mixed solution," *Trans. IMF*, vol. 92, no. 3, pp. 132–139, 2014.
[47] C. A. Huang, F.-Y. Hsu, and C. H. Yu, "Electropolishing behavior of pure titanium in sulfuric acid--ethanol electrolytes with an addition of water," *Corros. Sci.*, vol. 53, no. 2, pp. 589–596, 2011.
[48] O. Piotrowski, C. Madore, and D. Landolt, "The mechanism of electropolishing of titanium in methanol-sulfuric acid electrolytes," *J. Electrochem. Soc.*, vol. 145, no. 7, p. 2362, 1998.
[49] N. Eliaz and O. Nissan, "Innovative processes for electropolishing of medical devices made of stainless steels," *J. Biomed. Mater. Res. Part A An Off. J. Soc. Biomater. Japanese Soc. Biomater. Aust. Soc. Biomater. Korean Soc. Biomater.*, vol. 83, no. 2, pp. 546–557, 2007.
[50] C. Wagner, "Contribution to the theory of electropolishing," *J. Electrochem. Soc.*, vol. 101, no. 5, pp. 225–228, 1954.
[51] M. S. Rowe, C. E. Harper Jr, and C. R. Underwood, "Computer controlled electropolishing system." Google Patents, 1990.
[52] M. Datta and L. T. Romankiw, "Electrochemical tool for uniform metal removal during electropolishing." Google Patents, 1993.
[53] H. Ohmori, K. Katahira, Y. Akinou, J. Komotori, and M. Mizutani, "Investigation on grinding characteristics and surface-modifying effects of biocompatible Co-Cr alloy," *CIRP Ann. - Manuf. Technol.*, vol. 55, no. 1, pp. 597–600, 2006, doi: 10.1016/S0007-8506(07)60491-0.
[54] M. Rahman, A. Senthil Kumar, and I. Biswas, "A Review of Electrolytic In-Process Dressing (ELID) Grinding," *Key Eng. Mater.*, vol. 404, pp. 45–59, 2009, doi:

10.4028/www.scientific.net/kem.404.45.
[55] H. Ohmori *et al.*, "Surface generating process of artificial hip joints with hyper-hemispherical shape having higher smoothness and biocompatibility," *CIRP Ann. - Manuf. Technol.*, vol. 62, no. 1, pp. 579–582, 2013, doi: 10.1016/j.cirp.2013.03.027.
[56] Y. Okada *et al.*, "Verification of implant surface modification by a novel processing method," *Acta Med. Okayama*, vol. 71, no. 1, pp. 49–57, 2017, doi: 10.18926/AMO/54825.
[57] M. HAMADA, J. KOMOTORI, M. MIZUTANI, S. KUNIMURA, K. KATAHIRA, and H. OHMORI, "Corrosion Resistance of Co-Cr-Mo Alloy Treated by Electrolytic In-Process Dressing (ELID) Grinding/Thermal Oxidation Hybrid Process," *J. Solid Mech. Mater. Eng.*, vol. 6, no. 6, pp. 504–511, 2012, doi: 10.1299/jmmp.6.504.
[58] H. Kasuga, H. Ohmori, Y. Watanabe, and T. Mishima, "Surface Characteristics of Efficient-Ground Alumina and Zirconia Ceramics for Dental Applications," *Key Eng. Mater.*, vol. 404, pp. 69–75, 2009, doi: 10.4028/www.scientific.net/kem.404.69.
[59] J. G. Ryan, R. M. Geffken, N. R. Poulin, and J. R. Paraszczak, "The evolution of interconnection technology at IBM," *IBM J. Res. Dev.*, vol. 39, no. 4, pp. 371–381, 1995.
[60] G. Nanz and L. E. Camilletti, "Modeling of Chemical—Mechanical Polishing: A Review," *IEEE Trans. Semicond. Manuf.*, vol. 8, no. 4, pp. 382–389, 1995, doi: 10.1109/66.475179.
[61] B. Et and A. Usoo67873o8e32, "(12) United States Patent," vol. 2, no. 12, 2010.
[62] P. Bai *et al.*, "A 65nm logic technology featuring 35nm gate lengths, enhanced channel strain, 8 Cu interconnect layers, low-k ILD and 0.57/spl mu/m/sup 2/SRAM cell," in *IEDM Technical Digest. IEEE International Electron Devices Meeting, 2004.*, 2004, pp. 657–660.
[63] P. B. Zantye, A. Kumar, and A. K. Sikder, "Chemical mechanical planarization for microelectronics applications," *Mater. Sci. Eng. R Reports*, vol. 45, no. 3–6, pp. 89–220, 2004.
[64] D. Zhao and X. Lu, "Chemical mechanical polishing: Theory and experiment," *Friction*, vol. 1, no. 4, pp. 306–326, 2013, doi: 10.1007/s40544-013-0035-x.
[65] R. Alsaeedi and Z. Ozdemir, "Evaluation of chemical mechanical polishing-based surface modification on 3D dental implants compared to alternative methods," *Materials (Basel).*, vol. 11, no. 11, 2018, doi: 10.3390/ma11112286.
[66] A. B. Kahng and K. Samadi, "CMP fill synthesis: A survey of recent studies," *IEEE Trans. Comput. Des. Integr. Circuits Syst.*, vol. 27, no. 1, pp. 3–19, 2007.
[67] G. B. Basim, Z. Ozdemir, and O. Mutlu, "Biomaterials Applications of Chemical Mechanical Polishing," *Icpt2012*, pp. 15–17, 2012.
[68] Z. Ozdemir, A. Ozdemir, and G. B. Basim, "Application of chemical mechanical polishing process on titanium based implants," *Mater. Sci. Eng. C*, vol. 68, pp. 383–396, 2016, doi: 10.1016/j.msec.2016.06.002.
[69] I. Inasaki, "Monitoring and Optimization of Internal Grinding Process," *CIRP Ann. - Manuf. Technol.*, vol. 40, no. 1, pp. 359–362, Jan. 1991, doi: 10.1016/S0007-8506(07)62006-X.
[70] D. A. Wallace, "UNITED STATES PATENT OFFICE LAPPNG APPARATUS," 1944.
[71] X. Le and M. L. Peterson, "Material removal rate in flat lapping," *J. Manuf. Process.*, vol. 1, no. 1, pp. 71–78, Jan. 1999, doi: 10.1016/S1526-6125(99)70007-1.
[72] V. K. Jain, A. Sidpara, R. Balasubramaniam, G. S. Lodha, V. P. Dhamgaye, and R. Shukla, "Micromanufacturing: A review—Part I," *Proc. Inst. Mech. Eng. Part B J. Eng. Manuf.*, vol. 228, no. 9, pp. 973–994, 2014, doi: 10.1177/0954405414539487.
[73] V. Jain, "Special issue on 'Advances in Manufacturing Technologies,'" *Proc. Inst. Mech. Eng. Part B J. Eng. Manuf.*, vol. 228, no. 9, pp. 971–972, Sep. 2014, doi: 10.1177/0954405414540399.

[74] K. L. Tan, S. H. Yeo, and C. H. Ong, “Nontraditional finishing processes for internal surfaces and passages: A review,” *Proceedings of the Institution of Mechanical Engineers, Part B: Journal of Engineering Manufacture*, vol. 231, no. 13. SAGE Publications Ltd, pp. 2302–2316, 01-Nov-2017, doi: 10.1177/0954405415626087.
[75] S. S. Cho, Y. K. Ryu, and S. Y. Lee, “Curved surface finishing with flexible abrasive tool,” *Int. J. Mach. Tools Manuf.*, vol. 42, no. 2, pp. 229–236, Jan. 2002, doi: 10.1016/S0890-6955(01)00106-7.
[76] K. K. Kar, N. L. Ravikumar, P. B. Tailor, J. Ramkumar, and D. Sathiyamoorthy, “Preferential media for abrasive flow machining,” *J. Manuf. Sci. Eng. Trans. ASME*, vol. 131, no. 1, pp. 0110091–01100911, Feb. 2009, doi: 10.1115/1.3046135.
[77] B. Jung, K.-I. Jang, B.-K. Min, S. J. Lee, and J. Seok, “Parameter optimization for finishing hard materials with magnetorheological fluid using the penalized multi-response Taguchi method,” *Proc. Inst. Mech. Eng. Part B J. Eng. Manuf.*, vol. 223, no. 8, pp. 955–968, Aug. 2009, doi: 10.1243/09544054JEM1351.
[78] A. K. Singh, S. Jha, and P. M. Pandey, “Parametric analysis of an improved ball end magnetorheological finishing process,” *Proc. Inst. Mech. Eng. Part B J. Eng. Manuf.*, vol. 226, no. 9, pp. 1550–1563, 2012, doi: 10.1177/0954405412453805.
[79] F. Han, F. Ai, and Y. Wang, “Attempt at unitary magnetorheological finishing for a pierced die cavity,” *Proc. Inst. Mech. Eng. Part B J. Eng. Manuf.*, vol. 224, no. 6, pp. 879–886, Jun. 2010, doi: 10.1243/09544054JEM1673.
[80] V. K. Jain, A. Sidpara, M. R. Sankar, and M. Das, “Nano-finishing techniques: a review,” *Proc. Inst. Mech. Eng. Part C J. Mech. Eng. Sci.*, vol. 226, no. 2, pp. 327–346, 2012, doi: 10.1177/0954406211426948.
[81] S. T. Lim, M. S. Cho, I. B. Jang, and H. J. Choi, “Magnetorheological characterization of carbonyl iron based suspension stabilized by fumed silica,” in *Journal of Magnetism and Magnetic Materials*, 2004, vol. 282, no. 1–3, pp. 170–173, doi: 10.1016/j.jmmm.2004.04.040.
[82] E. C. Stoner and E. P. Wohlfarth, “A mechanism of magnetic hysteresis in heterogeneous alloys,” *Philos. Trans. R. Soc. London. Ser. A, Math. Phys. Sci.*, vol. 240, no. 826, pp. 599–642, May 1948, doi: 10.1098/rsta.1948.0007.
[83] A. Caciagli, R. J. Baars, A. P. Philipse, and B. W. M. Kuipers, “Exact expression for the magnetic field of a finite cylinder with arbitrary uniform magnetization,” *J. Magn. Magn. Mater.*, vol. 456, pp. 423–432, Jun. 2018, doi: 10.1016/j.jmmm.2018.02.003.
[84] N. Derby and S. Olbert, “Cylindrical magnets and ideal solenoids,” *Am. J. Phys.*, vol. 78, no. 3, pp. 229–235, Mar. 2010, doi: 10.1119/1.3256157.
[85] A. Barman and M. Das, “Nano-finishing of bio-titanium alloy to generate different surface morphologies by changing magnetorheological polishing fluid compositions,” *Precis. Eng.*, vol. 51, pp. 145–152, 2018, doi: 10.1016/j.precisioneng.2017.08.003.
[86] A. Barman and M. Das, “Simulation and experimental investigation of finishing forces in magnetic field assisted finishing process,” *Mater. Manuf. Process.*, vol. 33, no. 11, pp. 1223–1232, Aug. 2018, doi: 10.1080/10426914.2018.1453157.
[87] G. Ghosh, A. Sidpara, and P. P. Bandyopadhyay, “Experimental and theoretical investigation into surface roughness and residual stress in magnetorheological finishing of OFHC copper,” *J. Mater. Process. Technol.*, vol. 288, p. 116899, Feb. 2021, doi: 10.1016/j.jmatprotec.2020.116899.
[88] M. Hanief and M. F. Wani, “Effect of surface roughness on wear rate during running-in of En31-steel: Model and experimental validation,” *Mater. Lett.*, vol. 176, pp. 91–93, Aug. 2016, doi: 10.1016/J.MATLET.2016.04.087.
[89] P. H. Wooley and E. M. Schwarz, “Aseptic loosening,” *Gene Ther. 2004 114*, vol. 11, no. 4, pp. 402–407, Jan. 2004, doi: 10.1038/sj.gt.3302202.
[90] Hideo Nakae, Ryuichi Inui, Yosuke Hirata, and Hiroyuki Saito, “Effects of surface

roughness on wettability," *Acta Mater.*, vol. 46, no. 7, pp. 2313–2318, Apr. 1998, doi: 10.1016/S1359-6454(98)80012-8.
[91] A. Kumar Singh, S. Jha, and P. M. Pandey, "Nanofinishing of a typical 3D ferromagnetic workpiece using ball end magnetorheological finishing process," *Int. J. Mach. Tools Manuf.*, vol. 63, pp. 21–31, Dec. 2012, doi: 10.1016/J.IJMACHTOOLS.2012.07.002.
[92] L. Nagdeve, V. K. Jain, and J. Ramkumar, "Development of inverse replica fixture for nano-finishing of knee joint using R-MRAFF process," *J. Micromanufacturing*, vol. 2, no. 1, pp. 35–41, May 2019, doi: 10.1177/2516598418811460.
[93] A. Barman and M. Das, "Soft computing techniques to model and optimize magnetic field-assisted finishing process and characterization of the finished surface," *Proc. Inst. Mech. Eng. Part C J. Mech. Eng. Sci.*, vol. 232, no. 17, pp. 3156–3168, Sep. 2018, doi: 10.1177/0954406217731116.
[94] D. A. Khan and S. Jha, "Selection of optimum polishing fluid composition for ball end magnetorheological finishing (BEMRF) of copper," *Int. J. Adv. Manuf. Technol.*, vol. 100, no. 5–8, pp. 1093–1103, 2019, doi: 10.1007/s00170-017-1056-9.
[95] N. D. Boscher, Véronique Vaché, Paul Carminati, Patrick Grysan, and Patrick Choquet, "A simple and scalable approach towards the preparation of superhydrophobic surfaces – importance of the surface roughness skewness," *J. Mater. Chem. A*, vol. 2, no. 16, pp. 5744–5750, Mar. 2014, doi: 10.1039/C4TA00366G.
[96] L. Chang and Y.-R. Jeng, "Effects of negative skewness of surface roughness on the contact and lubrication of nominally flat metallic surfaces:," *http://dx.doi.org/10.1177/1350650112465365*, vol. 227, no. 6, pp. 559–569, Nov. 2012, doi: 10.1177/1350650112465365.
[97] Y. Chen and W. Huang, "Numerical simulation of the geometrical factors affecting surface roughness measurements by AFM," *Meas. Sci. Technol.*, vol. 15, no. 10, p. 2005, Aug. 2004, doi: 10.1088/0957-0233/15/10/010.
[98] M. Sedlaček, B. Podgornik, and J. Vižintin, "Correlation between standard roughness parameters skewness and kurtosis and tribological behaviour of contact surfaces," *Tribol. Int.*, vol. 48, pp. 102–112, Apr. 2012, doi: 10.1016/J.TRIBOINT.2011.11.008.
[99] M. Sedlaček, B. Podgornik, and J. Vižintin, "Planning surface texturing for reduced friction in lubricated sliding using surface roughness parameters skewness and kurtosis:," *http://dx.doi.org/10.1177/1350650112439809*, vol. 226, no. 8, pp. 661–667, Mar. 2012, doi: 10.1177/1350650112439809.
[100] Y. Oshida and F. Farzin-Nia, "Response of Ti–Ni alloys for dental biomaterials to conditions in the mouth," *Shape Mem. Alloy. Biomed. Appl.*, pp. 101–149, Jan. 2009, doi: 10.1533/9781845695248.1.101.
[101] A. P. Abbott, G. Frisch, J. Hartley, W. O. Karim, and K. S. Ryder, "Anodic dissolution of metals in ionic liquids," *Prog. Nat. Sci. Mater. Int.*, vol. 25, no. 6, pp. 595–602, Dec. 2015, doi: 10.1016/J.PNSC.2015.11.005.
[102] G. Yang, B. Wang, K. Tawfiq, H. Wei, S. Zhou, and G. Chen, "Electropolishing of surfaces: theory and applications," *http://dx.doi.org/10.1080/02670844.2016.1198452*, vol. 33, no. 2, pp. 149–166, Feb. 2016, doi: 10.1080/02670844.2016.1198452.
[103] E. Godlewska, M. Mitoraj, and K. Leszczynska, "Hot corrosion of Ti–46Al–8Ta (at.%) intermetallic alloy," *Corros. Sci.*, vol. 78, pp. 63–70, Jan. 2014, doi: 10.1016/J.CORSCI.2013.08.032.
[104] W. B. Kim, S. H. Lee, and B. K. Min, "Surface Finishing and Evaluation of Three-Dimensional Silicon Microchannel Using Magnetorheological Fluid," *J. Manuf. Sci. Eng.*, vol. 126, no. 4, pp. 772–778, Nov. 2004, doi: 10.1115/1.1811113.
[105] J. Seok, Y. J. Kim, K. I. Jang, B. K. Min, and S. J. Lee, "A study on the fabrication of curved surfaces using magnetorheological fluid finishing," *Int. J. Mach. Tools Manuf.*, 2007, doi: 10.1016/j.ijmachtools.2007.05.007.

[106] B. Jung, K. I. Jang, B. K. Min, S. J. Lee, and J. Seok, "Magnetorheological finishing process for hard materials using sintered iron-CNT compound abrasives," *Int. J. Mach. Tools Manuf.*, vol. 49, no. 5, pp. 407–418, Apr. 2009, doi: 10.1016/J.IJMACHTOOLS.2008.12.002.
[107] K. I. Jang, J. Seok, B. K. Min, and S. Jo Lee, "An electrochemomechanical polishing process using magnetorheological fluid," *Int. J. Mach. Tools Manuf.*, vol. 50, no. 10, pp. 869–881, Oct. 2010, doi: 10.1016/J.IJMACHTOOLS.2010.06.004.
[108] A. K. Singh, S. Jha, and P. M. Pandey, "Design and development of nanofinishing process for 3D surfaces using ball end MR finishing tool," *Int. J. Mach. Tools Manuf.*, vol. 51, no. 2, pp. 142–151, 2011, doi: https://doi.org/10.1016/j.ijmachtools.2010.10.002.
[109] K. I. Jang *et al.*, "Deburring microparts using a magnetorheological fluid," *Int. J. Mach. Tools Manuf.*, vol. 53, no. 1, pp. 170–175, Feb. 2012, doi: 10.1016/J.IJMACHTOOLS.2011.11.002.
[110] A. M. Sidpara and V. K. Jain, "Nanofinishing of freeform surfaces of prosthetic knee joint implant," *Proc. Inst. Mech. Eng. Part B J. Eng. Manuf.*, vol. 226, no. 11, pp. 1833–1846, 2012, doi: 10.1177/0954405412460452.
[111] S. Kumar, V. K. Jain, and A. Sidpara, "Nanofinishing of freeform surfaces (knee joint implant) by rotational-magnetorheological abrasive flow finishing (R-MRAFF) process," *Precis. Eng.*, vol. 42, pp. 165–178, Oct. 2015, doi: 10.1016/j.precisioneng.2015.04.014.
[112] S. Maan, G. Singh, and A. K. Singh, "Nano-surface-finishing of permanent mold punch using magnetorheological fluid-based finishing processes," *Mater. Manuf. Process.*, vol. 32, no. 9, pp. 1004–1010, Jul. 2017, doi: 10.1080/10426914.2016.1232823.
[113] T. S. Bedi and A. K. Singh, "Development of magnetorheological fluid-based process for finishing of ferromagnetic cylindrical workpiece," *Mach. Sci. Technol.*, vol. 22, no. 1, pp. 120–146, Jan. 2018, doi: 10.1080/10910344.2017.1336631.
[114] A. Barman and M. Das, "Toolpath generation and finishing of bio-titanium alloy using novel polishing tool in MFAF process," *Int. J. Adv. Manuf. Technol.*, vol. 100, no. 5–8, pp. 1123–1135, Feb. 2019, doi: 10.1007/s00170-017-1050-2.
[115] R. D. Yadav and A. K. Singh, "A novel magnetorheological gear profile finishing with high shape accuracy," *Int. J. Mach. Tools Manuf.*, vol. 139, pp. 75–92, Apr. 2019, doi: 10.1016/J.IJMACHTOOLS.2019.02.001.
[116] L. Nagdeve, V. K. Jain, and J. Ramkumar, "Optimization of process parameters in nano-finishing of Co-Cr-Mo alloy knee joint," *Mater. Manuf. Process.*, vol. 35, no. 9, pp. 985–992, 2020, doi: 10.1080/10426914.2020.1750633.
[117] J. Zhang, H. Wang, A. Senthil Kumar, and M. Jin, "Experimental and theoretical study of internal finishing by a novel magnetically driven polishing tool," *Int. J. Mach. Tools Manuf.*, vol. 153, p. 103552, Jun. 2020, doi: 10.1016/J.IJMACHTOOLS.2020.103552.
[118] A. Pottier, C. Chanéac, E. Tronc, L. Mazerolles, and J. P. Jolivet, "Synthesis of brookite TiO2 nanoparticlesby thermolysis of TiCl4 in strongly acidic aqueous media," *J. Mater. Chem.*, vol. 11, no. 4, pp. 1116–1121, Jan. 2001, doi: 10.1039/B100435M.
[119] Z. L. Wang, "On the first principle theory of nanogenerators from Maxwell's equations," *Nano Energy*, vol. 68, p. 104272, Feb. 2020, doi: 10.1016/J.NANOEN.2019.104272.
[120] K. Verosub, A. R.-J. of G. Research, and undefined 1995, "Environmental magnetism: Past, present, and future," *Wiley Online Libr.*, vol. 100, no. B2, pp. 2175–2192, 1995, doi: 10.1029/94JB02713.
[121] X. Liu and Z. Q. Zhu, "Comparative study of novel variable flux reluctance machines with doubly fed doubly salient machines," *IEEE Trans. Magn.*, vol. 49, no. 7, pp. 3838–3841, 2013, doi: 10.1109/TMAG.2013.2242047.
[122] T. Mori, K. Hirota, and Y. Kawashima, "Clarification of magnetic abrasive finishing

mechanism," *J. Mater. Process. Technol.*, vol. 143–144, no. 1, pp. 682–686, Dec. 2003, doi: 10.1016/S0924-0136(03)00410-2.
[123] A. S. Rajput, M. Das, and S. Kapil, "A comprehensive review of magnetorheological fluid assisted finishing processes," *https://doi.org/10.1080/10910344.2022.2129982*, vol. 26, no. 3, pp. 339–376, 2022, doi: 10.1080/10910344.2022.2129982.
[124] X. Xu, L. Wang, and S. T. Newman, "Computer-aided process planning – A critical review of recent developments and future trends," *https://doi.org/10.1080/0951192X.2010.518632*, vol. 24, no. 1, pp. 1–31, 2010, doi: 10.1080/0951192X.2010.518632.
[125] S. T. Newman, A. Nassehi, R. Imani-Asrai, and V. Dhokia, "Energy efficient process planning for CNC machining," *CIRP J. Manuf. Sci. Technol.*, vol. 5, no. 2, pp. 127–136, Jan. 2012, doi: 10.1016/J.CIRPJ.2012.03.007.
[126] C. R. Devireddy and K. Ghosh, "Feature-based modelling and neural networks-based CAPP for integrated manufacturing," *https://doi.org/10.1080/095119299130470*, vol. 12, no. 1, pp. 61–74, Jan. 2010, doi: 10.1080/095119299130470.
[127] S. P. Leo Kumar, J. Jerald, and S. Kumanan, "Feature-based modelling and process parameters selection in a CAPP system for prismatic micro parts," *https://doi.org/10.1080/0951192X.2014.953586*, vol. 28, no. 10, pp. 1046–1062, Oct. 2014, doi: 10.1080/0951192X.2014.953586.
[128] A. Mohib, A. Azab, and H. Elmaraghy, "Feature-based hybrid inspection planning: A mathematical programming approach," *https://doi.org/10.1080/09511920802382368*, vol. 22, no. 1, pp. 13–29, 2009, doi: 10.1080/09511920802382368.
[129] X. Qu and B. Stucker, "Circular hole recognition for STL-based toolpath generation," *Rapid Prototyp. J.*, vol. 11, no. 3, pp. 132–139, 2005, doi: 10.1108/13552540510601255/FULL/PDF.
[130] A. K. Verma and S. Rajotia, "A review of machining feature recognition methodologies," *https://doi.org/10.1080/09511921003642121*, vol. 23, no. 4, pp. 353–368, 2010, doi: 10.1080/09511921003642121.
[131] M. Hou and T. N. Faddis, "Automatic tool path generation of a feature-basedCAD/CAPP/CAM integrated system," *https://doi.org/10.1080/09511920500504354*, vol. 19, no. 4, pp. 350–358, Jun. 2007, doi: 10.1080/09511920500504354.
[132] T. Chen and Z. Shi, "A tool path generation strategy for three-axis ball-end milling of free-form surfaces," *J. Mater. Process. Technol.*, vol. 208, no. 1–3, pp. 259–263, Nov. 2008, doi: 10.1016/j.jmatprotec.2007.12.142.
[133] S. Wang, S. To, X. Chen, and X. Chen, "An investigation on surface finishing in ultra-precision raster milling of aluminum alloy 6061," *Proc. Inst. Mech. Eng. Part B J. Eng. Manuf.*, vol. 229, no. 8, pp. 1289–1301, Aug. 2015, doi: 10.1177/0954405414535588.
[134] M. N. Cheng, C. F. Cheung, W. B. Lee, S. To, and L. B. Kong, "Theoretical and experimental analysis of nano-surface generation in ultra-precision raster milling," *Int. J. Mach. Tools Manuf.*, vol. 48, no. 10, pp. 1090–1102, Aug. 2008, doi: 10.1016/j.ijmachtools.2008.02.006.
[135] B. H. Kim and B. K. Choi, "Machining efficiency comparison direction-parallel tool path with contour-parallel tool path," *CAD Comput. Aided Des.*, vol. 34, no. 2, pp. 89–95, Feb. 2002, doi: 10.1016/S0010-4485(00)00139-1.
[136] C. C. A. Chen, Y. S. Juang, and W. Z. Lin, "Generation of fractal toolpaths for irregular shapes of surface finishing areas," in *Journal of Materials Processing Technology*, 2002, vol. 127, no. 2, pp. 146–150, doi: 10.1016/S0924-0136(02)00115-2.
[137] X. Pessoles and C. Tournier, "Automatic polishing process of plastic injection molds on a 5-axis milling center," *J. Mater. Process. Technol.*, vol. 209, no. 7, pp. 3665–3673, Apr. 2009, doi: 10.1016/j.jmatprotec.2008.08.034.

[138] H. K. Nirala and A. Agrawal, “Residual stress inclusion in the incrementally formed geometry using Fractal Geometry Based Incremental Toolpath (FGBIT),” *J. Mater. Process. Technol.*, vol. 279, p. 116575, May 2020, doi: 10.1016/j.jmatprotec.2019.116575.
[139] Y. Mizugaki, M. Sakamoto, and T. Sata, “Fractal Path Generation for a Metal-Mold Polishing Robot System and Its Evaluation by the Operability,” *CIRP Ann. - Manuf. Technol.*, vol. 41, no. 1, pp. 531–534, Jan. 1992, doi: 10.1016/S0007-8506(07)61261-X.
[140] N. Huang, Y. Jin, Y. Lu, B. Yi, X. Li, and S. Wu, “Spiral toolpath generation method for pocket machining,” *Comput. Ind. Eng.*, vol. 139, p. 106142, Jan. 2020, doi: 10.1016/j.cie.2019.106142.
[141] T. Jin, J. Chen, T. Zhao, Q. Zhao, and Y. Tian, “Nanotwinned diamond cutting tool processed by femtosecond pulsed laser milling with trochoidal trajectory,” *J. Mater. Process. Technol.*, vol. 294, p. 117115, Aug. 2021, doi: 10.1016/j.jmatprotec.2021.117115.
[142] H. Gong, S. Ao, K. Huang, Y. Wang, and C. Yan, “Tool path generation of ultra-precision diamond turning: A state-of-the-art review,” *Nami Jishu yu Jingmi Gongcheng/Nanotechnology Precis. Eng.*, vol. 2, no. 3, pp. 118–124, Sep. 2019, doi: 10.1016/j.npe.2019.10.003.
[143] H. yuen Tam and H. Cheng, “An investigation of the effects of the tool path on the removal of material in polishing,” *J. Mater. Process. Technol.*, vol. 210, no. 5, pp. 807–818, Mar. 2010, doi: 10.1016/j.jmatprotec.2010.01.012.
[144] W. Shixiong, M. Wei, L. Bin, and W. Chengyong, “Trochoidal machining for the high-speed milling of pockets,” *J. Mater. Process. Technol.*, vol. 233, pp. 29–43, Jul. 2016, doi: 10.1016/j.jmatprotec.2016.01.033.
[145] J. Du Kim, Y. H. Kang, Y. H. Bae, and S. W. Lee, “Development of a magnetic abrasive jet machining system for precision internal polishing of circular tubes,” *J. Mater. Process. Technol.*, vol. 71, no. 3, pp. 384–393, 1997, doi: 10.1016/S0924-0136(97)00103-9.
[146] K. Sundararaj and M. Bangaru, “IMECE2017-72606,” pp. 1–6, 2018.
[147] D. Nguyen, J. Wu, N. M. Quang, L. A. Duc, and P. X. Son, “Applying fuzzy grey relationship analysis and Taguchi method in polishing surfaces of magnetic materials by using magnetorheological fluid,” *Int. J. Adv. Manuf. Technol.*, vol. 112, no. 5–6, pp. 1675–1689, Jan. 2021, doi: 10.1007/s00170-020-06567-1.
[148] L. Li *et al.*, “Optimized dwell time algorithm in magnetorheological finishing,” *Int. J. Adv. Manuf. Technol.*, vol. 81, no. 5–8, pp. 833–841, Nov. 2015, doi: 10.1007/s00170-015-7263-3.
[149] H. Huang, Z. M. Gong, X. Q. Chen, and L. Zhou, “Robotic grinding and polishing for turbine-vane overhaul,” *J. Mater. Process. Technol.*, vol. 127, no. 2, pp. 140–145, 2002.
[150] H. B. Cheng, Y. Yam, and Y. T. Wang, “Experimentation on MR fluid using a 2-axis wheel tool,” *J. Mater. Process. Technol.*, vol. 209, no. 12–13, pp. 5254–5261, 2009, doi: 10.1016/j.jmatprotec.2009.03.011.
[151] E. S. Gadelmawla, M. M. Koura, T. M. A. Maksoud, I. M. Elewa, and H. H. Soliman, “Roughness parameters,” *J. Mater. Process. Technol.*, vol. 123, no. 1, pp. 133–145, Apr. 2002, doi: 10.1016/S0924-0136(02)00060-2.
[152] X. Wu, Y. Kita, and K. Ikoku, “New polishing technology of free form surface by GC,” *J. Mater. Process. Technol.*, vol. 187, pp. 81–84, 2007.
[153] C. Prakash *et al.*, “Experimental investigation into nano-finishing of β-TNTZ alloy using magnetorheological fluid magnetic abrasive finishing process for orthopedic applications,” *J. Mater. Res. Technol.*, vol. 11, pp. 600–617, Mar. 2021, doi: 10.1016/j.jmrt.2021.01.046.

[154] Z. yuan Jia, X. xuan Zhao, J. wei Ma, S. yu Chen, F. ze Qin, and Z. Liu, "Toolpath generation in sub-regional processing with constraint of constant scallop-height at boundary for complex curved surface," *Precis. Eng.*, vol. 55, pp. 217–230, Jan. 2019, doi: 10.1016/j.precisioneng.2018.09.009.
[155] G. S. Kumar, P. Pandithevan, and A. R. Ambatti, "Fractal raster tool paths for layered manufacturing of porous objects," *Virtual Phys. Prototyp.*, vol. 4, no. 2, pp. 91–104, Jun. 2009, doi: 10.1080/17452750802688215.
[156] A. Sidpara, M. Das, and V. K. Jain, "Rheological characterization of magnetorheological finishing fluid," *Mater. Manuf. Process.*, vol. 24, no. 12, pp. 1467–1478, 2009, doi: 10.1080/10426910903367410.
[157] R. W. Gregorutti, J. E. Grau, F. Sives, and C. I. Elsner, "Mechanical, electrochemical and magnetic behaviour of duplex stainless steel for biomedical applications," *http://dx.doi.org/10.1179/1743284715Y.0000000017*, vol. 31, no. 15, pp. 1818–1824, Dec. 2015, doi: 10.1179/1743284715Y.0000000017.
[158] L. Guan *et al.*, "Pitting resistance of 316 stainless steel after laser shock peening: Determinants of microstructural and mechanical modifications," *J. Mater. Process. Technol.*, vol. 294, p. 117091, Aug. 2021, doi: 10.1016/J.JMATPROTEC.2021.117091.
[159] L. A. Dobrzański, Z. Brytan, M. Actis Grande, and M. Rosso, "Corrosion behavior of vacuum sintered duplex stainless steels," *J. Mater. Process. Technol.*, vol. 191, no. 1–3, pp. 161–164, Aug. 2007, doi: 10.1016/J.JMATPROTEC.2007.03.014.
[160] P. Muñoz-Escalona and P. Maropoulos, "Integrated optimisation of surface roughness and tool performance when face milling 416 SS," *https://doi.org/10.1080/09511920903529230*, vol. 23, no. 3, pp. 248–256, 2010, doi: 10.1080/09511920903529230.
[161] J. C. E. Ferreira and D. M. Ochoa, "A method for generating trochoidal tool paths for 2 1/2 D pocket milling process planning with multiple tools," *Proc. Inst. Mech. Eng. Part B J. Eng. Manuf.*, vol. 227, no. 9, pp. 1287–1298, Sep. 2013, doi: 10.1177/0954405413487897.
[162] M. Otkur and I. Lazoglu, "Trochoidal milling," *Int. J. Mach. Tools Manuf.*, vol. 47, no. 9, pp. 1324–1332, Jul. 2007, doi: 10.1016/j.ijmachtools.2006.08.002.
[163] N. Kardes and Y. Altintas, "Mechanics and dynamics of the circular milling process," *J. Manuf. Sci. Eng. Trans. ASME*, vol. 129, no. 1, pp. 21–31, Feb. 2007, doi: 10.1115/1.2345391.
[164] A. Pleta, D. Ulutan, and L. Mears, "An Investigation of Alternative Path Planning Strategies for Machining of Nickel-Based Superalloys," in *Procedia Manufacturing*, 2015, vol. 1, pp. 556–566, doi: 10.1016/j.promfg.2015.09.032.
[165] A. Pleta, D. Ulutan, and L. Mears, "Investigation of trochoidal milling in nickel-based superalloy inconel 738 and comparison with end milling," in *ASME 2014 International Manufacturing Science and Engineering Conference, MSEC 2014 Collocated with the JSME 2014 International Conference on Materials and Processing and the 42nd North American Manufacturing Research Conference*, 2014, vol. 2, doi: 10.1115/MSEC2014-4151.
[166] I. Szalóki, S. Csuka, and S. Sipos, "New test results in cycloid-forming trochoidal milling," *Acta Polytech. Hungarica*, vol. 11, no. 2, pp. 215–228, 2014, doi: 10.12700/aph.11.02.2014.02.13.
[167] E. Uhlmann, A. Dethlefs, and A. Eulitz, "Investigation of material removal and surface topography formation in vibratory finishing," *Procedia CIRP*, vol. 14, pp. 25–30, 2014, doi: 10.1016/j.procir.2014.03.048.
[168] T. Wang, H. B. Cheng, Z. C. Dong, and H. Y. Tam, "Removal character of vertical jet polishing with eccentric rotation motion using magnetorheological fluid," *J. Mater. Process. Technol.*, vol. 213, no. 9, pp. 1532–1537, Sep. 2013, doi:

10.1016/J.JMATPROTEC.2013.03.017.
[169] V. K. Jain, “Magnetic field assisted abrasive based micro-/nano-finishing,” *J. Mater. Process. Technol.*, vol. 209, no. 20, pp. 6022–6038, Nov. 2009, doi: 10.1016/J.JMATPROTEC.2009.08.015.
[170] R. H. Myers, D. C. Montgomery, G. Geoffrey Vining, C. M. Borror, and S. M. Kowalski, “Response Surface Methodology: A Retrospective and Literature Survey,” *Journal of Quality Technology*, vol. 36, no. 1. American Society for Quality, pp. 53–78, 2004, doi: 10.1080/00224065.2004.11980252.
[171] G. Kiswanto, D. L. Zariatin, and T. J. Ko, “The effect of spindle speed, feed-rate and machining time to the surface roughness and burr formation of Aluminum Alloy 1100 in micro-milling operation,” *J. Manuf. Process.*, vol. 16, no. 4, pp. 435–450, Oct. 2014, doi: 10.1016/J.JMAPRO.2014.05.003.
[172] E. Azarsa and A. Mostafapour, “Experimental investigation on flexural behavior of friction stir welded high density polyethylene sheets,” *J. Manuf. Process.*, vol. 16, no. 1, pp. 149–155, Jan. 2014, doi: 10.1016/J.JMAPRO.2013.12.003.
[173] P. K. Jain, P. M. Pandey, and P. V. M. Rao, “Experimental investigations for improving part strength in selective laser sintering,” *http://dx.doi.org/10.1080/17452750802065893*, vol. 3, no. 3, pp. 177–188, Sep. 2008, doi: 10.1080/17452750802065893.
[174] J. P. Kruth, P. Mercelis, J. Van Vaerenbergh, L. Froyen, and M. Rombouts, “Binding mechanisms in selective laser sintering and selective laser melting,” *Rapid Prototyp. J.*, vol. 11, no. 1, pp. 26–36, 2005, doi: 10.1108/13552540510573365/FULL/PDF.
[175] K. Munir, A. Biesiekierski, C. Wen, and Y. Li, “Selective laser melting in biomedical manufacturing,” *Met. Biomater. Process. Med. Device Manuf.*, pp. 235–269, Jan. 2020, doi: 10.1016/B978-0-08-102965-7.00007-2.
[176] B. Van Hooreweder, Y. Apers, K. Lietaert, and J. P. Kruth, “Improving the fatigue performance of porous metallic biomaterials produced by Selective Laser Melting,” *Acta Biomater.*, vol. 47, pp. 193–202, Jan. 2017, doi: 10.1016/J.ACTBIO.2016.10.005.
[177] M. M. Shalabi, A. Gortemaker, M. A. Van’t Hof, J. A. Jansen, and N. H. J. Creugers, “Implant surface roughness and bone healing: A systematic review,” *J. Dent. Res.*, vol. 85, no. 6, pp. 496–500, Jun. 2006, doi: 10.1177/154405910608500603/SUPPL_FILE/496-JANSEN-APX.PDF.
[178] A. S. Hammood, L. Thair, H. D. Altawaly, and N. Parvin, “Tribocorrosion Behaviour of Ti–6Al–4V Alloy in Biomedical Implants: Effects of Applied Load and Surface Roughness on Material Degradation,” *J. Bio- Tribo-Corrosion*, vol. 5, no. 4, pp. 1–12, Dec. 2019, doi: 10.1007/S40735-019-0277-X/FIGURES/11.
[179] S. Bremen, W. Meiners, and A. Diatlov, “Selective Laser Melting,” *Laser Tech. J.*, vol. 9, no. 2, pp. 33–38, Apr. 2012, doi: 10.1002/LATJ.201290018.
[180] I. Yadroitsev, P. Bertrand, and I. Smurov, “Parametric analysis of the selective laser melting process,” *Appl. Surf. Sci.*, vol. 253, no. 19, pp. 8064–8069, Jul. 2007, doi: 10.1016/J.APSUSC.2007.02.088.
[181] C. Y. Yap *et al.*, “Review of selective laser melting: Materials and applications,” *Appl. Phys. Rev.*, vol. 2, no. 4, p. 041101, Dec. 2015, doi: 10.1063/1.4935926.
[182] C. C. Ng, M. M. Savalani, M. L. Lau, and H. C. Man, “Microstructure and mechanical properties of selective laser melted magnesium,” *Appl. Surf. Sci.*, vol. 257, no. 17, pp. 7447–7454, Jun. 2011, doi: 10.1016/J.APSUSC.2011.03.004.
[183] A. Temmler, E. Willenborg, and K. Wissenbach, “Laser polishing,” *https://doi.org/10.1117/12.906001*, vol. 8243, pp. 171–183, Feb. 2012, doi: 10.1117/12.906001.
[184] S. Marimuthu, A. Triantaphyllou, M. Antar, D. Wimpenny, H. Morton, and M. Beard, “Laser polishing of selective laser melted components,” *Int. J. Mach. Tools Manuf.*, vol.

95, pp. 97–104, Aug. 2015, doi: 10.1016/J.IJMACHTOOLS.2015.05.002.
[185] D. Bhaduri *et al.*, "Pulsed laser polishing of selective laser melted aluminium alloy parts," *Appl. Surf. Sci.*, vol. 558, p. 149887, Aug. 2021, doi: 10.1016/J.APSUSC.2021.149887.
[186] T. Thenard, A. Catapano, R. Allena, M. El May, N. Saintier, and M. Mesnard, "Topography and wettability characterization of surfaces manufactured by SLM and treated by chemical etching," *https://doi.org/10.1080/15376494.2020.1836292*, vol. 29, no. 12, pp. 1674–1691, 2020, doi: 10.1080/15376494.2020.1836292.
[187] E. Farber, D. Nazarov, I. Mitrofanov, V. Sufiiarov, A. Popovich, and M. Maximov, "Development of the titanium meshes by selective laser melting and chemical etching for using as medical implants," *Mater. Today Proc.*, vol. 30, pp. 746–751, Jan. 2020, doi: 10.1016/J.MATPR.2020.01.558.
[188] M. A. Surmeneva *et al.*, "The influence of chemical etching on porous structure and mechanical properties of the Ti6AL4V Functionally Graded Porous Scaffolds fabricated by EBM," *Mater. Chem. Phys.*, vol. 275, p. 125217, Jan. 2022, doi: 10.1016/J.MATCHEMPHYS.2021.125217.
[189] S. Wan, C. Wei, C. Hu, G. Situ, Y. Shao, and J. Shao, "Novel magic angle-step state and mechanism for restraining the path ripple of magnetorheological finishing," *Int. J. Mach. Tools Manuf.*, vol. 161, p. 103673, Feb. 2021, doi: 10.1016/J.IJMACHTOOLS.2020.103673.
[190] A. S. Rajput, A. Singh, S. Kapil, and M. Das, "Investigations on the trochoidal toolpath for processing the biomaterial through magnetorheological fluid assisted finishing process," *J. Manuf. Process.*, vol. 76, pp. 812–827, Apr. 2022, doi: 10.1016/j.jmapro.2022.02.055.
[191] S. Lee, Z. Ahmadi, J. W. Pegues, M. Mahjouri-Samani, and N. Shamsaei, "Laser polishing for improving fatigue performance of additive manufactured Ti-6Al-4V parts," *Opt. Laser Technol.*, vol. 134, p. 106639, Feb. 2021, doi: 10.1016/J.OPTLASTEC.2020.106639.
[192] C. P. Ma, Y. C. Guan, and W. Zhou, "Laser polishing of additive manufactured Ti alloys," *Opt. Lasers Eng.*, vol. 93, pp. 171–177, Jun. 2017, doi: 10.1016/J.OPTLASENG.2017.02.005.
[193] V. Urlea and V. Brailovski, "Electropolishing and electropolishing-related allowances for powder bed selectively laser-melted Ti-6Al-4V alloy components," *J. Mater. Process. Technol.*, vol. 242, pp. 1–11, Apr. 2017, doi: 10.1016/J.JMATPROTEC.2016.11.014.
[194] G. M. Tsoeunyane, N. Mathe, L. Tshabalala, and M. E. Makhatha, "Electropolishing of Additively Manufactured Ti-6Al-4V Surfaces in Nontoxic Electrolyte Solution," *Adv. Mater. Sci. Eng.*, vol. 2022, 2022, doi: 10.1155/2022/6987353.
[195] E. M. M. Sutter and G. J. Goetz-Grandmont, "The behaviour of titanium in nitric-hydrofluoric acid solutions," *Corros. Sci.*, vol. 30, no. 4–5, pp. 461–476, Jan. 1990, doi: 10.1016/0010-938X(90)90051-6.
[196] R. Poduska, D. Fister, N. Green, and P. McAndrew, "Hazardous waste reduction from mixed acid titanium etching," *Clean Technol. Environ. Policy*, vol. 14, no. 1, pp. 69–78, Apr. 2012, doi: 10.1007/S10098-011-0377-X/TABLES/5.
[197] W. C. Say and Y. Y. Tsai, "Surface characterization of cast Ti-6Al-4V in hydrofluoric-nitric pickling solutions," *Surf. Coatings Technol.*, vol. 176, no. 3, pp. 337–343, Jan. 2004, doi: 10.1016/S0257-8972(03)00747-3.
[198] B. Sefer, I. Dobryden, N. Almqvist, R. Pederson, and M. L. Antti, "Chemical Milling of Cast Ti-6Al-4V and Ti-6Al-2Sn-4Zr-2Mo Alloys in Hydrofluoric-Nitric Acid Solutions," *Corrosion*, vol. 73, no. 4, pp. 394–407, Apr. 2017, doi: 10.5006/2277.
[199] G. Pyka, G. Kerckhofs, I. Papantoniou, M. Speirs, J. Schrooten, and M. Wevers,

"Surface Roughness and Morphology Customization of Additive Manufactured Open Porous Ti6Al4V Structures," *Mater. 2013, Vol. 6, Pages 4737-4757*, vol. 6, no. 10, pp. 4737–4757, Oct. 2013, doi: 10.3390/MA6104737.

[200] B. Wysocki *et al.*, "The influence of chemical polishing of titanium scaffolds on their mechanical strength and in-vitro cell response," *Mater. Sci. Eng. C*, vol. 95, pp. 428–439, Feb. 2019, doi: 10.1016/J.MSEC.2018.04.019.

[201] A. V. Balyakin, A. N. Shvetcov, and E. I. Zhuchenko, "Chemical polishing of samples obtained by selective laser melting from titanium alloy Ti6Al4V," *MATEC Web Conf.*, vol. 224, p. 01031, Oct. 2018, doi: 10.1051/MATECCONF/201822401031.

[202] A. S. Rajput, M. Das, and S. Kapil, "Investigations on a hybrid chemo-magnetorheological finishing process for freeform surface quality enhancement," *J. Manuf. Process.*, vol. 81, pp. 522–536, Sep. 2022, doi: 10.1016/J.JMAPRO.2022.07.015.

[203] M. Bezuidenhout, G. Ter Haar, T. Becker, S. Rudolph, O. Damm, and N. Sacks, "The effect of HF-HNO3 chemical polishing on the surface roughness and fatigue life of laser powder bed fusion produced Ti6Al4V," *Mater. Today Commun.*, vol. 25, p. 101396, Dec. 2020, doi: 10.1016/J.MTCOMM.2020.101396.

[204] J. Zhang, Y. Jian, X. Zhao, D. Meng, F. Pan, and Q. Han, "The tribological behavior of a surface-nanocrystallized magnesium alloy AZ31 sheet after ultrasonic shot peening treatment," *J. Magnes. Alloy.*, vol. 9, no. 4, pp. 1187–1200, Jul. 2021, doi: 10.1016/J.JMA.2020.11.012.

[205] R. W. Phillips, "Engineering applications of fluids with a variable yield stress D. Eng," Thesis, 1969.

[206] J. D. Carlson, "What makes a good MR fluid?," *J. Intell. Mater. Syst. Struct.*, vol. 13, no. 7–8, pp. 431–435, 2002, doi: 10.1106/104538902028221.

[207] J. D. Carlson, D. M. Catanzarite, and K. A. S. Clair, "Lord Corporation, Cary, NC 27511 USA," in *Commercial Magneto-Rheological Fluid Device, Proceedings of the 5th International Conference on ER Fluids, MR Fluids and Associated Technology, U. Sheffield, UK*, 1995, pp. 20–28.

[208] J. Huang, J. Q. Zhang, Y. Yang, and Y. Q. Wei, "Analysis and design of a cylindrical magneto-rheological fluid brake," *J. Mater. Process. Technol.*, vol. 129, no. 1–3, pp. 559–562, 2002, doi: 10.1016/S0924-0136(02)00634-9.

[209] P. L. Wong, W. A. Bullough, C. Feng, and S. Lingard, "Tribological performance of a magneto-rheological suspension," *Wear*, vol. 247, no. 1, pp. 33–40, 2001, doi: 10.1016/S0043-1648(00)00507-X.

[210] M. T. López-López, A. Zugaldía, F. González-Caballero, and J. D. G. Durán, "Sedimentation and redispersion phenomena in iron-based magnetorheological fluids," *J. Rheol. (N. Y. N. Y).*, vol. 50, no. 4, pp. 543–560, 2006, doi: 10.1122/1.2206716.

[211] R. E. Rosensweig, "Ferrohydrodynamics Cambridge University Press Cambridge," *New York, Melb.*, 1985.

[212] J. H. Kim, C. Kim, S. G. Lee, T. M. Hong, and J. H. Choi, "Viscosity of magnetorheological fluids using iron--silicon nanoparticles," *J. Nanosci. Nanotechnol.*, vol. 13, no. 9, pp. 6055–6059, 2013.

[213] K. Wang, X. Dong, J. Li, K. Shi, and K. Li, "Effects of silicone oil viscosity and carbonyl iron particleweight fraction and size on yield stress for magnetorheological grease based on a new preparation technique," *Materials (Basel).*, vol. 12, no. 11, pp. 7–9, 2019, doi: 10.3390/ma12111778.

[214] C. Sarkar and H. Hirani, "Synthesis and characterization of antifriction magnetorheological fluids for brake," *Def. Sci. J.*, vol. 63, no. 4, pp. 408–412, 2013, doi: 10.14429/dsj.63.2633.

[215] G. Bossis, O. Volkova, S. Lacis, and A. Meunier, "Magnetorheology: Fluids, Structures

and Rheology," in *Ferrofluids: Magnetically Controllable Fluids and Their Applications*, S. Odenbach, Ed. Berlin, Heidelberg: Springer Berlin Heidelberg, 2002, pp. 202–230.
[216] J. de Vicente, M. T. López-López, F. González-Caballero, and J. D. G. Durán, "Rheological study of the stabilization of magnetizable colloidal suspensions by addition of silica nanoparticles," *J. Rheol. (N. Y. N. Y).*, vol. 47, no. 5, pp. 1093–1109, 2003, doi: 10.1122/1.1595094.
[217] P. P. Phulé and J. M. Ginder, "Synthesis and properties of novel magnetorheological fluids having improved stability and redispersibility," *Int. J. Mod. Phys. B*, vol. 13, no. 14n16, pp. 2019–2027, 1999.
[218] P. J. Rankin, A. T. Horvath, and D. J. Klingenberg, "Magnetorheology in viscoplastic media," *Rheol. Acta*, vol. 38, no. 5, pp. 471–477, 1999, doi: 10.1007/s003970050198.
[219] J. H. Park, B. D. Chin, and O. O. Park, "Rheological properties and stabilization of magnetorheological fluids in a water-in-oil emulsion," *J. Colloid Interface Sci.*, vol. 240, no. 1, pp. 349–354, 2001, doi: 10.1006/jcis.2001.7622.
[220] B. D. Chin, J. H. Park, M. H. Kwon, and O. O. Park, "Rheological properties and dispersion stability of magnetorheological (MR) suspensions," *Rheol. Acta*, vol. 40, no. 3, pp. 211–219, 2001, doi: 10.1007/s003970000150.
[221] M. T. López-López, J. De Vicente, F. González-Caballero, and J. D. G. Durán, "Stability of magnetizable colloidal suspensions by addition of oleic acid and silica nanoparticles," *Colloids Surfaces A Physicochem. Eng. Asp.*, vol. 264, no. 1–3, pp. 75–81, 2005, doi: 10.1016/j.colsurfa.2005.05.026.
[222] J. Wang, W. Chen, and F. Han, "Study on the magnetorheological finishing method for the WEDMed pierced die cavity," *Int. J. Adv. Manuf. Technol.*, vol. 76, no. 9–12, pp. 1969–1975, 2015, doi: 10.1007/s00170-014-6402-6.
[223] M. S. Niranjan and S. Jha, "Experimental investigation into tool aging effect in ball end magnetorheological finishing," *Int. J. Adv. Manuf. Technol.*, vol. 80, no. 9–12, pp. 1895–1902, 2015, doi: 10.1007/s00170-015-6996-3.
[224] S. Chen, S. Li, H. Hu, G. Tie, C. Guan, and Q. Li, "Analysis of surface quality and processing optimization of magnetorheological polishing of KDP crystal," *J. Opt.*, vol. 44, no. 4, pp. 384–390, 2015, doi: 10.1007/s12596-015-0272-7.
[225] J. Pan and Q. Yan, "Material removal mechanism of cluster magnetorheological effect in plane polishing," *Int. J. Adv. Manuf. Technol.*, vol. 81, no. 9–12, pp. 2017–2026, 2015, doi: 10.1007/s00170-015-7332-7.
[226] A. S. Rajput, D. Prasad, A. K. Mondal, and D. Bose, "2D Computational Fluid Dynamics Analysis into Rotational Magnetorheological Abrasive Flow Finishing (R-MRAFF) Process," in *Advances in Materials and Manufacturing Engineering*, Springer, 2020, pp. 67–73.
[227] F. Ji *et al.*, "The Magnetorheological Finishing (MRF) of Potassium Dihydrogen Phosphate (KDP) Crystal with Fe3O4 Nanoparticles," *Nanoscale Res. Lett.*, vol. 11, no. 1, pp. 1–7, 2016, doi: 10.1186/s11671-016-1301-4.
[228] Y. Wang, Y. Zhang, and Z. Feng, "Analyzing and improving surface texture by dual-rotation magnetorheological finishing," *Appl. Surf. Sci.*, 2016, doi: 10.1016/j.apsusc.2015.11.009.
[229] H. Liu, M. Chen, B. Yu, and Z. Fang, "Configuration design and accuracy analysis of a novel magnetorheological finishing machine tool for concave surfaces with small radius of curvature," *J. Mech. Sci. Technol.*, vol. 30, no. 7, pp. 3301–3311, 2016, doi: 10.1007/s12206-016-0639-y.
[230] W. B. Kim, E. Nam, B. K. Min, D. S. Choi, T. J. Je, and E. C. Jeon, "Material removal of glass by magnetorheological fluid jet," *Int. J. Precis. Eng. Manuf.*, vol. 16, no. 4, pp. 629–637, 2015, doi: 10.1007/s12541-015-0084-3.

[231] M. Chen, H. Liu, Y. Su, B. Yu, and Z. Fang, “Design and fabrication of a novel magnetorheological finishing process for small concave surfaces using small ball-end permanent-magnet polishing head,” *Int. J. Adv. Manuf. Technol.*, vol. 83, no. 5–8, pp. 823–834, 2016.
[232] J. Seok, S. O. Lee, K.-I. Jang, B.-K. Min, and S. J. Lee, “Tribological properties of a magnetorheological (MR) fluid in a finishing process,” *Tribol. Trans.*, vol. 52, no. 4, pp. 460–469, 2009.
[233] S. D. Jacobs *et al.*, “<title>Magnetorheological finishing of IR materials</title>,” in *Optical Manufacturing and Testing II*, 1997, vol. 3134, pp. 258–269, doi: 10.1117/12.295132.
[234] V. K. Jain *et al.*, “Some investigations into magnetorheological finishing (MRF) of hard materials,” in *Proceedings of the ASME International Manufacturing Science and Engineering Conference 2009, MSEC2009*, 2009, vol. 2, pp. 261–270, doi: 10.1115/MSEC2009-84335.
[235] Z. Peng, W. L. Song, C. L. Ye, P. Shi, and S. B. Choi, “Model establishment of surface roughness and experimental investigation on magnetorheological finishing for polishing the internal surface of titanium alloy tubes,” *J. Intell. Mater. Syst. Struct.*, p. 1045389X2093009, Jun. 2020, doi: 10.1177/1045389X20930095.
[236] L. Nagdeve, V. K. Jain, and J. Ramkumar, “Development of inverse replica fixture for nano-finishing of knee joint using R-MRAFF process,” *J. Micromanufacturing*, vol. 2, no. 1, pp. 35–41, May 2019, doi: 10.1177/2516598418811460.
[237] C. Miao, J. C. Lambropoulos, and S. D. Jacobs, “Process parameter effects on material removal in magnetorheological finishing of borosilicate glass,” *Appl. Opt.*, vol. 49, no. 10, pp. 1951–1963, Apr. 2010, doi: 10.1364/AO.49.001951.
[238] M. S. Niranjan and S. Jha, “Optimum selection of machining parameters in ball end magnetorheological finishing process,” *Int. J. Precis. Technol.*, vol. 5, no. 3/4, p. 217, 2015, doi: 10.1504/ijptech.2015.073826.
[239] P. Ranjan, R. Balasubramaniam, and V. K. Jain, “Analysis of magnetorheological fluid behavior in chemo-mechanical magnetorheological finishing (CMMRF) process,” *Precis. Eng.*, vol. 49, pp. 122–135, 2017.
[240] N. Khatri, J. Xavier Manoj, V. Mishra, H. Garg, and V. Karar, “Experimental and simulation study of nanometric surface roughness generated during Magnetorheological finishing of Silicon,” in *Materials Today: Proceedings*, 2018, vol. 5, no. 2, pp. 6391–6400, doi: 10.1016/j.matpr.2017.12.250.
[241] G. Yang, B. F. Spencer, J. D. Carlson, and M. K. Sain, “Large-scale MR fluid dampers: modeling and dynamic performance considerations,” *Eng. Struct.*, vol. 24, no. 3, pp. 309–323, 2002, doi: https://doi.org/10.1016/S0141-0296(01)00097-9.
[242] J. D. Carlson and M. R. Jolly, “MR fluid, foam and elastomer devices,” *Mechatronics*, vol. 10, no. 4, pp. 555–569, 2000, doi: https://doi.org/10.1016/S0957-4158(99)00064-1.
[243] A. Ghaffari, S. H. Hashemabadi, and M. Ashtiani, “A review on the simulation and modeling of magnetorheological fluids,” *J. Intell. Mater. Syst. Struct.*, vol. 26, no. 8, pp. 881–904, 2015, doi: 10.1177/1045389X14546650.
[244] J. de Vicente, F. Vereda, J. P. Segovia-Gutiérrez, M. del Puerto Morales, and R. Hidalgo-Álvarez, “Effect of particle shape in magnetorheology,” *J. Rheol. (N. Y. N. Y).*, vol. 54, no. 6, pp. 1337–1362, 2010, doi: 10.1122/1.3479045.
[245] A. Farjoud, N. Vahdati, and Y. F. Fah, “Mathematical model of drum-type MR brakes using herschel-bulkley shear model,” *J. Intell. Mater. Syst. Struct.*, vol. 19, no. 5, pp. 565–572, 2008, doi: 10.1177/1045389X07077851.
[246] D. Kittipoomwong, D. J. Klingenberg, and J. C. Ulicny, “Dynamic yield stress enhancement in bidisperse magnetorheological fluids,” *J. Rheol. (N. Y. N. Y).*, vol. 49, no. 6, pp. 1521–1538, 2005, doi: 10.1122/1.2085175.

[247] V. C. Kelessidis and R. Maglione, “Modeling rheological behavior of bentonite suspensions as Casson and Robertson-Stiff fluids using Newtonian and true shear rates in Couette viscometry,” *Powder Technol.*, vol. 168, no. 3, pp. 134–147, 2006, doi: 10.1016/j.powtec.2006.07.011.
[248] M. E. Sayed-Ahmed and A. S. El-Yazal, “Laminar fully developed flow and heat transfer of Robertson Stiff fluids in a rectangular duct,” *Can. J. Phys.*, vol. 83, no. 2, pp. 165–182, 2005.
[249] D. H. Pelegrine, F. C. Silva, and C. A. Gasparetto, “Rheological behavior of pineapple and mango pulps,” *LWT - Food Sci. Technol.*, vol. 35, no. 8, pp. 645–648, 2002, doi: 10.1006/fstl.2002.0920.
[250] K. Song, Y. Kim, and G. Chang, “r o i v a h e B w o l F r a e h S y d a e t S : s n o i t u l o S m u G n a h t n a X d e t a r t n e c n o C f o y g o l o e h R,” vol. 7, no. 2, pp. 129–138, 2006.
[251] H. A. Barnes, “The yield stress - a review - everything flows?,” *J. Nonnewton. Fluid Mech.*, vol. 81, no. May 1998, pp. 133–178, 1999.
[252] J. De Vicente, D. J. Klingenberg, and R. Hidalgo-Alvarez, “Magnetorheological fluids: A review,” *Soft Matter*, vol. 7, no. 8, pp. 3701–3710, 2011, doi: 10.1039/c0sm01221a.
[253] H. J. Choi, T. M. Kwon, and M. S. Jhon, “Effects of shear rate and particle concentration on rheological properties of magnetic particle suspensions,” *J. Mater. Sci.*, vol. 35, no. 4, pp. 889–894, 2000, doi: 10.1023/A:1004742223080.
[254] A. W. Sisko, “The Flow of Lubricating Greases,” *Ind. Eng. Chem.*, vol. 50, no. 12, pp. 1789–1792, 1958, doi: 10.1021/ie50588a042.
[255] M. Nehdi and M. A. Rahman, “Estimating rheological properties of cement pastes using various rheological models for different test geometry, gap and surface friction,” *Cem. Concr. Res.*, vol. 34, no. 11, pp. 1993–2007, 2004, doi: 10.1016/j.cemconres.2004.02.020.
[256] W. I. Kordonsky *et al.*, “51) (52) 58) (56) MAGNETORHEOLOGICAL POLISHENG DEVICES AND METHODS,” Jun. 1993.
[257] D. C. Harris, “History of magnetorheological finishing,” *Proc.SPIE*, vol. 8016, pp. 8016-8016–22, 2011, doi: 10.1117/12.882557.
[258] S. D. Jacobs *et al.*, “Magnetorheological finishing: a deterministic process for optics manufacturing,” in *International Conference on Optical Fabrication and Testing*, 1995, vol. 2576, pp. 372–383.
[259] D. Golini, S. D. Jacobs, W. I. Kordonski, and P. Dumas, “Precision optics fabrication using magnetorheological finishing,” in *Advanced Materials for Optics and Precision Structures: A Critical Review*, 1997, vol. 10289, p. 102890H, doi: 10.1117/12.279809.
[260] J. D. Carlson, D. M. Catanzarite, and K. A. S. Clair, “Commercial magneto-rheological fluid devices,” *Int. J. Mod. Phys. B*, vol. 10, no. 23–24, pp. 2857–2865, Oct. 1996, doi: 10.1142/s0217979296001306.
[261] W. Kordonski and S. Gorodkin, “Material removal in magnetorheological finishing of optics,” *Appl. Opt.*, vol. 50, no. 14, pp. 1984–1994, May 2011, doi: 10.1364/AO.50.001984.
[262] M. Schinhaerl *et al.*, “Forces acting between polishing tool and workpiece surface in magnetorheological finishing,” *Curr. Dev. Lens Des. Opt. Eng. IX*, vol. 7060, p. 706006, 2008.
[263] Z. Yang, H. Hu, and Y. Gao, “The research in algorithm for MRF forming dwell time of optical components,” in *Advanced Materials Research*, 2010, vol. 102–104, pp. 750–753, doi: 10.4028/www.scientific.net/AMR.102-104.750.
[264] S. D. Jacobs, “Manipulating mechanics and chemistry in precision optics finishing,” *Sci. Technol. Adv. Mater.*, vol. 8, no. 3, p. 153, 2007.
[265] J. Seok, Y. J. Kim, K. I. Jang, B. K. Min, and S. J. Lee, “A study on the fabrication of

curved surfaces using magnetorheological fluid finishing," *Int. J. Mach. Tools Manuf.*, vol. 47, no. 14, pp. 2077–2090, 2007, doi: 10.1016/j.ijmachtools.2007.05.007.
[266] A. K. Singh, S. Jha, and P. M. Pandey, "Magnetorheological ball end finishing process," *Mater. Manuf. Process.*, vol. 27, no. 4, pp. 389–394, 2012.
[267] Z. Alam and S. Jha, "Modeling of surface roughness in ball end magnetorheological finishing (BEMRF) process," *Wear*, vol. 374–375, pp. 54–62, 2017, doi: https://doi.org/10.1016/j.wear.2016.11.039.
[268] G. Singh, A. K. Singh, and P. Garg, "Development of magnetorheological finishing process for external cylindrical surfaces," *Mater. Manuf. Process.*, vol. 32, no. 5, pp. 581–588, 2017.
[269] A. K. Singh, S. Jha, and P. M. Pandey, "Mechanism of material removal in ball end magnetorheological finishing process," *Wear*, vol. 302, no. 1–2, pp. 1180–1191, 2013.
[270] Z. Alam, F. Iqbal, S. Ganesan, and S. Jha, "Nanofinishing of 3D surfaces by automated five-axis CNC ball end magnetorheological finishing machine using customized controller," *Int. J. Adv. Manuf. Technol.*, vol. 100, no. 5–8, pp. 1031–1042, 2019, doi: 10.1007/s00170-017-1518-0.
[271] D. A. Khan, Z. Alam, and S. Jha, "Nanofinishing of Copper Using Ball End Magnetorheological Finishing (BEMRF) Process," 2016, doi: 10.1115/imece2016-65974.
[272] S. Jha and V. K. Jain, "Design and development of the magnetorheological abrasive flow finishing (MRAFF) process," *Int. J. Mach. Tools Manuf.*, vol. 44, no. 10, pp. 1019–1029, 2004.
[273] M. Das, V. K. Jain, and P. S. Ghoshdastidar, "Fluid flow analysis of magnetorheological abrasive flow finishing (MRAFF) process," *Int. J. Mach. Tools Manuf.*, vol. 48, no. 3, pp. 415–426, 2008, doi: https://doi.org/10.1016/j.ijmachtools.2007.09.004.
[274] M. Das, V. K. Jain, and P. S. Ghoshdastidar, "The Out-of-Roundness of the Internal Surfaces of Stainless Steel Tubes Finished by the Rotational–Magnetorheological Abrasive Flow Finishing Process," *Mater. Manuf. Process.*, vol. 26, no. 8, pp. 1073–1084, 2011, doi: 10.1080/10426914.2010.537141.
[275] S. Kumar, V. K. Jain, and A. Sidpara, "Nanofinishing of freeform surfaces (knee joint implant) by rotational-magnetorheological abrasive flow finishing (R-MRAFF) process," *Precis. Eng.*, vol. 42, pp. 165–178, 2015, doi: https://doi.org/10.1016/j.precisioneng.2015.04.014.
[276] A. K. Mondal, A. S. Rajput, D. Prasad, and D. Bose, "Magnetic Field Assisted Finishing Processes," in *Advances in Abrasive Based Machining and Finishing Processes*, Springer, 2020, pp. 211–234.
[277] M. Das, V. K. Jain, and P. S. Ghoshdastidar, "Parametric Study of Process Parameters and Characterization of Surface Texture Using Rotational-Magnetorheological Abrasive Flow Finishing (R-MRAFF) Process," in *ASME 2009 International Manufacturing Science and Engineering Conference*, 2009, pp. 251–260.
[278] M. Das, V. K. Jain, and P. S. Ghoshdastidar, "Nano-finishing of stainless-steel tubes using rotational magnetorheological abrasive flow finishing process," *Mach. Sci. Technol.*, vol. 14, no. 3, pp. 365–389, 2010.
[279] D. T.-I. J. for N. M. in and undefined 2002, "Topology optimization of resonating structures using SIMP method," *Wiley Online Libr.*, vol. 54, no. 11, pp. 1605–1622, Aug. 2002, doi: 10.1002/nme.484.
[280] G. I. N. Rozvany, "The SIMP method in topology optimization - Theoretical background, advantages and new applications," *8th Symp. Multidiscip. Anal. Optim.*, 2000, doi: 10.2514/6.2000-4738.
[281] W. Zuo and K. Saitou, "Multi-material topology optimization using ordered SIMP interpolation," *Struct. Multidiscip. Optim.*, vol. 55, no. 2, pp. 477–491, Feb. 2017, doi:

10.1007/S00158-016-1513-3.
[282] A. S. Rajput, A. Singh, S. Kapil, and M. Das, “Investigations on the toolpath strategies for CNC magnetorheological fluid assisted finishing (MFAF) process,” *Int. J. Adv. Manuf. Technol.*, vol. 121, no. 1, pp. 949–966, May 2022, doi: 10.1007/S00170-022-09307-9/TABLES/4.
[283] A. S. Rajput, S. Kapil, and M. Das, “Computer-aided process planning system for super finishing of flat surfaces with pockets through magnetorheological finishing process,” *https://doi.org/10.1080/0951192X.2023.2189313*, pp. 1–17, Mar. 2023, doi: 10.1080/0951192X.2023.2189313.

Publications

Journal Publications

1. **Atul Singh Rajput**, Ambrish Singh, Sajan Kapil, and Manas Das "Investigations on the trochoidal toolpath for processing the biomaterial through magnetorheological fluid assisted finishing process." *Journal of Manufacturing Processes* 76 (2022): 812-827.
2. **Atul Singh Rajput**, Ambrish Singh, Manas Das, and Sajan Kapil, "Investigations on the Toolpath Strategies for CNC Magnetorheological Fluid Assisted Finishing (MFAF) Process." *Journal of Advanced Manufacturing and Technology* 1-18.
3. **Atul Singh Rajput**, Manas Das, and Sajan Kapil, "Characterization of Wear Resistance and Corrosion during Magnetorheological Fluid Assisted Finishing (MFAF) of Ti-6Al-4V and Duplex Stainless Steel for enhanced biocompatibility." *Proceedings of the Institution of Mechanical Engineers, Part E: Journal of Process Mechanical Engineering. June 2022.*
4. **Atul Singh Rajput**, Manas Das, and Sajan Kapil, "A comprehensive review of the magnetorheological assisted finishing process." *Machining Science and Technology* 26:3 (2022), 339-376
5. **Atul Singh Rajput**, Manas Das, and Sajan Kapil, "Surface Properties and Biocompatibility studies on Bone Plate by the Magnetorheological Finishing (MRF) process." *Surface Engineering* (2022): 1-10
6. **Atul Singh Rajput**, Sajan Kapil, and Manas Das, "Investigation on Biotribology of Post Processed Additively Manufactured Biomaterial through Magnetorheological Fluid Assisted Finishing process". *Wear* 522 (2023): 204684.
7. **Atul Singh Rajput**, Manas Das, and Sajan Kapil, "Computer-Aided Process Planning (CAPP) System for Super Finishing of Flat Surfaces with Pockets through Magnetorheological Finishing (MRF) process." *International Journal of Computer Integrated Manufacturing* (2023): 1-17.
8. **Atul Singh Rajput**, Manas Das, and Sajan Kapil, "Investigation on tribological behavior of additively manufactured bone plate polished through Magnetorheological Fluid Assisted Finishing process." *3D Printing and Additive Manufacturing* (2023).
9. **Atul Singh Rajput**, Manas Das, and Sajan Kapil, "Surface Enhancement of Additively Manufactured Biomaterial with Hybrid-Electrochemical Magnetorheological (H-

ECMR) process." *CIRP Journal of Manufacturing Science and Technology* 45 (2023): 99-112.

10. **Atul Singh Rajput**, Ambrish Singh Manas Das, and Sajan Kapil, "Nanofinishing of Directed Energy Deposited Topologically Optimized fixation plates." *Materials and Manufacturing* (Accepted)
11. **Atul Singh Rajput**, Manas Das, and Sajan Kapil, "A Hybrid-Electrochemical Magnetorheological (H-ECMR) Finishing Process for the Surface Enhancement of Biomedical Implants." *Journal of Manufacturing Science and Engineering* (Under review)
12. **Atul Singh Rajput**, Manas Das, and Sajan Kapil, "Machine-learning-based optimization of hybrid electrochemical magnetorheological finishing process to achieve nano finishing on additively manufactured biomaterial." *Journal of Adhesion Science and Technology* (Under review)

Collaborative work

13. **Atul Singh Rajput**, Manas Das, and Sajan Kapil, "Investigations on a Hybrid Chemo-Magnetorheological Finishing process for the freeform surface quality enhancement."Journal of Manufacturing Processes 81(2022):522-536.
14. Ambrish Singh, **Atul Singh Rajput**, Sajan Kapil, and Manas Das "Parameter Sensitivity Analysis of Centrifugal Spreaders for Dispersing Metallic Powders and Material Property Calibration for DEM Simulation." Powder Technology.
15. **Atul Singh Rajput**, Manas Das, and Sajan Kapil, "Optimization of Surface Roughness Parameters in Chemo-Magnetorheological Finishing (C-MRF) Process using Response Surface Methodology and Genetic Algorithm." *Proceedings of the Institution of Mechanical Engineers, Part C* 2023;0(0).
16. **Atul Singh Rajput**, Abhishek Patil, Manas Das, and Sajan Kapil, "Investigations on Chemical Vapor Smoothing Process for Surface Enhancement of Additively Manufactured Clear Aligners." *Journal of the Mechanical Behavior of Biomedical Materials.*

Conference publications

1. Sayan Doloi, **Atul Singh Rajput,** Sajan Kapil, and Manas Das – Hybrid Additive Manufacturing of Knee Joint Implant: Possibilities and Challenges, All India

Manufacturing Technology, Design and Research. (AIMTDR), PSG College of Technology -India (2021)

2. **Atul Singh Rajput,** Sajan Kapil, and Manas Das – Hybrid Additive Manufacturing of Knee Joint Implant: Possibilities and Challenges, 2nd Virtual International Tribology Research Symposium, SRM University, India (2021)
3. **Atul Singh Rajput,** Sajan Kapil, and Manas Das – Surface Enhancement of Additively Manufactured biomedical implants through Hybrid-Electrochemical Magnetorheological (H-ECMR) finishing, International Conference on Precision, Micro, Meso and Nano Engineering (COPEN), IIT Kanpur, India (2022)
4. **Atul Singh Rajput,** Sajan Kapil, and Manas Das – Investigation on tribological behavior of additively manufactured bone plate polished through Magnetorheological Fluid Assisted Finishing process, IndiaTrib, IIT Delhi, India (2022)

Patents

1. **Atul Singh Rajput**, Manas Das, and Sajan Kapil, 2021, *" Method and Apparatus for Magnetorheological Fluid-Assisted Finishing (MFAF) of Cemented Carbide Based Cutting Tool"*, Indian Patent, Application Number: 202231006807
2. **Atul Singh Rajput**, Sajan Kapil, and Manas Das, 2021, *" An Apparatus for Enabling Magnetorheological Fluid Assisted Finishing (MFAF) Process"*, Indian Patent, Application Number: 202131048986
3. **Atul Singh Rajput**, Sajan Kapil, and Manas Das, 2021, *" A Method for Performing Magnetorheological Fluid-Assisted Finishing (MFAF) on a Product having a Hole Feature"*, Indian Patent, Application Number: 202231032416
4. **Atul Singh Rajput**, Sajan Kapil, and Manas Das, 2021, *" Method and apparatus for chemical etching of the additively manufactured head manufactured from Ti-6Al-4V "*, Indian Patent, Application Number: 202231064595

Book chapters

1. **Atul Singh Rajput,** Sajan Kapil, and Manas Das, "Methods for Surface Superfinishing of Prosthesis." Advanced Micro-and Nano-manufacturing Technologies. Springer, Singapore, 2022. 335-360
2. **Atul Singh Rajput,** Sajan Kapil, and Manas Das, "Computational Techniques for Predicting Process Parameters in the Magnetorheological Fluid-Assisted Finishing Process." Advanced Computational Methods in Mechanical and Materials Engineering. CRC Press, 2021. 125-146

3. **Atul Singh Rajput**, Deokant Prasad, Arpan Kumar Mondal, and Dipankar Bose, 2D Computational Fluid Dynamics Analysis into Rotational Magnetorheological Abrasive Flow Finishing (R-MRAFF) Process, In *Advances in Materials and Manufacturing Engineering*, Springer, 2020: pp. 67–73
4. Doloi, S., **Atul Singh Rajput**, Kapil, S., Das, M. (2023). Hybrid Additive Manufacturing of Knee Joint Implant: Possibilities and Challenges. In: Ramesh Babu, N., Kumar, S., Thyla, P.R., Sripriyan, K. (eds) Advances in Additive Manufacturing and Metal Joining. Lecture Notes in Mechanical Engineering. Springer

Awards

1. Received the **Young Tribologist Award** and prize money of 500 USD during **IndiaTrib-2022** (11^{th} International Conference on Industrial Tribology (ICIT)) organized by IIT Delhi.
2. Received **runner-up award for oral presentation** during **IndiaTrib-2022** (11^{th} International Conference on Industrial Tribology (ICIT)) organized by IIT Delhi.
3. Received **1^{st} prize** in an oral presentation during Research and Industrial Conclave (RIC'23) at IIT Guwahati.